Scanning Probe Microscopy of Adsorbed Molecules on Boron Nitride and Graphene Monolayers

by Andrew J. Pollard, MSci (Hons)

Thesis submitted to The University of Nottingham
for the degree of Doctor of Philosophy

December 2010

Abstract

In this thesis, a study of a range of functional surfaces formed in ultra-high vacuum (UHV) conditions using primarily scanning probe microscopy is presented. The construction of a combined scanning tunnelling and atomic force microscope, and the experiments performed using this instrument, are also detailed.

Boron nitride and graphene monolayers were formed on rhodium thin films in UHV and investigated with in-situ and ex-situ (ambient conditions) scanning tunnelling microscopy. Simultaneous scanning tunnelling and atomic force microscopy images were also produced for the graphene monolayers. X-ray photoelectron spectroscopy and diffraction results for graphene monolayers on Rh(111) surfaces, as well as low energy electron diffraction data, are also included.

The novel formation of monolayer and few-layer graphene on nickel thin films is also described. Graphene layers were detached from these nickel thin films and isolated on other substrates. The results of characterisation experiments using scanning probe microscopy, X-ray photoelectron spectroscopy, X-ray diffraction and electron microscopy techniques are detailed. Graphene layers with approximately 75% monolayer graphene coverage and an increased electronic quality, when compared to many other methods of graphene production, were revealed.

Different organic molecules were adsorbed on both the boron nitride and graphene monolayers formed on rhodium thin films in UHV conditions. Perylene tetracarboxylic diimide (PTCDI) and di(propylthio)-PTCDI molecules were investigated on these surfaces and compared with the adsorption of PTCDI on a graphite surface. Furthermore, dibutyl-coronene tetra-carboxylic diimide was deposited on the graphene (on rhodium) surface, in UHV. Although the boron nitride and graphene surfaces were similar, it was discovered that very contrasting molecular formations were formed on the different surfaces. The positioning of these nanostructures was determined by the Moiré superstructure formed due to the mismatch between the monolayers and the Rh(111) surface. Additionally, different hydrogen-bonded molecular junctions were formed depending on the length of the side chains of the adsorbed organic molecules.

List of publications

1. *Dynamic scanning probe microscopy of adsorbed molecules on graphite,*
   N. Berdunov, A. J. Pollard and P. H. Beton, *Appl. Phys. Lett.*, **94**, 043110 (2009)

2. *Perylene behaviour on boron-nitride nanomesh,*
   E. W. Perkins, A. J. Pollard and P. H. Beton, K. Schulte, Z. Li, *in preparation*

3. *How does Graphene Grow? An Easy Access to Well-Ordered Graphene Films,*
   F. Müller, H. Sachdev, S. Hüfner, A. J. Pollard, E. W. Perkins, J. C. Russell, P. H. Beton, S. Gsell, M. Schreck and B. Stritzker, *Small*, **5**, 2291-2296 (2009)

4. *Supramolecular Assemblies Formed on an Epitaxial Graphene Superstructure,*
   A. J. Pollard, E. W. Perkins, N. A. Smith, A. Saywell, G. Goretzki, A. G. Phillips, S. P. Argent, H. Sachdev, F. Müller, S. Hüfner, S. Gsell, M. Fischer, M. Schreck, J. Osterwalder, T. Greber, S. Berner, N. R. Champness and P. H. Beton, *Angew. Chem. Int. Ed.*, **49**, 1794–1799 (2010)

5. *Formation of monolayer graphene by annealing sacrificial nickel thin films,*
   A. J. Pollard, R. R. Nair, S. N. Sabki, C. R. Staddon, L. M. A. Perdigão, C. H. Hsu, J. M. Garfitt, S. Gangopadhyay, H. F. Gleeson, A. K. Geim and P. H. Beton, *J. Phys. Chem. C*, **113**, 16565-16567 (2009)

Acknowledgements

I would like to firstly thank my supervisor, Prof. Peter Beton, for his guidance over these several years and for going above and beyond the call of duty to help me with the different problems I have encountered.

I would also like to thank the many exceptional individuals I have had the privilege of working with in my research group, including my post-doc collaborators Martin Humphry, Nikolai Berdunov, Ed Perkins, Subhashis Gangopadhyay and Luis Perdigao, and fellow PhD students Rich Fawcett, Mike Hsu, Nick Smith, Alex Saywell and Faye Norfaezah. I also thank the technical staff that provided me with so much help, our collaborators in the Department of Chemistry, and our collaborators at the University of Manchester, University of Saarlandes and University of Ausburg. Without the efforts of all those mentioned my thesis would not be what it is today.

On a more personal note I would like to thank all the group members of the Nottingham Nanoscience Group (both past and present) for what has been one hell of a ride. Special thanks go to Tim, Medford and Fawcett for our social adventures and all my fellow Gears, Halo and Battlestar addicts – I won't shame anyone by mentioning their names here!

It is safe to say that I wouldn't be here without the amazing support from my Mum and Dad throughout my life, but I would also like to thank my brother, Ian, and sister, Laura, who have always participated in my outside interests with me.

But most of all I would like to thank my wife, Hayley, and two amazing kids, Louisa and Nathan, who are the reason I do all the things I do everyday, and who I dedicate this thesis too, with all my love.

"I don't step aside. I step up."
Vic Mackey (The Shield, Season 4, Episode 6)

Contents

List of Figures

List of Symbols

D = Particle diffusivity
F = Particle deposition rate
$\widehat{H}$ = Hamiltonian operator
Ψ = Electron wavefunction
$V(z)/V_\mu/V_\nu$ = Potential of the system/tip/surface state
$E/E_\mu/E_\nu$ = Energy of the electron in a system/tip/surface
k = Electron wave vector
κ = Decay constant
T = Transmission coefficient
V_o = Potential barrier
E_f = Fermi energy
ϕ = Work function
a = Barrier width
E_n = Sample energy state
$M_{\mu\nu}$ = Tunnelling matrix element
I_t = Tunnelling current
z_o = Centre of potential barrier
$\rho(E)/\rho_\mu(E)/\rho_\nu(E)$ = Density of states at energy, E, for system/tip/state
R = Radius of curvature
$\mathbf{r}_o$ = Centre of spherical potential well
z_r = Distance between centre of spherical potential well and surface
a_{acc} = Acceleration of slipstick slider
F_{frict} = Frictional force of slipstick slider
V_{bias} = STM bias voltage
f_o = Cantilever natural resonant frequency
v = Vibration frequency
v_o = Lowest resonant frequency of mechanical system
k = Cantilever spring constant
F_o = Cantilever driving force
w = Cantilever driving force angular frequency
w_o = Free cantilever angular resonant frequency
Q = Cantilever quality factor
F_{ts} = Tip-surface interaction force
k_e = Effective cantilever spring constant
m_o = Cantilever mass
A = Cantilever oscillation amplitude
A_o = Fixed cantilever oscillation amplitude
f_e = Effective cantilever resonant frequency
df = Cantilever resonant frequency shift
z_c = Cantilever support distance from surface
F_{exc} = Excitation of cantilever motion
f_s = PLL output signal
$\langle I_t \rangle$ = Time averaged tunnel current
a_m = Moiré superstructure periodicity

E^d/E^t = Binding energies for dimer/trimer molecular junctions
d = Distance between molecules for dimer bonding
r = Distance between molecules for trimer bonding

Chapter 1

Introduction

This body of work relates to a new scientific research area currently generating a substantial interest – nanoscience. As a brief background to relevant work already performed in this field, this chapter details the concept of self-assembly on the nanoscale (Section 1.1), boron nitride 'nanomesh' (Section 1.2), and graphene (Section 1.3). Nanoscale self-assembly is the process of atoms and molecules forming a nanostructure with a higher order (in this case length-scale) than the isolated components. Boron nitride 'nanomesh' is an example of a structure formed by a self-assembly process. Graphene is the carbon counterpart of the boron nitride 'nanomesh', and is formed epitaxially from singular carbon atoms to produce graphene layers with surface areas on the millimetre-scale.

1.1 Nanoscale Self-Assembly

1.1.1 Nanofabrication

Nanotechnology attracts considerable attention throughout the world, from both the scientific community and also the media. The fundamental processes used to achieve nanoscale structures, that are pivotal to this area of research, can generally be sorted into two groups; 'bottom-up' processes and 'top-down' processes. Top-down techniques involve a larger scale object that is manipulated in some way to produce smaller scale structures in a miniaturisation technique, whereas bottom-up techniques construct structures from smaller objects in a form of fabrication.

An example of a top-down process is nanolithography, which includes both photolithography and electron beam (or 'e-beam') lithography – a slower technique

but with higher resolution than photolithography. In electron beam lithography a semiconductor substrate with a covering thin film of material and a photoresist coating is exposed to an intense beam of electrons, in a pattern determined by a programmed design. This results in a semiconductor substrate with a thin film patterned at the nanoscale, according to the design dimensions. This example of a top-down technique has been readily applied for many years. However, it does have a limit to its resolution and electron beam lithography is only adopted for producing nanostructures with a minimum feature size of approximately 10 nm.

Bottom-up techniques can be used to produce even smaller scale structures with greater resolution through the positioning of objects that are smaller than the final nanoscale fabrication. Molecular self-assembly is a bottom-up technique that can generate structures with features of only a few nanometres over areas of hundreds of nanometres. The term 'self-assembly' is reserved for the spontaneous formation of supramolecular architecture from its molecular constituents and is distinguished from self-organisation, which relates to structures formed in systems far from thermodynamic equilibrium.

Supramolecular chemistry is defined as 'chemistry beyond the molecule' and was first coined by Jean-Marie Lehn (Chemistry Nobel Laureate in 1987). Whereas molecular chemistry focuses on covalent bonds, supramolecular chemistry involves forces such as van der Waals interactions and hydrogen-bonding. Although the literature on how supramolecular chemistry can be tuned to create desired supramolecular crystals or supramolecular compounds in solution is very broad, this knowledge cannot be used directly to calculate the assembly of adsorbed molecules into larger surface structures. For this to be accomplished, the influence of the substrate (due to its atomic lattice and electronic structure) upon the non-covalent bonds that are present also needs to be considered.

1.1.2 Hydrogen-Bonded Molecular Self-Assembly

This thesis concentrates on the utilisation of hydrogen-bonding to form supramolecular structures. Key examples of hydrogen-bonding are the interactions between water molecules and the bonding of DNA base pairs – shown in Figure 1.1. Hydrogen-bonding occurs when a polar group present in one molecule (denoted as X-H), effectively shares a proton with an electronegative atom (A) present in another molecule – forming a local bond between the two molecules. The hydrogen atom is covalently bonded to the electronegative 'X' atom, which is frequently oxygen or nitrogen but may be any atom that is highly electronegative.

Thus in the case of DNA, the appropriate geometrical correspondence of hydrogen-bond donors and acceptors allows only the 'correct' pairs to bond. Hydrogen-bonds have a binding energy of 0.1-0.3 eV depending on the molecular combination that forms the hydrogen-bond. They are also directional due to the proton donation and are ∼0.3 nm in length.

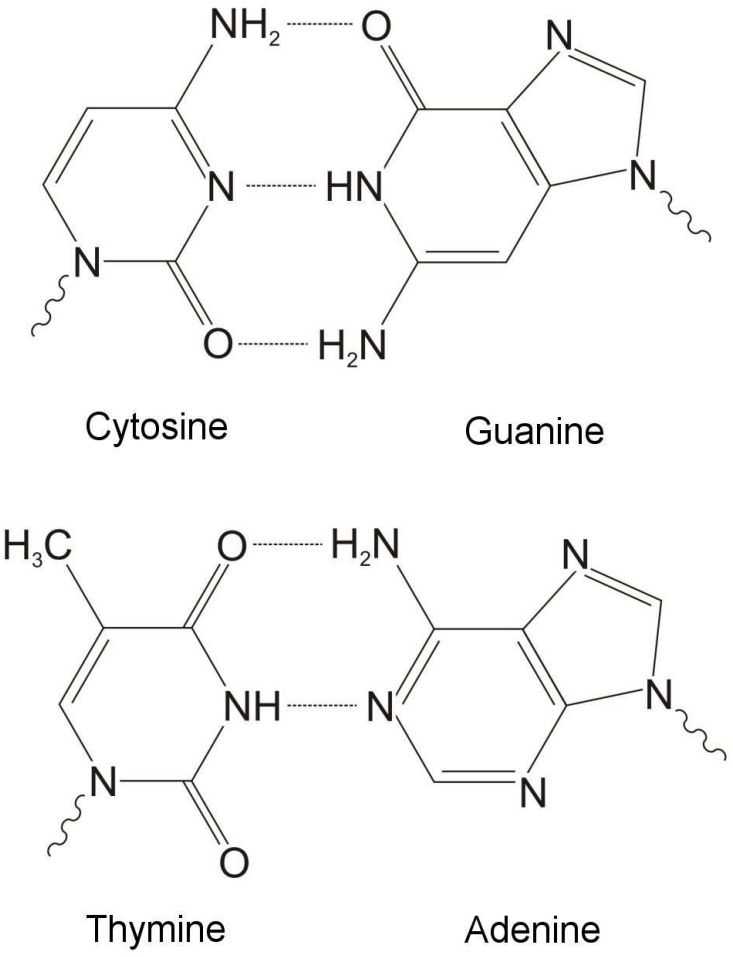

Figure 1.1: The bonding of cytosine and guanine (top) and thymine and adenine (bottom) molecules are both examples of hydrogen-bonding and lead to the formation of the DNA double helix. The dotted lines represent hydrogen-bonding between the hydrogen and oxygen or nitrogen atoms contained in the DNA base pairs.

The study of molecules adsorbed onto different surfaces is an active area of research with a focus on the exploitation of molecular properties to produce self-assembled nanostructures [1, 2]. A significant section of this field is concentrated on molecular deposition performed in high vacuum or ultra-high vacuum (UHV)

conditions and includes a selection of hydrogen-bonded structures [3, 4, 5]. The adsorption of self-assembling organic molecules onto surfaces in liquid conditions is also an expanding field [6, 7], however, this thesis focusses on UHV studies.

The primary growth mechanism for nanostructures formed by adsorbed particles is the transport of these particles on a flat terrace of the substrate, as shown in Figure 1.2. The species hop randomly from one position on the substrate lattice to another according to the thermal energy of the particles, which allows them to overcome the diffusion barriers between stable or metastable adsorption configurations. When atoms or molecules are deposited on a surface at a constant deposition rate F, with a diffusivity D (the mean square distance travelled by an adsorbate per unit time), then the ratio D/F determines the average distance that an adsorbate has to travel to encounter another adsorbate. A species may attach to a static island (as the available thermal energy is not enough to overcome the now larger barrier for detachment) or form a new aggregate. If the adsorbate deposition is slower than the diffusion rate (large values of D/F), growth occurs close to thermodynamic stability. If the adsorbate deposition rate is greater than the diffusion rate (small D/F), then the pattern of growth is essentially determined by kinetics. In this thesis, the formation of nanostructures involved thermodynamically controlled growth, as the structures were formed in a vacuum environment with a slow, controlled rate of deposition. Hence D is expected to be much greater than F.

Self-assembly is a powerful tool. Although only a few examples have been detailed in this section, there is an almost limitless variety of structures of varying dimensions that can be produced. This is due to the nature of molecular self-assembly which relies on the selection of different tectons – a tecton is a precursor molecule that becomes incorporated into a supramolecular engineered structure [8]. This may well be the future direction of the electronics industry – that requires constant miniaturisation – due to the length scales involved and because the processes occur without any micromanagement by the manufacturer, who is provided with exquisite control. However, the development of effective interfacing of the resulting nanostructures to the macroscopic world is vital for any real-world applications, the combination of both top-down and bottom-up techniques may possibly be required to bridge the gap between the nanoscale and macroscopic worlds.

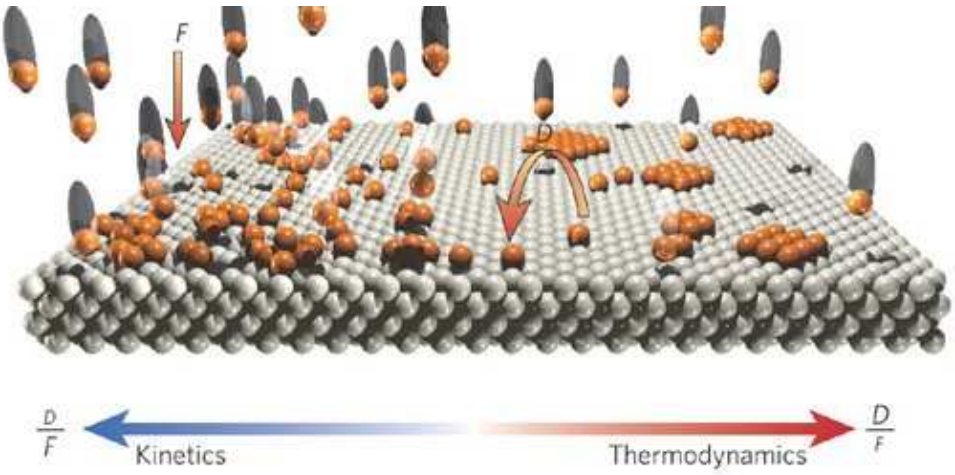

Figure 1.2: Particles (orange) are deposited from the vapour phase onto a flat surface comprised of grey atoms. On adsorption, the particles diffuse on terraces to meet other adspecies, resulting in nucleation of aggregates or attachment to already existing islands. The ratio of the diffusivity, D, and the deposition rate, F, governs the type of growth on the surface – either kinetic or thermodynamic. Adapted by permission from Macmillan Publishers Ltd: Nature, Ref. [2], © (2005).

1.2 Boron Nitride Nanomesh

1.2.1 Nanomesh Formation and Modelling

Boron nitride layers had previously been formed on several transition metal surfaces [9, 10, 11] before a revival of interest in 2003. This renewed enthusiasm was due to the scanning tunnelling microscopy (STM) investigations of a boron nitride network on a Rh(111) surface [12], as shown in Figure 1.3. A self-assembled monolayer of boron and nitrogen atoms was formed on a clean Rh(111) surface when borazine ($(BH)_3(NH)_3$) was incident upon the Rh(111) substrate at high temperature. This hexagonal boron nitride (h-BN) monolayer generated a curious topographical map when imaged with STM, which led to the title of 'boron nitride nanomesh' [12] (described as boron nitride nanomesh or BN/Rh(111) from herein).

The h-BN layer was found to readily cover a Rh(111) surface held at a temperature of 1070 K during borazine exposure in UHV conditions, achieving a complete coverage of the Rh(111) surface (assuming an adequate borazine exposure). The boron nitride nanomesh was also discovered to be still intact when in ambient conditions after extraction from a UHV system, as realised by subsequent imaging with STM [13]. The BN/Rh(111) surface has also been successfully imaged with

STM whilst immersed in liquid [14], although contamination was observed.

Originally the BN/Rh(111) surface was described as a two layer network as shown in Figures 1.4a-1.4c. This model was deduced from STM topography observed intermittently and shown in Figure 1.3b. It was surmised that the two layers were offset in such a way as to expose the minimum metal surface area [12]. However, in 2006 the boron nitride nanomesh was modelled using density functional theory (DFT) as a monolayer of boron and nitrogen atoms [15], as shown in Figures 1.4d-1.4e. This single layer model is now accepted as the correct modelling of the BN/Rh(111) surface, producing a superstructure with a 12 $\times$ 12 Rh and 13 $\times$ 13 *h*-BN periodicity to accommodate the lattice mismatch between the *h*-BN monolayer and the Rh(111) surface.

From Figure 1.4d, the corrugated nature of the BN/Rh(111) surface can be visualised by the displacement of the N atoms relative to the Rh atoms of the surface, varying from 2.17 Å to 2.72 Å. There were flatter regions where the boron and nitrogen atoms were close to their optimal (fcc, top) positions with respect to the underlying Rh atoms (as shown in Figure 1.4e), that is, where the *h*-BN monolayer was closer to the substrate. These regions covered approximately 70% of the surface [15] and are shown as blue areas in Figure 1.4d. The other distinct region shown in Figure 1.4d was formed because the *h*-BN atoms were not always in their optimal positions above the Rh atoms due to the lattice mismatch. This 'high' region could be further separated into two different heights that related to B and N atoms either in (top, hcp) positions, or their further displaced (hcp, fcc) positions. The attraction of the boron atoms to the Rh surface was weakest and the repulsion of the nitrogen atoms due to the Rh atoms was strongest for the (hcp, fcc) regions. 'Pores' and 'wires' were formed due to this corrugation, for areas where the *h*-BN monolayer was closer to and further from the rhodium surface respectively. STM imaging of the BN/Rh(111) surface revealed a Moiré pattern that corresponded to a 3.2 nm periodicity superstructure formed by the wires and 2 nm-aperture pores [12]. This corrugation of the monolayer – partially caused by the lattice mismatch between the *h*-BN monolayer and the underlying substrate – was the reason for its 'true' nanomesh distinction from *h*-BN monolayers formed on other transition metal surfaces.

1.2.2 'True' Boron Nitride Nanomesh

Flat *h*-BN monolayers have been discovered for several transition metal surfaces, including Ni surfaces [10, 11, 16], Cu(111) [17], Pt(111) [10, 18, 19],

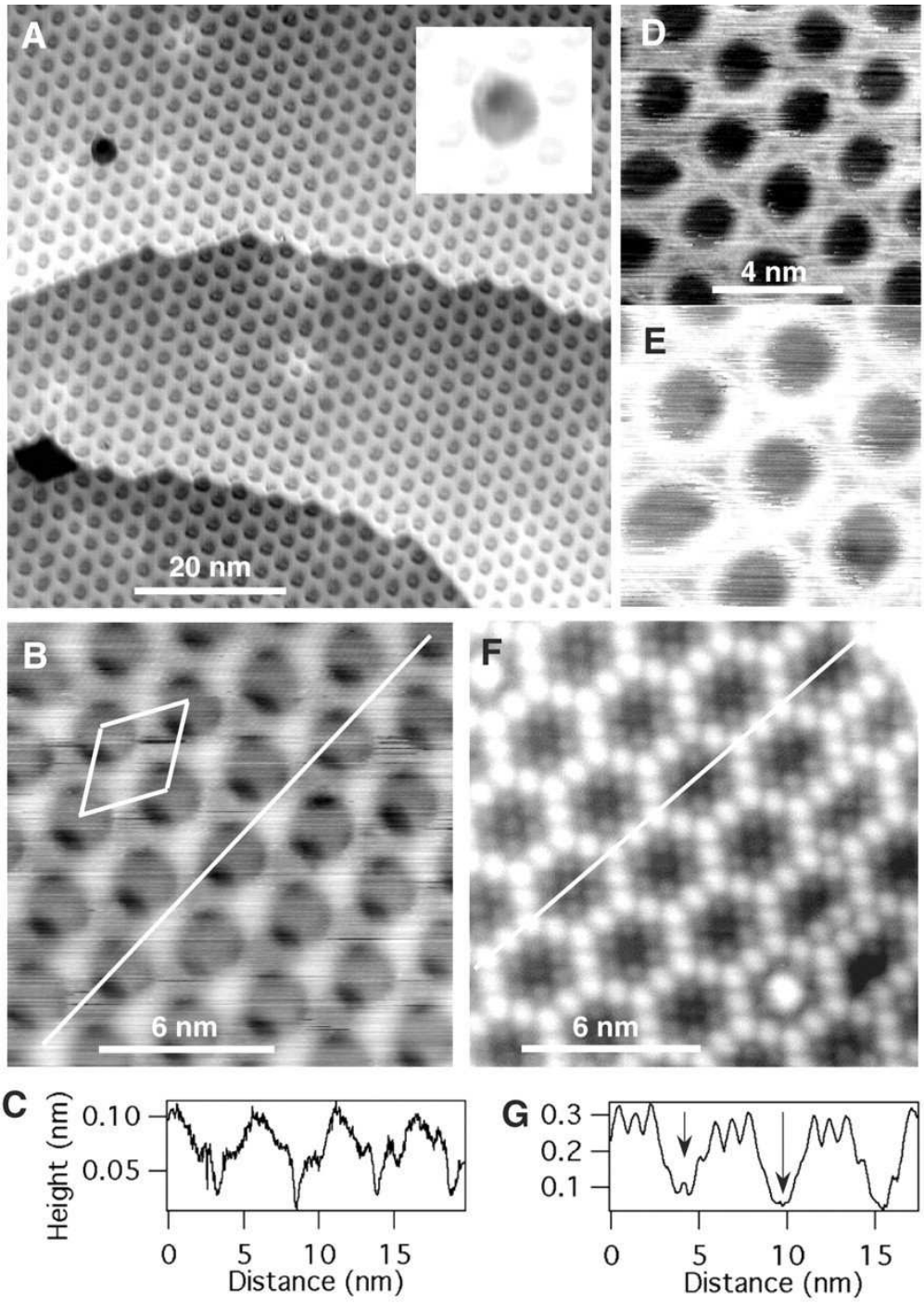

Figure 1.3: STM images of the boron nitride nanomesh formed on a Rh(111) surface. (a) larger scale image where steps in the Rh(111) surface as well as defects in the mesh are observed. (b) smaller scan size image where a tip effect is observed, with associated scan line (c). (d) and (e) are STM images of the surface produced when the tunnel current setpoint was increased. (f) STM image of the surface after exposure to C_{60} molecules with associated scan line (g), from Ref. [12]. Reprinted with permission from AAAS.

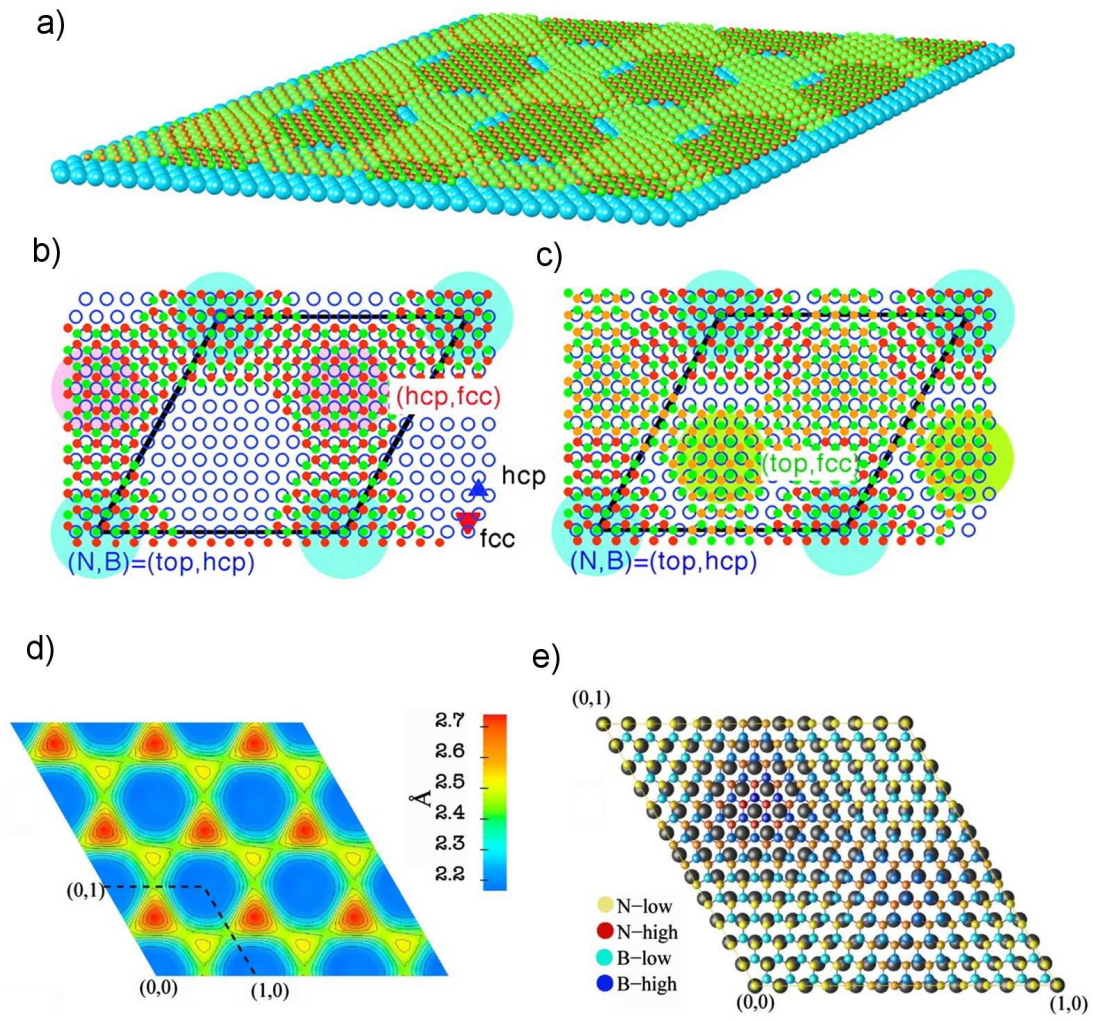

Figure 1.4: (a)-(c) original model of the BN/Rh(111) surface proposed by Corso et al. where (a) is a 3D model of the two-layers of boron (orange) and nitrogen (green) atoms on the rhodium atoms (blue), (b) is a schematic of the bottom layer and (c) illustrates both the top and bottom layers, from Ref. [12]. Reprinted with permission from AAAS. (d)-(e) show the currently accepted model of the BN/Rh(111) surface, as proposed by Laskowski et al., calculated using DFT. (d) is a contour map of the height of the N atoms relative to the Rh(111) substrate and (e) is a ball and stick model of the boron nitride nanomesh unit cell, from Ref. [15]. © (2007) by the American Physical Society.

Pd(111) [20] and Pd(110) [21] surfaces. However, the *h*-BN monolayers formed on the Pd(111) and Pt(111) substrates differed from the Cu(111) and Ni(111) surfaces due to a lattice mismatch between the *h*-BN monolayer and the Pd(111) or the Pt(111) lattice. This mismatch created a distinctive Moiré pattern when the surfaces were imaged with STM and was similar to the superstructure of the Rh(111) boron nitride nanomesh – shown in Figure 1.3. A commensurate 1 × 1 network was formed on the Ni(111) and Cu(111) surfaces, while a 10 × 10 metal / 11 × 11 *h*-BN network was revealed for the flat *h*-BN monolayers on Pd(111) [20] (Figure 1.5a) and Pt(111) [22].

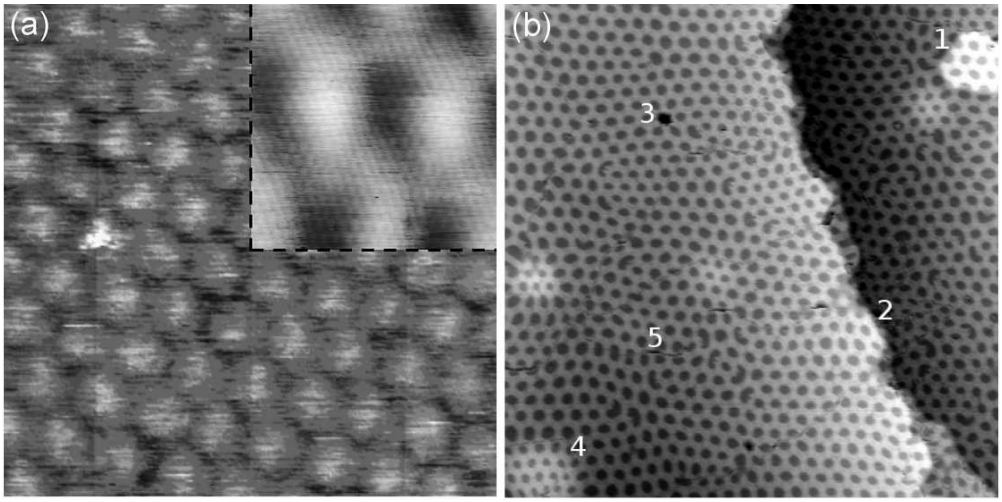

Figure 1.5: (a) 20 nm × 20 nm STM image of the BN/Pd(111) surface revealing the 10 × 10 Pd / 11 × 11 *h*-BN network and a 2.5 nm × 2.5 nm inset where atomic resolution of the N atoms was observed, reprinted from Ref. [20]. © (2009), with permission from Elsevier. (b) 86 nm × 86 nm STM image of the BN/Ru(0001) surface where the corrugated 12 × 12 Ru / 13 × 13 *h*-BN network was observed, Reprinted with permission from Ref. [23]. © 2007 American Chemical Society

These flat *h*-BN monolayers differed from the boron nitride nanomesh produced on the Rh(111) surface – where a 12 × 12 Rh / 13 × 13 *h*-BN superstructure was formed. However, a 12 × 12 metal / 13 × 13 *h*-BN Moiré pattern was later produced on a Ru(0001) surface in 2007 [23], as shown in Figure 1.5b. The important distinction between the *h*-BN monolayers formed on Rh(111) and Ru(0001) and the other transition metals was that the Rh(111) and Ru(0001) surfaces introduced a corrugation in the boron nitride monolayers [15, 23, 24, 25]. Both the BN/Rh(111) and BN/Ru(0001) surfaces revealed a mismatch between the transition metal substrates and the *h*-BN monolayer. This was also the case for the

Pd and Pt surfaces, however, these latter surfaces did not produce a corrugated *h*-BN layer, even though Moiré patterns were revealed with STM imaging. It was the strength of the bonding between the Rh or Ru atoms and boron atoms that resulted in the corrugation of the *h*-BN monolayer, as determined by the filling of the d-orbitals and further discussed in Reference [24]. Hence only the BN/Rh(111) and BN/Ru(0001) surfaces were deemed 'true' nanomesh structures, due to their corrugated nature.

Figure 1.5 shows STM images of both flat and corrugated *h*-BN monolayers formed on two different transition metals. The knowledge that the transition between low and high regions is relatively abrupt [15], raises the question of whether the corrugation of the *h*-BN monolayer would have any implications for the positioning of adsorbed molecules.

1.2.3 Molecular Deposition on Boron Nitride Nanomesh

Following the original discovery of the boron nitride nanomesh, Corso et al. deposited C_{60} molecules onto the BN/Rh(111) surface [12], as shown in Figure 1.3f. This resulted in molecules that followed the topography of the nanomesh, with the fullerene decorating the wires and intermittently filling the pores to create a monolayer of C_{60} molecules. Single C_{60} molecules were also revealed to subsequently fill the pores that were created in the C_{60} monolayer, as shown in the bottom right of Figure 1.3f.

The positioning of C_{60} molecules on the boron nitride nanomesh differed from the adsorption of gold nanoparticles [23] (Figure 1.6a) and naphthalocyanine ($C_{48}H_{26}N_8$) molecules (Figure 1.6b). These latter particles preferentially filled the pores of the nanomesh network, whether it was a BN/Ru(0001) surface (gold clusters) or a BN/Rh(111) surface (naphthalocyanine). From Figure 1.6a, Au nanoparticles smaller than the 2 nm apertures of the nanomesh were trapped in the pores and positioned next to the wires, while the larger nanoparticles were only positioned in the smaller pores as much as physically possible. From Figure 1.6b, the adsorbed naphthalocyanine molecules were also observed inside the pores, showing a preference to positions adjacent to the wires.

The placement of adsorbed particles was further investigated with Xe adsorption, and the pores were discovered to have a reduced work function due to the charge transfer with the underlying substrate [26]. The trapping of the Xe atoms was localised at the rims of the pores (as was the case for both Au clusters and naphthalocyanine molecules) due to the dipole rings formed by the contact of two

regions with dissimilar work functions (the nanomesh pores and wires) [26]. It should be noted that after the deposition of both the Au clusters and the naphthalocyanine, the surface was annealed and particles were desorbed before the surface was imaged with STM, possibly leaving only the more strongly bound molecules.

The deposition of cobalt atoms onto the BN/Rh(111) surface whilst in the presence of oxygen in a UHV environment produced a contrasting result – the Co atoms were observed between the boron nitride nanomesh and the Rh(111) surface. Two-dimensional (2D) islands of Co were formed underneath the boron nitride monolayer, as shown in Figure 1.6c. The topography of the *h*-BN layer was preserved until the amount of Co atoms underneath the *h*-BN layer exceeded a monolayer [27].

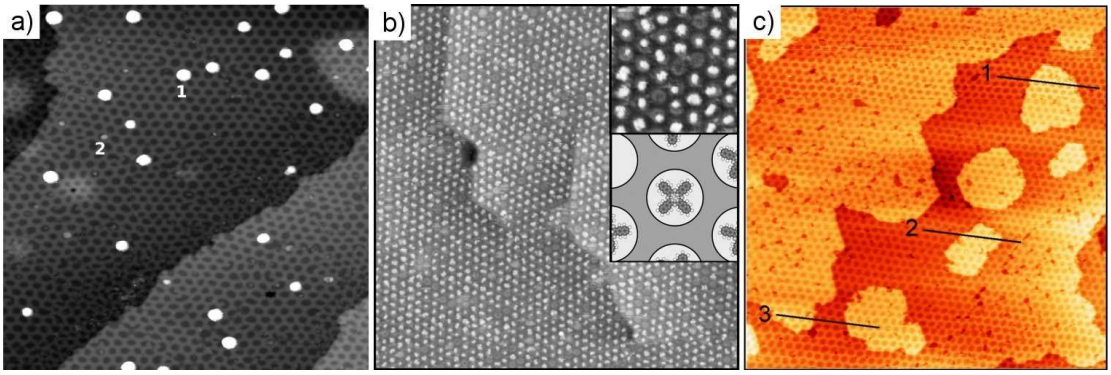

Figure 1.6: (a) STM image of Au nanoparticles (of varying size, where 1 denotes a ∼4 nm particle and 2 denotes a ∼1 nm particle) deposited onto a BN/Ru(0001) surface after annealing to 900 K for 5 min, reprinted with permission from Ref. [23]. © 2007 American Chemical Society. (b) 120 nm × 120 nm STM image of naphthalocyanine molecules deposited onto a BN/Rh(111) surface after annealing to 550 K, the insets are a 19 nm × 19 nm enlargement and schematic of the molecular placement, from Ref. [14]. © Wiley-VCH Verlag GmbH & Co. KGaA. Reproduced with permission. (c) 135 nm × 135 nm STM image of the BN/Rh(111) surface with Co atoms intercalated underneath the nanomesh layer, forming 2D islands under the *h*-BN monolayer, reprinted with permission from Ref. [27]. © 2009 American Chemical Society.

The boron nitride nanomesh is an excellent example of a self-assembled nanotemplate, one that has already shown potential for ordering further adsorbed layers of particles. This covalently bonded monolayer is seemingly similar to another, whose interest was also reinvigorated in 2004, namely graphene, with examples of these two different monolayers having recently been compared [28, 29].

1.3 Graphene

1.3.1 Structural Properties

The importance of the element carbon cannot be overstated as it is the chemical basis for all known life. It is also the basis of all organic chemistry and there are more compounds found containing carbon than all other chemical elements (except hydrogen) combined. Elemental carbon forms several allotropes with very different physical properties, for example, diamond is a very hard substance and graphite is a soft substance. Both these materials are allotropes of carbon and their differing physical properties are due to the different types of bonding of the carbon atoms in each allotrope.

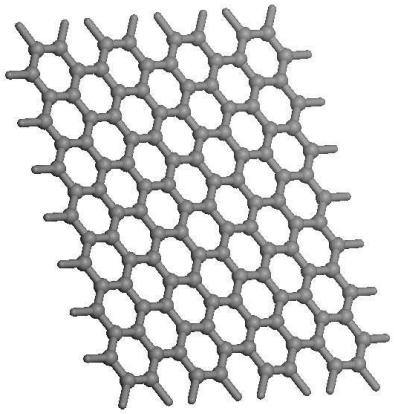

Figure 1.7: Schematic representation of a section of a graphene sheet, each of the grey carbon atoms are bonded to three other carbon atoms to create a honeycomb structure.

Graphene can be conceived as a 2D basic structural element of hexagonal graphite. It is an atomically flat planar sheet of carbon with each carbon atom bonded to three other carbon atoms through sp^2 hybridisation. This type of bonding of carbon atoms forms a nanoscale 'chicken-wire', that is, a honeycomb crystal structure, as shown in Figure 1.7. The hexagons that form this honeycomb structure can be envisaged as fused benzene rings without any hydrogen atoms bonded to the carbon atoms. Both carbon nanotubes and fullerenes can be constructed from a manipulated graphene sheet. A single-walled carbon nanotube (SWNT) is a sheet of graphene 'rolled up' into a cylinder and connected at the ends, the different lattice directions that the graphene can be rolled along leads to different chiralities of nanotubes. A multi-walled carbon nanotube (MWNT) consists

of several sheets of graphene wrapped within each other, where each new layer would encase the previous sheet. Fullerenes are molecules that consist of carbon atoms bonded to form a sphere, graphene can be thought of as being 'wrapped up' to form fullerenes, but this also requires pentagon formations to be introduced into the graphene sheets. Graphite consists of stacked layers and each layer of graphene is mismatched with its neighbouring layers. Van der Waals forces bond the layers of graphene together, therefore the layers are easily separated whereas the covalent σ bonds bonding the carbon atoms to each other *within* the graphene layers are very hard to break. The structures of graphite, an SWNT and a fullerene are shown in Figure 1.8, allowing a comparison with Figure 1.7 to reveal their relation to graphene.

1.3.2 History and Properties of Graphene

There were no serious investigations into graphene until the mid-20^{th} Century, when P. R. Wallace first described the band structure of graphene whilst interested in its 3D version, graphite [30]. Graphene was a purely theoretical material until more recently, when it was first isolated at the University of Manchester in 2004 [31] – which led to the very recent award of the Nobel Prize in Physics 2010 to Geim and Novoselov.

The first graphene films produced by mechanical exfoliation (repeated peeling of a highly orientated pyrolytic graphite (HOPG) surface using Scotch tape) in 2004 by Novoselov et al. were found to contain micron size flakes of few-layer graphene (FLG) whilst also producing thicker graphene films that were visible to the naked eye [31]. Figure 1.9 shows examples of these films and includes an atomic force microscope (AFM) image of a single layer of graphene (Figure 1.9c). The Hall bar device used to study the electrical properties of the graphene films is also shown in Figure 1.9.

The graphene films produced by peeling a HOPG surface were found to be stable in ambient conditions and revealed semimetal characteristics – a small overlap between valence and conductance bands [31]. By applying a gate voltage, graphene has been shown to have a remarkably high electron mobility, greater than 15000 $cm^2V^{-1}s^{-1}$ [32] at room temperature. This mobility is largely independent of temperature between 10 K and 100 K, leading to the belief that defects are the dominant cause of scattering [33]. Other notable features of graphene include; the strongest material ever measured [34], almost transparent to white light [35] and extremely flexible [36]. These impressive properties, coupled with the fact that

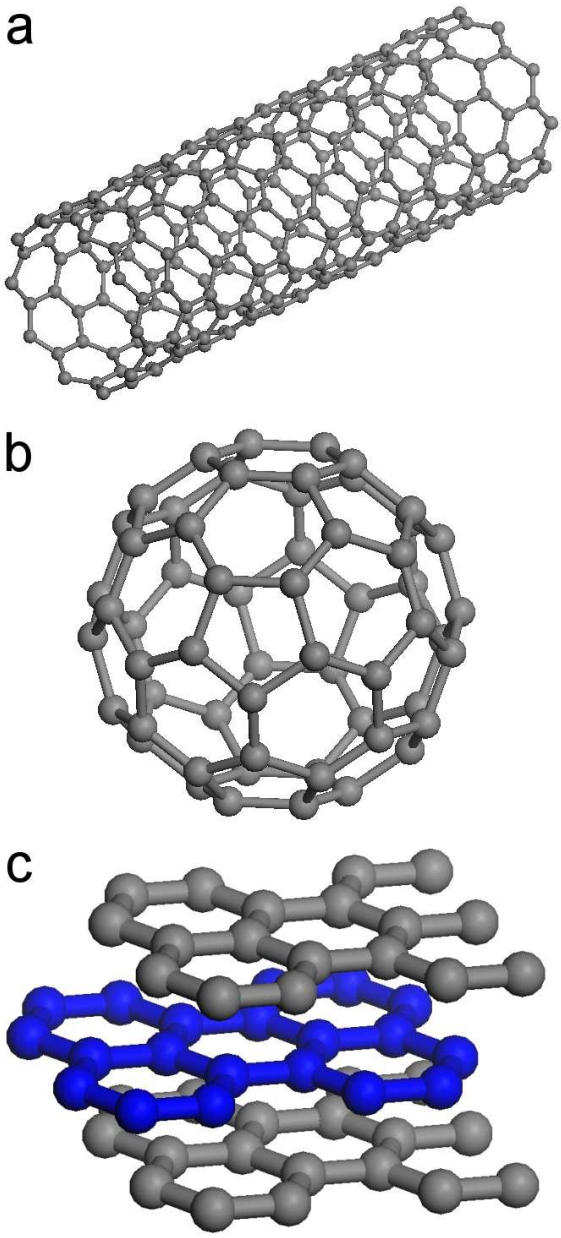

Figure 1.8: Carbon structures that could be constructed using graphene, (a) a SWNT can be thought of as a rolled up sheet of graphene that is reconnected into a cylinder shape, (b) a C_{60} molecule would require pentagons to be introduced into the graphene sheet and the sheet to be then manipulated into a sphere, (c) a section of graphite where the mismatched graphene layers are shown as different colours.

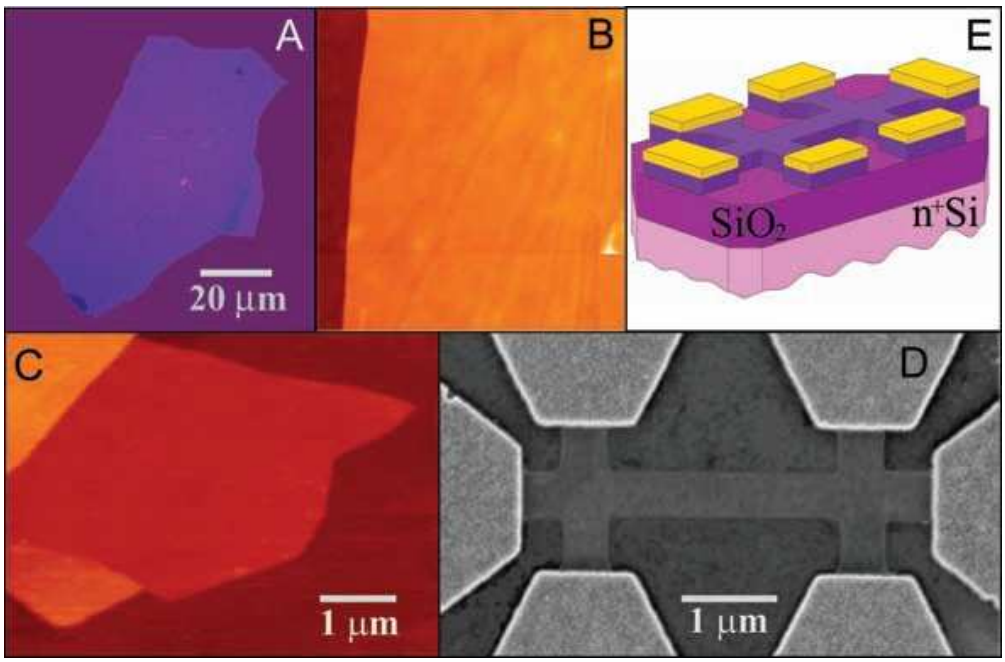

Figure 1.9: (a)-(c) AFM images of the graphene films produced using mechanical exfoliation, a single graphene layer is imaged in (c). (d) and (e) show the Hall bar device used to study the electrical properties of the films, from Ref. [31]. Reprinted with permission from AAAS.

the capability to control the electronic properties of a material by an externally applied voltage (as demonstrated by Novoselov et al. [31]) is central to modern electronics, have led many to believe that graphene may replace silicon as the dominant material present in electronic devices. Part of the surge of interest in graphene was caused by the discovery of massless Dirac fermions present in graphene, where quasiparticles show relativistic behaviour as described by the Dirac equation [37].

In this thesis, investigating the production of high-quality, large-area graphene has highlighted interesting features.

1.3.3 Production of Graphene

As detailed in the previous section, graphene layers were originally produced via mechanical exfoliation from bulk graphite. However, the production of monolayer or few-layer graphene on transition metals can also lead to isolated graphene layers. A common technique involves cracking alkenes onto a nickel surface and then annealing the substrate to produce what was originally coined 'monolayer graphite'. This avenue was investigated several years before Novoselov et al. had

isolated graphene from graphite [38]. More recently, the isolation of graphene was achieved by etching the underlying Ni layer and 'stamping' the resulting graphene layers onto substrates that are better suited to technological applications, such as SiO_2 substrates [36, 39, 40]. This is a very versatile approach for the formation of electrodes and active electronic components consisting of few-layer graphene. Although this process can produce larger areas of continuous released graphene than mechanical exfoliation, the percentage of monolayer graphene is still relatively small, and due to the frequency of domain boundaries the electrical conductivity of the films is reduced when compared to mechanically exfoliated graphene. However, the very recent production and release of graphene from copper foils [41, 42] has proved to greatly increase the percentage of monolayer graphene (95%) over large areas (from 1 cm^2 to over 3000 cm^2), although the conductivity does not yet match that of graphene released from graphite.

There is also great interest in the controllable growth of epitaxial graphene monolayers. Although originally concentrated on the growth of graphene on SiC wafers [43, 44] (as shown in Figure 1.10a), other transition metals have also been used to produce graphene, achieving complete surface coverages of monolayer graphene. Both iridium [45, 46] (Figure 1.10b) and ruthenium [47, 48] (Figure 1.10c) can produce a well-ordered monolayer of graphene when exposed to a partial pressure of ethylene in UHV conditions [46, 48], or through the segregation of interstitial carbon [47]. However, due to the high cost and limited scalability of single crystal metal substrates it will be diffcult to develop a viable process for technological applications based on this approach. Furthermore, graphene layers grown using this approach have not yet been isolated and their electronic quality is untested, unlike graphene on Ni and Cu surfaces.

As shown in Figure 1.10 with STM, graphene formed on Ir and Ru surfaces produced Moiré patterns due to the mismatch of the graphene on each of the substrates (described in the caption), which was also discovered for the boron nitride equivalents (see Section 1.2). Similar to the boron nitride Moiré patterns, the positioning of the carbon atoms of the graphene monolayer with respect to the atoms of the metal surface governed the periodicity of the resultant superstructure observed with STM. However, in contrast to the boron nitride nanomesh formed on Ru(0001), the areas of weakly bound and strongly bound graphene on Ru(0001) were equivalent to 'hills' and 'valleys' respectively when observed with STM imaging, rather than 'pores' and 'wires' [29]. Synchrotron-radiation-based core-level spectroscopies revealed that the graphene monolayer was more strongly bound to the Ru(0001) surface than the Ir(111) surface [49]. The top several

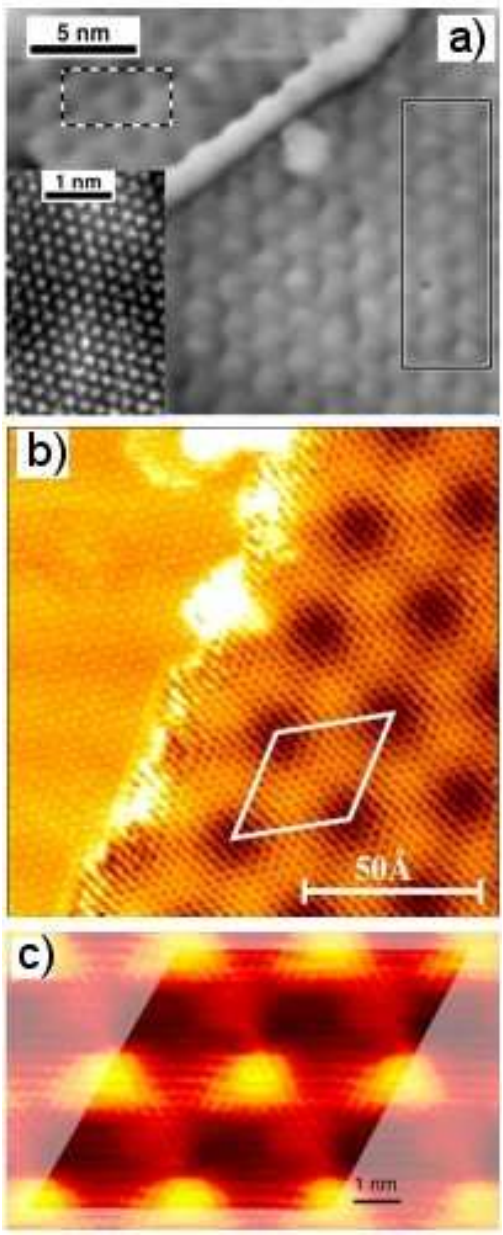

Figure 1.10: (a) STM image of graphene formed on a SiC substrate revealing a 6 × 6 surface unit cell attributed to Moiré coincidences between the graphene layers formed and SiC lattices, reprinted with permission from Ref. [43]. © 2004 American Chemical Society. (b) STM image of the Moiré pattern formed by graphene on the Ir(111) surface, where the 9.32 × 9.32 superstructure is marked by a white rhombus and has a periodicity of 25.3 Å, reprinted with permission from Ref. [46]. © 2008 American Chemical Society. (c) STM image of graphene on Ru(0001), highlighting the Moiré superstructure containing 25 × 25 graphene / 23 × 23 Ru unit cells, from Ref. [48]. © (2008) by the American Physical Society.

monolayers of Ru were also significantly corrugated due to the strong bonding between the Ru and C atoms [47, 48].

Development of both the production and the properties of graphene continues to be a fiercely investigated area of research which has the possibility of producing an array of advancements in current technology. One avenue of particular interest to the author is the possibility of reliably doping graphene in a simple procedure that produces nanoscale doping with spatial order.

1.4 Summary

The studies detailed in this thesis explore the connections between the three topics described in this chapter, that is, both boron nitride monolayer and graphene layer formation on transition metal surfaces and the resulting self-assembled nanostructures produced when organic molecules are adsorbed on these surfaces. These structures and surfaces are primarily investigated with scanning probe microscopy (SPM) techniques in this thesis, although X-ray photoelectron spectroscopy (XPS), X-ray diffraction (XRD), scanning electron microscopy (SEM), transmission electron microscopy (TEM) and Raman spectroscopy data are also included.

Chapter 2 describes the basic STM theory, STM system experimental processes and AFM theory necessary for the understanding of the following chapters. Chapter 3 continues the avenue of SPM studies with the development of a combined AFM/STM in UHV system for investigations of organic molecules adsorbed on a graphite surface. Chapter 4 details the method and SPM analysis of molecular adsorption on the boron nitride nanomesh surface, produced on a Rh(111) thin film. Chapter 5 highlights novel avenues of graphene formation on a Rh(111) thin film and the nanostructures formed through deposition of organic molecules. A comparison with the results of the similar investigations on graphite in Chapter 3 and the boron nitride nanomesh in Chapter 4 is included. Finally, Chapter 6 studies the advancement of the quality of isolated graphene produced using a sacrificial nickel thin film in UHV without requiring alkene dosing.

Chapter 2

Experimental Techniques

This thesis describes scanning tunnelling microscopy (STM) and atomic force microscopy (AFM) studies primarily performed with two ultra-high vacuum (UHV) scanning probe microscope (SPM) systems. In this chapter, basic STM theory, STM system experimental procedures and the theory of AFM are detailed.

2.1 The Theory of STM

The invention of the STM [50] by Binnig and Rohrer in 1982 ushered in a new age in surface science research and was recognised by the award of the Nobel Prize in Physics in 1986. This technique has allowed scientists from many different branches of science and technology to acquire images of metal and semiconductor surfaces by generating a real-space map of the local density of states (LDOS). This is achieved by exploiting the quantum-mechanical electron tunnelling effect of electrons between two states. For STM, electrons tunnel between states on two separate surfaces between which a potential difference is applied – one of these surfaces is the STM tip and the other is the sample under investigation. The tip is rastered across an area of the surface whilst the tunnelling current is measured to produce a topographic image. Within twelve months of the invention of the STM, atomic resolution of the Si(111)-(7×7) surface had already been achieved [51] and nowadays surface scientists can readily achieve sub-Ångström resolution with this technique.

2.1.1 Quantum Tunnelling

STM requires a sharp conducting tip with an applied potential bias, positioned very close to a conducting surface so an electrical current will flow between

the surface and the tip. This current occurs due to the quantum-mechanical tunnelling effect which becomes significant when the distance between the tip and the surface is less than a nanometre. This is contrary to the classical or Newtonian interpretation because the insulating gap between the tip and the surface provides an impenetrable potential barrier. However, within a quantum-mechanical description of the system there is a finite probability that an electron can penetrate this potential barrier. Figure 2.1 illustrates this quantum-mechanical behaviour of an electron for the simplest model of two conducting surfaces separated by a vacuum.

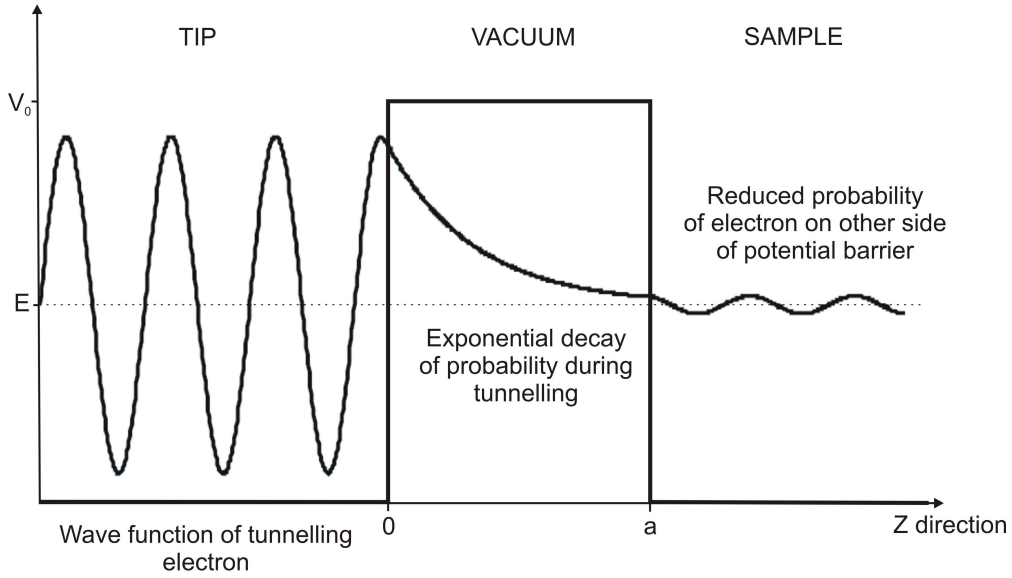

Figure 2.1: Diagram showing the tunnelling of an electron through a 1D potential barrier, for UHV-STM the potential barrier is due to the vacuum gap between the tip and the sample. Left axis is the wavefunction or energy for the electron or potential barrier respectively.

The quantum-mechanical tunnelling example illustrated in Figure 2.1 can be analysed using the 1D (Z direction in this case) time-independent form of the Schrödinger Equation, shown in Equation 2.1.

$$\widehat{H}\Psi(z) = -\frac{\hbar^2}{2m}\frac{d^2\Psi(z)}{dz^2} + V(z)\Psi(z) = E\Psi(z) \tag{2.1}$$

$\widehat{H}$ is the Hamiltonian operator, Ψ is the electron wavefunction, m is the mass of the electron, $-\frac{\hbar^2}{2m}\frac{d^2\Psi}{dz^2}$ is the kinetic energy of the electron, $V(z)$ is the potential and E is the total energy of the electron. The Schrödinger Equation can be solved for the three regions shown in Figure 2.1 when the solution takes the form of an

exponential wave [52]. In the 'tip' region there are two solutions, for the electron moving in either a positive or negative direction, as shown in Equation 2.2.

$$\Psi(z) = Ae^{\pm ikz} \tag{2.2}$$

The wave vector of the electron, k, can be described as shown in Equation 2.3.

$$k = \sqrt{2m \mid E \mid}/\hbar \tag{2.3}$$

The solution of Equation 2.1 for the classically forbidden 'vacuum' region is described in Equation 2.4 for an electron penetrating through the potential barrier in the $+z$ direction, where Equation 2.5 is the decay constant, κ.

$$\Psi(z) = Be^{-\kappa z} \tag{2.4}$$

$$\kappa = \sqrt{2m \mid V_0 - E \mid}/\hbar \tag{2.5}$$

The probability of an electron being transmitted from the 'tip' region and through the barrier to the 'sample' region is termed the transmission coefficient, T, and is determined by the width of the barrier, a, as shown in Equation 2.6.

$$T \propto e^{-2\kappa a} \tag{2.6}$$

The flow of electrons through the barrier decreases exponentially with increasing separation, a – as a increases, the amplitude of the wavefunction in the third region decreases. Therefore, the 'tunnel current' that occurs when an STM tip and sample (with an applied potential between them) are separated by less than 1 nm also decreases exponentially with increasing separation.

The theoretical model illustrated in Figure 2.1 can be envisioned as a metal-vacuum-metal junction. Therefore the potential barrier, V_0, can be approximated as the work function, ϕ, of a metal surface. The work function is the minimum energy required to remove an electron from the bulk of a metal to the vacuum level. If we neglect thermal excitation, the Fermi level is the upper limit of the occupied states in a metal and becomes equal in magnitude to the work function, $E_f = -\phi$. Figure 2.2 illustrates this relation between the work function and Fermi energy for a metal-vacuum-metal junction, where the tip and sample are treated as the same metal and therefore their work functions are equal. Electrons can tunnel from the tip to the sample or from the sample to the tip under these conditions. However, with an applied bias voltage a net tunnelling current occurs – in Figure 2.2 this is

from the tip to the sample as the sample has a positive applied bias voltage.

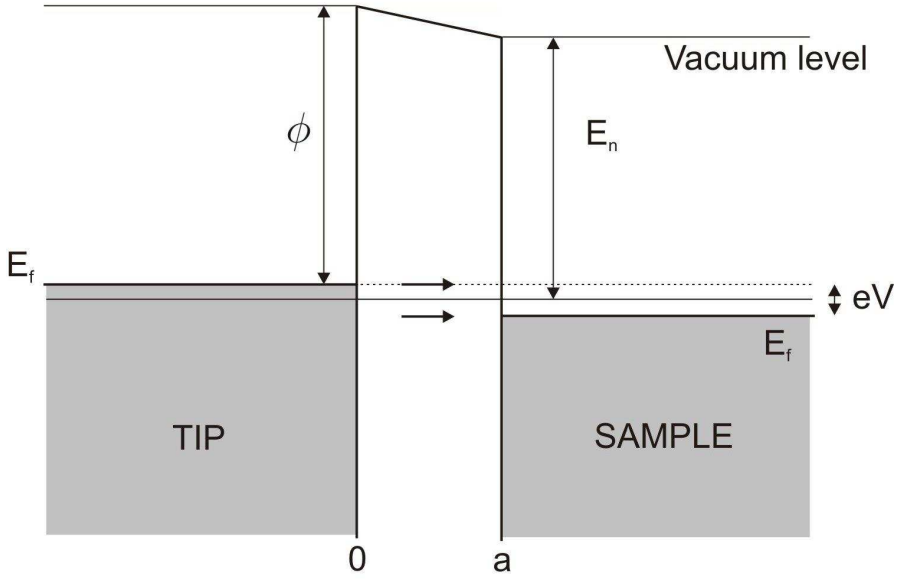

Figure 2.2: The effect of a positive bias voltage applied to a metal sample positioned close to a metal tip with the same work function, ϕ, in vacuum. The value E_n is the energy level of an unoccupied sample state.

As shown in Figure 2.2, when an unoccupied sample state with energy E_n lies between $E_f - eV$ and E_f, an electron may tunnel into the sample from an occupied state in the tip. If eV is very small compared to ϕ, then $\phi \approx \mid E_n \mid$ and the decay constant can be arranged in terms of the work function (which is a function of the applied bias) as shown in Equation 2.7.

$$\kappa = \frac{\sqrt{2m\phi}}{\hbar} = 5.1\sqrt{\phi(eV)} \tag{2.7}$$

If we substitute Equation 2.7 into Equation 2.6, the transmission co-efficient, T, is given in another form – as shown in Equation 2.8, where the units of a are nanometres.

$$T \propto e^{10.2\sqrt{\phi(eV)}a} \tag{2.8}$$

The tunnel current is therefore determined by the two work functions of the materials involved, the applied bias and the separation distance between the STM tip and sample. However, in this idealised treatment of STM the tunnelling mechanism is assumed to be 1D.

Bardeen/Tersoff-Hamann Model

A more complex treatment of the STM tip and sample states can be derived for large tip-sample separations. Under these conditions, the wavefunctions of the tip and sample may be considered as weakly coupled. The Bardeen theory of tunnelling initially treats the 1D model where Equation 2.1 becomes Equation 2.9 for the combined tip-sample system and V_μ and V_ν denote the potentials of the tip and surface states respectively.

$$i\hbar\frac{\partial\Psi}{\partial t} = \left[-\frac{\hbar^2}{2m}\frac{\partial^2}{\partial z^2} + V_\mu + V_\nu\right]\Psi = E\Psi \tag{2.9}$$

The wavefunctions ψ_μ and ψ_ν originate from the Hamiltonian for the tip and surface respectively and therefore neither wavefunction is an eigenfunction of the Hamiltonian of the combined system. Using the Bardeen tunnelling theory, the two sets of wavefunctions are approximately orthogonal [52].

$$\int \psi_\mu^* \psi_\nu d^3\mathbf{r} \cong 0 \tag{2.10}$$

If the Z direction is defined as in Figure 2.1 and z_o as the centre of the potential barrier between the tip and the surface (where $z > z_o$ describes the sample side of the barrier) a tunnelling matrix element, $M_{\mu\nu}$, can be constructed by substituting Equation 2.9 into Equation 2.10.

$$M_{\mu\nu} = \int\limits_{z>z_o} \psi_\mu V_\nu \psi_\nu^* d^3\mathbf{r} = \int\limits_{z>z_o} \psi_\mu \left(E_\nu + \frac{\hbar^2}{2m}\frac{\partial^2}{\partial z^2}\right)\psi_\nu^* d^3\mathbf{r} \tag{2.11}$$

This is assuming the condition of elastic tunnelling of electrons from a state in one system and through the barrier, into a state of another system of the same energy value, $E_\nu = E_\mu$. Bardeen has shown that this can be approximated as Equation 2.12 [52, 53].

$$M_{\mu\nu} = -\frac{\hbar^2}{2m}\int\limits_{z=z_o} \left(\psi_\nu^*\frac{\partial\psi_\mu}{\partial z} + \psi_\mu\frac{\partial\psi_\nu^*}{\partial z}\right) dxdy \tag{2.12}$$

For the tip, the number of available states is defined by the density of states of the tip at energy E, $\rho_\mu(E)$, and the energy interval defined by the bias voltage V. If the density of states of both the tip and sample do not vary appreciably near the Fermi level, E_F, and the limits of small voltages and temperature are taken, the tunnelling current, I_t, can be defined as in Equation 2.13 [52, 53].

$$I_t = \frac{2\pi e^2}{\hbar} V \sum_{\mu\nu} |M_{\mu\nu}|^2 \delta(E_\nu - E_F)\delta(E_\mu - E_F) \tag{2.13}$$

The Tersoff-Hamann model [54] treats the states in the tip and sample as weakly coupled and the tip is treated as a spherical potential well with a radius (a geometric point). Within this approximation of the tip states, only the s-wavefunctions (where angular momentum of the tip wavefunction, l, equals zero) are treated as interacting with the surface states. Consequently, according to the Tersoff-Hamann model, STM topography images would reveal the probability density of the sample states rather than a convolution of the sample *and* tip states.

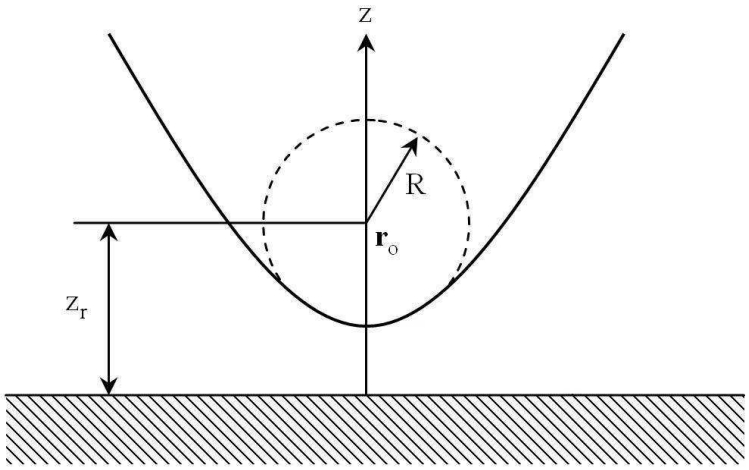

Figure 2.3: The Tersoff-Hamann model of STM, where the tip is modelled as a locally spherical potential well with radius of curvature R, centred on $\mathbf{r}_o$.

As shown in Figure 2.3, the Tersoff-Hamann model defines an STM tip centred on $\mathbf{r}_o = (0, 0, z_r)$ with a radius of curvature of R (the Z direction extends perpendicularly from the surface). If the tip wavefunctions are arbitrarily localised, then the matrix element is simply proportional to the amplitude of ψ_ν at the position $\mathbf{r}_o$ of the probe and Equation 2.13 reduces to Equation 2.14 [54].

$$I_t \propto \sum_{\nu} |\psi_\nu(\mathbf{r}_o)|^2 \delta(E_\nu - E_F) = \rho_\nu(\mathbf{r}_o, E_F) \tag{2.14}$$

Thus the tunnel current is proportional to the surface LDOS at the position of the point probe, and STM images are a contour map of constant surface LDOS.

There are limitations to this model, because in reality the surface probed by an STM tip is not solely imaged by the s-wavefunction of the atom at the STM tip apex. This is because transition metals with associated d-orbitals are commonly

used for the STM tip. However, for metals with a work function of approximately 5 eV, the contribution of non-spherical tip wavefunctions to the tunnel current can be neglected for surface feature sizes greater than 0.3 nm [52]. The Tersoff-Hamann model also breaks down if the weak coupling limit is not valid, as is the case when the tip and sample become too close and the tunnel current exceeds several nanoamps.

This model is a very powerful tool for interpreting STM images of metal surfaces, and when the length scale of features on a flat surface is approximately 1 nm or greater there is a good agreement with experimental results.

2.1.2 STM Tip Control

The precision positioning of the STM tip (or sample depending on the STM configuration) and therefore the tip-sample separation is achieved using piezoelectric transducers (or a 'piezo'). Piezoelectric transducers can displace two surfaces in relation to one another by applying a voltage across the electrodes of the transducer. Inverting the polarity of this applied voltage inverts the direction of the motion. A common type of piezoelectric transducer used in an STM system is a scan tube configuration, displayed in Figure 2.4.

Typically an STM tip is securely mounted on one end of a scan tube and the other end of the scan tube is fixed in place. Thus the tip can be displaced in the X, Y and Z directions by applying a voltage (V_X, V_Y and V_Z respectively) to the

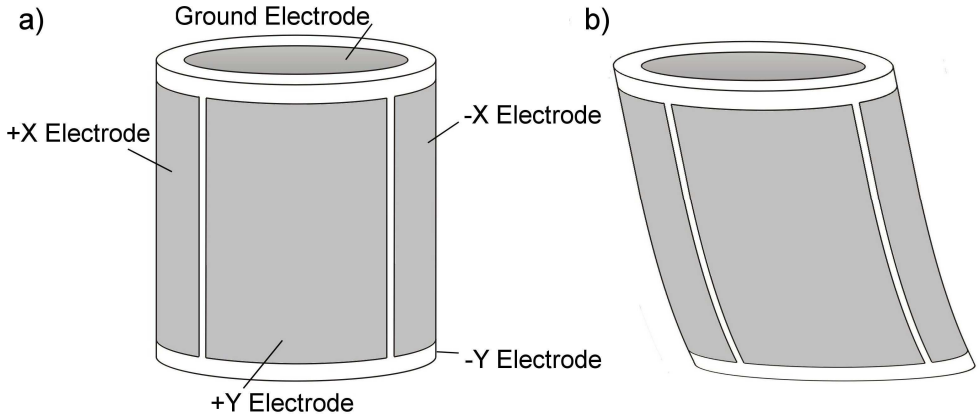

Figure 2.4: Schematic of a piezoelectric transducer scan tube with electrodes enabling controlled motion in both the X and Y directions. Displayed is the tube with no applied voltage (a) and with a positive voltage (with respect to the grounded inner electrode) applied to the +X electrode whilst a negative voltage is applied to the -X electrode (b).

corresponding electrodes whilst the electrode inside the scan tube is grounded. Figure 2.4 labels the four quadrant electrodes in terms of X and Y. A bi-polar arrangement of applied voltages is also possible, therefore doubling the displacement of the piezo for the same magnitude voltage when compared to a uni-polar configuration. A voltage is applied to one electrode of the piezoelectric material whilst a voltage of equal magnitude but opposite polarity is simultaneously applied to the other electrode, producing twice the movement in the piezo as if one waveform had been applied. This is shown in Figure 2.4 for the X direction, where V_{X+} is positive and V_{X-} is negative. If the polarities of the applied voltages are inverted, that is, if V_{X+} is negative and V_{X-} is positive, the scan tube will move in the opposite direction. By controlling the voltages applied to the four outer quadrant electrodes the secured STM tip can be accurately positioned in the X and Y directions. Applying voltages of up to 150 V can typically produce displacements of several microns – dependent on the size and type of piezoelectric material that is incorporated into the scan tube.

This scan tube configuration may be modified to displace the STM tip in the X, Y and Z directions with only four electrodes, without requiring the addition of a fifth electrode. If the voltages V_{X+}, V_{X-}, V_{Y+}, and V_{Y-} are replaced with voltages V_{Z+X}, V_{Z-X}, V_{Z+Y}, and V_{Z-Y}, then the scan tube will extend or retract in the Z direction whilst still displacing the STM tip in the X and Y directions correctly. Otherwise a separate electrode that extends around the whole scan tube (rather than separate quadrants) can be used for a separate Z channel and the quadrants solely for the X and Y channels. The latter type of configuration is discussed more in Section 3.1.2 where a scan tube used for an AFM/STM system is shown in Figure 3.7.

Coarse Positioning Motors

A scan tube typically acts as a 'fine' positioning system for the tip, that is, it will accurately (sub-Ångström resolution) raster the tip across the surface during imaging and will displace the tip in the Z direction according to the feedback system. But a less accurate or 'coarse' positioning system with a larger range of movement is also required for an STM system. This is because the fine positioning system may only have a total Z displacement of $\leq 2\mu$m. This range provides the minimum total displacement possible whilst still providing a functional STM system, so that any electrical noise will translate to a reduced extension or retraction of the STM tip. However, the maximum separation of the STM tip and sample

cannot be limited to a range of a few microns if the sample and tip are regularly replaced, which is the case for any experiment that requires sample preparation or tip treatment. Hence 'slipsticks' are commonly used for coarse positioning.

Slipstick motors commonly require shear piezoelectric transducers to step the STM tip (or sample) towards the sample (or the tip) and the principal concept is illustrated in Figure 2.5. By applying a sawtooth-waveform voltage to the linear piezoelectric transducer, the motors are displaced slowly in one direction and then extremely fast in the opposite direction, back to its original position. The STM tip is attached to the 'second surface' of the slipsticks shown in Figure 2.5. The tip is displaced slowly in the desired displacement direction and stays relatively motionless while the 'slider' (in this case a ball) slips underneath the second surface to its original position when the piezo deforms very quickly. The voltage waveform can be applied as many times as necessary to approach or retract the component and typically requires a high voltage (HV) amplifier that can produce voltages of up to 150 V and a variation of 150 V in less than a millisecond. A bi-polar configuration can also be exploited for increased displacement of the shear piezoelectric transducers of the coarse approach motors. This type of slipstick design is referred to as the linear-motor type and can displace a component with a step resolution of a fraction of a micron. However, piezoelectric transducer tubes can also be used for slipsticks in the Besocke-Beetle slipstick design [55], but this thesis is concerned with only the linear-motor slipstick design.

Probably the most crucial aspect of the slipsticks is the ability to displace the tip over a relatively large range in a reproducible fashion. In the slipstick process described in Figure 2.5, the acceleration of the slipsticks in the 'slow' and 'fast' stages must meet certain criteria. Equation 2.15 describes how the acceleration of the 'slider', a_{acc}, must be less than the frictional force, F_{frict}, acting on the slider, divided by the mass of the object that is displaced by the slipsticks, m, for the 'slow' stage. The applied waveform signal therefore has an upper limit on the voltage increase rate if the second surface is to move at the same speed as the slider. Equation 2.16 describes how the acceleration must be greater than the same limit in the 'fast' stage if the motors are to purposefully slip. Thus the decrease in voltage of the waveform signal applied to the piezoelectric transducer stack must occur in a short enough time period for the slider to slip.

$$a_{acc} < \frac{F_{frict}}{m} \tag{2.15}$$

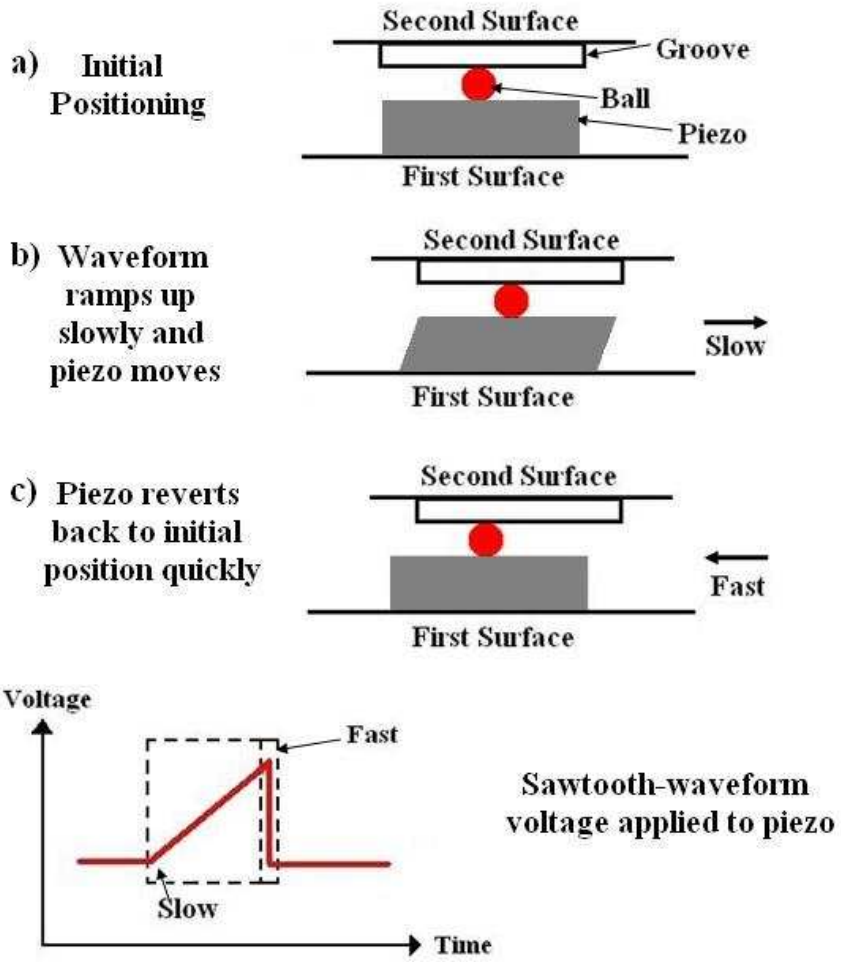

Figure 2.5: The basic displacement sequence of a linear-motor type slipstick assembly, providing coarse movement in one plane. The ball situated on the shear piezo is positioned in a groove attached to the second surface. The 'second surface' experiences a net movement in one direction as the waveform is applied repeatedly.

$$a_{acc} > \frac{F_{frict}}{m} \tag{2.16}$$

Crucial in the design of the slipsticks is the construction of the slider itself. In Figure 2.5 this is a ball that is secured to the piezo stack whilst positioned in a groove on the surface that will slip. These two contacting surfaces (the ball and groove) are typically made of a hard and a soft material so that the surfaces do not scratch each other, but instead the hard surface erodes the soft surface on a very minute scale that does not degrade the slipsticks.

User Control

As previously described, a bias is applied to an STM tip that is rastered across a surface (with less than 1 nm tip-sample separation) and the resulting tunnel current is monitored. There are two different operating modes for STM, 'constant height' mode and the more commonly used 'constant current' mode. In constant height mode there is no motion of the STM tip in the Z direction during the imaging of a surface. The subsequent variation in tunnel current is recorded to produce a topography map of the surface. The tunnel current is greater for areas of the surface that are closer to the tip and therefore these areas are displayed as higher in a topographic map (although there is also an effect caused by the LDOS of the surface). However, operating in constant height mode may crash the tip into the surface (when the tip scans towards a step-edge on the surface) or not image the surface at all if the surface is out of the range of the tip. This is commonly experienced as the sample surface will not be perfectly perpendicular to the Z direction at the nanometre scale.

Constant current mode is the more widely implemented mode as it overcomes these problems. In constant current mode, the STM tip is displaced towards the surface until the measured tunnel current reaches a predesignated setpoint. A feedback loop is then employed to maintain the tunnel current at a constant value by controlling the tip position in the Z direction so the tip-sample separation is fixed whilst the tip is scanned across the surface.[1] Thus a topographic map of the surface (related to the LDOS of the surface, as explained in Section 2.1.1) is produced by recording the Z direction position of the tip during the scan. Unless specified, this thesis only considers constant current mode STM from this point.

[1]However, as shown in Equation 2.8, the work function of the sample affects the tunnel current. Therefore the tip-sample separation may not always be fixed for a constant tunnel current if the tip is scanned over different materials (as would be the case for a sample that is covered in adsorbed molecules), but this circumstance will be ignored in this explanation.

Figure 2.6 illustrates the basic components of a constant current STM system where the bias voltage is applied to the sample. The resulting tunnel current is converted into a voltage signal by an amplifier so that the variation in tunnel current can be monitored. The feedback is performed by a digital signal processor (DSP) housed in a PC that is used to operate the STM, as shown in Figure 2.6.

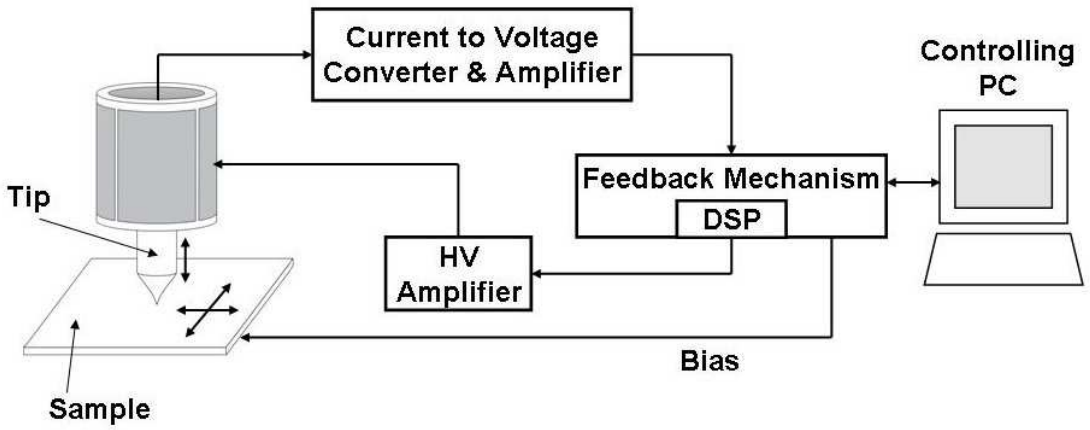

Figure 2.6: Diagram of an STM system illustrating the primary electronic components.

A graphical user interface (UI) allows a user to control both the tunnel current setpoint (to control the tip-sample separation in the feedback loop) and the sample bias and thus directly control the tip-sample separation. The feedback loop also has adjustable parameters that modify the reaction of the feedback system to variations in the tunnel current, these are the proportional and integral gain parameters for the PI feedback controller. Other parameters that can be controlled by the user are the scanning speed of the tip and the scan size.

2.1.3 STM Imaging

Noise Considerations

Atomic resolution is achievable with STM for many different surfaces, however, there are several factors that limit the resolution and must be addressed. One such factor is the speed at which the STM tip is rastered across the surface – generally if the acquisition speed of an image is decreased, the signal-to-noise ratio is increased. However, there is a delicate balancing act; STM images can become distorted due to thermal drift. This drift is caused by the differing rates of small-scale expansion of different parts of the STM due to temperature and

the resulting image distortion increases with slower scan speeds. Additionally, the piezoelectric transducers that position the STM tip and sample may distort images due to the spatial hysteresis they experience. As previously mentioned, electrical noise may also affect the STM images and can be minimised by shielding wires with grounded sheaths to minimise parasitic capacitance coupling.

Vibrational (or mechanical) noise must also be addressed as it affects the tip-sample distance directly and thus the interpreted topography of the sample. There are several methods that can be used to reduce vibrations in the system. These methods decouple the STM from the outside environment so that the effect of any external vibrations becomes insignificant. 'Air legs' are an example of this, where the system that the STM is housed in (for example a UHV system) or the STM itself is afloat on pillars with pistons and pressurised gas (pressurised air or nitrogen for example) and thus are decoupled from the surrounding environment. If the STM is not in a UHV system it can be housed inside an acoustic hood to protect it from acoustic noise sources such as heating and cooling vents and even conversation.

In an optimal STM system (where all sources of noise have been minimised) the thermal noise is the limiting factor of the resolution. This noise can be reduced in low temperature systems that employ liquid nitrogen (boiling point of 77 K) and liquid helium (boiling point of a few Kelvin). However, this obviously affects the thermal energy of the atoms in the surface under investigation and cooling the system is not strictly necessary to achieve atomic resolution.

Tip Convolution

Although it would seem logical to control the composition and shape of the STM tip to meet exact criteria for improved resolution, these variables are impossible to control accurately in reality. Due to the exponential dependence of the tunnel current on the tip-sample distance it is only the very end of the tip (the last few atoms closest to the sample) that affects STM imaging. The tip apex cannot be sculpted to this precision and due to the finite response of the STM feedback loop there are likely to be instances where the tip and surface collide. Therefore any perfectly crafted tip would not last for a sustained period of time and the actual composition of the tip is generally unknown.

STM imaging can be plagued with tip artefacts caused by the shape of the STM tip apex. A common example of this is the 'multi-tip' effect, where there are two (or more) protrusions near the STM tip apex that are roughly equal

in distance from the surface. Electron tunnelling occurs between the surface and both protrusions and thus any feature on the surface will appear twice in the STM image. Effects such as these can be removed by 'pulsing' the tip, that is causing a restructuring of the STM tip apex by greatly increasing the applied bias for a very short period of time (on the order of milliseconds to seconds) [56]. This will typically change the shape and length of the STM tip apex. The STM tip can be pulsed whilst scanning the surface and is only effective whilst electron tunnelling between the STM tip and the surface is possible. If this does not improve the quality of the STM tip, the tip can be removed from the STM and processes such as electron-beam (e-beam) bombardment or sputtering can be performed in UHV conditions – the latter is explained in more detail in Section 2.2.3. When the tip apex is bombarded by electrons (produced by heating a filament) the STM tip heats up, this can sharpen the tip apex by removing any loosely-bound material.

Surface Effects

Ignoring noise and tip effects, STM images may still be difficult to interpret due to the mapping of the LDOS of a surface rather than the surface topography directly. An example of this is when the same area of a semiconducting surface is imaged with both polarities of the applied bias consecutively. The electrons do not flow between the Fermi level of the tip and the Fermi level of the semiconductor. Instead the electrons flow from the STM tip Fermi level to the surface conduction band states when the sample is positively biased and from the surface valence band states to the STM tip Fermi level when the sample is negatively biased. The topography of the valence bands and conduction bands may vary differently over the surface and therefore the interpreted topography may differ depending on the applied bias polarity, as shown in Figure 2.7.

Scanning Tunnelling Spectroscopy

The STM was originally conceived as an instrument to achieve tunnelling spectroscopy for areas of 100 Å in diameter [58], rather than for producing high resolution topography maps of conducting surfaces as it is now most commonly implemented. However, scanning tunnelling spectroscopy (STS) is a technique stemming from STM that provides the convolution of the tip and sample LDOS at points on the surface and can be used to map the variation of the LDOS with voltage over an entire scan [59, 60]. STS is commonly performed with an STM with modified data acquisition protocols. The feedback loop of the STM is

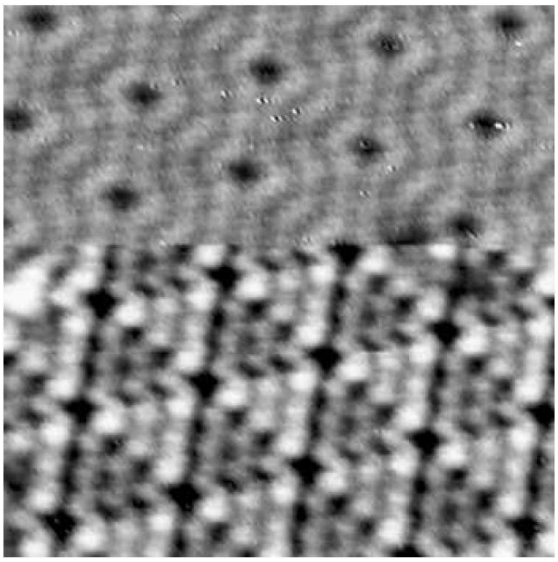

Figure 2.7: An STM image of a Si(111)-(7×7) surface reconstruction where the top half of the image was imaged with a positive bias applied to the sample and the bottom half with a negative bias applied to the sample. Imaging parameters V_{bias}= ± 3 V, I_t= 0.1 nA, scan size = 145 Å, from Ref. [57].

disabled and the tip position is fixed whilst the applied voltage bias is varied and the tunnel current recorded. This produces an I-V curve for a specific point in relation to the surface for a range of voltages (commonly several volts to several volts of the opposite polarity). It is common for the STM user to scan an area of a surface and then select a point of interest from the resulting topography to acquire an I-V curve – this is the case for any tunnelling spectroscopy performed in this thesis. It is also possible to produce a map of tunnelling spectroscopy points with this technique by engaging the STM feedback loop after one spectra is recorded. The tip can then be positioned at the next point where a pixel of an STM image would be recorded, and tunnelling spectra recorded instead. This process can be repeated for the equivalent of each pixel of an STM image. These results can then be displayed as many constant height mode images of the same area, each with a different applied bias.

The STM is a very versatile instrument that is commonly used throughout the worldwide scientific community, whether in UHV, at low temperature or ambient conditions, with many different STM models commercially available from various SPM suppliers. Although a combined AFM/STM will also feature prominently, in terms of solely acquiring STM data this thesis is concerned primarily with a UHV-STM system that is operated at room temperature and has been purchased from *Nanograph Systems Limited*.

2.2 System Procedures

2.2.1 Nanograph STM-01 Operation

STM results detailed in Chapters 4, 5 and 6 were obtained using the Nanograph STM-01 system from *Nanograph Systems Ltd.* in UHV conditions at room temperature. As shown in Figure 2.8, the STM was mounted on a Nanograph vibration isolation stage that consisted of a circular titanium plate suspended by four springs – each positioned at equidistant points around the edge of the plate. Each spring was suspended from one of four posts that were mounted onto the UHV flange underneath the STM, and a magnetic eddy damping system was attached to the underside of the plate to reduce the amplitude of any mechanical excitations. The anti-vibration isolation of the Nanograph STM-01 system was further enhanced by the addition of Viton® spacers and rings to ensure increased isolation of the stage from the environment outside the UHV chamber. It was also possible to provide additional vibration isolation for the UHV chamber itself, which was mounted on pneumatic legs supplied with N_2 gas, however this was generally not required.

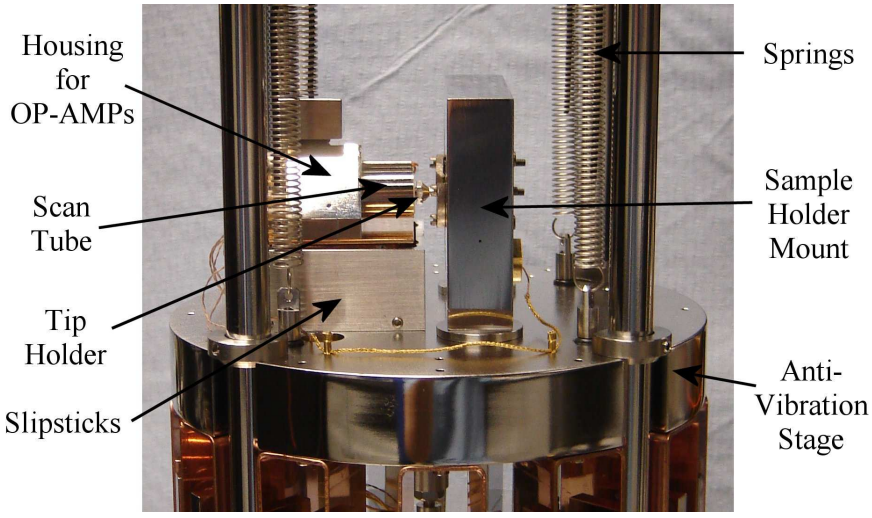

Figure 2.8: The Nanograph STM-01 UHV system. A tungsten (W) tip is housed on the end of a scan tube approaching the sample on the right. The slipsticks are observed underneath the tip assembly and all components are securely fixed to a isolation stage suspended from four springs.

The STM tip could be positioned in both the Z direction (towards and away from the sample) and X direction (to the left and right of the sample when viewing the sample from behind the scan tube) using the coarse approach motors. The

operational amplifier (OP-AMP) used to amplify and convert the tunnel current into a voltage was housed behind the scan tube in a fully grounded metal case. The OP-AMP was fully shielded from the HV signals controlling the piezoelectric transducers, but was also positioned as close to the STM tip as possible to minimise any amplification of noise. The wires connecting the electrical contacts on the STM head were oxygen-free copper (OFC) wires coated in Kapton to insulate them from any conducting surfaces. The wires connecting the STM tip to the OP-AMP passed through the central core of the scan tube and were thus shielded by the inner electrode of the scan tube used as a ground, as shown in Figure 2.4. Any sensitive channels were connected by thin coaxial wire (also coated with Kapton) with a grounded sheath to minimise electrical noise. It was possible to apply the bias to the sample when the sample holder was locked into place to make an electrical connection.

The electrical contacts on the STM head were connected to a HV amplifier (a Nanograph Studio SPM controller) and DSP, as shown in Figure 2.6, via two UHV feedthroughs. The user could control the STM using Nanograph Studio software on the supplied PC to produce STM images as well as I-V curves at selected points in a generated image. Both forward and reverse topography STM images were generated and the error signal (variation in the tunnel current) for both the forward and reverse images was also recorded. The STM was operated in constant current mode and the tunnel current setpoint, bias voltage, proportional and integral gains, scan size and scan speed were all controlled using the UI in Nanograph Studio.

The bespoke sample holder for the Nanograph STM-01 system was designed and built on-site and is shown in Figure 2.9. The sample holder was cylindrical (20 mm in diameter) and was largely constructed from machinable glass (MACOR). The sample was held at the top of the cylinder (the front of the sample holder) by molybdenum clips which were secured by molybdenum screws. The sample was pressed against a circular sapphire window and could be heated to temperatures in excess of 1000°C without damage to the sample holder or any contamination of the sample. The back of the sample holder was separated into two copper sections and each section was electrically connected to a molybdenum clip by the screw of each clip. Thus it was possible to connect directly to the sample from the back of the sample holder, as is described in more detail in Section 2.2.3.

The STM tip was housed in a bespoke STM 'tip nut' that could screw into the end of the scan tube. The other end of the tip nut was tapered and had

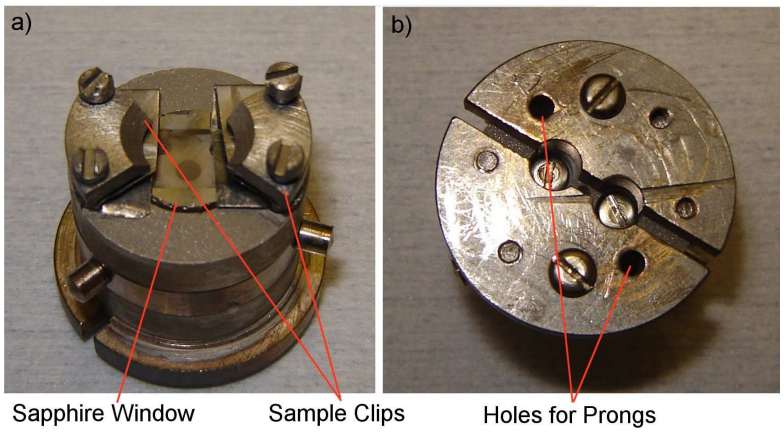

Figure 2.9: Bespoke sample holder for the Nanograph STM-01 system showing (a) the front and side and (b) the back of the sample holder. The two molybdenum clips on the front of the sample holder are shown with their screws holding them in place, either side of a sapphire window (no sample is in the holder). On the back of the sample holder were two electrically isolated copper sections, where the two large holes for the UHV arm prongs are observed.

a centrally bored hole for a metal wire to be secured in with a grub screw, as shown in Figure 2.10. The tapering allowed greater freedom of movement in the X direction for the STM tip when between the sample holder clips, as shown in Figure 2.8. Both the sample holder and the tip nut could be relocated to several places in the UHV system and mechanically removed from the system.

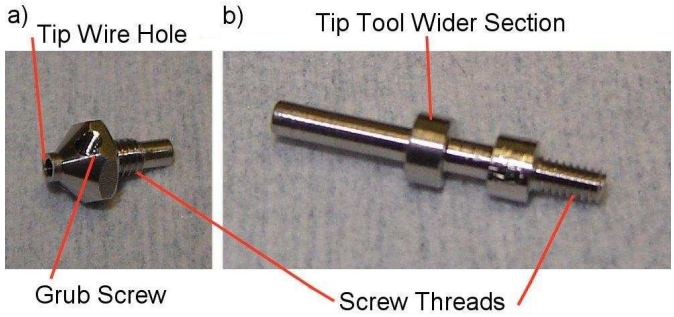

Figure 2.10: (a) Bespoke STM tip nut with a centrally bored hole for the tip wire and a grub screw to secure the tip wire in place. The back of the tip nut had a screw thread to secure into the Nanograph STM-01 scan tube and the tip nut was designed to fit into the tip tool shaft (as shown in Figure 2.12). (b) One prong (of a pair) from a UHV manipulator arm, the thinner section was used to manipulate the sample holder and tip tool whilst the wider section was only required for engaging the tip tool. A second wider section allowed the prong to secure into the UHV manipulator arm.

2.2.2 STM UHV System

Figure 2.11 shows an overview of the UHV system that housed the Nanograph STM-01 system and illustrates the placement of the UHV manipulator arms required to transport both the STM tip and sample within the UHV system. It was a necessity that the sample could be relocated within the UHV system so that it could be sputtered, annealed or deposited upon in separate UHV chambers to the STM system, as described in Section 2.2.3. Each manipulator arm had two specifically shaped prongs designed and built to work with both the sample holders and the tip tool – one prong is shown in Figure 2.10. The rear of the prongs were screwed into a small spring-loaded plate and attached to the manipulator arm, therefore when the manipulator arm was positioned it did not put excessive force on the STM system or any other components inside the UHV system.

The front end of the UHV arm prongs were designed to fit into the two holes in the back of the sample holder (shown in Figure 2.9). The prongs slid into the sample holder up to the point where the prongs widen and the UHV arm could then manipulate the sample holder. Although only friction held the sample holder onto the UHV arm prongs, once the sample holder was rotated to unlock it from the STM system or any other UHV component there was negligible force to resist the UHV arm if it was aligned correctly.

The STM tip nut was manipulated with a bespoke 'tip tool' designed and constructed on-site – the tip tool is pictured in Figure 2.12. This tip tool required more delicacy with the UHV manipulator arms than for the sample holder and required the UHV arm prongs to have a wider diameter section (as shown in Figure 2.10). The wider section could fit into the two large holes in the tip tool base and once past the entrance of the tip tool base, the prongs could be rotated in both directions, but could only be removed from the tip tool when the prongs were aligned with the two large holes. Thus any frictional forces holding the tip tool in place could be overcome when the prongs were locked within the tip tool and the tip tool was then displaced in the direction of the UHV manipulator arm. This was required when the tip tool was securing a tip nut in the STM, for example. The tip nut slotted into the end of the tip tool shaft (the opposite end to where the UHV arm prongs would fit) securely so the tip nut did not fall out, but not so securely the tip nut could not be removed from the tip tool using physical manipulation. The tip nut was shaped so that when the tip tool was rotated the tip nut would rotate, similar to how a nut or bolt would interact with the correct sized spanner. A ratchet and spring were also incorporated so the tip nut could

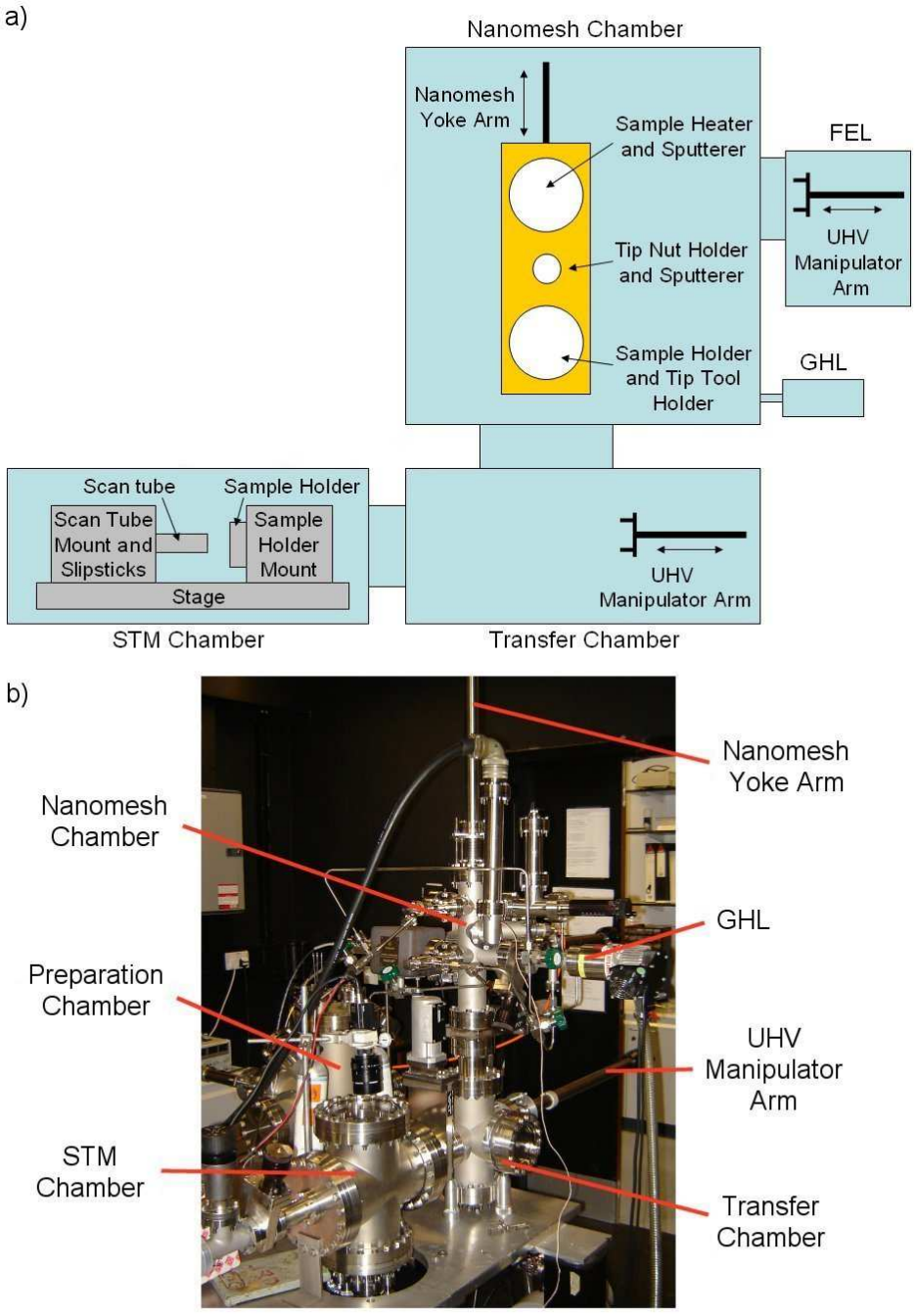

Figure 2.11: Nanograph STM-01 UHV system schematic (a) illustrating several chambers of the UHV system, and a photograph of the chambers (b). The fast entry load-lock (FEL) and gas handling line (GHL) chambers are also shown. Note that the preparation chamber is in the same plane as the transfer and STM chambers but is not shown in the schematic.

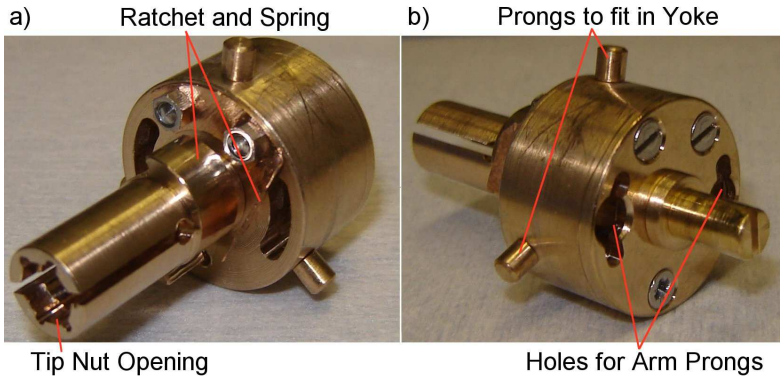

Figure 2.12: The bespoke tip tool required to secure the STM tip nut into and out of the Nanograph STM-01 STM system and Nanomesh yoke, (a) the end of the tip tool shaft where the tip nut was held and (b) the two holes for the UHV manipulator arm prongs which allowed the prongs to rotate with respect to the tip tool.

not be tightened excessively when it was secured on the delicate scan tube of the STM.

The tip tool base was specifically designed to fit and lock into the same components as the sample holder, as shown in Figure 2.12. Thus the tip tool could be shuttled around the UHV system via the sample holder storage sections and manipulated by all the UHV manipulator arms. However, the tip tool could also pass through the opening in the STM sample holder mount when the sample holder had been removed. Whilst on a UHV manipulator arm, the tip tool would approach and carefully slide onto the tip nut, then the UHV arm would be rotated anticlockwise. Once the UHV arm prongs were locked inside the tip tool, the tip tool could be rotated anticlockwise. Rotating the tip tool anticlockwise allowed the tip tool to unscrew the tip nut from the scan tube and release the tip nut – the UHV arm could then be retracted with both the tip tool and tip nut safely secured on the UHV arm prongs. The tip tool could then be transported around the UHV system and secured into any sample holder storage section, with the STM tip itself protected within the tip tool. The tip tool could also be removed from the system in this configuration so the STM tip could be replaced, as described later in Section 2.2.3.

Figure 2.11 illustrates the different chambers of and components within the Nanograph STM-01 UHV system, note that all chambers were separated by a gate valve except the connection between the transfer chamber and preparation chamber. Figure 2.11 also shows how the sample holders and STM tip nuts could

be transported within and also into and out of the UHV system. The primary moving components inside the UHV system – other than the STM system itself – were two UHV manipulator arms (each mounted with a pair of prongs) and two 'yokes' each mounted on a UHV manipulator arm. Using a combination of these arms it was possible to simultaneously utilise two sample holders and the tip tool within the UHV system, however the tip tool was only introduced to the UHV system when the STM tip required treatment or replacing. This versatility was primarily made possible by the custom built 'Nanomesh yoke', shown in Figure 2.13.

The Nanomesh yoke had two storage spaces for sample holders which could also fit the tip tool. These storage spaces contained grooves for the sample holder to rotate and lock when the UHV arm was removed from the sample holder, thus the sample holder would not fall out of the yoke unless there was a severe user error.

2.2.3 Preparation of Samples and STM Tips

UHV Techniques

Generally, an external current was passed through the sample itself to anneal the sample surface. However, for certain samples a silicon backing heater strip was required so there was no current flow through the sample as this could lead to surface damage. A pyrometer was used to measure the temperature of the sample through a UHV view-port when the sample was heated in the yoke.

An argon sputterer was attached to one flange of the Nanomesh chamber which allowed both samples and STM tips to be cleaned. The Nanomesh yoke was designed so if an STM tip nut was sputtered, any stored sample holders were facing away from the argon sputterer. The sputter current produced through the sample was recorded using the linear drive as an electrical contact with the rear of the sample holder. An electrically isolated bar was included on the Nanomesh yoke (as shown in Figure 2.13) so that the current produced whilst sputtering the STM tip could also be observed. The STM tip nut was secured into a copper screw hole which was embedded in MACOR – thus the tip nut did not contact the rest of the yoke, and the copper screw hole was connected to the protruding bar on the other side of the yoke. The linear drive could then contact this bar as it would for the back of the sample holder. A shield surrounded the tip nut holder in the yoke to guide the tip tool onto and off of the tip nut more accurately and minimise the chance of damaging the tip during the tip nut transfer process.

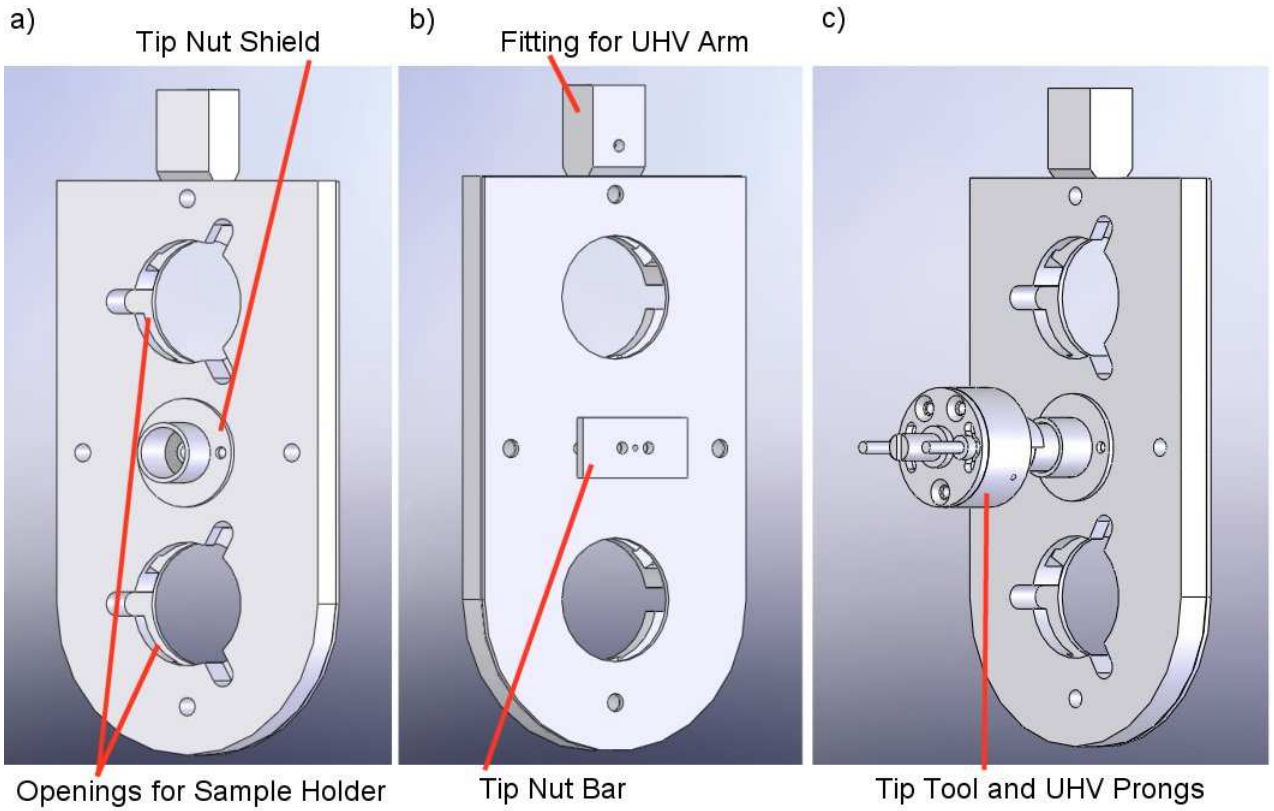

Figure 2.13: (a) and (b) the Nanomesh yoke from different angles and (c) with the tip tool placing a tip nut into the tip nut section (note the UHV arm prongs are also shown). (a) shows the entrance side of the yoke for the sample holders, note the sample holders faced the opposite direction to a tip nut and the tip nut section had a shield encompassing it to protect the STM tip during transfer. Design images created in Solidworks.

Two UHV leak valves were attached to allow other gases to be introduced to the Nanomesh chamber; one leak valve was a dedicated oxygen leak valve while the other was kept for experiment specific gases. Three gas lines were arranged to accommodate the argon sputterer, oxygen leak valve and experiment leak valve. Each of the three gas lines had sections that could be isolated using *Swagelock* valves and incorporated the required gas cylinder purchased from *Air Liquide UK*. All the lines were connected to the gas handling line (GHL) chamber (as shown in Figure 2.11) so the pressure of each gas line could be reduced to approximately 10^{-7} mbar using the GHL turbomolecular pump. The gas line could then be flushed with gas from the gas cylinder and finally refilled to achieve a full gas line of purity approximately equal to the gas cylinders specification of 99.95%.

The fast entry load-lock (FEL) chamber was also pumped by a turbomolecular and scroll pump combination which allowed a relatively quick method of moving samples and STM tips into and out of the UHV system. To introduce an item into the UHV system, the item was loaded into the FEL chamber whilst at atmospheric pressure and isolated from the Nanomesh chamber. The FEL chamber was then pumped down using the scroll pump to approximately 10^{-2} mbar – this pressure was measured using a Pirani gauge attached to the scroll pump backing lines. The turbomolecular pump then further reduced the pressure in the FEL chamber and once an adequate pressure had been reached ($\leq 10^{-7}$ mbar) the FEL chamber was opened to the isolated Nanomesh chamber. The UHV manipulator arm in the FEL chamber could be used to secure sample holders or the tip tool directly into the Nanomesh yoke and could also secure STM tip nuts into the Nanomesh yoke using the tip tool. The UHV arm was then retracted and the FEL chamber sealed off from the Nanomesh chamber via a gate valve. The Nanomesh chamber was pumped by an ion pump and stabilised at a pressure of approximately 1×10^{-9} mbar. A titanium sublimation pump (TSP) was also used to reduce the pressure in the chamber. The UHV chambers of the system (not the FEL and GHL chambers) were kept at UHV with a combination of ion pumps and TSPs once they had been baked. During the baking process the chambers were kept at 100-150°C for several days to deplete the water vapour inside the UHV system and therefore reduce the overall pressure in the system once it had cooled down to room temperature. Exposure to higher pressure chambers such as the FEL chamber was minimised for the UHV chambers – the Nanomesh chamber was the only chamber regularly subject to higher pressures and only for several minutes at a time, whilst it was isolated from other UHV chambers. The Nanomesh chamber ion pump was switched off during higher pressure sputtering cycles due to the

partial pressure of argon, instead the Nanomesh chamber was pumped using the turbomolecular pump in the FEL chamber.

Any item secured in the Nanomesh yoke could be transported into the transfer chamber (as shown in Figure 2.11) and then removed from the Nanomesh yoke using the transfer chamber UHV arm. This allowed the item to be placed in a different section of the Nanomesh yoke (for example, moving a sample holder from the bottom storage section to the top storage section for annealing) without requiring the FEL chamber. The transfer chamber UHV arm could also secure items in the STM system as described previously or transfer the item to the preparation chamber yoke.

The preparation chamber included a larger ion pump than the Nanomesh chamber and the preparation chamber was maintained at 2–4$\times 10^{-10}$ mbar, in combination with another TSP. The preparation chamber yoke was a simpler version of the Nanomesh yoke and had just one storage section for a sample holder. The preparation yoke also had the ability to anneal a sample, with copper leaf springs (connected to an external power supply unit (PSU)) that contacted the sample holder clips when the sample holder was locked in place. However, the preparation yoke was mainly used for the deposition of atoms or molecules onto the samples from evaporators, such as – in the case of organic molecules – Knudsen cells [61].

Molecular Deposition in UHV

A Knudsen cell (or 'K-cell') is used to heat a solid material in UHV conditions until the material sublimes and atoms or molecules are ejected from the Knudsen cell. Figure 2.14 shows a labelled photograph of a Knudsen cell used in the UHV systems described in this thesis.

The Knudsen cell is essentially a cylindrical furnace with a tantalum filament, a crucible containing the material to be deposited in UHV and a thermocouple to monitor the temperature of the crucible. A Knudsen cell may be heated from room temperature to temperatures in excess of 1000°C, using a PSU to control the filament temperature. To achieve a relatively pure sublimation of a certain material, the Knudsen cell and crucible were first cleaned with solvents outside of the UHV system. The Knudsen cell was then annealed inside the UHV system to a temperature much greater than the sublimation temperature ($T_{sublime}$) of the deposition material. The Knudsen cell was then removed from UHV, the deposition material was added to the crucible and the Knudsen cell was again

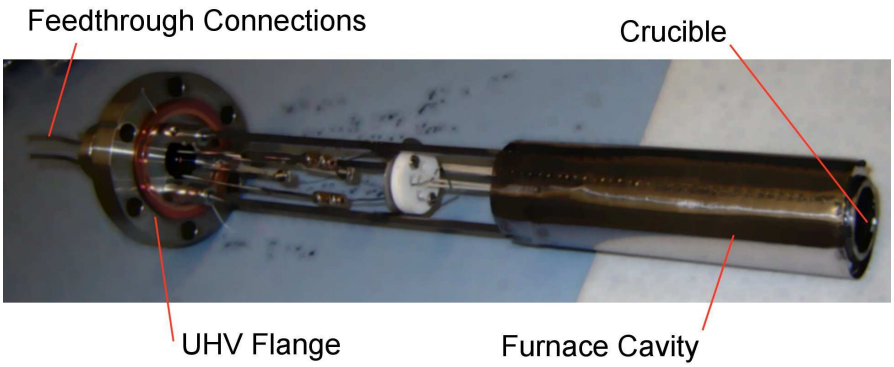

Figure 2.14: A photograph of a Knudsen cell. The crucible was loaded with material for UHV deposition and the connections outside of UHV were used to control the temperature with a PSU and filament, and also monitor the temperature with a thermocouple.

introduced to the UHV system. The Knudsen cell was then degassed prior to its first deposition by annealing the Knudsen cell to a temperature close to but below $T_{sublime}$ for several hours, so that the initial pressure burst subsided. The Knudsen cell was then ready for a deposition cycle and was brought to a temperature a few degrees above $T_{sublime}$ for several minutes. The temperature was then lowered to $T_{sublime}$ and maintained for several minutes so the Knudsen cell deposition rate settled before positioning the sample surface in the path of the sublimed molecules. The deposition rate of the material was measured with a quartz crystal microbalance (QCM) positioned close to the sample surface and angled in the same direction. As the distance of the sample from the Knudsen cell was large compared to the size of the sample and the Knudsen cell aperture, the flux of the molecules incident on the sample can be assumed to be uniform. Three Knudsen cells were attached to the preparation chamber at any one time. A gate valve was situated between one of the Knudsen cells and the preparation chamber to allow easy and efficient replacement of the K-cell using a turbomolecular and scroll pump combination.

STM Tip Etching

As discussed previously, a metal wire with a sharp apex securely held in a tip nut by a grub screw was used as an STM tip. All STM tips (though not combined AFM/STM tips) used in this thesis were constructed from either ⌀0.5 mm tungsten (W) wire (99.95% purity) or a ⌀0.25 mm wire containing platinum (90%) and iridium (10%) (Pt-Ir), all metal wires were purchased from *Goodfellow*.

Pt-Ir tips were used for ambient condition STM experiments and testing of STM systems in UHV due to the ease of producing a suitable tip very quickly. Due to its softness Pt-Ir wire could be cut using a standard cutting tool and Pt-Ir wire cut at a 45° angle to the wire usually produced a suitable tip apex. To produce tungsten STM tips, W wire required electrochemically etching with a 3 M sodium hydroxide (NaOH) solution used as the electrolyte. However, it was also possible to etch the Pt-Ir wire if a tip with fewer 'mini-tips' was required – these mini-tips could lead to a multi-tip affect in the STM imaging, as described in Section 2.1.3. The etching of Pt-Ir tips was performed using an alternating current rather than a direct current, which was used for etching W tips. Etching of the Pt-Ir wire was achieved with calcium chloride ($CaCl_2$) solution [62]. The equipment used to etch STM tips is shown in Figure 2.15.

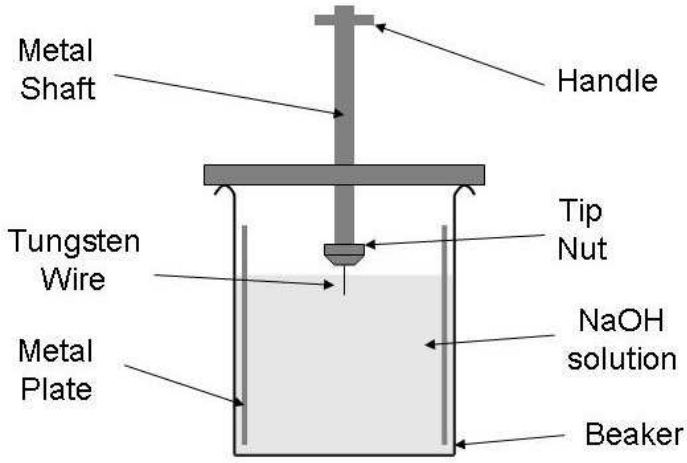

Figure 2.15: The electrochemical etching equipment for producing a tungsten STM tip. The tip nut containing the tip wire is lowered or raised using the handle at the top of the shaft. The shaft is connected to one terminal of a PSU while the metal plate situated in the solution is attached to the other terminal.

For tungsten tips, W wire was secured in the tip nut so the length of the protruding wire was equal to the length of the desired tip plus approximately 10 mm. The tip nut was then mounted in a shaft secured in a beaker lid. The lid was secured onto the beaker containing the NaOH solution and a metal plate shaped to follow the outer wall of the beaker. One terminal of a PSU was then connected to the metal plate while the other terminal was connected to the metal shaft. The handle at the top of the shaft lowered the tip wire into the solution until approximately 10 mm of the tip wire was immersed, thus the meniscus of

the solution was positioned where the tip apex would form. When a voltage was applied using the PSU, the tip wire was electrochemically etched at the meniscus. Once the wire was thin enough the weight of the tip wire below the meniscus caused the thin part of the tip wire to break and the circuit was broken. The tip nut was then removed and washed in de-ionised water to remove traces of the NaOH solution and dried using a nitrogen gun. The tip was then introduced into UHV where any contaminants could be removed using e-beam bombardment or argon sputtering.

This section has described the processes required to perform experiments with the Nanograph STM-01 system operated in UHV. Two systems were primarily used for the experiments in this thesis, the Nanograph STM-01 system and a combined AFM/STM system which was custom built on-site and also operated in UHV.

2.3 The Theory of AFM

In 1985 Binnig, Quate and Gerber invented the atomic force microscope (AFM) [63] which has become the instrument of choice for nanoscientists interested in areas of biology, chemistry and physics throughout the world. The primary function of an AFM is to produce nanoscale topographical images of surfaces by probing the forces encountered at the surface, but AFM also allows the measurement of surface properties such as stiffness and elasticity. The AFM is a combination of the principles of STM and the stylus profilometer, but while STM imaging is confined to conducting surfaces, the forces of both conducting and insulating surfaces can be mapped using AFM. The most striking difference between AFM and STM is that instead of a static tip measuring the electron tunnelling effect, AFM typically requires a cantilever to measure the surface forces.

2.3.1 Probing Forces with a Cantilever

A topographical image of a surface can be generated by using an AFM to measure the forces acting on the sharp tip of an AFM cantilever whilst the tip is scanned over the sample surface. The surface forces are experienced by the cantilever tip due to the close proximity (down to sub-nanometre separation) of the tip to the surface of the sample. A feedback mechanism adjusts the cantilever-sample distance so the average force on the tip is constant and the variation in cantilever-sample distance that ensues is recorded. Software is then employed to produce

topographical images from this data. As is the case for other SPM techniques, piezoelectric transducers are necessary for the movement of the cantilever system in the Z direction – which requires a feedback loop. Piezoelectric transducers are also incorporated into the mechanical design of an AFM to allow movement of the sample with respect to the probe in the X-Y plane.

Depending on the mode of operation (explained in Section 2.3.2) the cantilever of an AFM oscillates either at or close to its natural resonant frequency, f_o, whilst it is scanned across the sample surface. The amplitude of these oscillations is of the order of 0.01-100 nm depending on the AFM mode of operation.

There are several ways to excite the cantilever; acoustically, magnetically or electrically. The latter technique is associated with piezoresistive cantilevers and tuning forks, and is described in Section 2.3.4.

The acoustic (also called mechanical) excitation of the cantilever is a commonly adopted method that requires a piezoelectric actuator attached in close proximity to the cantilever-tip ensemble, as shown in Figure 2.16.

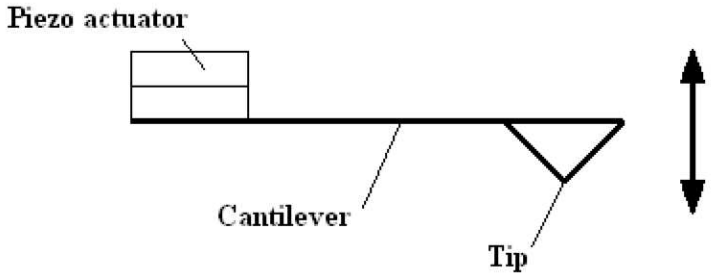

Figure 2.16: Diagram of a piezoelectric actuator exciting a cantilever, the oscillatory motion of the cantilever is indicated.

When an oscillating voltage is applied to the piezoelectric actuator, the piezo vibrates and thus the cantilever oscillates. The frequency of the waveform applied to the piezo can be varied to modify the oscillation frequency of the cantilever accordingly. By measuring the displacement of the cantilever as the cantilever oscillates at a range of frequencies, the value of f_o can be acquired.

When exciting the cantilever magnetically a piezoelectric actuator is not required, but instead the cantilever must be magnetised. An oscillating magnetic field excites the cantilever directly, thus providing the same oscillating motion for the cantilever as mechanical excitation [64].

Cantilever Motion Detection

When the AFM was first developed by Binnig, Quate and Gerber [63], an STM system was used to monitor the cantilever displacement. Although electron tunnelling as a sensor was extremely sensitive, a technique that was not as prone to surface contaminant degradation but still provided sub-Ångström resolution without perturbing the cantilever was preferred. Optical methods are now the most common motion detection systems incorporated into ambient condition AFMs, which are divided into interferometry and beam deflection techniques. For AFMs operating in UHV conditions, developed techniques include vacuum tunnelling, the capacitance sensor, and optical lever detection [65], as well as piezoresistive cantilevers or tuning forks (described in Section 2.3.4).

Noise Considerations and Optimal Resolution

Topographical images of a surface can be generated using an AFM and thus there are two separate resolutions to be distinguished, 'lateral' and 'vertical'. The vertical resolution is ultimately limited by both noise from the detection system and thermal fluctuations of the cantilever. In general, the lateral resolution depends on tip size, tip-surface separation and tip-surface force.

Mechanical noise has been addressed in Section 2.1.3, and it may seem logical that this would cause a significant problem in vertical resolution for AFM. However, from Reference [66], the immunity of an AFM to external vibration depends on the frequency, v, of the vibration relative to the lowest resonant frequency, v_o, of the mechanical system. The amplitude of the relative tip displacement due to noise is attenuated by a factor $(v/v_o)^2$ in the limit $v \ll v_o$. Thus if the lowest resonant frequency of a cantilever is greater than 20 kHz, a typical 20 Hz building vibration of amplitude 1 μm results in relative vertical tip motion of less than 0.01 Å, nearly insignificant. Cantilevers have a very high value of f_o so the limiting factor is typically the AFM mechanical structure, thus mechanical components that are rigid and compact are constructed to reduce the effect of mechanical noise.

The tip radius must be as sharp as possible to minimise any broadening effects in the AFM images. There is a much greater broadening effect for AFM tips than STM tips because the forces probed with AFM do not have the same exponential relation to the tip-sample separation – the attractive forces are experienced by an AFM tip at a much longer range. Thus atoms in the tip further from the sample than the tip apex will contribute to the total force experienced by the AFM cantilever, rather than just the tip apex – which is the case in STM. Therefore

surface features that are smaller than the tip radius can appear broader. Cantilevers can be microfabricated from silicon, SiO_2 or Si_3N_4 using photolithographic techniques to achieve a sharp tip apex. This technique can produce cantilever lateral dimensions in the order of 100 μm and 1 μm in thickness. This produces a cantilever spring constant, k, of the range 0.1-1 Nm^{-1} and a cantilever f_o value of $\sim$10-100 kHz.

There are several AFM operational modes and for the highest quality images the mode selected typically depends on the surface being studied. There are both attractive and repulsive contributions of the force experienced by the AFM tip and the AFM scanning parameters can be modified to image the surface primarily with attractive force contributions or repulsive force contributions to improve imaging. For example, attractive forces give better results for biomolecules by reducing the tip-molecule force, whereas stiffer materials are best imaged with repulsive forces as the forces exerted are more sensitive to surface changes.

2.3.2 Modes of Operation

The different modes of AFM operation can be segregated into 'contact mode' and 'dynamic methods' – often called non-contact AFM (NC-AFM). Dynamic modes can be further organised into amplitude modulation AFM (AM-AFM) and frequency modulation AFM (FM-AFM) modes.

Contact Mode

AFM was originally only operated in contact mode, where the cantilever is in physical contact with the surface whilst it is scanned across the surface and the static deflection of the cantilever is recorded. Figure 2.17 shows a diagram of a cantilever in contact mode.

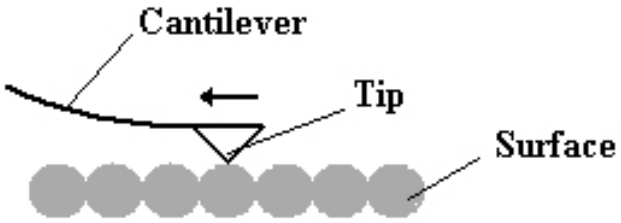

Figure 2.17: Diagram of a contact mode AFM, the cantilever scans across the sample whilst in direct contact with the sample.

However, as the tip of the cantilever scans the surface whilst in direct contact with the atoms of that surface, damage to the surface can result.

Contact mode AFM is conceptually similar to imaging topography with a stylus profilometer, however AFM implements a small and well-controlled loading force. That is, stylus profilometry methods exert a loading force of 10^{-2} N to 10^{-5} N while AFM has a loading force of 10^{-7} N to 10^{-11} N.

Atomic resolution has been achieved in contact mode for graphite in 1987 [67] and has also been achieved for other layered materials such as molybdenum sulphide and boron nitride in 1988 [68].

Dynamic AFM Methods

In contact mode the interaction is dominated by relatively short-range repulsive interatomic forces. When the tip is displaced from the sample by 10-100 nm and an oscillating cantilever is adopted, the tip is subjected to longer range forces – such as magnetic, electrostatic and van der Waals forces.

The tip-cantilever ensemble can be modelled as a point-mass spring, when driven, the motion of the tip can be approximately described by a non-linear, second-order differential equation, as in Equation 2.17.

$$m\ddot{z} + \frac{mw_o}{Q}\dot{z} + kz = F_{ts} + F_o\cos(wt) \tag{2.17}$$

F_o and w are the amplitude and angular frequency of the driving force respectively. Q, w_o and k are the quality factor (or Q-factor), angular resonant frequency and the spring constant of the free cantilever respectively [69]. F_{ts} contains the tip-surface interaction forces in the Z direction. In the absence of any tip-surface forces (that is when the tip is away from the surface) $F_{ts} = 0$ and Equation 2.17 describes the motion of a forced harmonic oscillator with damping.

By substituting $F_{ts} = 0$ into Equation 2.17, the shape of the resonance curve, as illustrated in Figure 2.18, can be described. At low driving frequencies with respect to f_o the response is controlled by the stiffness of the spring, that is, the cantilever moves in phase with the driving force and with an amplitude close to F_o/k. At frequencies very large compared to f_o, $kz \ll \ddot{z}$ and the response is controlled by inertia, causing a relatively small amplitude with a phase shift of 180°.

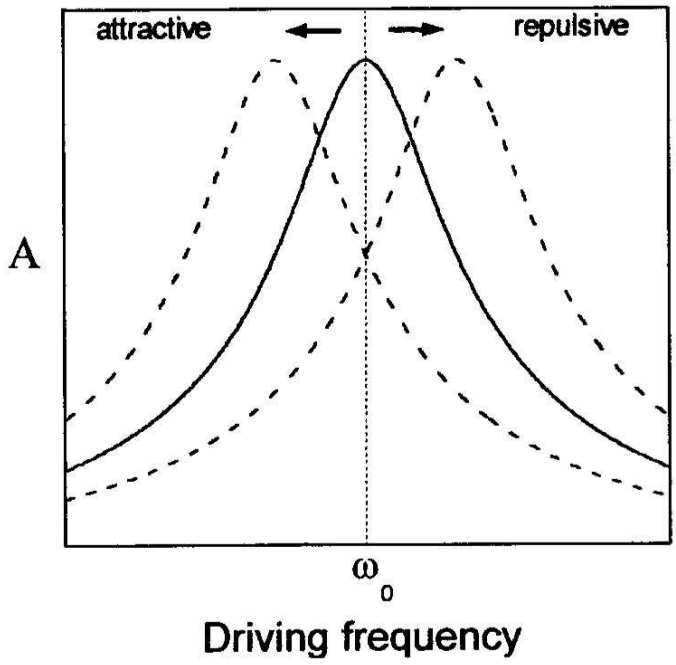

Figure 2.18: Resonance curve for a single harmonic oscillator (solid line) and under the influence of attractive and repulsive forces (dashed lines), A = oscillation amplitude, modified from Ref. [69], © (2002), with permission from Elsevier.

Attractive and Repulsive Forces

The presence of a force gradient in the Z direction, $\partial F_{ts}/\partial z$, modifies the effective spring constant of the cantilever, k_e:

$$k_e = k - \partial F_{ts}/\partial z \tag{2.18}$$

If the sample exerts a negative force gradient on the cantilever, the spring constant will effectively soften. This then affects the resonant frequency of the cantilever with mass m_o.

$$f_o = (1/2\pi)(k_e/m_o)^{1/2} \tag{2.19}$$

From Equation 2.19, a softer cantilever leads to a decrease in f_o. If the cantilever was driven at its resonant frequency before the force gradient was experienced by the cantilever, the amplitude of oscillations of the cantilever will decrease due to the change in f_o. When a positive force gradient is exerted by the sample, the spring constant will effectively stiffen. Thus f_o will increase, affecting the

amplitude of the oscillations, as shown in Figure 2.18.

From Figure 2.18, the force gradient of the external force, F_{ts}, produces a shift of the resonant curve without introducing any shape or size modifications. This is the case when the resonance curves are derived by modelling the cantilever as a weakly perturbed harmonic oscillator as in Reference [69]. However, this does not take into account that the shape of the resonance curve changes with variation in the separation distance of cantilever and sample. The peak becomes more and more truncated at the centre of the curve the smaller the tip-sample separation distance.

Whether a positive or negative force gradient is exerted on the tip by the sample is dependent on the tip-sample distance. In the absence of any field being applied externally, the dominant forces are van der Waals interactions, short-range repulsive interactions and capillary forces. Capillary forces are attractive forces that arise due to a thin film of water between tip and sample. This thin film is present in ambient conditions but not for UHV conditions. If the tip is in contact with the thin film of water the capillary force acts by creating a bridge between the tip and sample. Van der Waals forces are long-range attractive interactions that arise from spontaneous fluctuations of electrons. Van der Waals forces are exerted upon the cantilever tip by all types of surfaces as these fluctuations are always present.

Pauli repulsion causes the short-range repulsive forces between atoms and molecules. These repulsive forces are more than just an electrostatic repulsion between the electron clouds of the two atoms. When the particles are widely separated, the wavefunctions of the core electrons of the particles do not significantly overlap and the electrons can have identical quantum numbers. The Pauli exclusion principle states that no two fermions can occupy the same state. As the particles get closer, a new set of energy states is formed for the composite, two-nucleus system, the lower energy states are filled and some of the electrons are pushed into higher states. This requires energy and is experienced as a repulsion, preventing the particles from reducing their separation distance.

The different forces exerted on the cantilever tip by the surface lead to two different regimes, as shown in Figure 2.19, with the arbitrary point $z = 0$ separating the two regimes. From Figure 2.19, the 'attractive regime' describes AFM operation when the tip-sample distance, z, is positive and the 'repulsive regime' describes operation when $z < 0$. The repulsive regime is defined as the distance in which repulsive forces act on the tip and is very short-range (fractions of nm). The attractive regime is for tip-sample distances beyond the repulsive regime where the

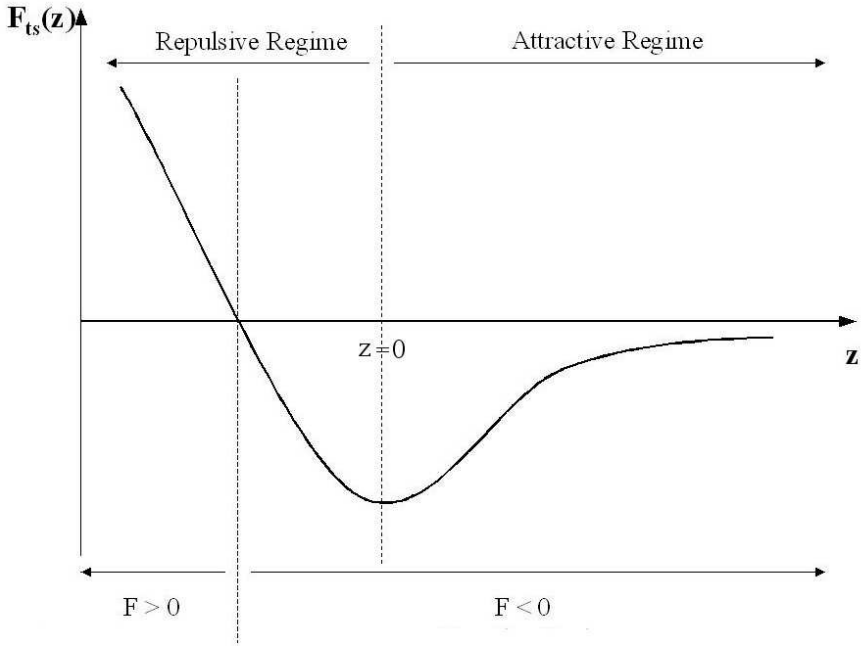

Figure 2.19: Sketch of the force exerted on the tip of the AFM cantilever by the surface, F_{ts}, versus tip-sample separation distance, z, illustrating the repulsive and attractive regimes.

forces acting on the tip are only attractive (up to 100 nm). Thus the force gradient changes from negative (attractive forces for $z > 0$) to positive (repulsive forces for $z < 0$), as the mean tip-sample separation distance, z, decreases.

Figure 2.18 shows how the resonant frequency is affected by the two different types of forces. The longer range attractive forces decrease the resonant frequency, f_o, and the shorter range repulsive forces increase f_o. Therefore in practical terms, there are two different stable states in which an AFM can operate. In FM-AFM mode the feedback system must be able to control the tip-cantilever assembly in the Z direction for either increases or decreases in f_o (due to both positive and negative force gradients) accordingly, depending on the regime of operation.

An AFM can be operated in NC-AFM mode (attractive forces), 'tapping' AFM mode (where the cantilever still experiences attractive forces, but also repulsive forces for a fraction of its oscillation cycle) or contact mode (which primarily probes repulsive forces) without requiring the ability to alter the feedback polarity. In FM-AFM mode, care must be taken in the selection of a frequency shift set-point because of the trough in the F_{ts} versus z curve (Figure 2.19). Operation in this trough is very difficult as practically only one polarity of feedback is possible at any one time. Thus the tip may crash into the sample if the polarity of the feedback

mechanism is incorrect.

2.3.3 Amplitude Modulation AFM

In AM-AFM mode the measured oscillation amplitude, A, is the feedback parameter. The excitation amplitude (and excitation frequency) is kept constant throughout, but the oscillation amplitude, A, is monitored and the Z direction feedback piezo adjusts the mean Z-position of the cantilever to maintain A at a constant value. The topography of the surface is therefore mapped by recording the movement of the Z direction piezo – analogous to the constant current STM mode. AM-AFM is sometimes referred to in the literature as tapping mode and FM-AFM referred to as NC-AFM. This is because AM-AFM was historically operated in an intermittent contact mode and FM-AFM in a non-contact mode. However, both these dynamic modes of AFM can now be implemented in either fashion.

Nowadays AM-AFM is the dominant mode of AFM for experiments in air and in liquids, whereas FM-AFM is primarily implemented in UHV. The feedback response is reduced for AM-AFM mode in UHV due to the higher quality factor of the cantilever ($Q \sim 10^4$) and therefore FM-AFM is preferred. However, atomic resolution of Si(111)-(7×7) was achieved in UHV in 1997 for AM-AFM mode [70]. AM-AFM typically involves excitation amplitudes in the 1-100 nm range and is used for biomolecular imaging, for imaging DNA, membrane proteins and polymers. It may also be used to manipulate at the nanometre scale, the manipulation of single 50 nm diameter gold nanoparticles as an example [71].

The tip dynamics of AM-AFM can be described in terms of a tip-sample interaction potential with long-range van der Waals forces and short-range Pauli repulsive forces. However, even with simplified assumptions, these forces have power law dependencies on the tip-surface separation. Therefore the non-linearity of the tip-sample interactions has large implications in the resulting tip motion, making it difficult to find analytical solutions, but the action of a cantilever in AM-AFM can be understood qualitatively for ease of understanding. If the cantilever was excited by a driving force, F_o, at the natural resonant frequency of the cantilever, f_o, and then approached towards the surface, the cantilever tip would experience forces exerted by the sample. These forces would modify the resonant frequency which in turn implies a modification of the cantilever oscillation amplitude, A (as shown in Figure 2.18). Therefore the new oscillation amplitude would be smaller than the free oscillation amplitude. However, if the cantilever

was initially off resonance, the oscillation amplitude, A, could decrease or increase depending on the modified resonant frequency and the driving force frequency both with respect to f_o.

2.3.4 Frequency Modulation AFM

FM-AFM monitors the resonant frequency of the cantilever and utilizes it as the Z direction piezo feedback parameter. FM-AFM is the AFM mode primarily used in UHV and has achieved atomic resolution for over a decade. FM-AFM has led to an increased sensitivity over AM-AFM through the ability to use higher Q-factor cantilevers without any restriction on bandwidth.

In FM-AFM mode the oscillation amplitude, A, of the cantilever may or may not be kept constant at A_o (detailed later in this section). The example of the 'constant amplitude' mode will be assumed, where the oscillating amplitude of the cantilever, A, is fixed and equal to the amplitude setpoint, A_o. Initially the resonance of the cantilever is measured while the tip-sample distance is large and $F_{ts} = 0$, thus f_o can be recorded and the associated amplitude at f_o defined as A_o. Whilst scanning the sample in constant amplitude mode, a feedback loop monitors the oscillation amplitude, A, as an input signal from the cantilever motion detector and modifies the excitation amplitude accordingly to force the cantilever to oscillate at the amplitude setpoint, A_o.

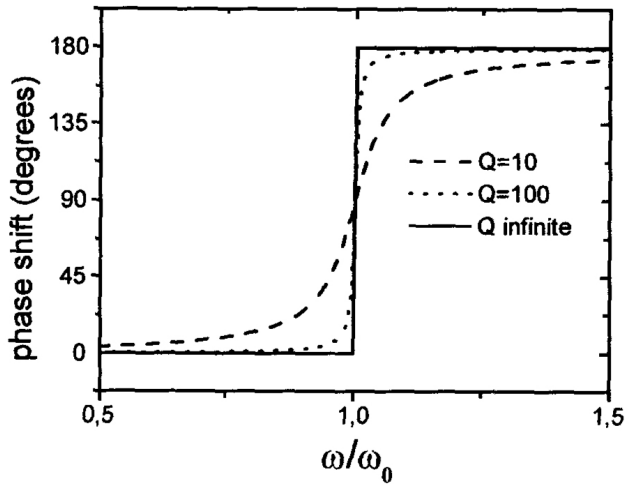

Figure 2.20: Phase shift behaviour of a driven harmonic oscillator as a function of driving frequency, due to damping there is a continuous change in the phase shift rather than a sharp transition, reprinted from Ref. [69], © (2002), with permission from Elsevier.

Figure 2.20 shows the variation in phase of a driven harmonic oscillator with respect to frequency when the oscillator is brought to resonance and off resonance again. In FM-AFM, a feedback loop called the phase-locked-loop (PLL) (described in greater detail later in this section) varies the frequency of the driving signal in order to excite the cantilever at resonance conditions. The PLL maintains the phase of the driving signal at the phase set-point. The frequency of the driving signal is modified according to the polarity of the phase shift, as per Figure 2.20. Therefore the cantilever will always be driven at its effective resonant frequency, f_e, even though this parameter varies due to the tip-sample interaction.

The frequency shift, df, caused by forces from the surface, is equal to $f_e - f_o$ and the tip-sample distance is varied with the Z direction piezo to maintain df at a desired frequency shift set-point. The movement of the Z direction piezo during a scan of the sample is then plotted as a topography map of the surface.

The cantilever motion in FM-AFM mode can be described as a weakly perturbed harmonic oscillator with a modified frequency due to the tip-surface interaction, as the AM-AFM mode was previously. However, the FM-AFM model has been proven to be justified by previous calculations [69]. Using this model Equation 2.17 can be modified into Equation 2.20 to describe FM-AFM operation.

$$m\ddot{z} + \frac{mQ}{w_o}\dot{z} + kz - F_{ts}[A + z_c] = F_{exc} \tag{2.20}$$

Where z_c is the cantilever support distance from the surface (compared to z which is the tip-surface separation), and F_{exc} is the excitation term that describes the excitation of the cantilever motion due to the cantilever being driven. The numerical results from this model described in Equation 2.20 and the experimental results measured for the frequency shift for varying tip-sample separation distance are described in Reference [69].

Optimal AFM Operation Parameters

When Binnig first published his invention of the AFM in 1986 [63], he surmised that the AFM had the potential to achieve atomic resolution, adding that scanning in UHV with microfabricated cantilevers would be required. In 1995 this experimental set-up did indeed achieve atomic resolution of the reactive Si(111)-(7×7) reconstructed surface [72], implementing microfabricated cantilevers and in UHV conditions as Binnig had predicted, but operated in FM-AFM mode rather than the original contact mode.

The optimum parameters used for FM-AFM operation to achieve atomic res-

olution have been determined since its invention essentially by trial and error. The 'classical' mode of operation is characterized by k ∼20 Nm^{-1}, f_o ∼100 kHz, Q ∼10^4-10^5, A_o ∼10 nm and df ∼ -10 to -100 Hz for the cantilever stiffness, natural resonant frequency, quality factor, the driving amplitude and the frequency shift set point respectively. The quality of imaging in FM-AFM mode quickly became comparable to STM imaging [73] but also had the ability to image insulators with equal resolution [74].

However there are advantages of operation with very small amplitudes of $A_o \lesssim 1$ nm, such as noise reduction and the enhanced sensitivity to the short-range chemical interactions providing enhanced lateral resolution [75], explained in detail in Reference [76].

Piezoresistive Cantilevers and Tuning Forks

Integrated deflection sensors based on the piezoresistive or piezoelectric effect are extremely powerful tools for cantilever deflection sensing, as these sensors do not need large physical detection systems. The detector is integrated into the cantilever itself, thus making it considerably easier to perform AFM in adverse conditions such as UHV. The need for precise alignment of the detection system – which is required for optical methods – is also removed.

A typical piezoresistive cantilever consists of a single crystal silicon structure with a diffused conductive channel and an integrated ultrasharp asymptotic silicon tip. Deflection of the cantilever alters the resistance of the conductive channel – the piezoresistive effect. The cantilever can be excited mechanically by a piezo and then the deflection can be monitored. Measuring the resistance of the conductive channel of the cantilever through two electrical contacts determines the cantilever deflection. This technique has demonstrated its ability to achieve atomic resolution for several materials including MoS_2 in UHV [65]. Piezoresistive cantilevers can also be used at low temperatures and in AFM/STM systems, the cantilever can be biased with DC current with one electrical contact and thus the silicon tip becomes the tunnelling probe. The other contact of the cantilever is grounded, thus there is no movement of the cantilever. However, these cantilevers are not necessarily stiff, typically $k \leq 100\ \mathrm{Nm}^{-1}$, allowing the cantilever to jump to contact the surface. Stable tunnelling between an integrated cantilever tip and a sample is only possible if the force gradient of the attractive interaction between tip and sample is smaller than the force gradient of the cantilever. It should be noted that the higher resolution images obtained with piezoresistive cantilevers were generally

measured with the stiffest cantilevers available.

The qPlus-sensor (QPS) was invented in 1998 [77] and continued on from work performed by Giessibl with piezoresistive cantilevers [65]. This new sensor was an integrated deflection sensor system that consisted of a quartz tuning fork (TF) (produced in large quantities for the watch industry) as the cantilever. These quartz tuning forks had an eigenfrequency of $f_o \simeq 32\ 280$ Hz, with a length of 3 mm, thickness 330 μm and width 120 μm as a common example. It was found that these tuning forks not only had an inherently large Q-factor ($\geq$ 1000 in air, $\geq$ 10 000 in vacuum) the QPS tuning forks were also very stiff, with theoretical $k \simeq 3143$ Nm^{-1} determined with Young's modulus of quartz $E = 7.87 \times 10^{11}$ Nm^{-2} [78]. Thus, TFs could be used instead of piezoresistive cantilevers as an integrated deflection sensor system for small oscillation FM-AFM imaging with high sensitivity (due to the large Q-factors), and because of the inherently large k values of a TF, the tip would not jump to contact the surface.

The tuning fork sensor is similar to a piezoresistive cantilever as there are two electrodes which can be utilised to monitor the deflection of the tines of the tuning fork. The tuning forks consist of piezoelectric material, therefore when the tines are deflected a voltage is measured between the electrodes – thus the TF can be used as a force sensor. One of these tines is mounted on a surface and the other tine is allowed to oscillate. A tip can be attached to the end of this free tine to create an AFM cantilever, as shown in Figure 2.21.

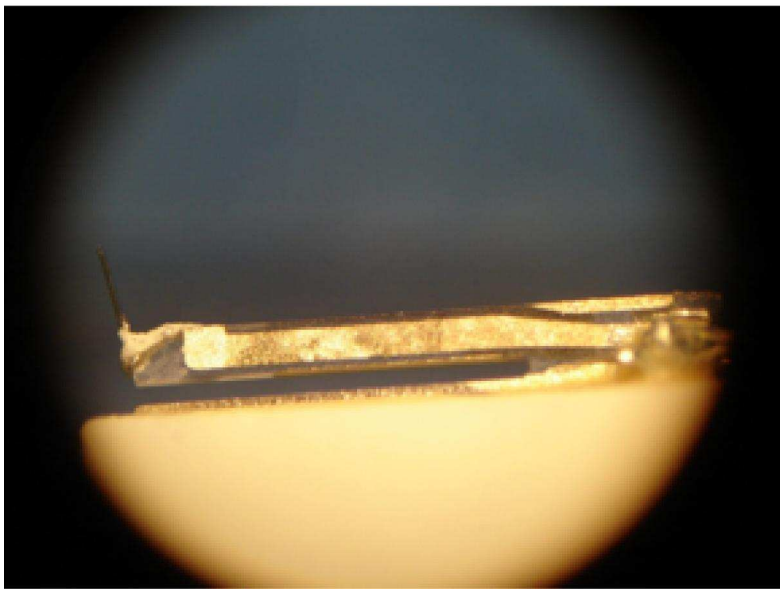

Figure 2.21: A mounted tuning fork with tungsten tip attached, viewed through an optical microscope.

Conductive epoxy is used to attach the tip to the free tine. This electrically connects the tip to one of the electrodes of the TF so the QPS can be implemented in an AFM/STM set-up. The attachment of the tip is critical, as there must be a compromise in the amount of epoxy attaching the tip to the tine. There must be enough epoxy to hold the tip solidly and provide a low resistance electrical contact between tip and electrode. However, as more mass is added to the TF, f_o reduces, typically a tip reduces the resonant frequency of the TF from 32 kHz to approximately 28 kHz. The quality of the bond between the tip and TF is crucial because it affects the Q-factor of the QPS as well. The tip itself can be composed of any material employed as an STM tip. For example a thin tungsten wire can either be attached to the TF and then etched, or etched and then attached. A Pt-Ir wire can be attached to the tine instead and then cleaved with a cutting tool to produce a sharp tip. These processes are very delicate and must be performed with extreme care, as described in more detail in Section 3.3.1.

In 2000, atomic resolution on Si(111)-(7×7) was achieved with the QPS in a non-contact FM-AFM regime [79]. The piezoelectric detection scheme also had extremely low power dissipation, to the order of picowatts, a good quality for low-temperature experiments. The fact that this optimal range of small amplitudes could be implemented not only achieved the maximum signal-to-noise ratio (as described in Reference [75]), but allowed tunnel current to be obtained simultaneously with FM-AFM images. Very recently the outstanding resolution possible with a QPS system has been demonstrated in Reference [80], where the chemical structure of a pentacene molecule was resolved using an AFM tip functionalised with a CO molecule.

The Phase-Locked-Loop

One crucial component of an FM-AFM system is the phase-locked-loop, or PLL. This is a closed-loop feedback control system that maintains a generated driving signal in a fixed relationship to a reference signal. The PLL responds both to the frequency and phase of the input signal, automatically increasing or decreasing the frequency of a controlled oscillator until the oscillator matches the phase of the reference waveform.

Figure 2.22 shows the main components of a PLL; a phase detector, low pass filter and voltage controlled oscillator (VCO), in a negative feedback configuration. The VCO generates a periodic output signal, if the frequency of the signal is approximately equal to the reference signal frequency but the two phases are not

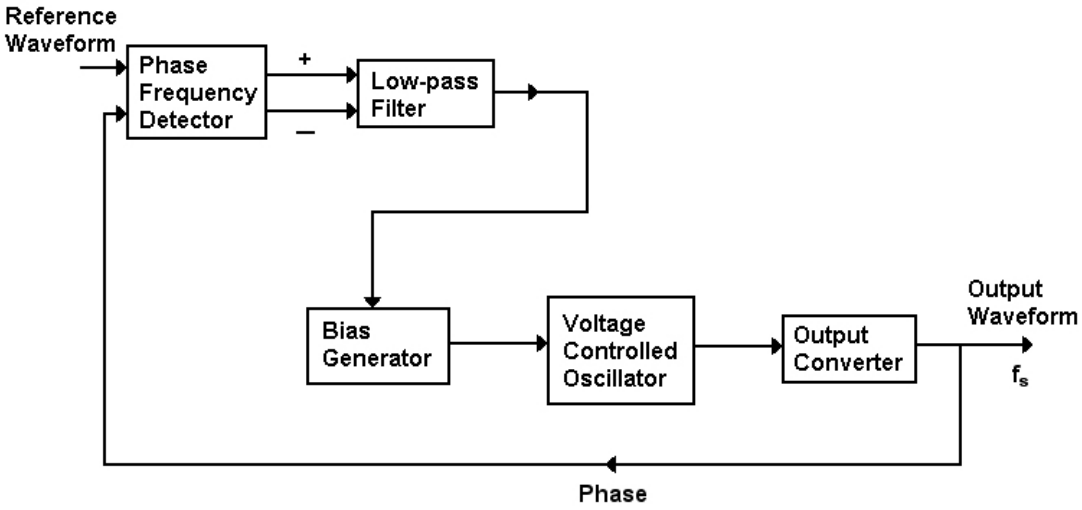

Figure 2.22: Flow diagram of a basic PLL system.

equal, the PLL will adjust the frequency of the output signal. If the phase of the output signal, f_s, is after or precedes the reference signal the phase detector will modify the control voltage to increase or decrease the frequency of the output signal respectively to compensate. The low-pass filter then smooths out the abrupt control inputs.

In the case of an FM-AFM system, the deflection of the cantilever is the PLL input channel. The PLL reference signal is the resonance curve (amplitude A_o, frequency f_o) and phase recorded with the cantilever at resonance whilst $F_{ts} = 0$. Thus, by maintaining an equivalent phase for both the output and reference signal, the PLL ensures the cantilever oscillates at the effective resonant frequency, f_e.

The EasyPLL

The Nanosurf easyPLL plus system can control and measure the resonance of vibrating sensors and is therefore primarily used (in conjunction with a PC) to control the resonance of an AFM cantilever and to measure the cantilever resonant frequency.

The system includes a controller and a detector. The controller regulates the amplitude and phase of the cantilever oscillation and also generates the output signal for the amplitude and dissipation of the cantilever. The detector outputs an analogue voltage that is proportional to *df* and also contains a digital PLL. The *df* output can be used as the tip-sample separation distance feedback parameter.

There are then several FM-AFM feedback modes possible, although two feature prominantly.

In 'constant amplitude' mode, the easyPLL maintains the cantilever oscillation amplitude at A_o by varying the driving amplitude using a modified PLL circuit with an extra feedback loop. The easyPLL also varies the frequency of the output signal for the cantilever to maintain the cantilever at its resonant frequency. This is achieved with the built-in PLL circuit and dissipation information can also be recorded.

The 'constant excitation' mode setting does not vary the output signal driving the cantilever other than through the PLL loop and therefore the controller unit is not necessary. The PLL is simultaneously the excitation generator and the frequency-to-voltage converter for the Z direction feedback. However, the controller can still be used in this mode to monitor oscillation amplitude variations.

In both of the FM-AFM modes detailed above, the cantilever oscillates at its resonant frequency. Changes in the resonant frequency (df) and oscillation amplitude of the cantilever are measured. As previously discussed, the phase response of the cantilever is used to control the cantilever oscillation frequency. The frequency of the driving excitation signal, f_s, is adjusted so that the phase corresponds to the phase set-point. This set-point is the phase at the natural resonant frequency, f_o, unless otherwise specified by the user. The difference between the natural resonant frequency, f_o, and the effective driven resonant frequency, f_e, is the output value of frequency shift, df. This frequency shift is the value input as the Z direction piezo feedback parameter for FM-AFM.

2.4 Summary

The theory and operation of scanning tunnelling microscopy has been described. One of the primary SPM systems used in this thesis, the Nanograph STM-01, has been detailed, along with the experimental procedures used for experiments conducted in its associated UHV system. The theory of atomic force microscopy has also been discussed, including the many modes of operation and of particular interest for this thesis, the use of tuning forks as cantilevers for a qPlus-sensor arrangement for FM-AFM in UHV.

Chapter 3

Construction of a Combined AFM/STM UHV System

This chapter describes the construction of a combined AFM/STM for operation in UHV. Experimental results obtained using the constructed microscope are also presented. The probe assembly design of this system was developed from the original concept of the *q*Plus-sensor (QPS), described in Section 2.3.

3.1 Mechanical Design and Development

The probe assembly of an AFM/STM system plays a crucial role in the resolution of the system, and is discussed in detail in Section 3.3, but other key components are also required. These include the vibration isolation stage, coarse approach motors or 'slipsticks', the X-Y plane scanning piezoelectric transducers and Z-fine feedback piezoelectric transducer, and the electronics (described in Section 3.2).

The development of the AFM/STM system can be split into two stages; Phase One and Phase Two. The following sections outline the major design changes as well as more minor improvements to the AFM/STM.

3.1.1 Phase One System Design

The system was constructed using a Nanograph Systems vibration isolation stage as a supporting base. This stage was a circular titanium plate suspended by four springs, as previously described for the Nanograph STM-01 system in Section 2.2.1. There was additional vibration isolation for the UHV chamber itself, which was mounted on pneumatic legs supplied with N_2 gas. The vibration

isolation of the system was then further enhanced at the later stages of construction by the addition of Viton® spacers and rings to ensure increased damping of environmental noise.

There were two main components of the system secured on top of the base plate, the 'sample holder ensemble' and the 'tip holder ensemble'. In the Phase One design the sample holder ensemble was attached to the top of the X and Z slipsticks for coarse positioning and incorporated the X-Y scanning piezos. The tip holder ensemble controlled the position of the tip in the Z direction. Figure 3.1 shows a photograph of the Phase One design.

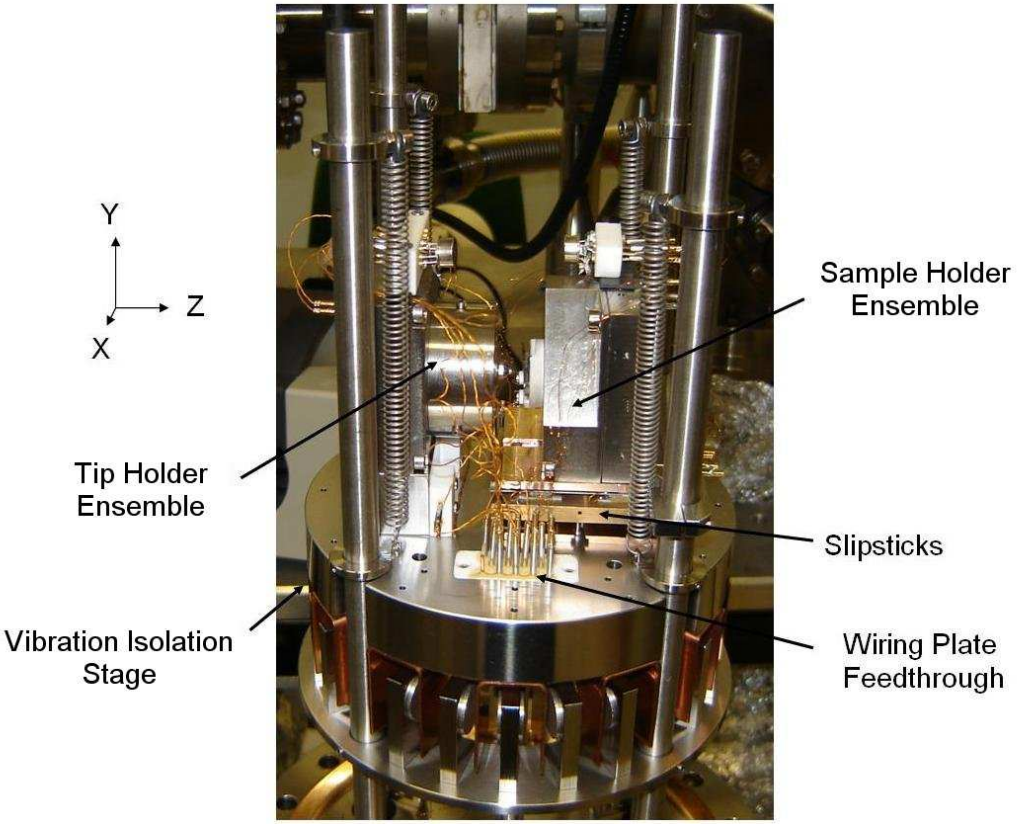

Figure 3.1: Photograph of the Phase One system design with sample holder ensemble secured to the top of custom built slipsticks.

The microscope user could remove and replace the tip holder and sample holder with UHV manipulator arms, similar to the UHV arms described previously in Section 2.2.2. The sample could be removed from its rear with a UHV arm. A tip tool could also be secured on this same UHV arm and used to remove an STM tip nut from the tip holder in the same direction as the sample holder. The system-specific tip tool is described in Section 3.3. The tip tool could pass through the

gap in the sample holder ensemble (on removal and storage of the sample holder) to unscrew and remove the STM tip. Note that an AFM/STM tip holder could *not* be removed in this manner. The components required for these processes are shown in Figure 3.2.

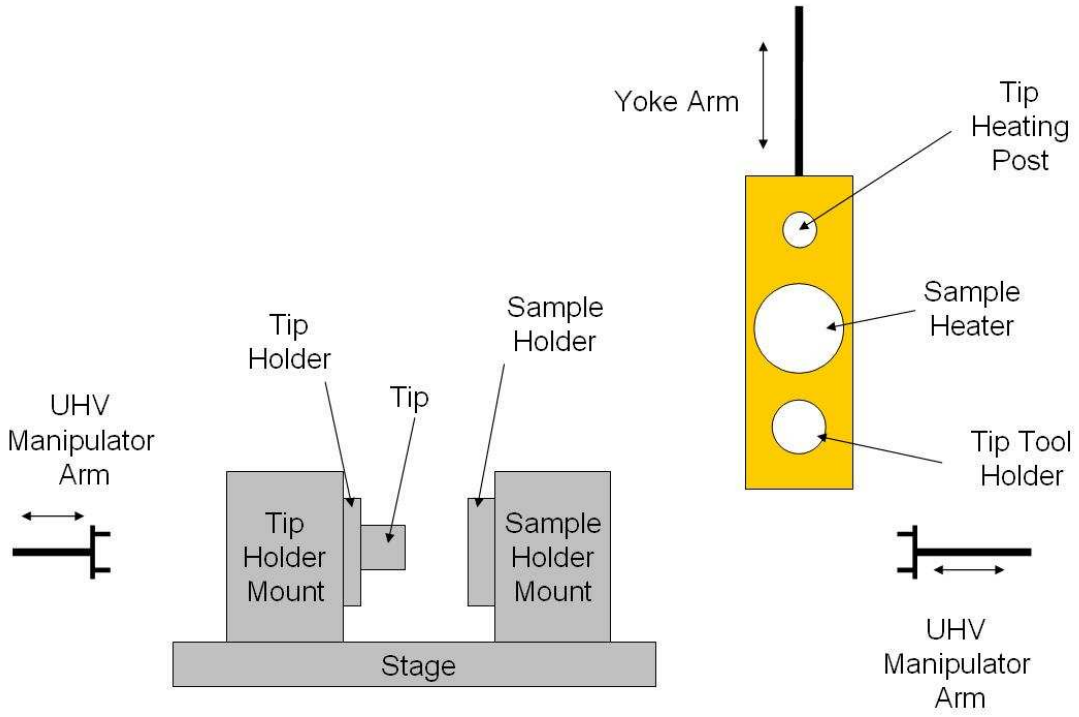

Figure 3.2: Simplified diagram illustrating the components required to move the tip, tip holder or sample holder in the UHV system.

Another UHV manipulator arm from the rear of the tip holder could remove the complete tip holder rather than just the tip nut, as shown in Figure 3.2. This second method was implemented for removal of an AFM/STM tip holder from the UHV system.

The tip holder and sample holder were the same diameter and had three rectangular blocks protruding from the outer diameter of each holder. When a holder was inserted into its mount, it was positioned so that the protruding blocks would slide into slots of similar size. The holder was then rotated so the blocks locked into place between two metal runners. The sample holder and tip holder are shown in Figure 3.3, along with a photograph of the associated locking system.

In the Phase One design, the tip holder was secured inside a piezoelectric trans-

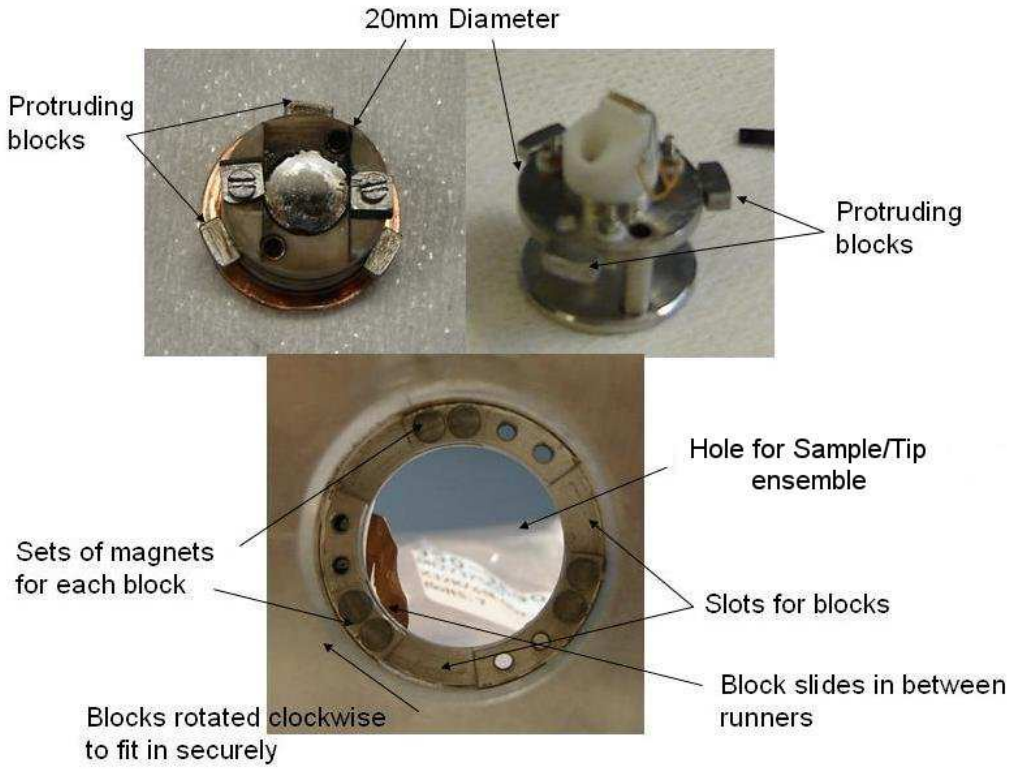

Figure 3.3: Photograph of the sample holder, tip holder and locking system.

ducer tube with an inner diameter larger than the tip holder – this piezoelectric transducer tube controlled the Z-fine motion. During scanning, the sample holder was displaced in the X-Y plane using three stacks of shear piezoelectric transducers. This arrangement of a piezoelectric transducer stack was more complicated than a single piezoelectric transducer but produced a higher displacement to voltage ratio. Two shear piezoelectric transducers were attached with an electrode between them. The top and bottom of the stack were grounded and the transducers were aligned to produce an overall displacement twice that expected for a single piezoelectric plate, as illustrated in Figure 3.4.

The three piezoelectric transducer stacks in the X-Y sample scanner consisted of 20 shear piezoelectric transducers each. Each stack was arranged into two sections and these two sections were insulated from each other. The piezoelectric transducers were aligned in different planes for each section of the stacks, one section in the X-plane and one section in the Y-plane, as shown in Figure 3.5. The electrodes were arranged so that separate X and Y signal voltages could be applied to produce the required scanning motion.

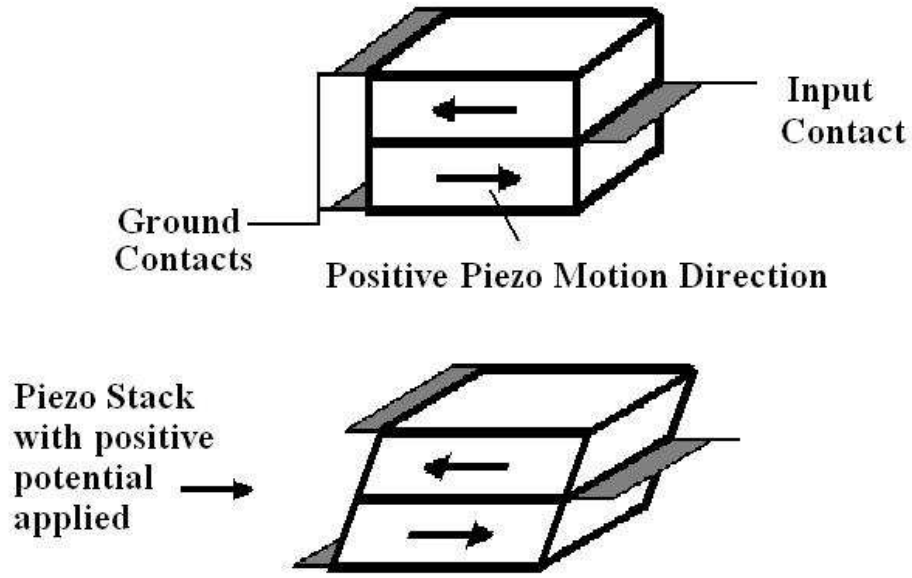

Figure 3.4: The motion of a piezoelectric transducer stack when a voltage is applied to the middle electrode and the bottom and top electrodes are grounded.

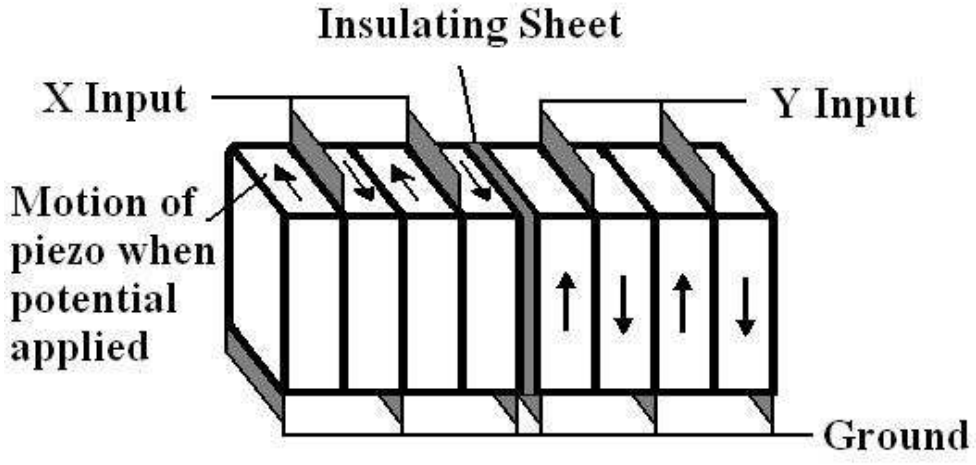

Figure 3.5: Diagram of the Phase One piezoelectric transducer stack design for the X-Y motion of the sample holder.

The three piezoelectric transducer stacks were attached to a triangular section of metal which contained the sample holder locking system shown in Figure 3.3. Each stack was attached near a vertex of the triangular metal section. Applying the same X and Y signal voltages to all three of the piezoelectric transducer stacks displaced the triangular section of metal (and therefore the sample) in the desired scanning motion. However, this design lacked the robustness required for frequent sample exchanges which led to a new system design.

A selection of STM and AFM images achieved with the Phase One design are shown in Figure 3.6.

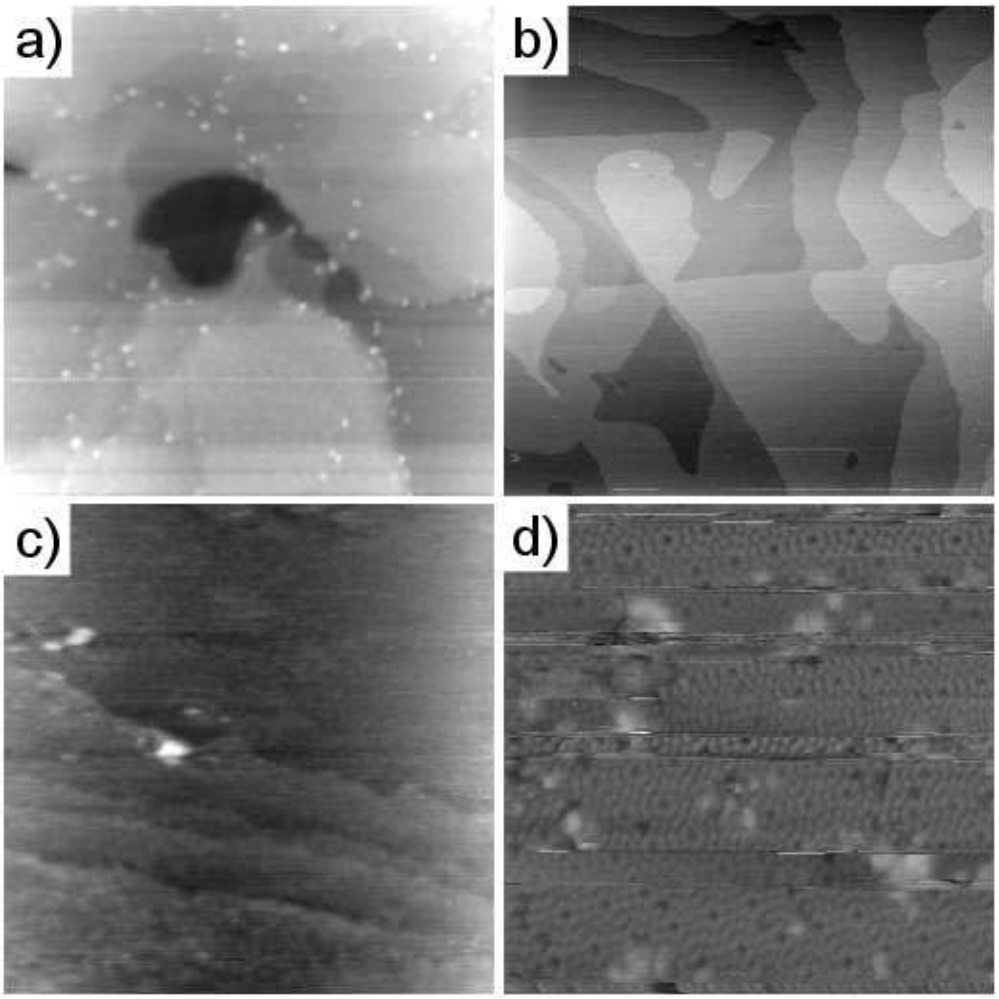

Figure 3.6: Images acquired with the AFM/STM system in the Phase One configuration; (a) Au(111) (on mica) surface in AFM mode and (b) STM mode, (c) Si(111) surface in AFM mode and (d) STM mode. Image scanning parameters (including scan sizes) were not retrievable as they were not recorded by the software under development at the time. Images courtesy of Martin Humphry.

3.1.2 Phase Two System Design

The novel three piezo stack scanning system was replaced with a more conventional piezoelectric transducer scan tube design. A tip holder could be secured on the end of the scan tube which provided the scanning motion in the X-Y plane, as well as the Z-fine movement. This was similar to the scan tube described in Section 2.1.2 but with an extra electrode allowing the option of mechanical excitation of the TF (as detailed in Section 3.2.1).

The new scan tube was purchased from *EBL Products Inc.* and had dimensions 0.250" OD × 0.020" wall × 0.820" length. The scan tube comprised of EBL#2 piezoelectric material with nickel electrodes. At the end of the scan tube where the tip holder was mounted there was an electrode with a width of 2 mm. This 'grounded electrode' was connected to the electrode on the inner part of the tube. This reduced the electrical noise in the sensitive electrical channels contacted at the tip holder – noise caused by the electric field of the piezoelectric material when a varying potential was applied. Figure 3.7 shows a labelled photograph of the scan tube of the AFM/STM Phase Two system design.

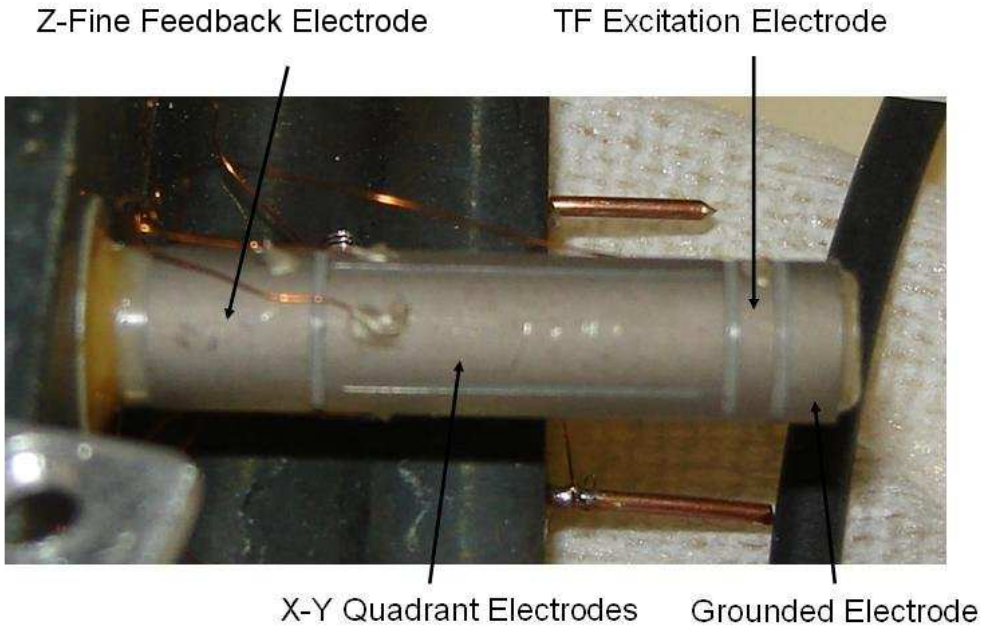

Figure 3.7: Photograph of the scan tube used in the Phase Two design. From left to right; the electrode for the Z-fine positioning of the tip, the quadrant electrodes for X-Y positioning and scanning of the tip, the TF excitation electrode for oscillating the AFM cantilever and the grounded electrode for shielding.

As shown in Figure 3.7, adjacent to the grounded electrode there was a 'TF excitation electrode' that provided 0.1 μm displacement when a potential of 300 V was applied – this electrode was used to mechanically excite the TF. There were four 90° quadrant electrodes ('X-Y quadrant electrodes') that each produced up to 1.5 μm tip displacement with an applied potential of up to 300 V. These four quadrants provided the X-Y scanning motion. Finally, there was a 'Z-fine feedback electrode' which provided a 0.5 μm Z range. At the tip holder end of the scan tube there was a 2 mm length of the scan tube where no electrode was present.

The Phase Two design allowed the height (measured from the vibration isolation stage) of both the tip and sample holder ensembles to be reduced to improve stability. This was due to the inclusion of the scan tube, which also allowed the sample holder ensemble to become completely static with respect to the vibration isolation stage. Another modification of the tip holder ensemble redistributed the weight of the ensemble over a larger area of the slipsticks to reduce the risk of the slipsticks failing.

A bespoke slipstick assembly was constructed in-house for the AFM/STM, but after rigorous testing it was concluded that the stability of the slipstick assembly was not adequate for reliable SPM measurements. This was possibly due to some unknown misalignment in the construction of the plates and piezoelectric transducer stacks. Thus, commercial slipsticks were purchased from *Omicron NanoTechnology GmbH*. The PN01577-5 XY course motor assembly was integrated into the system with a separate power supply and control unit. These slipsticks produced reliable motion in the X and Y directions of up to 5 mm with excellent stability and are pictured in Figure 3.8 – a photograph of the final AFM/STM system configuration.

3.2 Electrical System

From Figure 3.9, the electrical wiring of the microscope can be segregated into two main parts, the high voltage (HV) and lower voltage signals. The HV signals were used to control the piezoelectric transducers and slipstick motors of the system. The lower voltage signals included the sample bias, tunnel current, TF excitation and TF deflection sensor. The combination of these electrical channels and a PC provided the AFM/STM user with complete control of the AFM/STM system.

To achieve the minimum electrical noise and thus the optimal resolution of the microscope, it was crucial that capacitive coupling was minimised for the lower

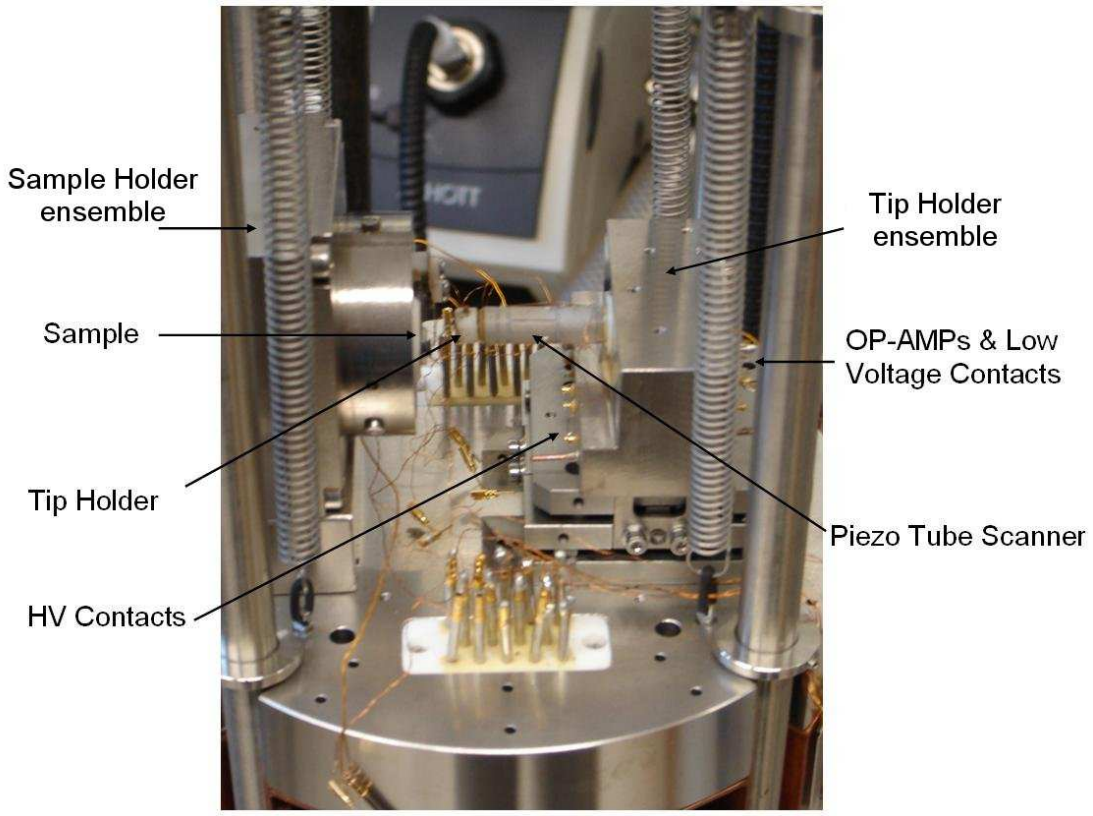

Figure 3.8: Photograph of the Phase Two design, including commercial slipsticks. Note some wires are disconnected.

voltage signals. A primary source of noise on the microscope head was the HV signals and the effect of the HV signals was minimised in two ways. Firstly the HV wiring was situated at the maximum possible distance away from the sensitive signals and secondly the sensitive signals were shielded.

To separate the two sets of signals, the HV wiring entered the UHV chamber via one 10-pin feedthrough connector, whilst the lower voltage signals were connected to a second UHV feedthrough. Two large rectangular holes were machined on either side of the plate – along the centre line of the plate running between the tip and sample holder ensembles – and MACOR blocks were then fixed into these holes (as shown in Figure 3.8). These blocks contained fourteen ∅1 mm OFC wires running through each block. The wiring was connected straight from the UHV feedthroughs to the MACOR blocks at the bottom of the plate. Other wires connected the top of the MACOR blocks to the relevant connection on the tip or sample holder ensembles. The length of the wires below the anti-vibration plate allowed the plate to move freely on its vibration isolation springs in this configuration.

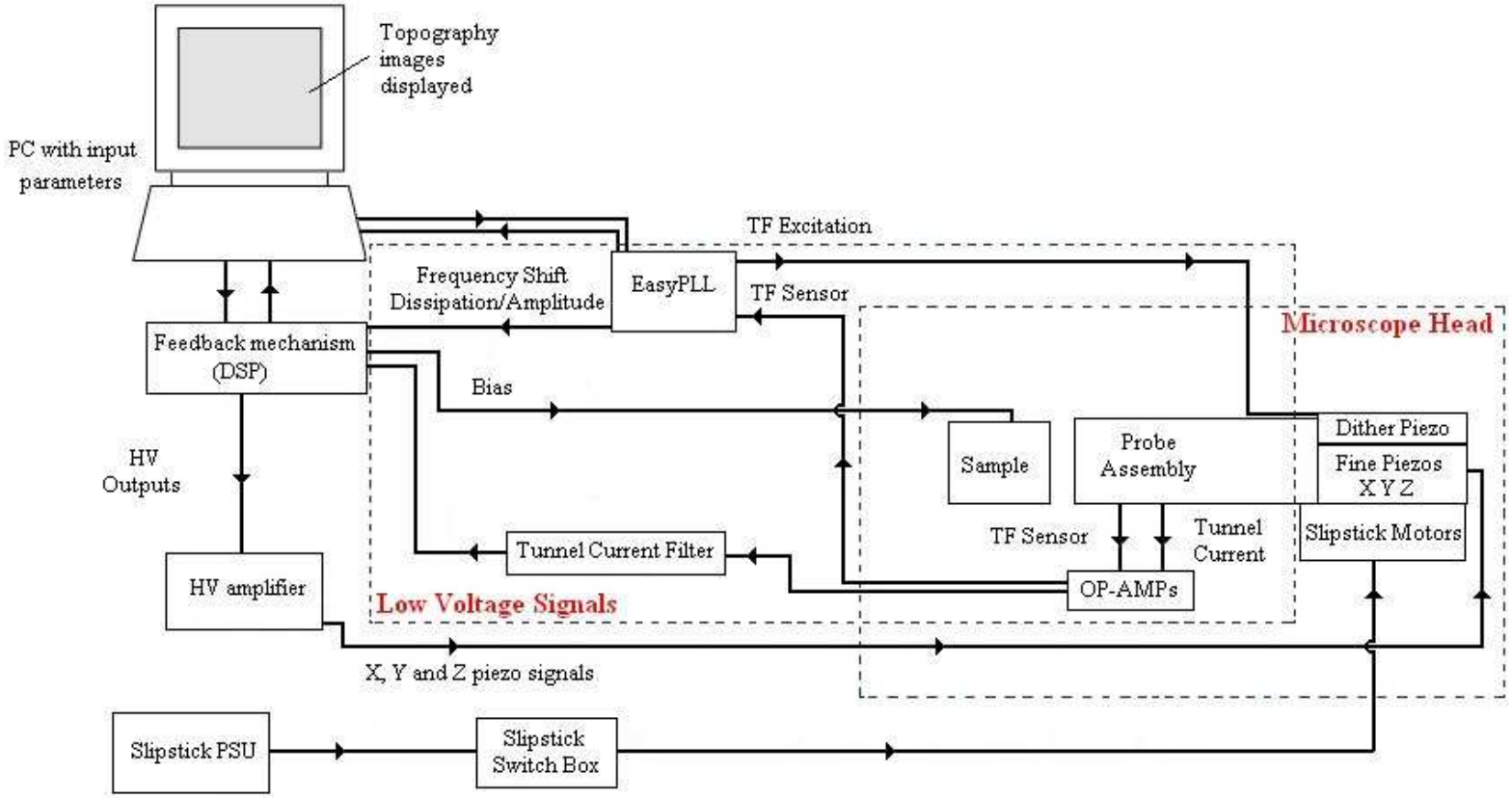

Figure 3.9: Diagram of the AFM/STM electrical design, including the lower voltage signals and the components physically situated on the microscope head.

The tip holder ensemble required both the HV connections for the several scan tube electrodes and connections for the lower voltage signals for the probe assembly at the end of the scan tube. To continue the separation of the HV and lower voltage wiring, the HV contacts were connected at the bottom of the front of the tip holder ensemble while the lower voltage signals were connected to the back of the tip holder ensemble. Therefore the HV wiring and the lower voltage signals generally remained on opposite sides of the instrument.

The wiring of the microscope comprised of thin copper wires insulated by Kapton purchased from *Allectra Limited*. Both 0.25 mm and 0.1 mm diameter wire (part numbers 311-KAPM-025 and 311-KAP-010 respectively) were included on the microscope head depending on the placement of the wire. The thicker wire was used on the top of the microscope head main plate. These wires connected contacts that were rigid, that is, they were not connected to the tip holder ensemble as this was mounted on the slipsticks. The thinner Kapton wire (with a reduced mass) connected more sensitive contacts to minimise any vibrations caused by the wiring when in UHV, where reduced damping of movement is experienced compared to atmospheric pressure.

To shield the lower voltage signal wires from the HV signals, thin Kapton wire was wrapped around the signal wire. The wires wrapped around the lower voltage signal wires were electrically connected to the common ground to create an electrical shield sheath.

The Kapton wires were attached to 1.2 mm inner diameter crimping pins (from *Allectra Limited*, part number 212-PINF-25-S). These pins pushed on to the ∅1 mm OFC static wire contacts on the microscope head, as shown in Figure 3.8.

3.2.1 Electronics Configuration

Unlike the AFM deflection signal which was over 30 kHz in frequency, the response of the software and hardware was only of the order of ∼2 kHz. Thus when the tunnel current was the feedback parameter, only tunnel current variations of ≤ 2 kHz would contribute to the system feedback and therefore the tip movement. A low-pass filter was integrated into the tunnel current channel, thus reducing any high frequency noise that may affect the tunnel current and thus the resulting topography images of the surface.

A digital signal processor (DSP) received user defined data via a PC to control the microscope head, as illustrated in Figure 3.9. The DSP simultaneously

recorded the data from the microscope head. This data was processed and displayed visually with gnome X scanning microscopy (GXSM) computer software [81]. The majority of outputs from the DSP to the microscope head were connected via a HV amplifier. The HV signals from the HV amplifier controlled the piezoelectric transducers of the scan tube that positioned the probe with respect to the surface. All of these channels were connected directly to the HV UHV feedthrough. The slipsticks were powered and controlled separately by a specific Omicron PSU which was connected to a switch box. The microscope user could use this switch box to switch between X and Z direction slipstick motion.

There were two output channels from the microscope head used to generate images for the STM and AFM modes of operation (as shown in Figure 3.9). These channels were the tunnel current and the TF sensor channel, connected to the tip wire and TF electrodes respectively. Both these signals were processed by the DSP so the GXSM software could generate topographic images and spectroscopy data. Operational amplifiers (OP-AMPs) were included in the design of the system to amplify these two signals as close to the probe assembly as possible, to reduce the signal-to-noise ratio and to accommodate the input signal range of the DSP.

The tip holder ensemble had two recesses in which the OP-AMPs could be separately secured. The tip holder ensemble was grounded to provide a sealed electrical shield around the OP-AMPs. Only the contacts of the OP-AMPs protruding through the MACOR seal were accessible, unless the tip holder ensemble was dismantled.

Extra electrical shielding was required for the wires that connecting the probe assembly to the OP-AMPs, as these were extremely small (nanoamp) signals. The wires were very short in length to minimise signal loss, and thus it was difficult to successfully wrap a grounded thin Kapton wire around the signal wire to provide shielding. Therefore very thin coaxial wire (insulated with Kapton) was connected to the corresponding terminals instead. The coaxial shielding was then grounded, thus providing complete shielding of the sensitive wires, which received additional shielding from the grounded inner electrode of the scan tube.

The bias voltage was applied to the sample and the tunnel current measured through the STM tip, which was connected to one of the OP-AMPs situated inside the tip holder ensemble. An OPA111 OP-AMP converted the tunnel current signal from the tip wire attached to the TF into a voltage which was recorded with the DSP. The tunnel current signal was amplified by a factor of 10^9 with the inclusion of a 1 GΩ resistor. The resistors used for both OP-AMP set-ups were physically very small, high value thick film chip resistors (RH73 series from *RS Components*).

An AD744 OP-AMP was used to amplify the signal of the TF sensor. The two TF electrodes were the two inputs of the TF sensor OP-AMP – the OP-AMP was used as a differential amplifier. A 100 MΩ resistor was connected in conjunction with the TF sensor OP-AMP to produce a Gain of 10^8.

The output of the TF sensor OP-AMP was input directly into the Nanosurf easyPLL plus. The measured resonant frequency shift, oscillation amplitude and dissipation signal were then input into the microscope PC. More information on the easyPLL plus can be found in Section 2.3.4.

The output of the tunnel current OP-AMP was input into the DSP via a low-pass filter, as explained previously. This had the added benefit of reducing the high frequency (20-32 kHz) component of the tunnel current that varied according to the oscillation frequency of the AFM/STM cantilever when operated in AFM/STM mode. Thus the time averaged tunnel current could be recorded as a separate channel alongside AFM data when the TF was excited. This also allowed for a 'dynamic STM' mode [82, 83, 84] in which the time averaged tunnel current flowing between the sample and oscillating tip was used as the feedback signal. In this mode the AC component of the tunnel current could also be recorded with the inclusion of a lock-in amplifier. Dynamic STM is discussed in Section 3.4.

The bias voltage applied to the sample was supplied directly from the DSP, for any operational mode of the system. Other signals not yet described but also labelled as a lower voltage signal were the power lines for the OP-AMPs previously described. The OP-AMPs were powered with ±15 V from the HV amplifier. The final lower voltage signal was the channel used to excite the tuning fork.

Tuning Fork Excitation

The *q*Plus-sensor (QPS), which has been described previously, required a sinusoidal voltage waveform applied to one electrode to create a varying potential difference between the TF electrodes. This caused the tines of the TF to oscillate relative to each other at the frequency of the waveform. However, this was found to be a complex design that led to difficulties with the sensor deflection. That is, it was not known to a certainty that the easyPLL plus was indeed providing the correct motion of the cantilever by both driving and monitoring the QPS.

Therefore the electrodes of the TF were not used in the excitation process, but the electrodes were still monitored as the sensor deflection system. Instead of the drive signal from the easyPLL plus driving the TF directly, it was connected to the small 'dither' piezoelectric transducer previously described in Section 3.1.2.

The dither piezo had a range of 0.1 μm with a 300 V potential applied. Therefore for every 1 V applied to the dither piezoelectric transducer, there was a 3.33 Å displacement of the tip holder from its original position. The amplitude of the TF driving signal controlled by the easyPLL plus was of the order of several volts to produce an estimated cantilever oscillation of several Ångströms.

3.3 Tuning Fork Sensor Construction

The tip holder locking system at the end of the scan tube incorporated crimp connectors and ∅1 mm copper wire. A circular MACOR block of 6 mm diameter with three crimp connectors mounted inside was glued into the end of the scan tube, as shown in Figure 3.7. Three copper wire prongs were secured in the (separate) MACOR tip holder to match the positions of the crimp connectors in the scan tube. A photograph of the Phase Two tip holder is displayed in Figure 3.10.

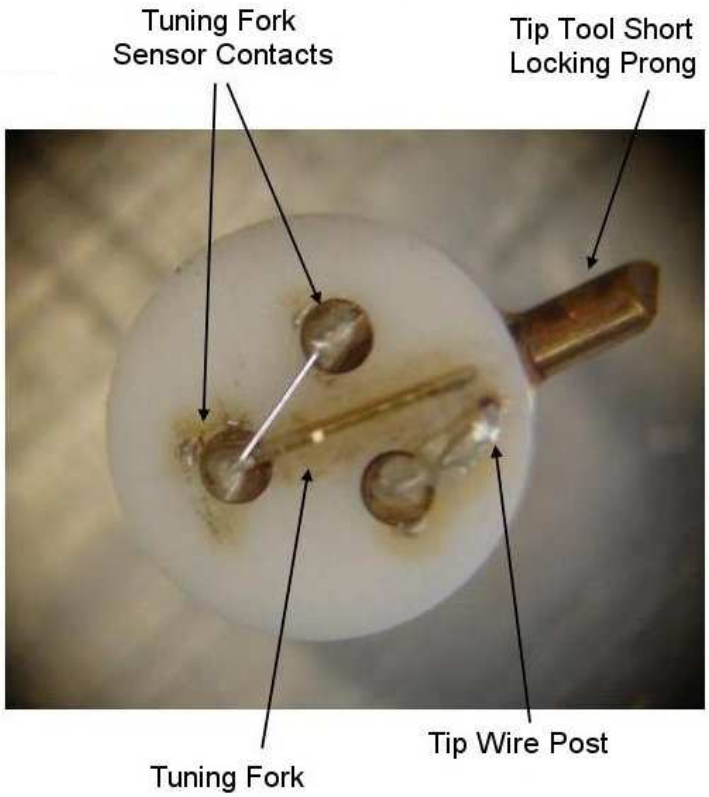

Figure 3.10: Photograph of the Phase Two tip holder through an optical microscope of the tip holder, viewing the AFM/STM tip ensemble from the direction of the sample.

As shown in Figure 3.10, another shorter ∅1 mm copper wire prong was glued into the side of the tip holder. This prong locked the tip holder into the tip tool so the tip holder could be transported throughout the UHV system. A slot in the tip tool allowed the insertion of the tip holder into the tip tool hole and then the tip holder was rotated and locked in the tip tool. Photographs of the tip tool in Figure 3.11 show the slot and other features of the tip tool. Tip exchanges could be performed inside the UHV system with a combination of the tip tool and the UHV arms – the UHV arm prongs would lock into holes in the opposite end of the tip tool. This tip tool could also fit into the yoke arm of the UHV system for storage (as shown in Figure 3.2).

Figure 3.11: Photographs of the Phase Two design tip tool, displaying the hole and slot to hold and lock the tip holder in place. The holes for the UHV arms to manipulate the tip tool and the thread allowing the tip tool to screw into in the yoke arm are also labelled.

The TF itself was mounted with non-conductive epoxy (EPO-TEK H77 from *Epoxy Technology Inc.*) onto the tip holder (as shown in Figure 3.10) to secure one tine of the TF to the tip holder whilst the other TF tine was free to oscillate.

3.3.1 Tuning Fork Tip Attachment

The TF used in the construction of the AFM/STM tip ensemble was purchased from *MICRO CRYSTAL*, E158 as used in crystals DS26. These were the same TFs incorporated in the QPS system [85] and had a resonant frequency of 32.768 kHz.

The attachment of the tip to the free TF tine was critical, there was enough epoxy to hold the tip solidly whilst minimising the total amount of epoxy applied. This was because the extra mass on the tuning fork reduced the cantilever resonant frequency, from 32 kHz to approximately 28 kHz, depending on the added mass

of epoxy. Thus the sensitivity of the AFM was reduced as the amount of epoxy applied to the TF was increased. The quality of the bond between the tip and the tuning fork was also crucial for the Q-factor of the QPS, if the tip was not attached rigidly the Q-factor would decrease.

In the Phase Two design of the system the TF tine was electrically isolated from the tip wire and a longer length of wire was used for the tip. The tip wire (with or without a tip already produced at one end) was attached to the free TF tine and the other end of the wire connected to a separate contact using conductive epoxy – EPO-TEK H20E-PFC from *Epoxy Technology Inc.*. The tip wire was manipulated into a right angle before attachment so that the tip wire could be attached with greater ease – this process is illustrated in Figure 3.12. The tip wire was either ∅25 μm Pt-Ir wire (90% to 10% ratio respectively) or ∅50 μm W wire (purity 99.95%), purchased from *Goodfellow*. Non-conductive epoxy was applied to the tip wire to attach it to the TF tine – as shown in Figure 3.12 – with special care taken that the tip wire was not in electrical contact with the TF electrode.

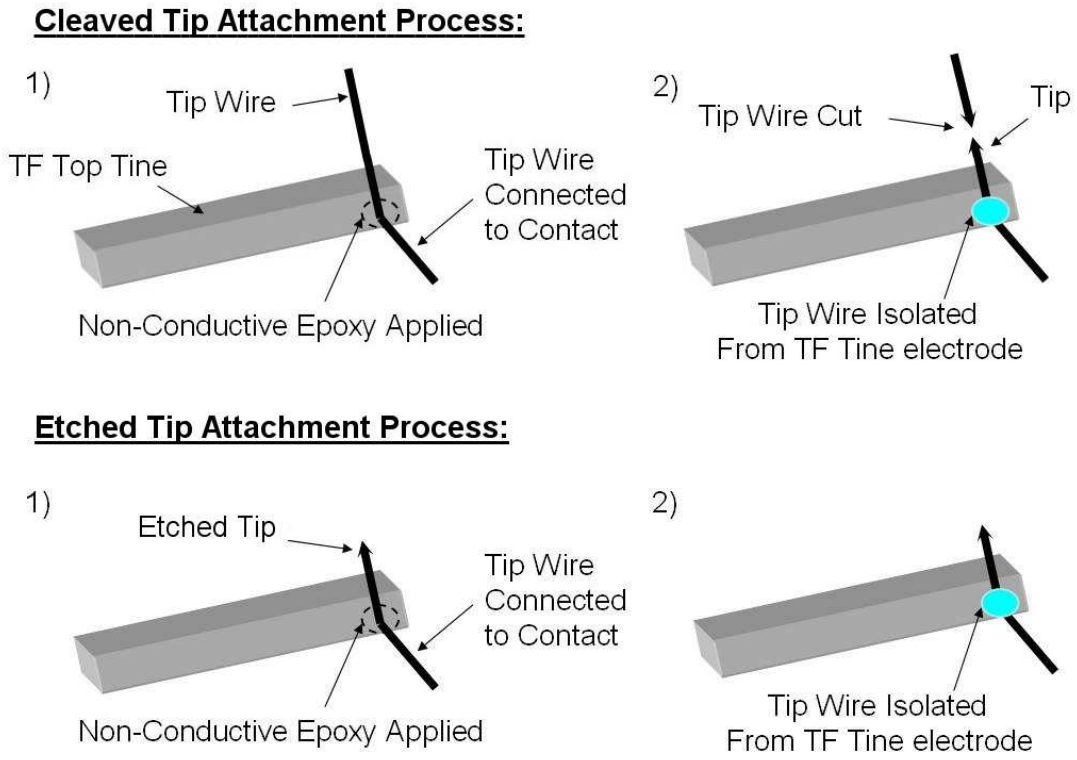

Figure 3.12: The different methods of attaching a tip wire to the top TF tine of the probe assembly.

The contacts on the tip holder were the same three ∅1 mm copper wires

that secured into the crimp connectors in the scan tube as the copper wires were accessible from both the top and bottom of the MACOR tip holder. The crimp connectors were then connected to the appropriate contacts of the microscope head by Kapton coated coaxial wires inside the scan tube.

$\varnothing$50 μm Pt-Ir wire was attached to the electrodes of the TF with conductive epoxy and the appropriate copper wire contacts on the tip holder as shown in Figure 3.10. This process was performed for each probe assembly constructed on the tip holder.

The tip wire protruded perpendicular from the TF tine and bent 90° to connect directly to a tip wire post, as shown in Figure 3.10. The tip wire post was situated as close to the end of the TF (and therefore the tip) as possible and was electrically connected to one of the copper wire contacts with conductive epoxy. Thus the length of tip wire protruding from the tine was only $\backsim$0.5 mm in length. Connecting the tip wire directly to the $\varnothing$1 mm copper contact produced an acceptable Q-factor for the TF in ambient conditions, but there was acoustic noise pick-up in UHV conditions due to the length and frailty of the tip wire. Hence the tip wire post was required to reduce any vibrational noise. This tip wire post structure is also illustrated in Figure 2a of Reference [86].

The tip wire post was initially constructed from $\varnothing$1 mm copper wire but this was too thick to allow any manipulation of the post. Therefore any lateral strain experienced by the top TF tine due to the tip wire could not be rectified after the epoxy had set. However, this method did produce some probe assemblies with an acceptable value of Q of $\sim$1000. The final design of the tip holder used $\varnothing$0.15 mm OFC wire as the tip wire post. This produced a similar Q-factor for the probe assembly as the thicker post design, but allowed the lower Q-factor probe assemblies to be improved upon by manipulating the tip wire post. The Q-factor of the probe assemblies varied from 500-1500, however only tip assemblies with a Q-factor $\geq$ 1000 were then used for experimentation.

Tip Apex Production

As discussed in Chapter 2, W tips were produced by chemically etching. This was a more lengthy and difficult process than simply cleaving the wire at an angle, which produced acceptably shaped tips for Pt-Ir wires. If the tip wire was attached to the TF before etching, the TF could be damaged or destroyed during the etching process due to handling difficulties. If the tip wire was etched and then attached to the TF there was also a high risk of damaging the tip during the

attachment process shown in Figure 3.12. W tips were also harder to manipulate, there are physical limitations to how close to the delicate tip a right-angle bend can be created. Thus, although W tips may seem the obvious choice for the tip wire, W tips were much more difficult to implement.

A tip etching assembly was constructed to produce W tips more reliably and easily and is illustrated in Figure 3.13. This etching assembly allowed the tip holder to slowly and securely approach a thin meniscus of NaOH solution that bridged across a hole in a metal sheet. A voltage was applied (as described previously in Section 2.2.3) to etch the tip wire. Other methods of aligning the tip wire to achieve a very short tip usually resulted in a high percentage of broken tips.

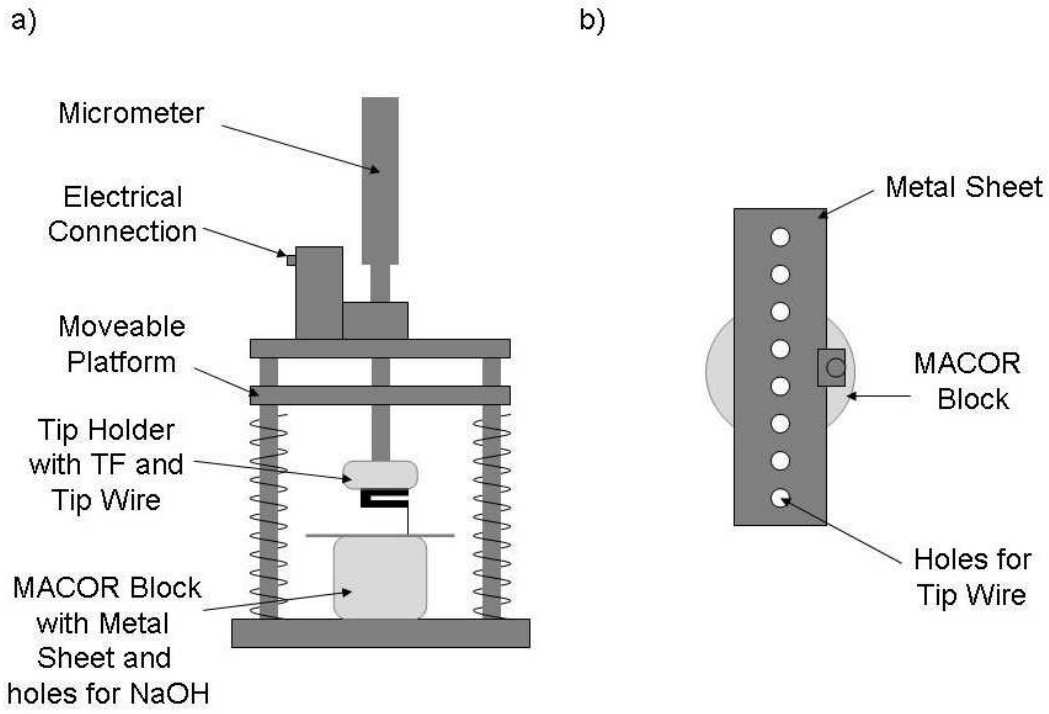

Figure 3.13: Diagrams of the AFM tip etching assembly, (a) the side view of the entire assembly including a tip holder with a TF and a W tip wire attached to one tine, (b) the top view of the MACOR block that held a metal sheet with several holes for the NaOH solution.

The UHV system contained an argon sputterer that allowed sputtering of the surface of samples, as described in Section 2.2.3. The UHV sputterer could be used in the preparation of the AFM/STM tips as well. Techniques such as e-beam bombardment could not be performed on the AFM/STM probe assemblies as the heat produced caused the epoxy on the tip ensemble to decompose. This obviously

destroyed or damaged the probe so that the probe could not be used to generate AFM/STM images with an acceptable resolution. The sputtering process changed the tip shape; tips that previously only produced bad resolution images could be used to generate images with improved resolution after a sputter cycle and vice versa.

Several factors led to a higher Q-factor of the probe assembly and thus improved sensitivity. The epoxy used to attach separate parts of the probe assembly played an important role. The epoxy was supplied as two separate materials that required mixing. The epoxy was then baked at approximately 150°C to produce a strong bond between surfaces. The ratio of the two materials mixed together to form the pre-baked epoxy affected the Q-factor of the probe assembly. It is hypothesised that this is due to variations in the rigidity of the resulting dry epoxy. That is, the resonant frequency of the probe was damped when the epoxy was less rigid. The period of time the mixed pre-baked epoxy was exposed to ambient conditions also had an effect on the Q-factor of the TF secured onto the MACOR holder. It was found that the Q value of a TF (without a tip wire attached) would not exceed 1500 if the epoxy had been prepared more than 24 hours previously. However the TF could achieve a Q-factor of $\sim$3000 with freshly mixed epoxy.

3.4 AFM/STM Imaging of PTCDI on HOPG

As an example of the several different modes of operation and achievable resolution of the combined AFM/STM system, a study of the organisation of perylene tetra-carboxylic diimide (PTCDI) molecules adsorbed on a graphite (HOPG) substrate are discussed. It was possible to resolve single molecules using dynamic STM and additional attractive features (when compared with conventional (DC) STM) were also demonstrated.

3.4.1 Experimental Set-up

The combined AFM/STM system – and associated TF sensor – was implented in three different operational modes; FM-AFM (frequency shift as the feedback signal), conventional (DC) STM in constant current mode (tunnel current as the feedback signal) and dynamic (AC) STM in constant average-current mode (time averaged tunnel current as the feedback signal). For measurements requiring an oscillating tip, the TF was mechanically excited as described previously. For the investigation described in this section, the constructed tip assembly

consisted of a mechanically cleaved and then electrochemically-etched ∅25 μm diameter Pt-Ir wire. The Pt-Ir tip was attached at the end of the TF after cleaving and etching, either without a separate tunnel current channel (and only used for AFM measurements), or with a connection to a tip post to produce tunnel current measurements. After attachment of the tip the resonant frequency (measured in UHV) of the TF, f_o, was in the range of 25-32 kHz with a Q-factor of 2000-5000. After the TF tips were introduced to UHV they were cleaned by argon ion sputtering.

The AFM/STM system also permitted the inclusion of a conventional STM tip, rather than the TF assembly. Dynamic STM was possible in this configuration (as well as with a TF tip assembly) and was realised by applying a sinusoidal signal to the section of the scan tube used to excite the TF mechanically, thus inducing an oscillation of the tip in the Z direction. Typically a 28-29 kHz signal was used to produce a tip oscillation amplitude in the range of 0.2-0.3 nm. For each experiment the HOPG sample was cleaved in ambient conditions and transferred immediately into the UHV system. PTCDI was then sublimed onto the HOPG substrate (which was at room temperature) at an approximate deposition rate of 0.2 MLmin^{-1} using a Knudsen cell.

3.4.2 Perylene Tetra-Carboxylic Diimide

A perylene molecule consists of 7 fused benzene rings that form a planar molecule, as shown in Figure 3.14. However, PTCDI has two nitrogen atoms (depicted as blue balls in Figure 3.14) that replace a carbon atom at each end of the molecule, whilst two sets of two oxygen atoms replace the hydrogen atoms bonded to the neighbouring carbon atoms.

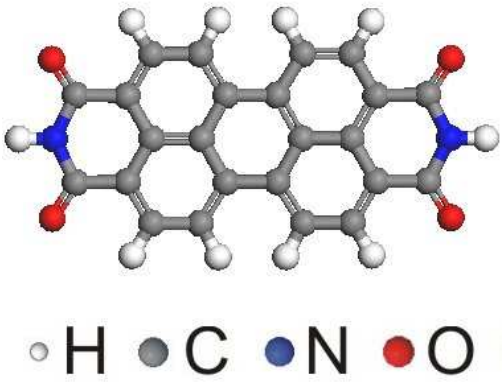

Figure 3.14: A perylene tetra-carboxylic diimide molecule.

PTCDI is available commercially and has been investigated on several surfaces, including MoS_2 [87], Ag-Si(111) $\sqrt{3} \times \sqrt{3}$R30° [88] and Au(111) [89]. In 2003, PTCDI was found to produce a periodic network on a silver-terminated silicon surface when combined with melamine [5] and this has subsequently been found to be reproducible on an Au(111) surface [89]. A honeycomb network was formed with melamine molecules at the vertices and PTCDI molecules as the edges of the hexagons. This type of structure was created due to hydrogen-bonds formed between the different molecules. The electronegativity of the oxygen and nitrogen atoms caused the O-H and N-H bonds to become polar and thus attractive bonds act between the hydrogen (bonded to nitrogen atoms) and oxygen atoms, as described in Section 1.1.

3.4.3 Imaging Results

Deposition of PTCDI on a graphite surface resulted in the formation of highly faceted rod-like islands with typical widths of ∼6 nm. These islands spread across step edges and formed branched structures. This is shown in Figure 3.15,

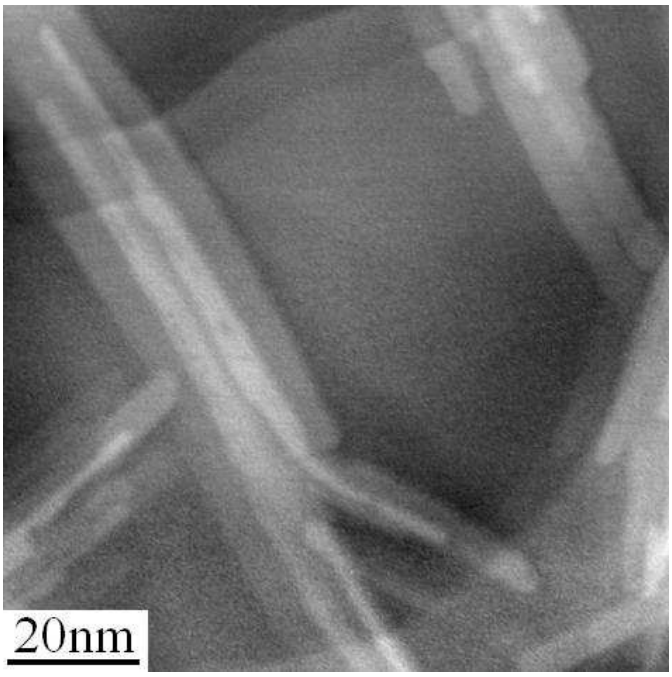

Figure 3.15: Topography of PTCDI islands on a HOPG surface generated in FM-AFM mode, with a Pt-Ir tip attached to a TF cantilever assembly without an STM capability. Imaging parameters df= -3 Hz, A_o= 0.5 nm. Image courtesy of Nikolai Berdunov.

which displays an FM-AFM topography image acquired with a Pt-Ir tip. The tip was attached onto the TF without a separate STM channel and thus no corresponding tunnel current data was recorded. All STM images in this section have been processed using WSxM software [90].

Second layer formation of PTCDI occurred even for submonolayer coverage indicating a Volmer-Weber growth mode. In Volmer-Weber growth, molecule-molecule interactions are stronger than those between the molecules and the surface, leading to the formation of 3D molecule clusters or islands. This might be expected for a passive substrate such as graphite, and has also been observed in earlier reports of PTCDI growth on MoS_2 [87].

While there have been many studies of adsorbed molecules on graphite at a liq-

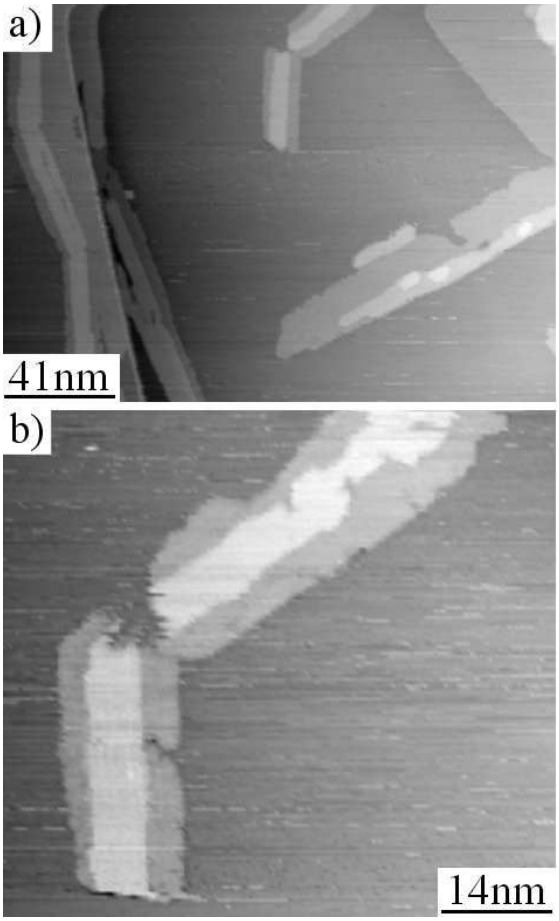

Figure 3.16: PTCDI islands on a HOPG surface imaged in dc-STM mode with a Pt-Ir tip attached to a TF cantilever assembly with an STM channel, where (a) is a larger scan with magnification of the top region in (b). The shape of the islands was different after several scans, as shown in (b). Imaging parameters V_{bias}= 2.0 V, I_t= 80 pA. Images courtesy of Nikolai Berdunov.

uid/solid interface [4], there have been relatively few STM studies performed under vacuum conditions and many of the published images were acquired at low temperature [91, 92, 93]. One reason for this is the relatively weak adsorbate-graphite interaction which results both in rapid diffusion of adsorbates and potentially leads to overlayer damage due to the interaction with the STM tip.

Conventional STM imaging (dc-STM) of the PTCDI islands often results in island disruption, presumably due to tip-molecule interactions. Such tip-induced surface modification is demonstrated in Figure 3.16, where the double-layer island was significantly disrupted following several consecutive dc-STM scans with a Pt-Ir tip mounted on a TF sensor to enable a separate STM channel.

However, images of PTCDI islands were readily acquired using dynamic STM (ac-STM) mode with the same tip assembly. As previously described in Section 3.2.1, in this mode the time averaged tunnel current flowing between the sample surface and the oscillating tip was used to control the probe height. Figure 3.17 shows a topographic image acquired in dynamic STM mode using a TF mounted tip. Unexpectedly, the PTCDI islands were imaged as a depression of approximately 0.1 nm in contrast to a 0.14 nm protrusion in AFM and conventional STM measurements. The topographic dynamic STM images were acquired simultaneously with the frequency shift of the TF oscillation, *df*, and the AC com-

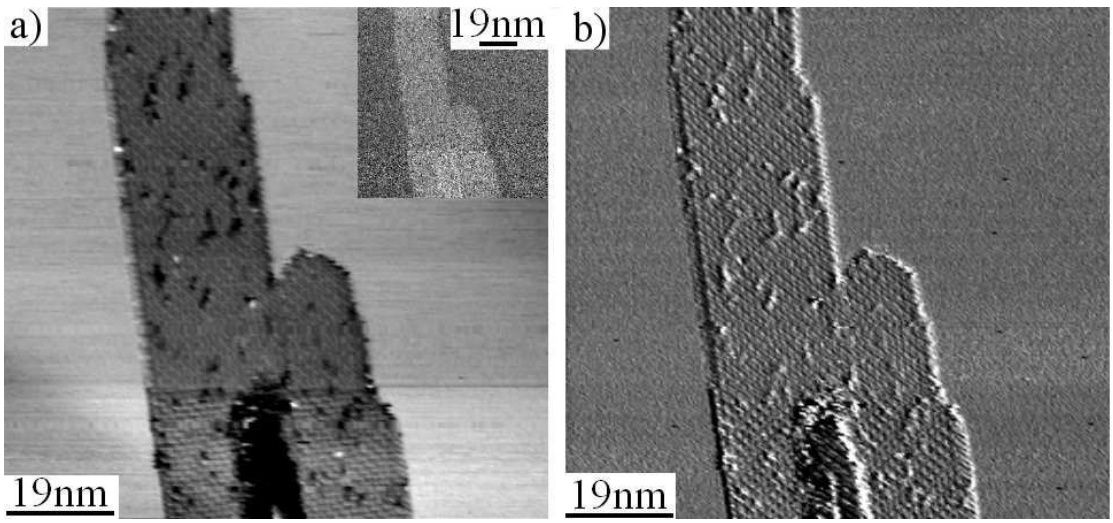

Figure 3.17: PTCDI islands adsorbed on a HOPG surface, imaged in dynamic STM mode with a Pt-Ir tip attached to a TF cantilever assembly. Where (a) is the topography image, showing negative height contrast of ∼0.1 nm, and simultaneously acquired *df* signal where a positive contrast is observed (inset). (b) is the AC component of the tunnel current. Imaging parameters V_{bias}= -0.9 V, $\langle I_t \rangle$= 30 pA, A_o= 0.5 nm. Images courtesy of Nikolai Berdunov.

ponent (with frequency f_e) of the tunnel current. Positive *df* values correspond to a positive force gradient, thus the *df* image in Figure 3.17 shows an increase of tip-surface repulsive interaction when the tip was positioned over the PTCDI island. This is consistent with the topography image in Figure 3.17 as the tip was closer to the sample when positioned over the PTCDI islands. The AC component of the tunnel current in Figure 3.17 does not show a significant contrast variation between bare graphite and PTCDI.

The high resolution dynamic STM image in Figure 3.18 reveals a close-packed arrangement of PTCDI with a unit cell of 1.5 × 1.8 nm^2. The elongated shape of the islands can be explained by anisotropy of intermolecular interactions, which arises from the interaction of imide and carbonyl groups on neighbouring molecules, as has previously been observed for PTCDI and related molecules [88, 94].

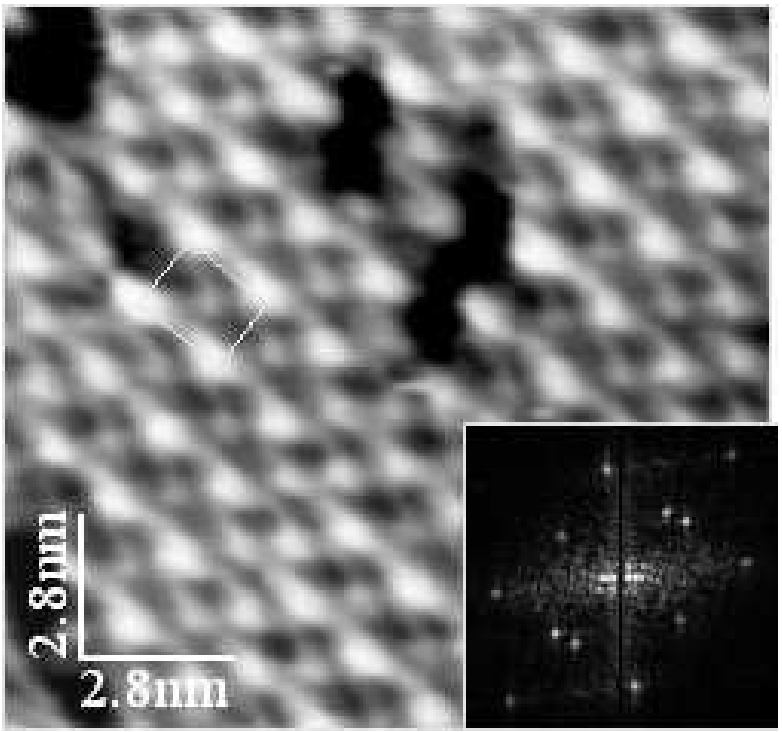

Figure 3.18: High resolution image of a PTCDI island on a HOPG surface obtained with dynamic STM mode, showing the close-packed arrangement of the PTCDI islands and 2D FFT (inset). Imaging parameters V_{bias}= -0.9 V, $\langle I_t \rangle$= 30 pA, A_o= 0.5 nm. Figure modified with permission from Reference [95].

To determine the origin of the negative contrast in Figure 3.17, images of the PTCDI islands using dynamic STM with a conventional (non-TF) tip for several different applied bias voltages were acquired [95]. These images revealed that for

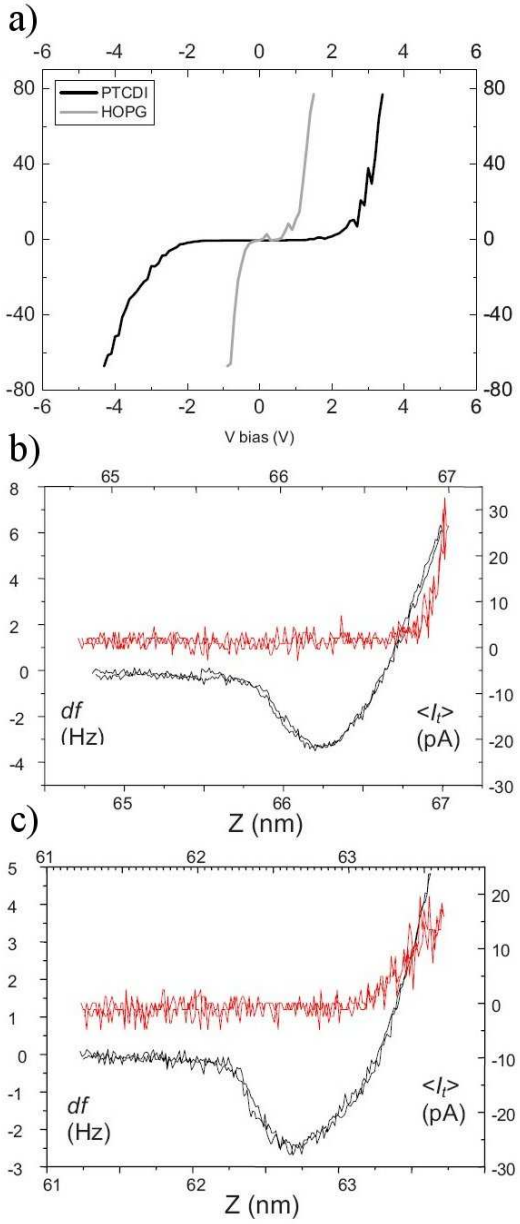

Figure 3.19: Tunnelling and force spectroscopy graphs for PTCDI on HOPG, (a) I-V curves for the bare HOPG surface and weakly bound PTCDI on HOPG whilst operated in constant height dynamic STM mode, (b) *df* (black) and tunnel current (red) versus distance curves for bare HOPG and (c) a PTCDI island. The tunnelling spectroscopy in (a) was obtained with a conventional STM tip whilst the curves in (b) and (c) were obtained with a tip attached to a TF with a separate STM channel. Figure modified with permission from Reference [95]. © 2009, American Institute of Physics.

large absolute bias voltages (1.5 V and −1.7 V) a positive contrast was observed whereas for smaller absolute bias (0.8 V and −1.0 V) a negative contrast was revealed, similar to the observed contrast in Figure 3.17. For the lower absolute voltages it was not possible to acquire images with dc-STM mode.

Figure 3.19a shows an I-V curve acquired with the oscillating tip positioned over either the graphite substrate or a PTCDI island. A tunnelling gap was clearly present over the PTCDI molecules and this low tunnel current region accounts for the negative contrast that is observed in Figure 3.17. The tip-sample separation was reduced over the PTCDI islands during scanning to maintain a constant tunnel current and thus a depression was imaged for the topography, as it is a map of the Z piezo response. The large tunnelling gap observed when the tip was positioned over a molecule indicates that there was weak electronic coupling between the PTCDI molecules and the HOPG surface.

In Figure 3.19 both the variation of frequency shift, df, and average current, $\langle I_t \rangle$, versus the tip position, z, was acquired over either the bare graphite substrate or a PTCDI island [95]. A broadening of the minimum of the dependence of df on z was encountered when force spectroscopy was performed over a PTCDI island, suggesting the presence of significant tip-molecule forces. Also, the gradient of the $\langle I_t \rangle$ versus z curve was shallower than the equivalent curve acquired on the bare HOPG surface.

3.5 Summary

In conclusion, a combined AFM/STM system has been constructed for operation in UHV and used to perform surface experiments, namely the investigation of PTCDI molecules adsorbed on a HOPG surface. The many system improvements required during the development period have been detailed, as have the final mechanical and electrical system arrangements.

The AFM/STM system allowed conventional STM operation with either a conventional STM tip or a TF tip. TF tip assemblies were used for AFM imaging with no simultaneously recorded STM data, or included an STM channel for tunnel current measurements whilst the tip was mechanically oscillated – unlike the electrically excited QPS arrangement. The STM channel was electrically isolated from the TF and required a thin copper post positioned adjacent to the TF to optimise the tip assembly Q-factor. This allowed dynamic STM operation and an FM-AFM mode with the ability to simultaneously record tunnel current data. Surface dissipation effects could be investigated with the inclusion of a TF

assembly and both tunnelling and force spectroscopy were also possible using the GXSM software.

The AFM/STM system has displayed the required resolution to resolve steps of approximately 0.1 nm in FM-AFM mode and molecular lateral resolution in dynamic STM mode. Dynamic STM mode was found to have the advantage of exerting reduced lateral forces on the adsorbed molecules when compared to conventional STM. It was also possible to image PTCDI islands with ac-STM that could not be imaged with dc-STM using the same reduced bias voltages, in this case a low enough bias that a tunnel current could not flow through the PTCDI islands to the STM tip from the HOPG surface. The relative stability of dynamic STM may be considered analogous to the enhanced stability of tapping mode AFM, as compared with contact mode AFM. Further experimental data acquired with the AFM/STM system are shown in Chapter 5, Section 5.1.3.

Chapter 4

Boron Nitride Nanomesh on Rh(111) Thin Films

In 2003, a hexagonal boron nitride (h-BN) monolayer was grown on the surface of a Rh(111) single crystal by Osterwalder et al. at the University of Zürich, Switzerland, by exposing the surface to borazine ($(BH)_3(NH)_3$) in UHV [12]. The hexagonal boron nitride monolayer on the Rh(111) surface (BN/Rh(111)) was labelled as 'nanomesh' and was later found to be a *corrugated* h-BN layer [15]. The h-BN layer was bound to the surface with varying degrees of strength according to the placement of the boron or nitrogen atoms with respect to the underlying rhodium atoms [29].

In this chapter the experimental details of the formation of the boron nitride nanomesh on Rh(111) thin films are discussed as well as UHV-STM investigations of the resulting surface. In-situ STM images of molecular adsorption upon the BN/Rh(111) surface whilst in UHV [96] are also presented.

4.1 Boron Nitride Nanomesh Formation

The substrates used for the production of the boron nitride nanomesh were obtained from the University of Augsburg, Germany. Each sample consisted of a 150 nm Rh(111) thin film grown on a 25 nm heteroepitaxial yttria-stabilised zirconia (YSZ) buffer layer deposited on a Si(111) wafer. Sections of wafer with dimensions ∼10 mm × 10 mm were used for nanomesh production. The preparative procedures for the Rh(111) thin film samples are described in detail in Reference [97].

The Rh(111)/YSZ/Si(111) sample was mounted on a UHV sample holder (as

described in Chapter 2, and shown in Figure 2.9) which incorporated a low resistance silicon strip heater with machinable glass (MACOR) shims and tantalum foil connections, as previously described in Section 2.2.3 of Chapter 2. The sample holder clips were used to secure the Rh(111)/YSZ/Si(111) sample between the MACOR shims and the silicon backing heater. The tantalum foil provided electrical contacts to allow STM measurements of the surface whilst the heater current flowed through only the backing heater and not the Rh(111)/YSZ/Si(111) sample. The sample holder was inserted into the Nanograph STM-01 UHV system described in Chapter 2, Section 2.2.2, and the sample was then degassed by heating to ∼500°C for 48-72 hours in the Nanomesh yoke, with the Nanomesh chamber pressure not exceeding 1×10^{-8} mbar.

Cycles of Ar^+ sputtering, O_2 dosing and annealing, or only O_2 dosing and annealing were performed to clean the sample. A voltage of 500 eV was used for Ar^+ sputtering at a partial pressure of Ar of 2×10^{-5} mbar (base pressure 5×10^{-8} mbar), resulting in an ion current of ∼0.8 μA. O_2 dosing was performed with a partial pressure of O_2 of 1×10^{-7} mbar (base pressure 1×10^{-9} mbar), whilst the sample was annealed at 800°C for 10-20 min. The O_2 leak valve was then closed and the sample was subjected to a 30 min post anneal at ∼400°C. The current through the backing heater was then slowly ramped down to zero over ∼60 seconds.

After each cleaning cycle, the Rh(111)/YSZ/Si(111) sample was imaged with STM in-situ to determine the condition of the surface. STM was performed with the Nanograph STM-01 system described in Chapter 2, Section 2.2.1. All UHV-STM imaging in this chapter was performed with the Nanograph STM-01 system with a W tip that was etched and then introduced to UHV and sputtered, unless stated otherwise. If the STM results revealed that the sample required one or more additional cleaning cycles, these cycles were then performed and the sample was subsequently investigated again with STM – this process was repeated until the sample had the appropriate morphology and was free of contamination (presumed to be carbon).

Figure 4.1 shows STM images of a Rh(111) thin film surface before and after a cleaning cycle in UHV. Although the morphologies of the sample in Figure 4.1 both before and after cleaning are comparable, a typical sample (before any cleaning cycles were performed) had many instances of contamination which required removal. Removing the contaminants with Ar^+ sputtering generated a particularly rough sample that required a subsequent anneal afterwards to produce a flatter morphology. Annealing the sample would segregate carbon contaminants

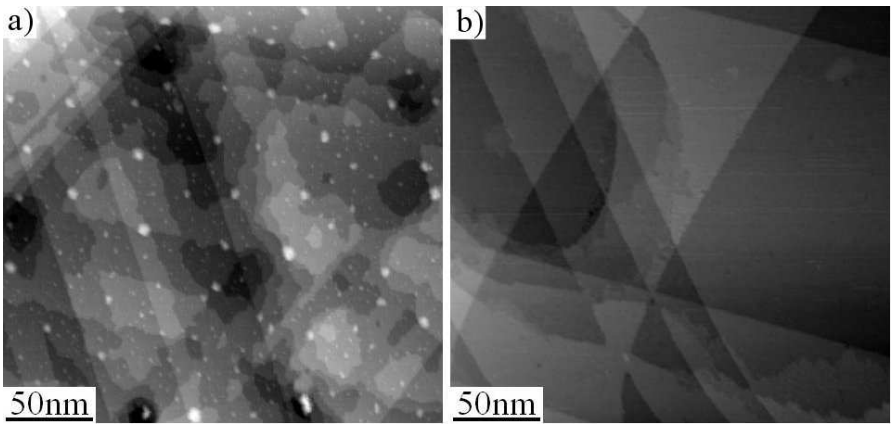

Figure 4.1: STM images of the surface of a Rh(111) thin film (a) before and (b) after cleaning cycles. Imaging parameters (a) V_{bias}= 1.0 V, I_t= 200 pA, (b) V_{bias}= -1.0 V, I_t= 200 pA.

to the surface of the rhodium from the bulk, therefore one or more cycles of O_2 dosing and annealing were required after one cycle of Ar^+ sputtering to produce the clean sample shown in Figure 4.1b.

Once the surface contamination of the sample had been removed, the sample was exposed to borazine within the same UHV system. A glass vial contained liquid borazine maintained at -10°C by a water-pumped Peltier cooler. This sealed glass vial was connected to the end of one of the gas lines of the UHV system (described in Section 2.2.3) and a leak valve on a port of the Nanomesh chamber. To introduce borazine via the leak valve, the glass vial required a 'freeze-pump' cycle to fill the gas line with borazine gas and remove impurities in the gas line, such as boranes. The freeze-pump cycle entailed switching off the Peltier cooler so the borazine would slowly reach room temperature and the Peltier cooler was then removed to allow the glass vial (that contained a borazine liquid/gas mixture) to be immersed in liquid nitrogen. After immersion in liquid nitrogen for 1-2 min, the borazine was frozen within the glass vial and this allowed the borazine gas line to be pumped with a turbomolecular pump. The gas line was then sealed off and left in static vacuum and the borazine was allowed to settle at room temperature, thus producing a high-purity borazine gas within the gas line, ready to be introduced to the Nanomesh chamber.

The Nanomesh chamber was sealed off from the other UHV chambers and pumped with a turbomolecular pump (base pressure of the Nanomesh chamber $\sim 5\times10^{-8}$ mbar), the sample was then annealed at 800°C in a partial pressure of borazine of 3×10^{-7} mbar for 3 min. The borazine gas line leak valve was then

closed and the sample was annealed for a further 1 min before reducing the current flowing through the backing heater to zero over ∼60 seconds.

4.2 Nanomesh STM Analysis

After dosing the sample with borazine, a *h*-BN monolayer was produced on top of the Rh(111) surface atoms and created a Moiré superstructure. This superstructure consisted of 13 × 13 *h*-BN unit cells overlaid on 12 × 12 unit cells of Rh(111) atoms, with a periodicity of 3.2 nm, as revealed using LEED [12]. A schematic of the resulting Moiré superstructure is shown in Figure 4.2, where four unit cells of the Moiré superstructure are illustrated, rhodium atoms are grey circles and the *h*-BN honeycomb structure is dark blue.

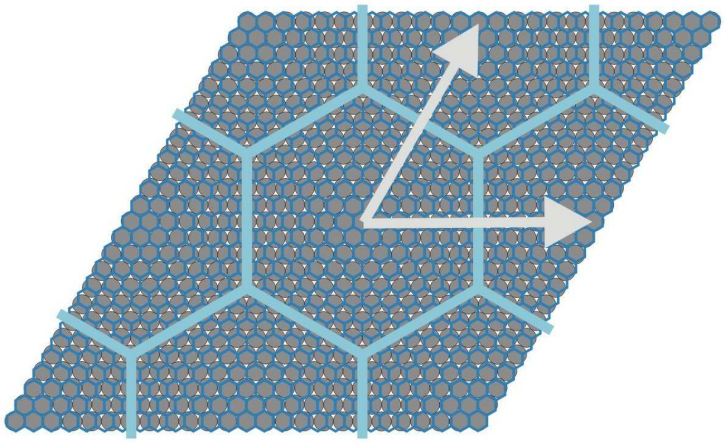

Figure 4.2: Schematic diagram of a honeycomb mesh (dark blue) representing a hexagonal boron nitride monolayer, overlaid on an array of grey circles representing rhodium atoms. The superstructure (light blue) formed by 13 × 13 unit cells of *h*-BN overlaid on 12 × 12 unit cells of Rh(111) atoms is observed as a long range periodic pattern with a_m lattice vectors marked by white arrows.

From Figure 4.2, the Moiré effect of the BN/Rh(111) surface can be clearly observed, a light blue hexagonal lattice is overlaid to represent the Moiré superstructure and the corresponding lattice vectors of a_m are shown as white arrows. Areas where the rhodium atoms are centrally located with respect to the pores of the *h*-BN network ((hcp,fcc) bonding areas) are visually distinguishable from areas where rhodium atoms are not centrally located ((fcc,top) and (top,hcp) bonding areas). These areas will be described as 'centre-moire' ((hcp,fcc)) and 'edge-moire' ((fcc,top) and (top,hcp)) respectively in this thesis. It has been shown that the

h-BN monolayer of the centre-moire areas are strongly bound to the rhodium surface and are lower topographically than the weakly bound edge-moire areas and thus a corrugated *h*-BN monolayer with a height variation of ∼0.05 nm is formed [14, 15]. This is also the case for the Ru(0001) nanomesh (as detailed recently in Reference [29]).

After the formation of the nanomesh surface in UHV, the surface was investigated using the Nanograph STM-01 system (described in Chapter 2) within the same UHV system. STM imaging of the surface revealed the Moiré pattern with a periodicity of 3.2 nm, as discovered when the BN/Rh(111) surface was originally produced in 2003 [12]. 'Pore' and 'wire' areas were imaged due to the corrugation of the *h*-BN monolayer, where the observed pore diameter of 2 nm corresponded to roughly 8 N-N spacings over which the strong bonding of the *h*-BN monolayer to the Rh(111) surface was maintained [14]. The STM imaging of a typical BN/Rh(111) surface is shown in Figure 4.3.

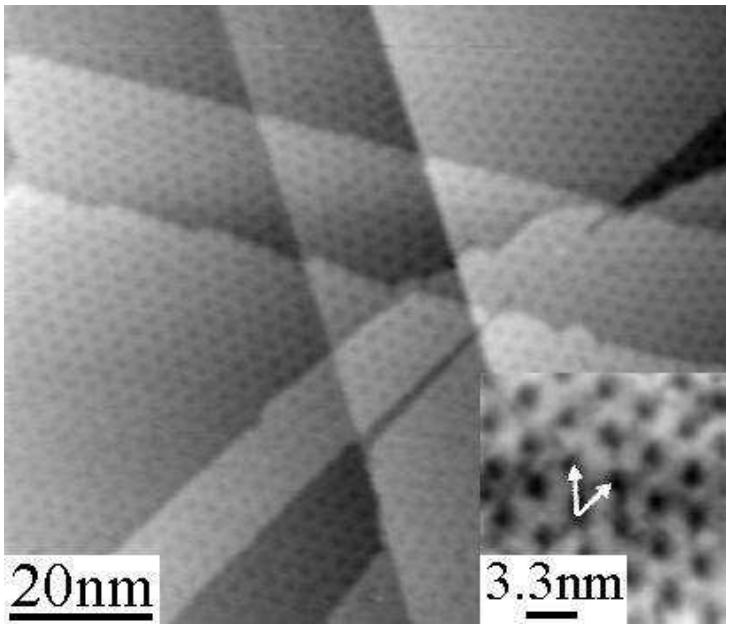

Figure 4.3: STM imaging of the BN/Rh(111) surface, revealing the Moiré superstructure modelled in Figure 4.2, including a smaller scan size STM image (inset) with the corresponding a_m lattice vectors marked by white arrows. Imaging parameters V_{bias}= 1.6 V, I_t= 200 pA and (inset) V_{bias}= 1.8 V, I_t= 200 pA.

The lattice vectors of the Moiré superstructure, a_m, are shown as white arrows in Figure 4.3, as in Figure 4.2, to clarify the periodicity of the Moiré pattern, as well as the centre-moire regions (observed as pores) and the edge-moire regions

(observed as wires raised from the surface). These images coincide with previous STM images obtained in UHV [12, 13, 23] at room temperature, but the individual N atoms of the h-BN monolayer are not resolved, as has been achieved with low temperature (77 K) STM [14]. A contrast inversion when imaging the BN/Rh(111) surface with STM was also revealed, as shown in Figure 4.4, where the nanomesh wires appeared as depressions and the pores became apparently higher topographically. This phenomena is attributed to the electronic inequivalence of the pore and wire regions in the h-BN layer, which is illustrated by the split σ-band peak observed in UPS investigations [14]. As shown in Figure 4.4b, the change in contrast was quite readily encountered, a change in the tip apex configuration or material (a 'tip change') during the scanning of the sample (presumably from acquiring material from the surface) inverted the contrast of the image and there was then another tip change shortly afterwards which recovered the original contrast again.

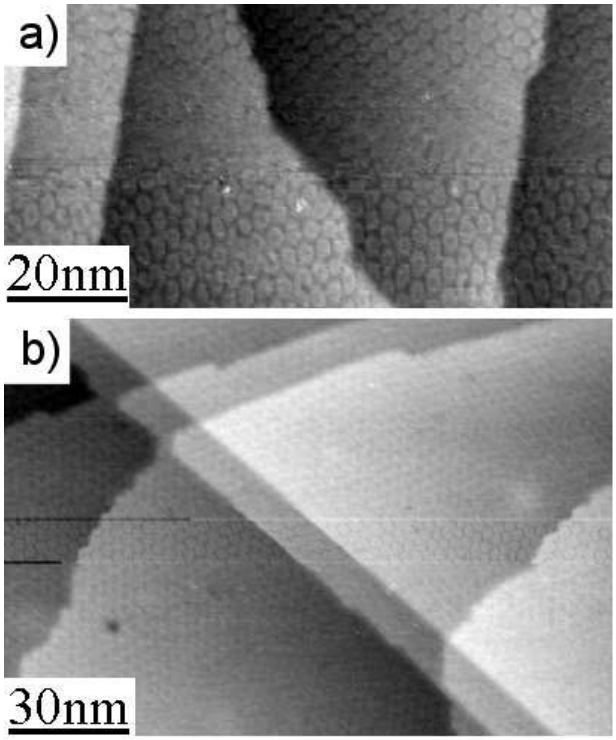

Figure 4.4: STM images of the BN/Rh(111) Moiré superstructure showing the frequently encountered contrast inversion. (a) STM image with only the contrast inversion and (b) a change in the tip configuration whilst scanning the surface produced the contrast inversion for several scan lines before the contrast was reverted back again. Imaging parameters for (a) V_{bias}= 1.3 V, I_t= 300 pA and (b) V_{bias}= 1.5 V, I_t= 400 pA.

In addition to UHV-STM experiments, the BN/Rh(111) surface was imaged in both ambient and liquid conditions using STM, yielding similar results to References [13] and [14] respectively. Figure 4.5 shows images of the nanomesh acquired in ambient conditions and whilst the BN/Rh(111) surface was immersed in heptanoic acid, at two different scan sizes. Generally, the imaging of the BN/Rh(111) surface was found to be more stable and produce higher resolution in liquid conditions and the surface was found to have a higher coverage of contaminants when imaged in ambient conditions. After imaging the surface in heptanoic acid, the sample could be cleaned with ethanol, dried using high pressure N_2 gas and then imaged again in ambient conditions with minimal degradation of the sample surface.

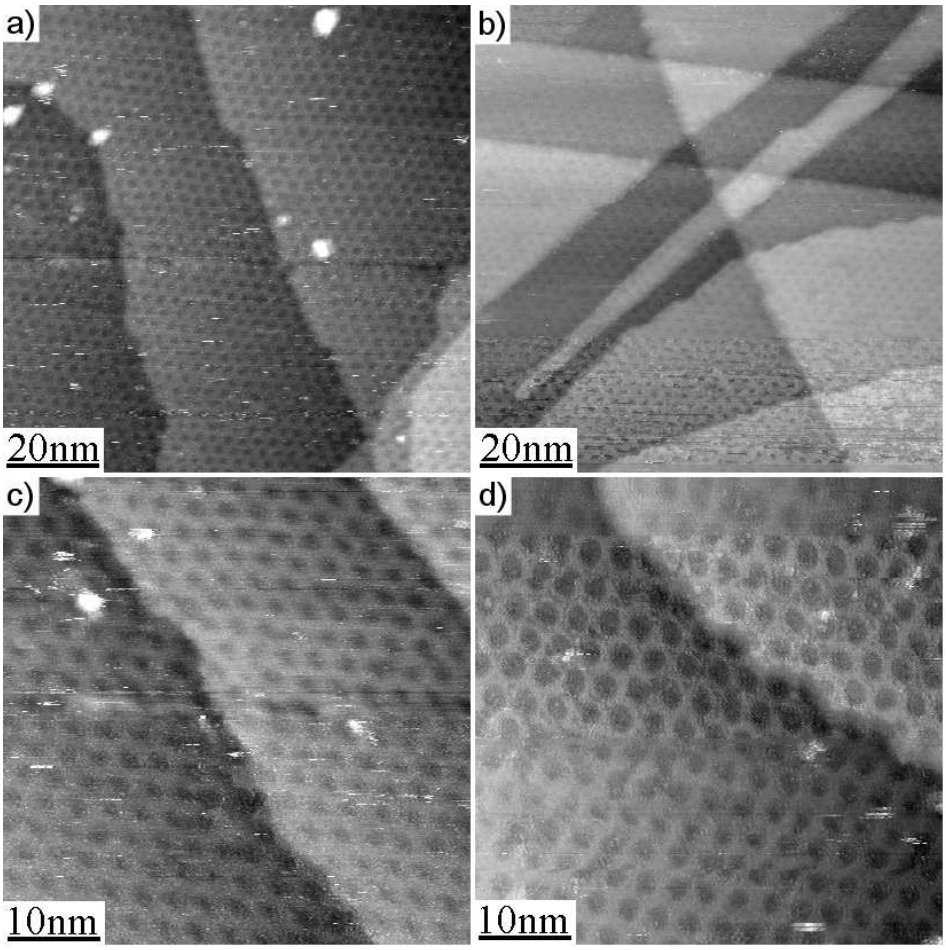

Figure 4.5: STM images of the BN/Rh(111) surface in ambient conditions (a) and (c), and immersed in heptanoic acid, (b) and (d). Images acquired using a PicoSPM (and PicoSCAN controller) supplied by *Agilent Technologies*, imaging parameters for (a), (b), (c) V_{bias}= 1.2 V, I_t= 150 pA and (d) V_{bias}= 1.2 V, I_t= 100 pA. Images courtesy of Matthew Blunt.

4.3 Molecular Deposition on BN/Rh(111)

Once the BN/Rh(111) sample had been prepared in UHV, organic molecules were deposited onto the surface through sublimation of the deposition material in a Knudsen cell attached to the UHV system, as described in Section 2.2.3 in Chapter 2.

4.3.1 PTCDI Adsorption

Perylene tetra-carboxylic diimide (PTCDI) was the first organic molecule investigated on the BN/Rh(111) surface – PTCDI has been described in detail in Section 3.4.2 of Chapter 3 and the PTCDI molecule is shown in Figure 4.6.

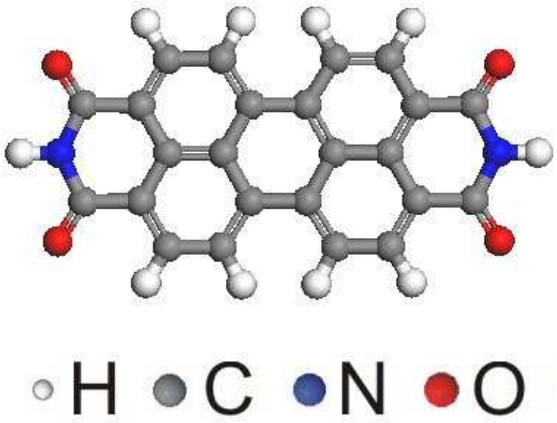

Figure 4.6: A perylene tetra-carboxylic diimide molecule.

PTCDI molecules were deposited onto the BN/Rh(111) surface in UHV using a Knudsen cell operating at 355°C, depositing PTCDI onto the surface at a rate of $\sim 3\times10^{-3}$ MLmin^{-1}. After PTCDI deposition, the surface was investigated with an STM in-situ and close-packed PTCDI islands were observed on the surface, as shown in Figure 4.7. Irregular-shaped PTCDI islands were revealed to occupy a large percentage of the BN/Rh(111) surface (as shown in Figure 4.7a) and there were also instances of single and multiple PTCDI molecules trapped in the pores of the corrugated boron nitride monolayer (as shown in Figure 4.7b).

When imaging the PTCDI islands on the BN/Rh(111) surface with STM, the islands were commonly observed to follow the contours of the corrugated *h*-BN layer (Figure 4.7) as might be expected. Due to the directional nature of the hydrogen-bonding between the PTCDI molecules, monolayer PTCDI islands with

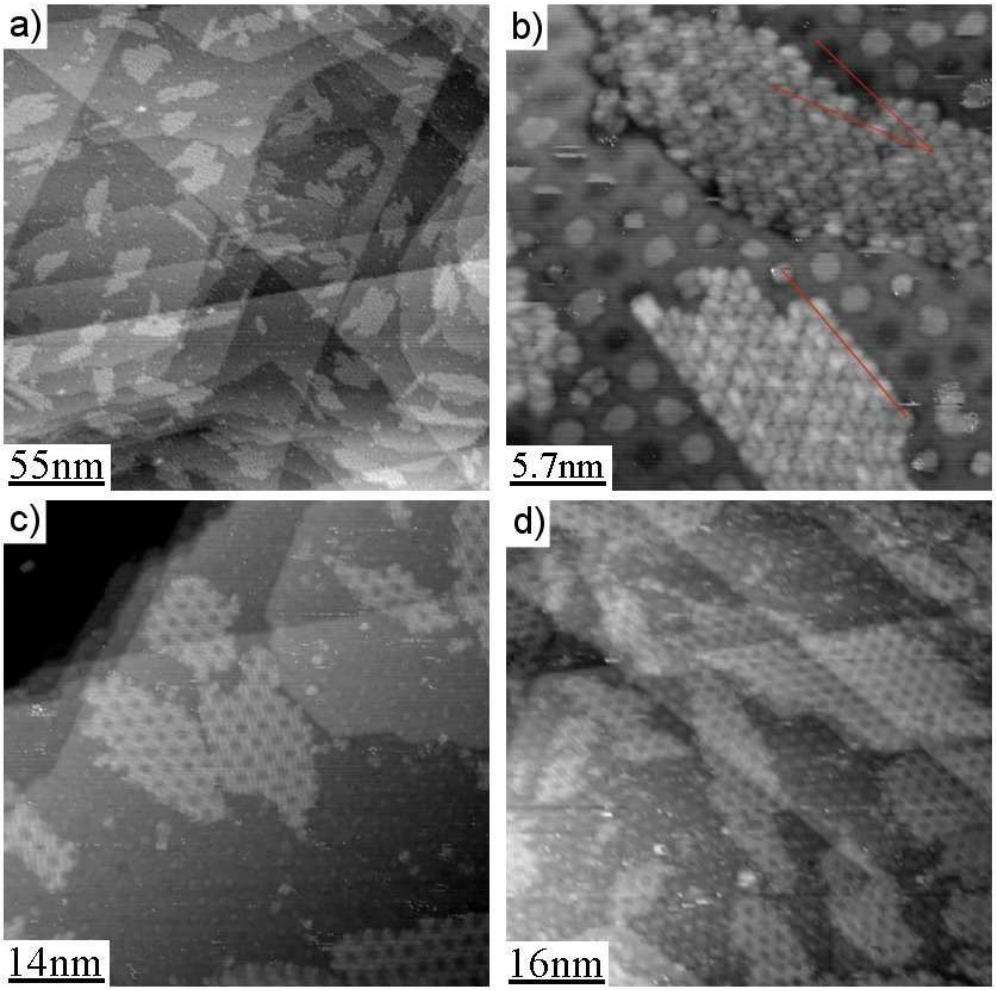

Figure 4.7: STM images of PTCDI adsorbed on a BN/Rh(111) surface as a comparison of the PTCDI islands formed. (a) large scan size image with multiple PTCDI islands observed, (b) small scan size image with PTCDI molecules within the islands resolved and revealing both PTCDI molecules aligned with the Moiré superstructure and molecules misaligned, (c) PTCDI islands that follow the contours of the surface and show varying orientations of neighbouring islands and (d) further PTCDI deposition leading to higher PTCDI island coverage. Images acquired using an STM supplied by *WA Technology*, imaging parameters for (a) V_{bias}= 1.0 V, I_t= 50 pA, (b) V_{bias}= -1.7 V, I_t= 30 pA, (c) V_{bias}= 2.3 V, I_t= 50 pA and (d) V_{bias}= 2.3 V, I_t= 30 pA.

several orientations were observed on the surface, as shown in Figure 4.7b and Figure 4.7c. In these STM images, both PTCDI islands that were aligned with the Moiré superstructure and PTCDI islands with an orientation mismatch of $21°\pm2°$ were revealed (visual guides are illustrated in Figure 4.7b). There were also domains within the PTCDI islands themselves, where the orientation of the molecules in each domain varied from one domain to another neighbouring domain. Further deposition of PTCDI molecules using the Knudsen cell produced higher coverage of islands, as shown in Figure 4.7d.

The deposited PTCDI molecules were commonly observed in the pores formed by the corrugated *h*-BN monolayer, as shown in Figures 4.7 and 4.8. This was similar to the behaviour of naphthalocyanine deposited on a BN/Rh(111) surface as these molecules were also revealed to be trapped due to their comparable size with the nanomesh pores [14]. The BN/Rh(111) surface has also been found to act as a template for Au nanoparticles [23]. The molecules generally occupied the majority of the pores on the surface even when PTCDI islands were also present on the surface. It was difficult to ascertain the preference between the trapping of molecules in pores or 2D island formation, but the molecules did not appear to fill all of the pores of the nanomesh before 2D islands were formed. 2D islands that were tens of nanometres across were observed whilst up to approximately 30% of the visible nanomesh pores did not contain PTCDI molecules.

The pores trapped both single PTCDI molecules and more than one molecule on an approximately 10:1 ratio respectively. However, the number of PTCDI molecules in each pore was difficult to distinguish due to the intramolecular double lobe contrast of the highest occupied molecular orbital (HOMO) of the PTCDI molecules (as described in Reference [88]) coupled with the limited resolution of the STM. Only exceptional images revealed the exact number of molecules, Figure 4.8d as an example. STM images in Figure 4.8 show frequent manipulation of the PTCDI molecules from one pore to a neighbouring pore on the same axis as the STM tip raster motion. This can produce a mass redistribution of PTCDI molecules within the pores themselves as seen in Figure 4.8, where Figure 4.8b is an STM image acquired several scans after the image in Figure 4.8a, and where many pores that were previously empty have become filled. It should be noted that this effect was not seen in previous naphthalocyanine experiments on the same surface [14].

As previously described, it was possible to control the coverage of the close-packed PTCDI islands by altering the duration of PTCDI deposition – the coverage increased with deposition time. However, the coverage of the PTCDI islands

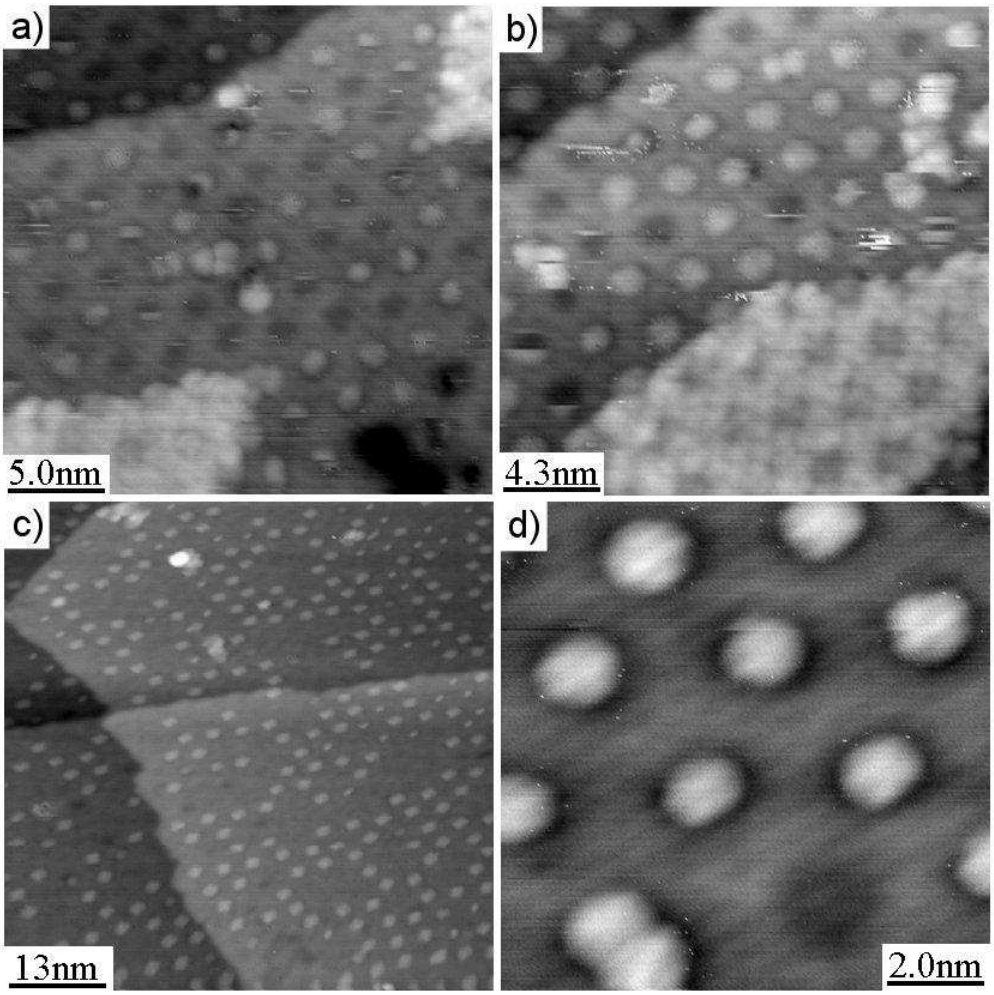

Figure 4.8: STM images of PTCDI adsorbed on a BN/Rh(111) surface where PTCDI molecules are both trapped in pores and formed 2D islands, as shown in (a) and (b). (c) annealing the sample desorbed the PTCDI molecules, reducing the coverage of the PTCDI islands until only the more strongly bound PTCDI molecules in the pores of the BN/Rh(111) surface were present. (d) examples of both single and pairs of molecules trapped in the pores. Images acquired using an STM supplied by *WA Technology*, imaging parameters for (a) V_{bias}= 1.7 V, I_t= 30 pA, (b), (d) V_{bias}= -2.0 V, I_t= 30 pA and (c) V_{bias}= 2.0 V, I_t= 30 pA.

could also be decreased by annealing the sample. Low temperature anneals of less than 300°C (the temperature was not measured, but was monitored visually) for 30 min partially reduced the coverage of the PTCDI islands until there were no PTCDI islands present on the BN/Rh(111) surface. However, the PTCDI molecules trapped in the pores of the boron nitride monolayer still occupied the pores after annealing – as shown in Figure 4.8c – similar to previous naphthalocyanine investigations, which determined that the molecules did not desorb after 300°C anneals of the surface [14]. Only occupied pores were observed after the anneals rather than both occupied pores and PTCDI islands in the same areas (as shown in Figures 4.7 and 4.8), although there are indications of clusters of molecules that may have previously been part of a PTCDI island. Figure 4.8d shows a small scan size STM image of the surface after a low temperature anneal, revealing single PTCDI molecules trapped in the *h*-BN pores as well as two PTCDI molecules in one pore, as a more conclusive example of multiple molecules in one pore. However, the double-lobe contrast usually observed for PTCDI molecules is not resolved and therefore the orientations of the PTCDI molecules are unknown.

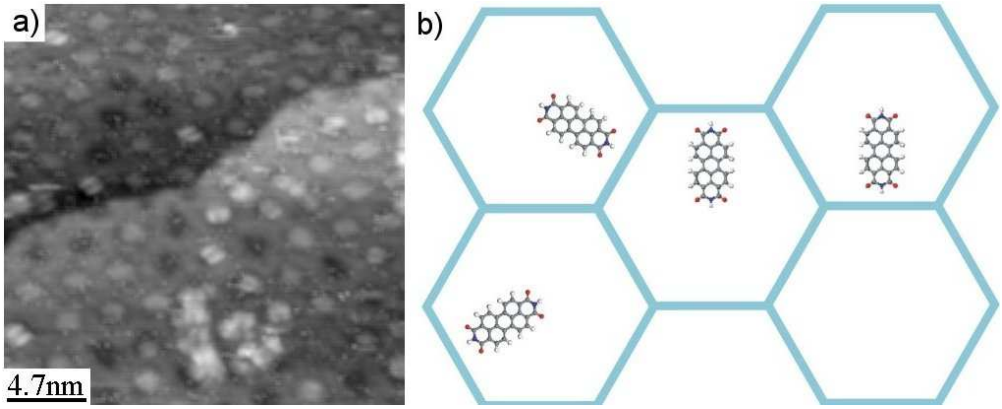

Figure 4.9: (a) STM image of PTCDI adsorbed on a BN/Rh(111) surface where PTCDI molecules trapped in the pores of the corrugated monolayer are observed and (b) schematic of the proposed PTCDI molecule placement in the pores and orientation as observed in (a). Image acquired using an STM supplied by *WA Technology*, imaging parameters V_{bias}= 2.0 V, I_t= 30 pA.

Figure 4.9a is an STM image of a BN/Rh(111) surface after PTCDI deposition and subsequent annealing to produce PTCDI molecules primarily trapped in the pores of the boron nitride monolayer, many of the PTCDI molecules imaged display a double lobe contrast. Thus, the orientation of the PTCDI molecules trapped in the pores was determined as a random distribution. The PTCDI molecules were frequently orientated with their functional ends directed towards an edge of the

h-BN pores, however, they did not show a net orientation. The PTCDI molecules were generally positioned towards the edge of the pores, as shown schematically in Figure 4.9b, where the light blue hexagonal lattice represents the Moiré superstructure and the pores of the *h*-BN network, as described in Figure 4.2.

The possibility of a bimolecular hydrogen-bonded network of organic molecules formed on top of the covalently bonded corrugated *h*-BN monolayer was also explored, by depositing melamine onto the BN/Rh(111) surface after PTCDI deposition. On both Ag-Si(111) $\sqrt{3} \times \sqrt{3}$R30° [5] and Au(111) [89] surfaces the molecules formed a honeycomb network with a periodicity of ∼3.5 nm. However, no extended honeycomb networks were observed for PTCDI and (subsequent) melamine deposition experiments on the BN/Rh(111) surface when investigated with in-situ STM.

4.3.2 DP-PTCDI Adsorption

Di(propylthio)-PTCDI (DP-PTCDI) was also investigated on the boron nitride nanomesh surface. DP-PTCDI was a derivative of the previously described PTCDI molecule. Two sulphur atoms replaced two of the hydrogen atoms that were bonded to carbon atoms (contained in the 7 benzene rings that form the organic molecule), such that a predominately 1,7-isomer (although there were trace amounts of the 1,6-isomer) was created. A propyl chain was attached to each of the sulphur atoms – depicted as yellow balls in the schematic of the DP-PTCDI molecule shown in Figure 4.10. The synthesis of the DP-PTCDI molecule is detailed in Reference [98]. Previous investigations of DP-PTCDI on a Ag-Si(111) $\sqrt{3} \times \sqrt{3}$R30° surface revealed both dimer and trimer junctions were formed [98], leading to both close-packed islands and a honeycomb network on the surface. The formation of a DP-PTCDI/melamine network has also been investigated on the same surface [98] and was found to produce a hexagonal network similar to the PTCDI/melamine network. However, the propyl side chains of the DP-PTCDI molecule affected the filling of the network pores with C_{60}, with fewer fullerenes trapped within the DP-PTCDI/melamine pores than for the PTCDI/melamine network.

Similar to the PTCDI experiments, DP-PTCDI was deposited onto the *h*-BN monolayer whilst in UHV using a Knudsen cell operating at 405°C to produce a $\sim 7 \times 10^{-4}$ MLmin^{-1} deposition rate. After deposition of DP-PTCDI molecules, the sample was investigated using in-situ STM and similar results to the adsorption of PTCDI were found, as shown in Figure 4.11. Irregular-shaped 2D DP-PTCDI

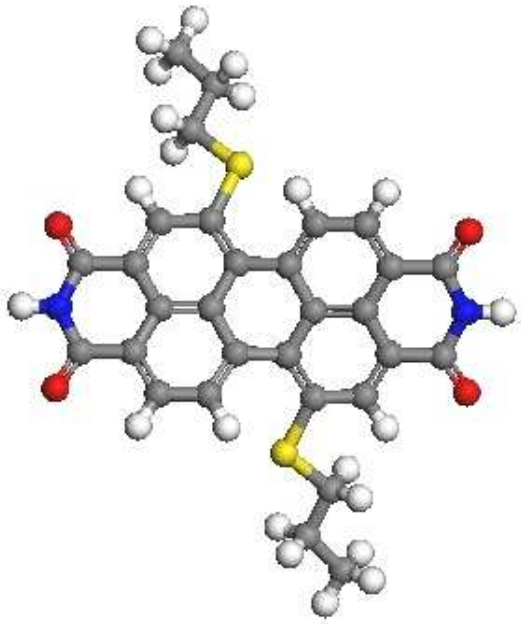

Figure 4.10: A di(propylthio)-perylene tetra-carboxylic diimide molecule.

islands were formed and followed the contours of the corrugated *h*-BN monolayer, as shown in Figures 4.11a and 4.11b. Figures 4.11c and 4.11d show STM images where the orientation of the DP-PTCDI molecules within the islands was resolved, revealing a similar structure to the 2D PTCDI islands formed on the same surface. However, the exact placement of the DP-PTCDI molecules could not be fully resolved using the Nanograph STM-01 system, unlike the PTCDI adsorption experiment which was performed using a higher resolution UHV-STM. Figure 4.11b shows an area of the BN/Rh(111) surface where DP-PTCDI molecules were trapped in the pores of the corrugated *h*-BN monolayer and 2D DP-PTCDI islands were also present. Similar to the PTCDI deposition experiments, it was not possible to ascertain the preference for 2D molecular islands over the trapping of the molecules in the nanomesh pores.

DP-PTCDI molecules were also desorbed from the BN/Rh(111) surface by annealing the sample at temperatures ≤ 300°C (temperature not measured), reducing the coverage of the DP-PTCDI islands until there were only DP-PTCDI molecules trapped in the pores of the periodic superstructure. Figure 4.12 shows a small scan size STM image, where DP-PTCDI molecules trapped in the pores of the BN/Rh(111) surface are observed – the surface was imaged with a contrast inversion as previously described in Section 4.2. The orientation of the DP-PTCDI

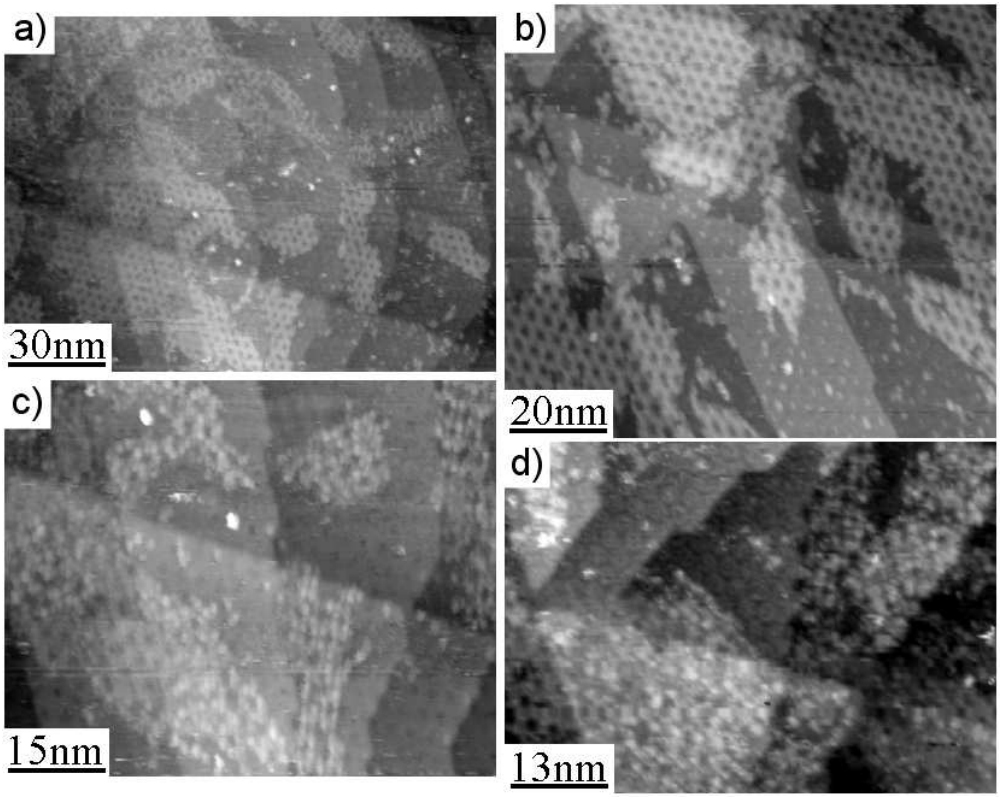

Figure 4.11: STM images of DP-PTCDI molecules adsorbed onto a BN/Rh(111) surface. (a) large scan size image with multiple DP-PTCDI islands observed, (b) smaller scan size image revealing DP-PTCDI islands and DP-PTCDI molecules trapped in the BN/Rh(111) pores, (c) and (d) the different orientations of neighbouring DP-PTCDI islands. Imaging parameters for (a), (b), (c) and (d) V_{bias}= 1.0 V, I_t= 50 pA.

molecules was unknown, however, the placement appears to be the same as the trapped PTCDI molecules and is therefore similar to the schematic in Figure 4.9b that describes the placement of PTCDI molecules on the nanomesh surface.

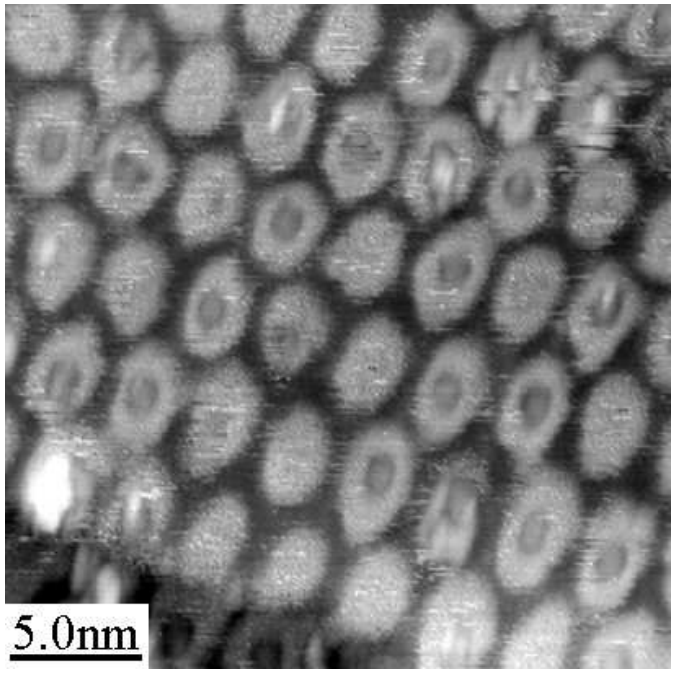

Figure 4.12: STM image of DP-PTCDI adsorbed on a BN/Rh(111) surface where DP-PTCDI molecules that are trapped in the pores of the corrugated monolayer are observed after annealing. Imaging parameters V_{bias}= 1.0 V, I_t= 50 pA.

4.4 Summary

The formation of a corrugated *h*-BN monolayer on the surface of a Rh(111) thin film and subsequent investigation of the surface using STM has been detailed. STM images of the surface whilst in UHV, ambient and liquid conditions were included, as well as the frequently observed STM contrast inversion.

The adsorption of perylene derivatives on the BN/Rh(111) surface whilst in UHV has also been discussed. Irregular 2D close-packed islands were formed on the nanomesh surface, with islands aligned to the Moiré superstructure as well as islands that were misaligned. PTCDI islands were also shown to have domains of varying orientation within the 2D islands. These results are especially interesting when compared to similar experiments on graphene and are discussed in Chapter 5.

The pores of the *h*-BN layer (created by the corrugation of the boron nitride layer) trapped the PTCDI and DP-PTCDI molecules, and examples of single and multiple molecules trapped in the pores have been discussed. Both 2D islands and molecules trapped in the pores were observed within the same STM images of the surface. However, annealing the surface at temperatures of less than 300°C removed the organic molecules that had formed the close-packed islands, with only the trapped molecules in the pores of the surface remaining. The placement of PTCDI molecules trapped in the pores of the BN/Rh(111) surface was also illustrated.

Chapter 5

Graphene Formation on Rh(111) Thin Films

Section 1.3 of Chapter 1 describes how the seminal work of Novoselov et al. [31, 32] since 2004 has stimulated great interest in the controllable growth of epitaxial graphene monolayers. While initial research was focussed on the use of SiC wafers [44], the promise of transition metals as substrates has also been demonstrated [36, 39, 45, 46, 48] and both approaches are scalable to large-area production. The growth of graphene on transition metals, such as ruthenium and iridium, leads to a Moiré-like superstructure [45, 46, 48], similar to that observed for the boron nitride 'nanomesh' monolayer on a Rh(111) (BN/Rh(111)) surface [12, 14, 23] which has been described in Chapter 1 and Chapter 4.

This chapter details recently developed methods used to produce a monolayer of graphene on a Rh(111) thin film surface and the adsorption of organic molecules onto the graphene monolayer. This section of work primarily discusses UHV-STM results but also features results obtained with dynamic STM and AFM in UHV, and STM in ambient conditions. X-ray photoelectron spectroscopy (XPS), X-ray photoelectron diffraction (XPD) and low energy electron diffraction (LEED) results provided by Müller, Hüfner and Sachdev [99] are also detailed.

5.1 Production of a Graphene Monolayer on a Rh(111) Thin Film

The substrates (150 nm Rh(111) thin film grown on a 25 nm heteroepitaxial yttria-stabilised zirconia (YSZ) buffer layer deposited on a Si(111) wafer) used for the production of graphene were obtained from the University of Augsburg,

Germany – as they had been for the formation of boron nitride 'nanomesh' surfaces detailed in Chapter 4.

The process of reducing the contaminants present on the Rh(111) thin film surface by argon sputtering, oxygen dosing and annealing the sample in UHV has been described in Chapter 4. Once the sample had then been studied with STM to ascertain its quality, it was exposed to an external source of carbon using one of the two methods explained in the following sections. However, it should be noted that even an unintentional source of carbon could produce well-ordered graphene. In the Supplementary Information of Reference [99], a Rh(111) thin film sample was purposefully contaminated with a fingerprint and then annealed in UHV to produce a graphene monolayer. This graphene formation was attributed to residues from a fingerprint mainly consisting of water, carbonic acids and fatty acids and could therefore be described as a $C_xH_yO_z$ system where $x << y, z$. This result stresses that there must be a very careful consideration of the condition of the sample and of the processes (such as solvent cleaning) that are performed on a transition metal sample used to produce graphene, when considering the graphene growth mechanism.

5.1.1 Solvent Immersion Carbon Exposure

In this thesis, the most frequently used method of producing graphene on a Rh(111) thin film was immersion of a clean Rh(111)/YSZ/Si(111) sample in a solvent. This required that the sample was removed from the UHV system via the fast entry load-lock (FEL) chamber. The exposure to carbon in this approach was very simple. Once the sample was removed from UHV it was immersed in the solvent for 10-15 seconds, although times of up to 1 min were also used to the same effect. This immersion was performed whilst the sample was still in the UHV sample holder, so that the sample was not damaged by its removal or its subsequent securing in the sample holder. The sample was then dried using a N_2 gun for ∼1 min. The sample was reintroduced to UHV immediately after its immersion, although the sample could also be kept at atmospheric pressure for up to several days before immersion and reintroduction to the UHV system if required.

Once the sample and sample holder were in the UHV system, the sample was degassed again to ∼500°C over ∼24 hours (base pressure 1×10^{-9} mbar, maximum pressure 1×10^{-8} mbar). The sample was then annealed at 800°C for 30 min to produce the graphene monolayer. Subsequent STM imaging of the sample

indicated the coverage of graphene. Further annealing cycles at 800°C for 5-15 min could then be performed – where necessary – to maximise graphene coverage.

Müller, Hüfner and Sachdev have found that immediately after introduction to the vacuum system the surface of the sample was completely disordered when observed with LEED [99]. From Figure 5.1, the XPS spectra found for the sample before annealing contained a 2:1 carbon-to-oxygen ratio, as expected for the composition of the precursor (in this case acetaldehyde, H_3C-C(O)H). After annealing the sample to ∼800°C, the oxygen intensity in the XPS spectra dropped below the detection limit, as shown in Figure 5.1.

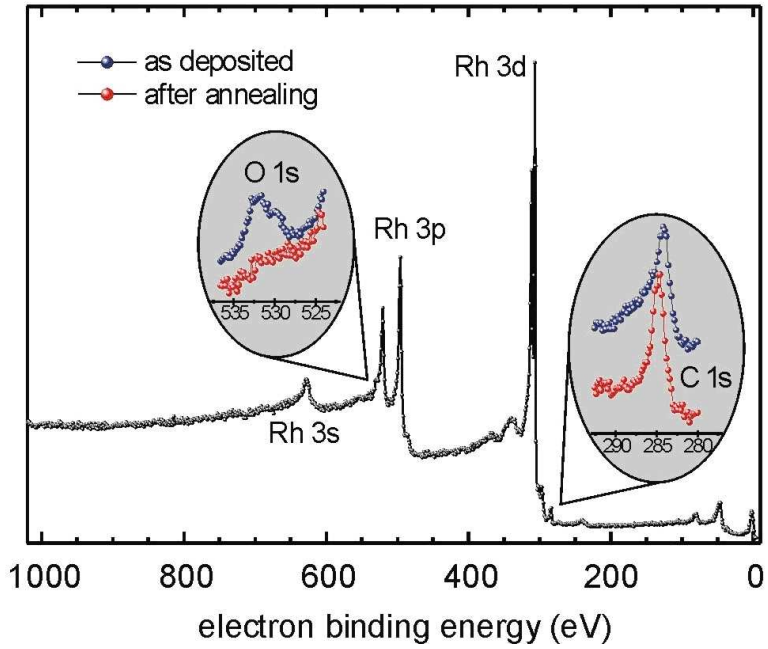

Figure 5.1: XPS spectra of a Rh(111) thin film sample after ex-situ immersion in acetaldehyde. The survey spectrum (black) corresponds to a sample after annealing up to ∼800°C, the magnified spectra displays the relative amounts of carbon and oxygen before (blue) and after annealing (red). Results provided by F. Müller, from Ref. [99]. © Wiley-VCH Verlag GmbH & Co. KGaA. Reproduced with permission.

The mean thickness of the carbon species remaining on the surface after annealing was calculated as approximately one monolayer. This value was estimated from the angular distribution of the photoelectron intensity [99]. However, the damping of the substrate intensities was used as a measure of the mean thickness of the carbon film, the same value of the mean thickness could be explained as a partial coverage of multilayer graphene. After investigation with XPD, this explanation was ruled out. The isotropy of the XPD results indicated that the

emitting atom was located exclusively at the topmost layer. No forward scattering modulations of the angular distribution of the C-1s photoelectron intensity were observed [99], confirming that a graphene monolayer film was formed rather than multilayer domains.

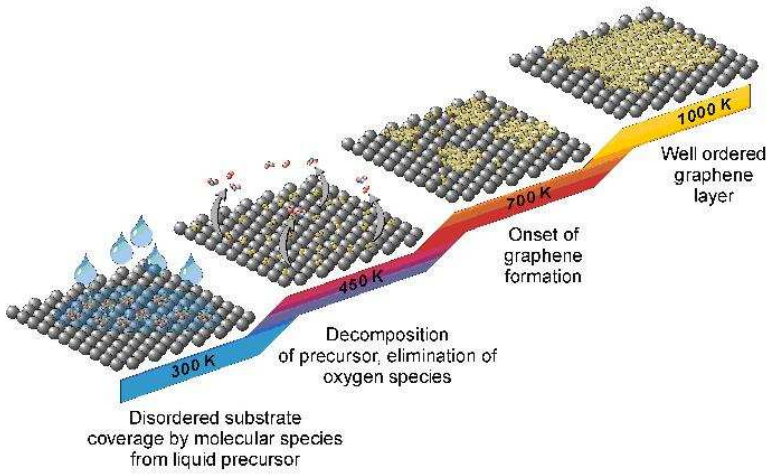

Figure 5.2: The graphene formation model for Rh(111), illustrating the effects of the solvent immersion and subsequent annealing of the sample. C_2-radicals were produced, which then combined to form a graphene monolayer. Modified diagram from Ref. [99]. © Wiley-VCH Verlag GmbH & Co. KGaA. Reproduced with permission.

LEED, photoelectron spectroscopy and STM investigations [99] supported a model in which the precursor molecules underwent a gross decomposition process with dicarbon species (C_2-radicals) as intermediates, which then combined to form a graphene monolayer, as shown in Figure 5.2. Water and methane were eliminated from the precursor, followed by the desorption of hydrogen during higher temperature annealing. This resulted in mobile and reactive C_2 species acting as the actual growth species for graphene. When the same graphene formation procedure was performed without any immersion of the sample no graphene was produced.

Upon formation of the graphene monolayer a Moiré superstructure [45, 46, 48] was observed, similar to that observed for the BN/Rh(111) surface [12, 14, 23] described in Chapter 4. The superstructure was 12 × 12 graphene unit cells overlaid on 11 × 11 Rh(111) unit cells (lattice constants of ∼0.246 nm [100] and ∼0.269 nm [101] respectively) and had an overall period, a_m = 2.95 nm, as determined with LEED [99]. A schematic of the Moiré pattern is shown in Figure 5.3 where four unit cells of the Moiré superstructure are depicted, rhodium

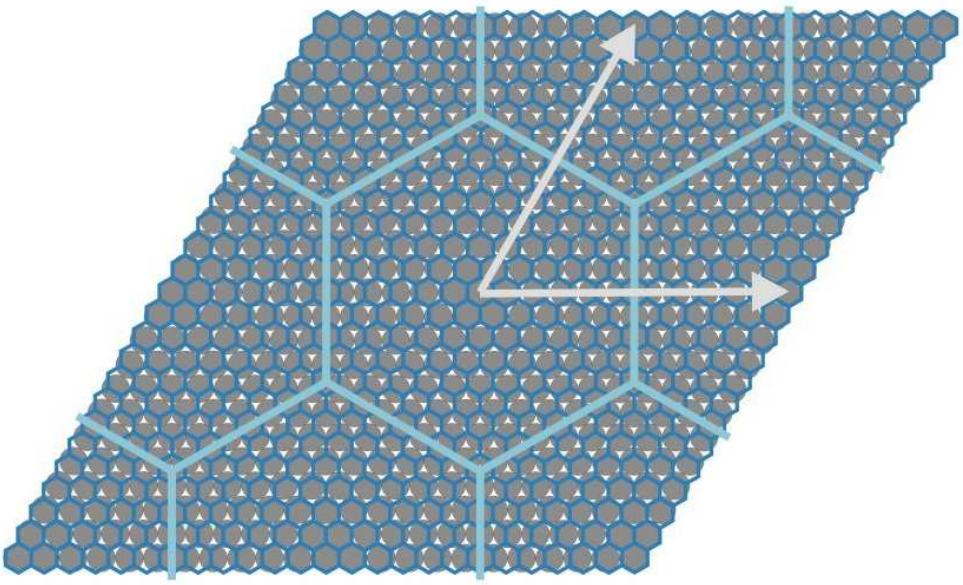

Figure 5.3: Schematic diagram of a honeycomb mesh (dark blue) representing graphene, overlaid on an array of grey circles representing rhodium atoms. The superstructure (light blue) formed by 12 × 12 unit cells of graphene overlaid on 11 × 11 unit cells of Rh(111) atoms leads to a long range periodic pattern with lattice vectors, a_m, marked by white arrows. The central areas of the superstructure hexagons are 'centre-moire' areas and the edges are the 'edge-moire' areas.

atoms are grey and the graphene honeycomb structure is dark blue.

The Moiré effect can be clearly seen in Figure 5.3, with topographically higher areas where rhodium atoms were centrally located with respect to the graphene honeycomb 'pores' ((hcp,fcc) bonding areas) and topographically lower areas where the rhodium atoms were not centrally located ((fcc,top) and (top,hcp) bonding areas). Brugger et al. have shown that the (hcp,fcc) areas of the graphene monolayer are weakly bound to ruthenium surfaces and are higher topographically than the strongly bound areas ((fcc,top) and (top,hcp) bonding areas) [29]. It is therefore highly likely that the (hcp,fcc) areas of a graphene monolayer are weakly bound to a rhodium surface (and strongly bound for the (fcc,top) and (top,hcp) areas) but no direct study has been performed. These areas of the graphene monolayer will be described as 'centre-moire' ((hcp,fcc)) and 'edge-moire' ((fcc,top) and (top,hcp)) respectively in this thesis, as was the case for the boron nitride monolayers in Chapter 4. The overlaid light blue hexagonal lattice in Figure 5.3 relates to the Moiré superstructure and the corresponding lattice vectors, a_m, are shown as white arrows.

Imaging the sample surface with STM after the annealing procedure revealed the superstructure associated with the graphene monolayer on the Rh(111) thin film (g/Rh(111)) surface. The Moiré pattern was found for a g/Rh(111) surface regardless of the precursor used to generate the graphene – these different precursors are discussed in the following sections.

Acetone Immersion

Although several solvents were found to produce a g/Rh(111) surface through immersion, acetone was the precursor regularly used to produce graphene in this thesis. The previously detailed procedures were used and imaging with STM found that approximately 100% coverage could be achieved with a 30 min anneal. Figure 5.4 shows STM images of the Moiré superstructure, where the circular brighter areas were the weakly bound (centre-moire) areas of the graphene monolayer, the lattice vectors of the Moiré superstructure are shown as white arrows and correspond to the lattice vectors described in Figure 5.3.

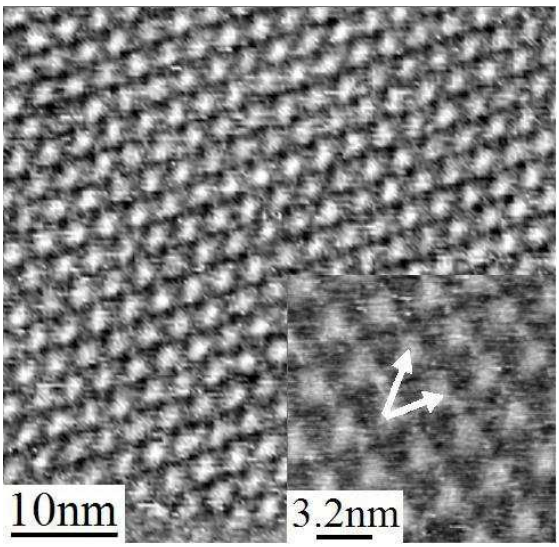

Figure 5.4: STM images of the Moiré superstructure for a g/Rh(111) surface produced by acetone immersion. Inset is a smaller scan size image of the same area. White arrows show the lattice vectors for the superstructure and correspond to the lattice vectors in Figure 5.3. Imaging parameters V_{bias}= 1.0 V, I_t= 200 pA.

The graphene produced by acetone immersion readily covered the Rh(111) surface and a graphene monolayer was imaged with STM over extended areas, as shown in Figure 5.5. The scan size used to observe the continuous graphene coverage was only limited by the resolution required to distinguish the Moiré

pattern from noise. In the majority of the STM images of the graphene monolayer the Moiré pattern was imaged with the centre-moire areas as topographically higher areas, however a stable contrast inversion was also possible, as shown in Figure 5.5. However, this observed contrast inversion was not observed as readily as the equivalent STM contrast inversion for the BN/Rh(111) surface detailed in Chapter 4.

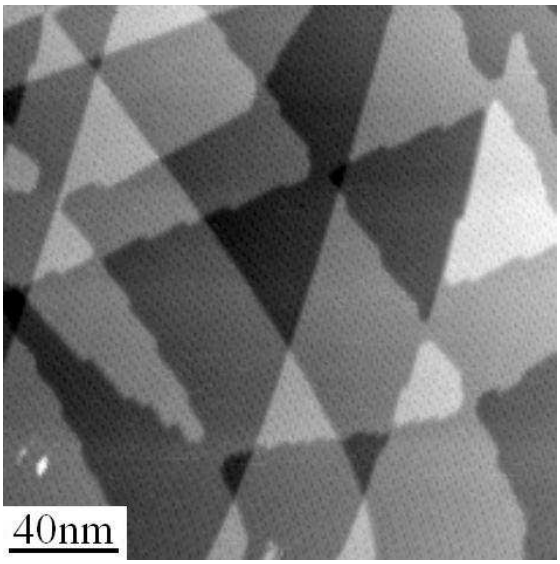

Figure 5.5: STM image of the Moiré superstructure for a g/Rh(111) surface produced through acetone immersion, showing the graphene coverage for a larger scale image and the contrast inversion found intermittently. Imaging parameters V_{bias}= 1.0 V, I_t= 200 pA.

The proposed graphene monolayer formation model suggests small domains of graphene form and then grow laterally in size to produce increased surface coverage. This is observed in Figure 5.6 which shows a Rh(111)/YSZ/Si(111) sample with partial graphene coverage (the sample was later annealed for longer to produce full graphene coverage).

The g/Rh(111) surface was primarily imaged with the Nanograph-01 STM system in UHV (described in Chapter 2) because this STM system was housed within the UHV system where the graphene samples were produced. However, when samples were removed from UHV and imaged in ambient conditions a similar quality surface was revealed. This demonstrated the durability of the g/Rh(111) samples, a valuable quality when considering future applications for Rh(111) graphene production. This also allowed further varied experimentation to be performed, whether in ambient conditions or in a different UHV system. Figure 5.7

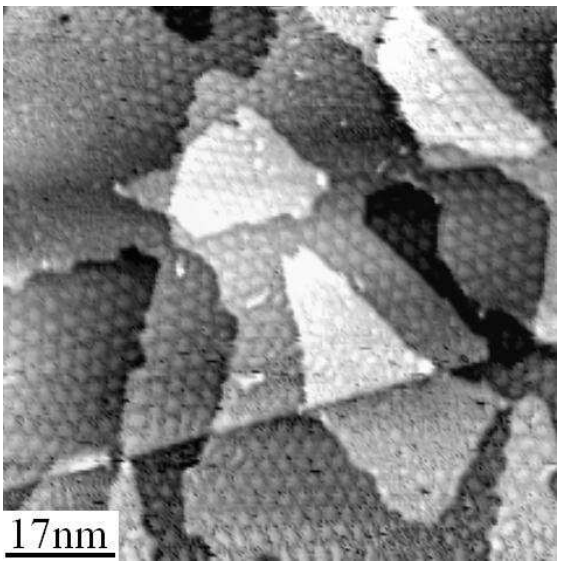

Figure 5.6: STM image of a g/Rh(111) surface produced by acetone immersion, bare areas of rhodium and the edges of the graphene monolayer are observed as the Moiré superstructure does not cover the entire surface. Imaging parameters V_{bias}= 1.0 V, I_t= 200 pA.

shows an STM image of the g/Rh(111) surface in ambient conditions, where the Moiré superstructure is clearly visible.

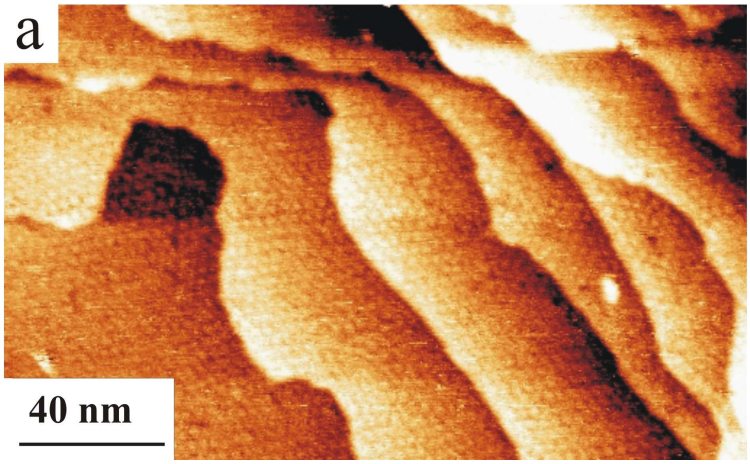

Figure 5.7: Ambient STM image of a g/Rh(111) surface produced in UHV, the Moiré superstructure is clearly resolved even after the sample has been exposed to air. Imaging parameters V_{bias}= 0.1 V, I_t= 1.0 nA. Modified diagram from Ref. [99].

Paraldehyde Immersion

In Reference [99], the precursor used for the immersion method of producing graphene on Rh(111) was acetaldehyde. A third precursor was also investigated, paraldehyde ($C_6H_{12}O_3$), a cyclic trimer of acetaldehyde. The same method of immersion was used as previously described, but the sample and sample holder were immersed in paraldehyde rather than acetone. STM imaging of the surface revealed the same Moiré pattern after the sample was annealed in UHV. Figure 5.8 shows an STM image of a graphene monolayer produced by immersion in paraldehyde. The coverage of graphene appeared to be lower than that produced with acetone, even after further annealing. The amount of surface contaminants also seemed increased, possibly due to contaminants in the solution. However, STM is used to produce localised images of the surface rather than investigating the surface as a whole and so other surface analysis techniques would be required for conclusive results. For these reasons acetone was the precursor primarily used for producing graphene when performing the immersion technique.

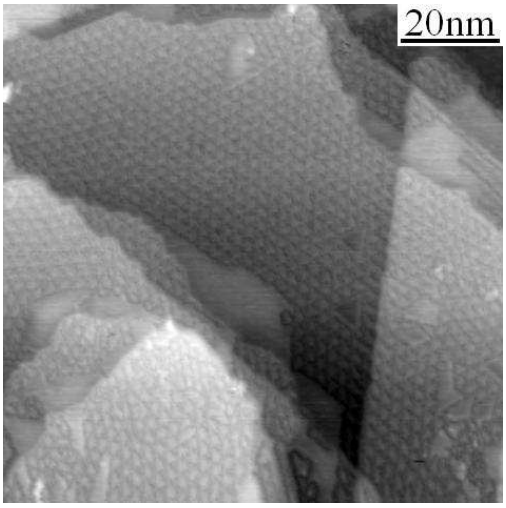

Figure 5.8: STM image of a g/Rh(111) surface in UHV produced by paraldehyde immersion. Areas without the Moiré pattern can be seen and some domain boundaries of the graphene monolayer are apparent due to mismatches in the Moiré pattern. Imaging parameters V_{bias}= -1.0 V, I_t= 200 pA.

5.1.2 In-situ Propylene Exposure

The second technique used for producing a g/Rh(111) surface was the dosing of a sample with an alkene whilst in UHV. For this procedure a gas cylinder

containing 99.95% propylene (C_3H_6) was attached to the third gas line of the Nanograph STM-01 UHV system. This allowed a Rh(111)/YSZ/Si(111) sample to be cleaned in the UHV system with Ar^+ sputtering and O_2 dosing (as previously described) and then dosed immediately afterwards. Therefore the sample was not subjected to ambient pressure at any point during this process.

After the Rh(111)/YSZ/Si(111) sample was imaged with STM to confirm the surface was clean of contaminants, the sample was annealed at ∼800°C (base pressure of the Nanomesh chamber $\sim 5\times10^{-8}$ mbar) and a partial pressure of propylene 1×10^{-6} mbar was introduced to the Nanomesh chamber for 5 min. During the dosing stage the Nanomesh chamber was sealed off from the other UHV chambers apart from the gas handling line (GHL) chamber and both chambers were pumped with a turbomolecular pump. The propylene gas inlet valve was closed after 5 min and the sample was annealed for another 1 min before the sample heater current was reduced to zero over ∼60 seconds.

This method of carbon exposure produced a g/Rh(111) surface similar to the graphene produced by immersion in acetone. The mechanism of growth for the graphene in this process is believed to be the same as for the immersion technique since transition metals catalyse dehydrogenation reactions. Figure 5.9 shows STM images of the graphene monolayer produced by propylene exposure.

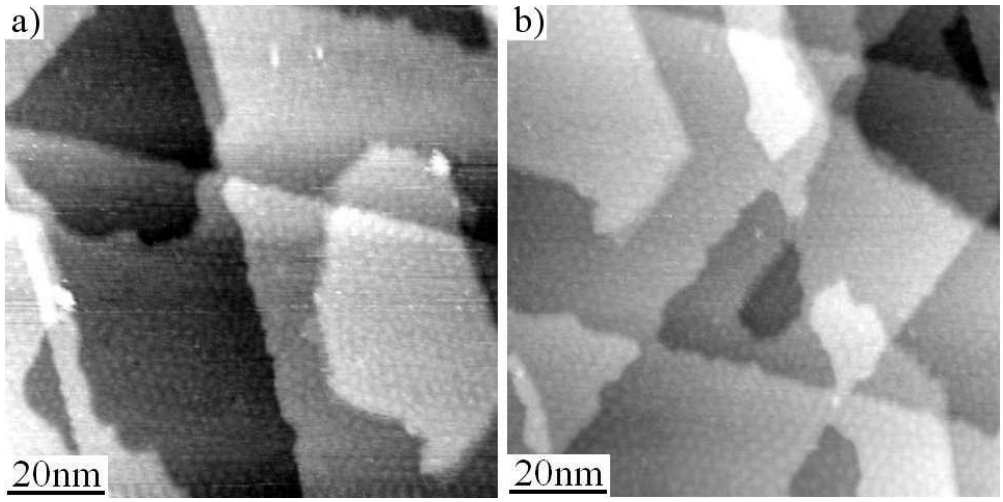

Figure 5.9: STM images of a g/Rh(111) surface in UHV formed by exposure to propylene. Imaging parameters for (a) and (b) V_{bias}= -1.0 V, I_t= 200 pA.

5.1.3 AFM/STM of Graphene on Rh(111)

After preparation of a g/Rh(111) sample through exposure to propylene and subsequent imaging with the Nanograph STM-01 system, the sample was transferred through ambient conditions and introduced to the UHV system housing the constructed AFM/STM system described in Chapter 3. This required delicate handling of the sample while it was removed from one sample holder (Figure 2.9) and loaded into another (Figure 3.3). A silicon backing heater was secured between the sample and the sample holder (as previously described) to allow heating of the sample without passing an electrical current through the sample itself.

A major difficulty encountered during the sample transfer process was the size of the sample. The width (and length) of the Rh(111)/YSZ/Si(111) sample was approximately 10 mm when received which complied with the size requirements for the Nanograph STM-01 sample holder. However, the AFM/STM system sample holder could only fit a maximum sample width of approximately 9.5 mm. Samples smaller than 10 mm in width were difficult to fit into the Nanograph STM-01 sample holder and therefore the Rh(111) thin film samples supplied by the University of Augsburg needed to be carefully selected or cut to size before their introduction to the Nanograph STM-01 UHV system for the graphene production process.

The AFM/STM system could be used to acquire images in STM, dynamic STM and AFM modes depending on the type of tip assembly mounted in the system. Images of the g/Rh(111) surface acquired using this AFM/STM system used a Pt-Ir tip wire attached to a tuning fork (TF) to provide a tunnel current channel separate to the TF displacement monitoring channels. Conventional STM (as had previously been performed with the Nanograph STM-01 system), dynamic STM (average tunnel current used as feedback) and FM-AFM were performed on the g/Rh(111) sample produced by propylene exposure. Imaging of the sample surface was performed in UHV after the sample was annealed at $\sim$500°C to attempt to remove adsorbates encountered from the ambient exposure during the transfer between the UHV systems.

STM images revealed that many areas of the surface were still covered with the Moiré superstructure of the graphene monolayer and appeared largely unaffected by the transfer of the sample. However some areas of the surface were found to be unscannable – with large height variations – whilst other areas showed a similar morphology to the STM images obtained with the Nanograph STM-01 but with increased amounts of adsorbates.

Dynamic STM images of the Moiré superstructure were also obtained, as shown

in Figure 5.10, in most cases with improved resolution and stability when compared to conventional STM images obtained with the AFM/STM system.

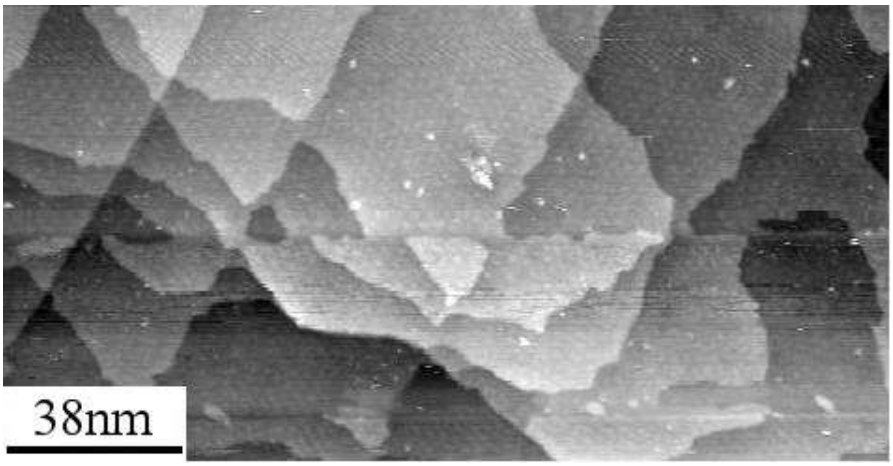

Figure 5.10: Dynamic STM image of a g/Rh(111) surface after it was introduced to another UHV system via ambient conditions. Imaging parameters V_{bias}= 1.5 V, $\langle I_t \rangle$= 35 pA A_o= 0.7 nm.

Whilst imaging the surface of the sample in dynamic STM mode, the dissipation (when operating in constant amplitude mode) and frequency shift (df) data could be recorded. Images of the Moiré superstructure were obtained in dynamic STM mode for both the topography and dissipation images simultaneously, as shown in Figure 5.11. The Moiré superstructure is clearly observed in both sets of data – where the centre-moire areas of the superstructure were imaged as brighter circular areas. It was found that the Moiré superstructure was imaged as areas of high dissipation and low dissipation for centre- and edge-moire areas respectively. Therefore the cantilever oscillation amplitude was reduced for centre-moire areas of the graphene monolayer when compared to edge-moire areas, whilst the average tunnel current was kept constant.

As there was no resolution of the Moiré superstructure in the df data, it is believed that the tip was only experiencing attractive forces as the tip apex was too far from the surface to experience the repulsive forces that may have achieved the df resolution to distinguish the Moiré pattern. Therefore the dissipation results revealed an increase in tip-surface attractive interaction for the centre-moire areas of the graphene monolayer, as would be the case if the graphene monolayer was corrugated – with the centre-moire areas further from the rhodium substrate than the edge-moire areas. It is hypothesised that the areas of the graphene monolayer that were further away from the surface may have buckled when the tip was

positioned over them and the ensuing non-conservative forces affected the dissipation signal. However, the observed dissipation variation could have also been due to a change in surface topography that was not mimicked by the tunnel current feedback due to variations in the work function of the surface.

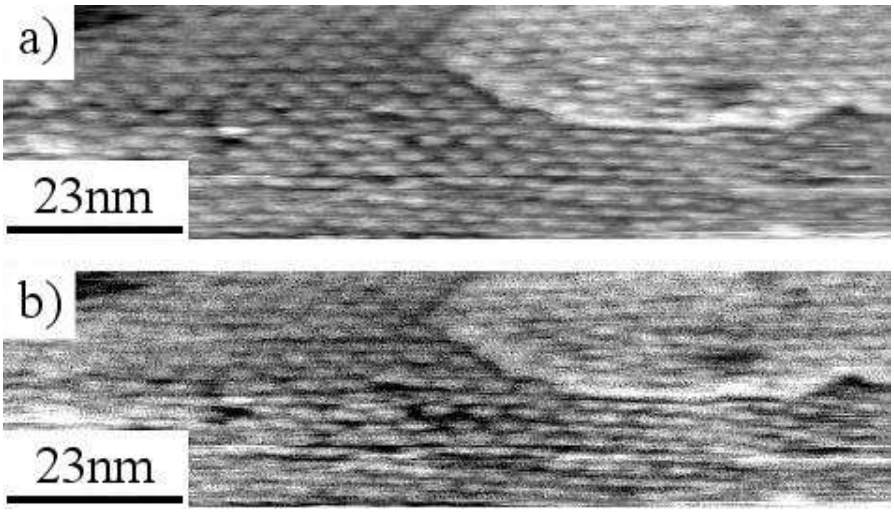

Figure 5.11: (a) Dynamic STM topography and (b) dissipation image of a g/Rh(111) surface after introduction to another UHV system via ambient conditions. The Moiré pattern can be seen in both the topography (controlled by the tunnel current) and the dissipation signal from the PLL. Imaging parameters for (a) and (b) V_{bias}= 1.0 V, $\langle I_t \rangle$= 70 pA A_o= 0.7 nm.

From Reference [29], the graphene on Ru(0001) surface showed both a physical corrugation in the graphene monolayer – with the centre-moire areas higher in topography – and a variation in the surface work function, with a higher work function for the centre-moire areas. Therefore the variation in dissipation observed in Figure 5.11 was likely to be due to both a physical and electronic effect of the Moiré superstructure. This was an interesting result that could be studied in further detail, of particular interest would be the effect on the dissipation if there was a contrast inversion of the tunnel current data.

FM-AFM was also performed upon the g/Rh(111) surface (df signal as the feedback parameter), however the Moiré superstructure was not resolved with this technique in terms of df. However, when the frequency shift was greatly increased whilst still maintaining stability, it was possible to intermittently image the Moiré pattern in the simultaneously-acquired average tunnel current data, as shown in Figure 5.12.

The apex of the particular tip used for imaging the surface must not have been sufficiently sharp, because the lateral resolution of the Moiré pattern periodicity

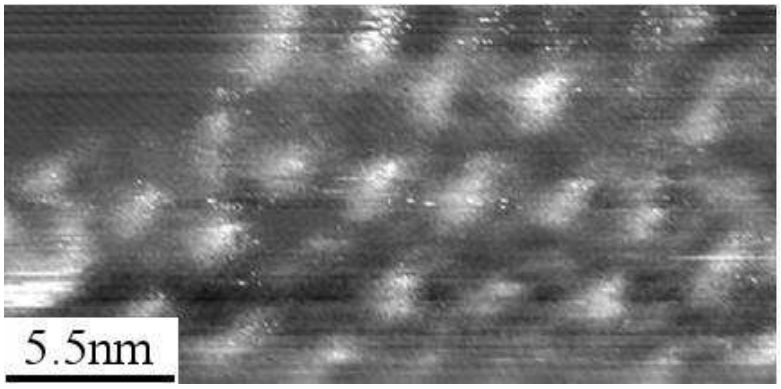

Figure 5.12: Tunnel current data for an AFM/STM cantilever imaging in FM-AFM mode for a g/Rh(111) surface. Although there was no resolution of step edges or the Moiré pattern in the AFM topography, these features were resolved in the simultaneous tunnel current data. Imaging parameters V_{bias}= -1.0 V, df= -200 Hz A_o= 0.7 nm.

was not achieved whilst operating in AFM mode. However, when the average tip-sample distance was reduced, it was possible to resolve the Moiré pattern in the tunnel current data. Further FM-AFM experiments to achieve the resolution of the Moiré superstructure could be performed. This could lead to a force spectra investigation of adsorbed molecules on the graphene monolayer and the graphene monolayer itself, similar to results detailed in Chapter 3 and as an expansion of the results described in Section 5.2.

5.2 Molecular Deposition on Graphene

Three Knudsen cells were mounted on the preparation chamber of the Nanograph STM-01 UHV system allowing the deposition of organic molecules onto the samples inside the UHV system. Perylene and coronene derivatives as well as the buckminsterfullerene were deposited onto the g/Rh(111) surface using Knudsen cells and the resulting nanostructures were investigated (although not exclusively) with the Nanograph STM-01 system in-situ.

5.2.1 PTCDI Adsorption

The deposition of perylene tetra-carboxylic diimide (PTCDI) was investigated on the g/Rh(111) surface – the PTCDI molecule is described in more detail in Section 3.4.2 of Chapter 3. PTCDI adsorption had previously been investigated on a number of surfaces, such as graphite (described in Chapter 3) and

the BN/Rh(111) surface (described in Chapter 4) – surfaces with similar characteristics to the g/Rh(111) surface. As previously described, PTCDI was found to form 3D islands on a HOPG surface [95] due to its weak interaction with the surface. However, the BN/Rh(111) surface trapped the PTCDI molecules in the pores of the nanomesh network with random orientations and also allowed monolayer growth of PTCDI over the boron nitride monolayer [96]. PTCDI has also been adsorbed on the Ag-Si(111) $\sqrt{3} \times \sqrt{3}$R30° surface where 2D PTCDI island growth was observed [88]. The PTCDI islands formed on Ag-Si(111) $\sqrt{3} \times \sqrt{3}$R30° surfaces were composed of dimers of PTCDI molecules stacked to produce a close-packed island. An example of a hydrogen-bonded PTCDI dimer is shown in Figure 5.13, where two hydrogen-bonds align the ends of the molecules to each other.

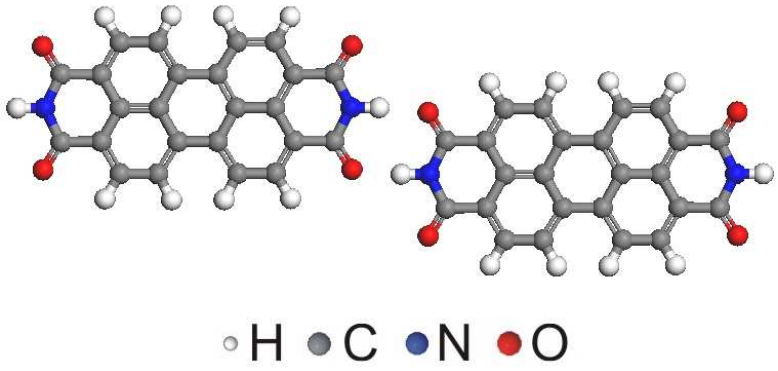

Figure 5.13: Two PTCDI molecules forming a dimer junction stabilised by two hydrogen-bonds.

Several different PTCDI surface coverages were deposited on the g/Rh(111) surface by varying the Knudsen cell deposition time. The Knudsen cell containing PTCDI was operated at 355°C, depositing PTCDI at a rate of $\sim 3 \times 10^{-3}$ MLmin^{-1}. Figure 5.14 shows an STM image acquired after PTCDI deposition in which rows with a width corresponding to one molecule were clearly resolved running parallel to the principal directions of the surface, with lengths up to 25 nm. There were many examples of pairs of extended rows which were adsorbed on neighbouring sites of the Moiré superstructure with a spacing of $\sqrt{3}a_m/2$, which appeared to be the minimum spacing for neighbouring rows. Close-packed islands were not observed and the molecular arrangement on the graphene superstructure differed significantly from that observed for a graphite substrate.

Previous experimental estimates of the spacing of molecules within PTCDI rows range from 1.41-1.46 nm [88] and, noting the near match between this spac-

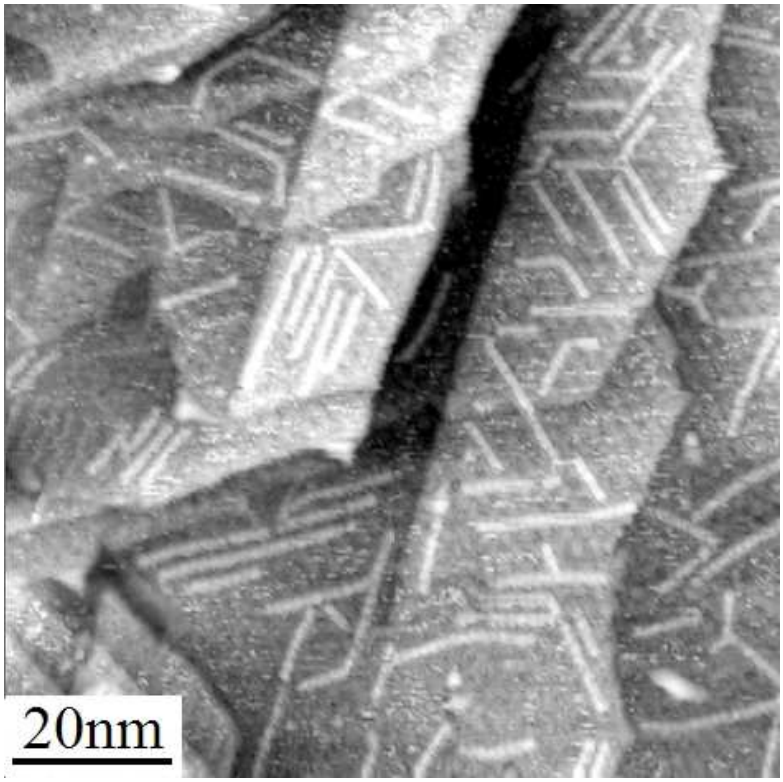

Figure 5.14: STM image of PTCDI molecules adsorbed on the Moiré superstructure of the g/Rh(111) surface. Extended rows of PTCDI molecules that followed the principle directions of the Moiré superstructure were observed. Imaging parameters V_{bias}= -1.0 V, I_t= 200 pA.

ing and $a_m/2 = 1.47$ nm of the graphene superstructure, a structural model for commensurate PTCDI rows was proposed, as shown in Figure 5.15. The PTCDI molecules bonded together in a dimer formation but did not stack above and below as has been observed on other surfaces, thus there were commensurate rows of PTCDI molecules that were only one molecule wide.

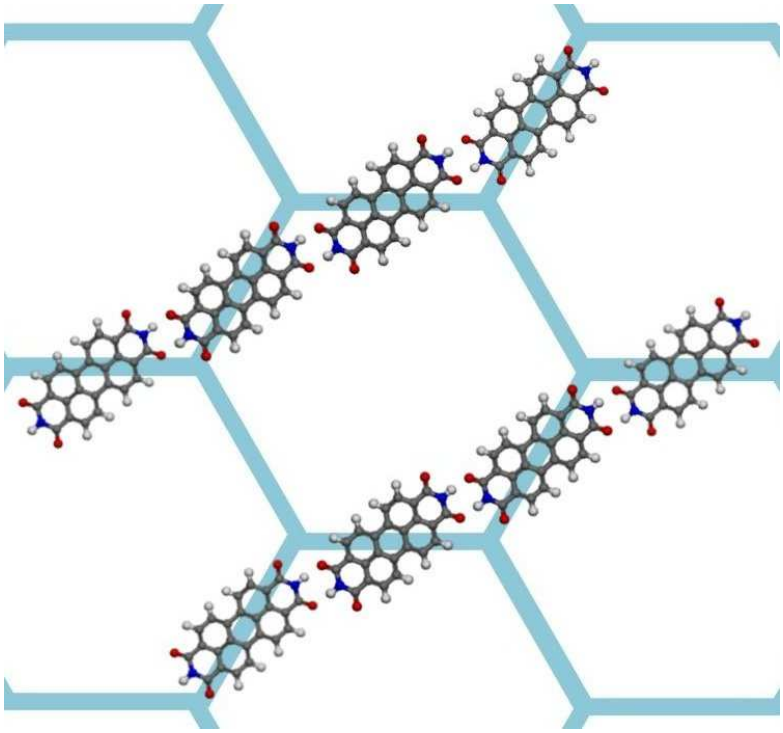

Figure 5.15: Model of PTCDI dimers forming commensurate rows on the Moiré superstructure.

Figure 5.16 is a small area STM scan of PTCDI adsorbed on a g/Rh(111) surface, the positioning of the PTCDI molecules correspond to the proposed model of PTCDI molecules on the Moiré superstructure. An intramolecular double lobe contrast of the adsorbed PTCDI molecules was observed in Figure 5.16, previous experiments show these lobes correspond to the highest occupied molecular orbital of PTCDI [88]. Thus there was also agreement for the molecular orientations proposed in Figure 5.15.

Figure 5.16 shows parallel PTCDI rows in greater detail and also instances where a PTCDI row encountered another PTCDI row. The growth of the PTCDI rows appeared space-limited, that is, affected by the space available for the addition of another PTCDI to the end of the row. However, the growth of the PTCDI rows was also affected by the availability of PTCDI molecules – depending on the PTCDI coverage of the surface. From Figure 5.16, it becomes clear that a PTCDI

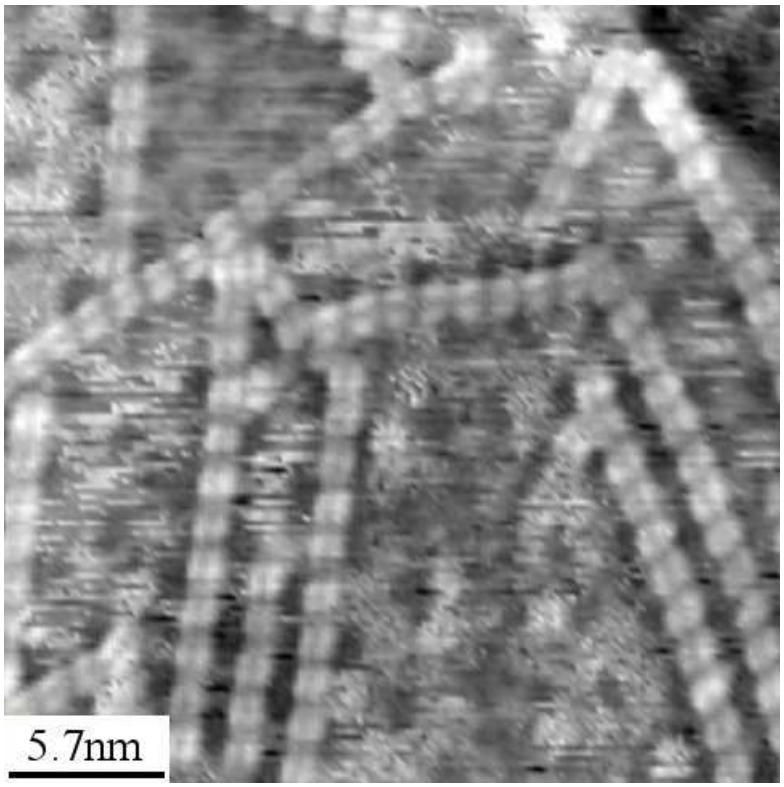

Figure 5.16: A smaller scan size STM image of PTCDI molecules adsorbed on the Moiré superstructure of the g/Rh(111) surface. The positioning of the molecules with respect to the Moiré superstructure can be observed and are in accordance with the proposed model in Figure 5.15. Imaging parameters V_{bias}= -1.0 V, I_t= 150 pA.

molecule at the end of a row would not be hydrogen-bonded with the middle of another PTCDI row because the PTCDI molecules would not be orientated correctly.

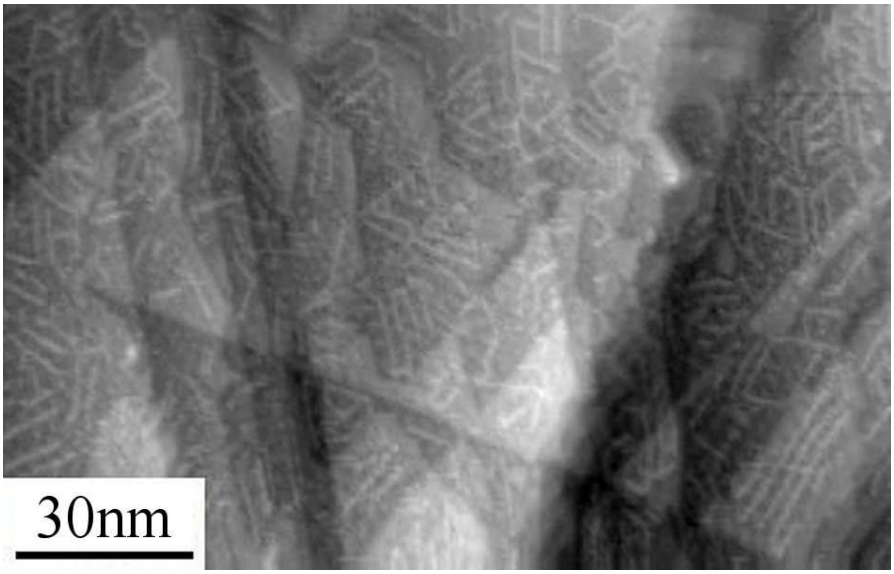

Figure 5.17: STM image of high PTCDI coverage of the g/Rh(111) surface and its associated Moiré superstructure. The spacing between PTCDI molecular rows was preserved even with higher coverage. Imaging parameters V_{bias}= -1.0 V, I_t= 100 pA.

Figure 5.17 shows an STM image of a g/Rh(111) surface with high PTCDI coverage. The PTCDI rows were still parallel to each other and the spaces between PTCDI rows were still unoccupied. This was the case even though the g/Rh(111) surface was close to saturation point, that is, where further PTCDI molecules could not be positioned on the edge-moire areas of the graphene monolayer without filling the spaces between PTCDI rows. The PTCDI molecules continued to form dimer junctions on the surface and thus the new PTCDI rows that were created became iteratively reduced in length, as the space available for the growth of rows was constantly reduced.

The importance of a commensurate match between molecular dimensions and the Moiré periodicity is highlighted by a comparison with adsorption of PTCDI on the BN/Rh(111) surface, previously described in Chapter 4. This boron nitride monolayer was isoelectronic with graphene and also displayed a Moiré pattern but with a slightly larger periodicity of 3.2 nm. This periodicity did not have a simple commensurability with the molecular dimensions. In contrast, on the g/Rh(111) surface, isolated PTCDI was not observed and the molecular orientation was non-

random. The commensurability on the g/Rh(111) surface led to a gap between molecules trapped in neighbouring Moiré sites which very closely matched the PTCDI molecular dimensions, leading to the formation of continuous rows and the stabilisation of the molecule in an orientation directed at a neighbouring occupied site.

Annealing PTCDI on Graphene

Although there were no PTCDI close-packed islands on the g/Rh(111) surface at room temperature, when the substrate was annealed to ∼300°C the formation of close-packed islands was observed. Figure 5.18 shows an STM image of a close-packed PTCDI island on the g/Rh(111) surface approximately 20 nm × 25 nm in surface area. The formation of the close-packed PTCDI islands was similar to the 2D PTCDI island formation observed for the Ag-Si(111) $\sqrt{3} \times \sqrt{3}$R30° surface, where stacked dimer junctions formed the island. Defects were observed in the PTCDI island in Figure 5.18 due to missing PTCDI molecules and single PTCDI molecules on the edges of the island were also imaged. The Moiré pattern of the graphene monolayer was imaged when scanning the PTCDI island itself, therefore the PTCDI island followed the contours of the graphene monolayer. Interestingly the Moiré pattern of the bare graphene monolayer was imaged in an inverted contrast to the PTCDI island, which may be attributed to a band-gap created by the presence of PTCDI islands.

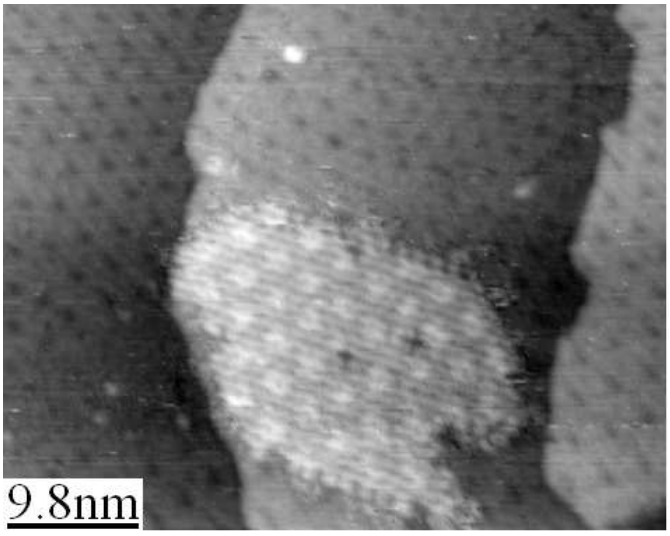

Figure 5.18: STM image of PTCDI adsorbed on the g/Rh(111) surface after the substrate has been annealed. A close-packed PTCDI island was observed. Imaging parameters V_{bias}= 1.0 V, I_t= 100 pA.

The STM image in Figure 5.19 revealed both commensurate PTCDI rows and PTCDI close-packed islands on the g/Rh(111) surface. The annealing of the sample may have caused PTCDI molecules to more readily diffuse on the surface and therefore form large numbers of longer parallel rows – rows double the length of ones observed before the annealing of the sample are revealed in Figure 5.19 and the number of parallel rows also appears increased. The PTCDI molecules may have subsequently overcome the trapping potential of the Moiré superstructure and formed close-packed islands covering the g/Rh(111) surface. This would account for the rows observed in Figure 5.19 which extended from a close-packed PTCDI island. Many examples of PTCDI rows and PTCDI islands have been imaged after an anneal of a sample, however in other cases only PTCDI islands were observed after an anneal. In one experiment only PTCDI rows were observed after an anneal but after a further higher temperature anneal only close-packed islands were observed. Therefore it can only be concluded that either a longer anneal time or higher temperature anneal of the sample eventually produced exclusively PTCDI islands. The distinction cannot be made which of these two processes led to the transition due to two factors; the intrinsically local nature of the STM measurements meant the whole of the sample was not sampled after each anneal, and the temperature measurement of samples annealed at temperatures below 500°C was also inaccurate.

Figure 5.19 also contains examples of PTCDI islands that extend over the step edges of the g/Rh(111) surface and an apparent change in the principal directions of the Moiré superstructure, and therefore also the PTCDI rows, in both Figure 5.19a and the top-left of Figure 5.19b. There appears to be a corresponding shift in the alignment of the top and bottom sections of the PTCDI island in Figure 5.19b to match the graphene monolayer beneath.

5.2.2 DP-PTCDI Adsorption

Di(propylthio)-PTCDI (DP-PTCDI) was adsorbed on the g/Rh(111) surface using a Knudsen cell operating at 405°C to produce a $\sim 7\times10^{-4}$ MLmin^{-1} deposition rate. DP-PTCDI was a derivative of PTCDI with two sulphur atoms replacing two hydrogen atoms to form a predominately 1,7-isomer (with trace amounts of the 1,6-isomer) and a propyl chain attached to each of the sulphur atoms – the DP-PTCDI molecule is discussed in more detail in Section 4.3.2 of Chapter 4. The synthesis of this molecule is detailed in Reference [98]. DP-PTCDI adsorbed on the BN/Rh(111) surface showed similar results to PTCDI on the same surface;

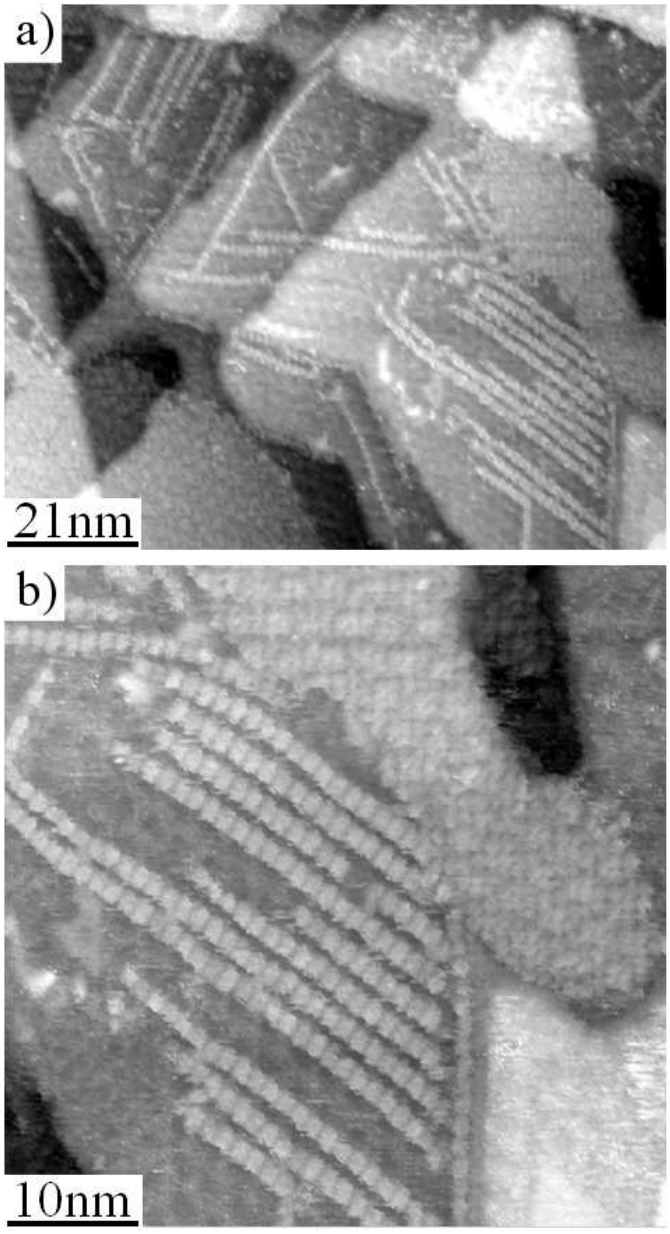

Figure 5.19: (a) STM image of PTCDI adsorbed on the g/Rh(111) surface and (b) a smaller scan STM image of the same area of the surface. Close-packed islands of PTCDI extend over step edges of the g/Rh(111) surface and commensurate rows of PTCDI were also visible, extending from the close-packed islands. Imaging parameters (a) V_{bias}= -1.0 V, I_t= 100 pA, (b) V_{bias}= -1.0 V, I_t= 100 pA.

trapped molecules in the pores of the network and 2D close-packed islands [96]. Previous investigations of DP-PTCDI on a Ag-Si(111) $\sqrt{3} \times \sqrt{3}$R30° surface revealed both dimer and trimer junctions were formed [98]. Figure 5.20 shows the DP-PTCDI dimer bonding junction and trimer bonding junction.

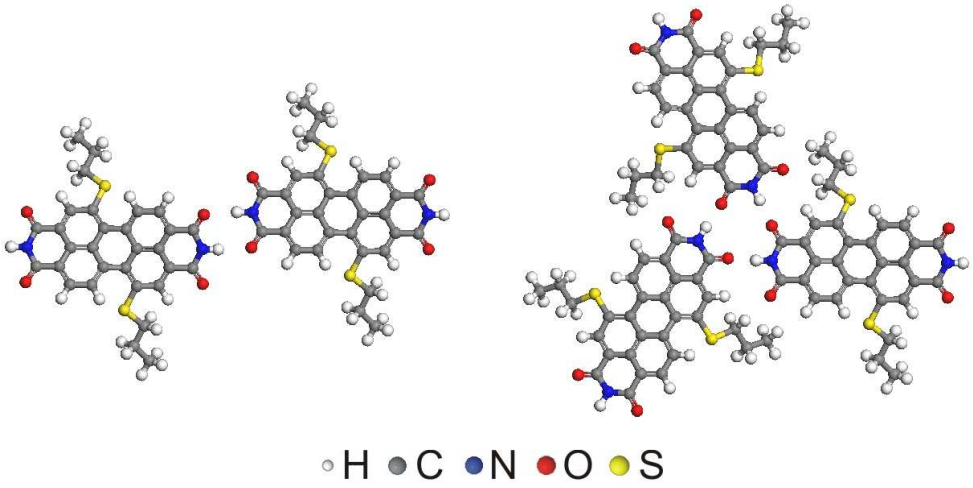

Figure 5.20: DP-PTCDI dimer and trimer junctions stabilised by hydrogen-bonding.

Figure 5.21 shows an STM image of DP-PTCDI molecules adsorbed on the g/Rh(111) surface. Similar to the adsorption of PTCDI, commensurate rows of DP-PTCDI molecules were formed. However, there were fewer examples of pairs of parallel rows for adsorbed DP-PTCDI molecules and trimer junctions were also observed.

Figure 5.22 shows a smaller scan size STM image of DP-PTCDI molecules on the g/Rh(111) surface where the double-lobe contrast of the DP-PTCDI molecules was resolved. Thus the two different types of hydrogen-bonded DP-PTCDI junctions were clearly revealed as the orientations of the molecules were observed. The ratio of dimer:trimer junctions (as shown schematically in Figure 5.20) was approximately 75:25 when consulting STM images of DP-PTCDI on the g/Rh(111) surface. This was in contrast to PTCDI where $\geq$ 99% of the junctions observed were dimers.

Annealing DP-PTCDI on Graphene

After imaging the adsorbed DP-PTCDI molecules on the g/Rh(111) sample, the sample was annealed to approximately 300°C. 2D close-packed DP-PTCDI

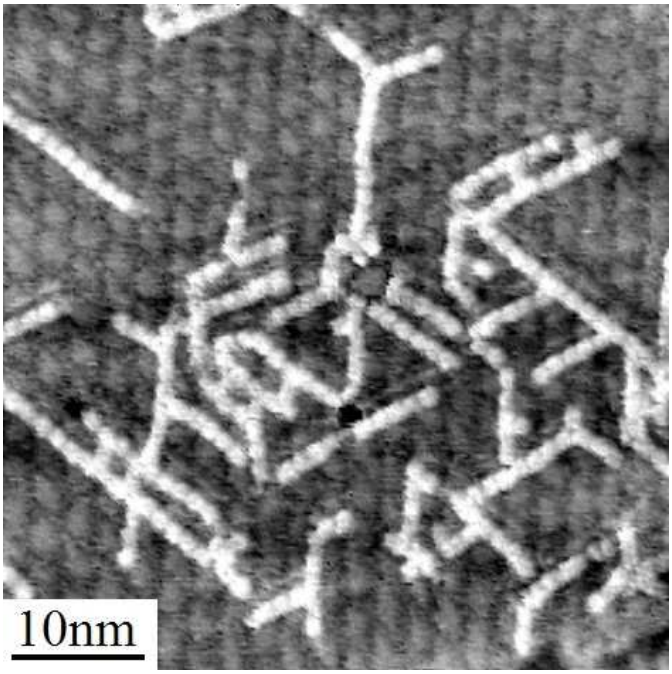

Figure 5.21: An STM image of DP-PTCDI molecules adsorbed on a g/Rh(111) surface. Commensurate rows of DP-PTCDI molecules were observed although they were shorter than their PTCDI counterparts and there were less rows that ran parallel to each other. Trimer junctions were also observed on the Moiré superstructure. Imaging parameters V_{bias}= 1.0 V, I_t= 100 pA.

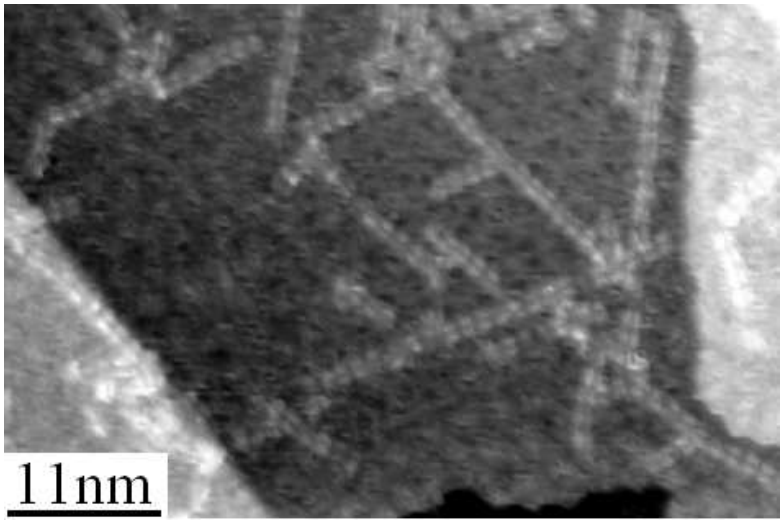

Figure 5.22: Small scan size STM image of DP-PTCDI molecules adsorbed on the g/Rh(111) surface. The double-lobe contrast of the DP-PTCDI molecules was resolved and thus so were the orientations of the molecules. Imaging parameters V_{bias}= -1.0 V, I_t= 150 pA.

islands were formed, as was the case for adsorbed PTCDI on the g/Rh(111) surface. Figure 5.23 shows a large area STM image of the g/Rh(111) surface after DP-PTCDI adsorption and subsequent annealing. There were many examples of close-packed islands on the surface but no commensurate rows of DP-PTCDI molecules were imaged with STM after the annealing process. Although no intermediate row formation was observed for DP-PTCDI adsorption, this could be attributed to unfortunately not imaging any areas of the surface where both rows and islands were present. It is not known whether DP-PTCDI molecules formed close-packed islands more readily than PTCDI molecules or if the DP-PTCDI molecules in this case had received more energy through the annealing process due to the inaccuracy of the temperature measurement. Figure 5.23 shows how the Moiré pattern of the graphene monolayer was imaged within the DP-PTCDI close-packed island structure using STM.

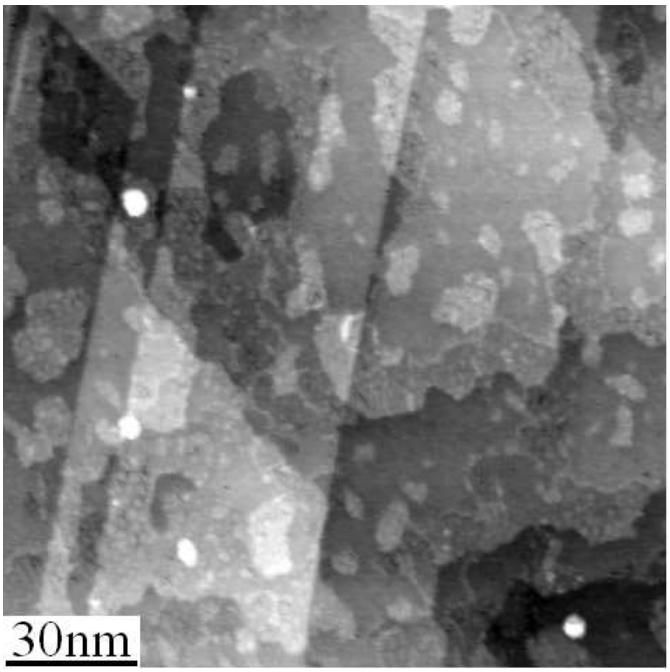

Figure 5.23: An STM image of DP-PTCDI adsorbed on the g/Rh(111) surface after annealing. Several DP-PTCDI close-packed islands were observed. Imaging parameters V_{bias}= -1.0 V, I_t= 150 pA.

Figure 5.24 shows three examples of smaller scan STM images of the DP-PTCDI islands on the g/Rh(111) surface. Similar to the formation of PTCDI islands on the same surface, DP-PTCDI molecular dimer junctions formed close-packed islands. From Figure 5.19b, the islands followed the direction of the Moiré pattern of the graphene monolayer underneath the DP-PTCDI island. Although

the Moiré superstructure was not observed in all three STM images in Figure 5.24, there appeared to be a directional nature to the growth of the islands because the islands became rod-like. This was not as apparent for PTCDI molecules on the same surface, but PTCDI islands formed on graphite were also rod-like [95]. The formation of DP-PTCDI islands on the Ag-Si(111) $\sqrt{3} \times \sqrt{3}$R30° surface also revealed a directional nature. The DP-PTCDI islands shown in Figure 5.24 were smaller in surface area than the islands observed for PTCDI adsorption and the DP-PTCDI islands may have lost their overall directional nature if they had increased in size due to further deposition. However, the preference of the islands to expand along one axis rather than the other may have been due to the DP-PTCDI side chains governing the initial island growth.

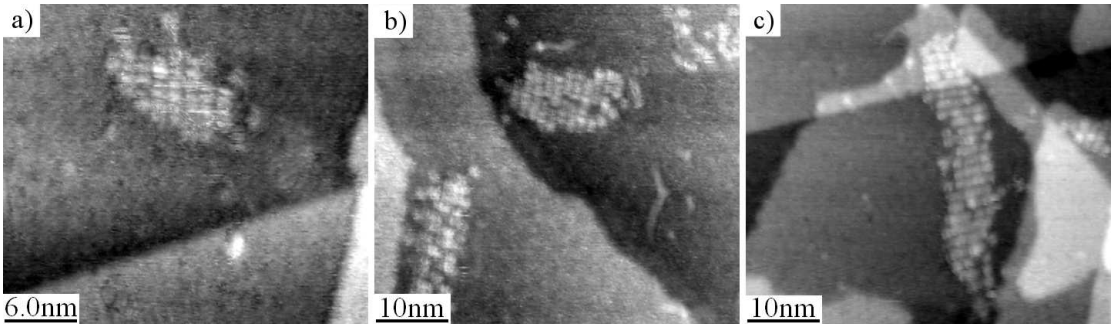

Figure 5.24: Post-anneal STM images of DP-PTCDI adsorbed on three separate areas of a g/Rh(111) surface. Imaging parameters (a) and (b) V_{bias}= -1.0 V, I_t= 100 pA, (c) V_{bias}= -1.0 V, I_t= 300 pA.

5.2.3 DB-CTCDI Adsorption

To investigate how longer molecular side chains affected the structures formed on the g/Rh(111) Moiré superstructure, dibutyl-coronene tetra-carboxylic diimide (DB-CTCDI) was adsorbed on the graphene surface. Deposition was performed with a Knudsen cell operating at 400°C, producing a molecular deposition rate of $\sim 3 \times 10^{-3}$ MLmin^{-1}. DB-CTCDI was a coronene derivative containing carboxylic and imide groups that enabled hydrogen-bonding between molecules, attached butyl alkane chains produced a predominantly 1,7-isomer. The core of the DB-CTCDI molecule was therefore larger than a PTCDI or DP-PTCDI molecular core, but more importantly, the length of the DB-CTCDI side chains were longer than the DP-PTCDI side chains. The synthesis of DB-CTCDI is detailed in the Supplementary Information of Reference [102] – unlike PTCDI and DP-PTCDI, the deposition of DB-CTCDI molecules had not been previously studied on other

surfaces. Figure 5.25 shows a single DB-CTCDI molecule and also the structure of a theoretical DB-CTCDI trimer junction stabilised by hydrogen-bonds.

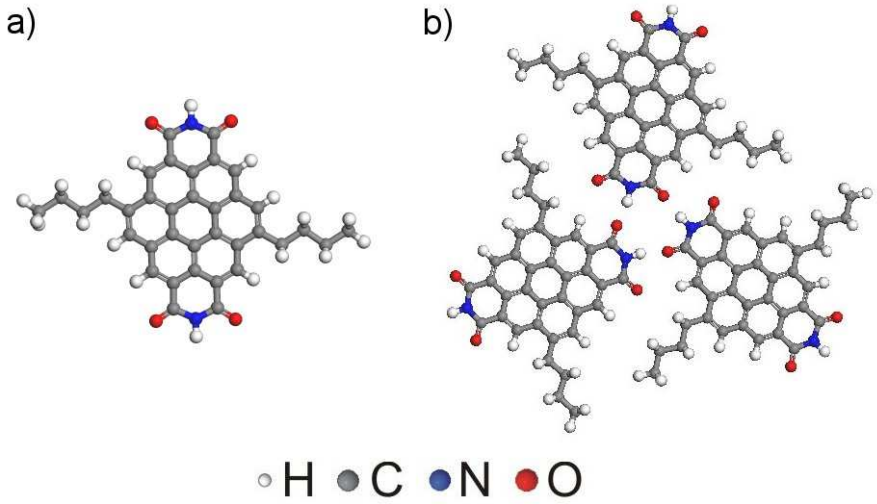

Figure 5.25: (a) the DB-CTCDI molecule and (b) the hydrogen-bonded DB-CTCDI trimer junction.

For DB-CTCDI molecules adsorbed on a g/Rh(111) surface, the formation of trimer junctions dominated the observed molecular arrangements, as shown in Figure 5.26. It was not possible to identify unambiguously any DB-CTCDI linear dimer junctions. The array of trimers resulted in a honeycomb arrangement of molecules which was aligned with the graphene monolayer superstructure and enclosed the areas of centre-moire areas of the graphene monolayer. Figure 5.27 shows an STM image resolving both the DB-CTCDI network and the Moiré pattern, revealing the alignment of the trimer junctions with the Moiré pattern.

The STM images in this section were obtained with the Nanograph STM-01 system in the same UHV system where the sample was prepared unless otherwise specified. However, the STM images in Figures 5.27 and 5.29 were acquired using an STM supplied by *WA Technology* after transferring the sample to a separate UHV system through ambient conditions. The samples were annealed to ∼550°C for an hour and then annealed at ∼800°C for 20 min to remove physisorbed material.

From the STM image in Figure 5.27, the trimer junctions of DB-CTCDI (and therefore the trimer junctions of DP-PTCDI) were positioned at the Moiré superstructure intersections, as were the commensurate rows of PTCDI molecules. The placement of the DB-CTCDI molecules on the Moiré superstructure is modelled in Figure 5.28.

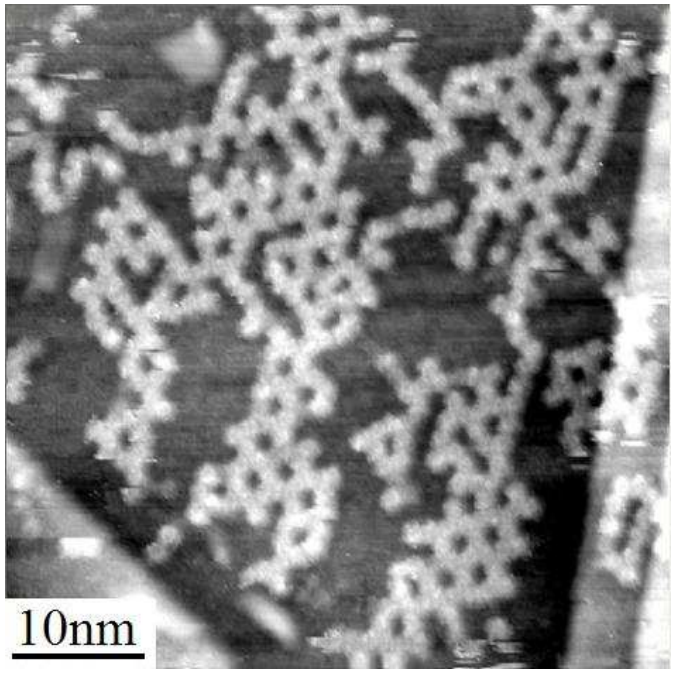

Figure 5.26: STM image of DB-CTCDI molecules adsorbed on the g/Rh(111) surface. Trimer junctions are formed leading to a hexagonal network on the Moiré superstructure. Imaging parameters V_{bias}= 1.0 V, I_t= 100 pA.

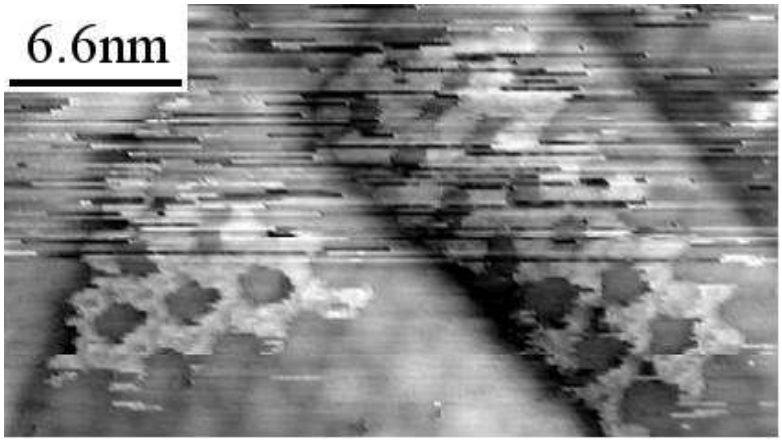

Figure 5.27: STM image of a DB-CTCDI hexagonal network aligned with the Moiré superstructure of the g/Rh(111) surface. Image acquired using an STM supplied by *WA Technology*, imaging parameters V_{bias}= 1.5 V, I_t= 50 pA.

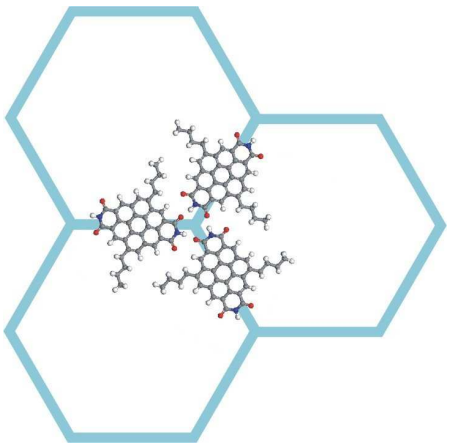

Figure 5.28: Model of DB-CTCDI trimer junctions positioned at the intersections of the Moiré superstructure.

The trimer junction of the honeycomb network was clearly observed in a higher resolution STM image shown in Figure 5.29a, where breakages were also seen in the hexagonal arrangement of the DB-CTCDI molecules.

The trimer junction for both the DB-CTCDI and DP-PTCDI molecules was intrinsically chiral because the attachment of alkane chains to DP-PTCDI and DB-CTCDI leads to a surface-induced chirality [103]. An image of the DB-CTCDI network shown in Figure 5.29b confirmed that the molecules were in a chiral arrangement, specifically the bright intramolecular features formed a hexagon with an axis of symmetry rotated with respect to the principal axes of the molecular network (which were parallel to those of the graphene superstructure). Both

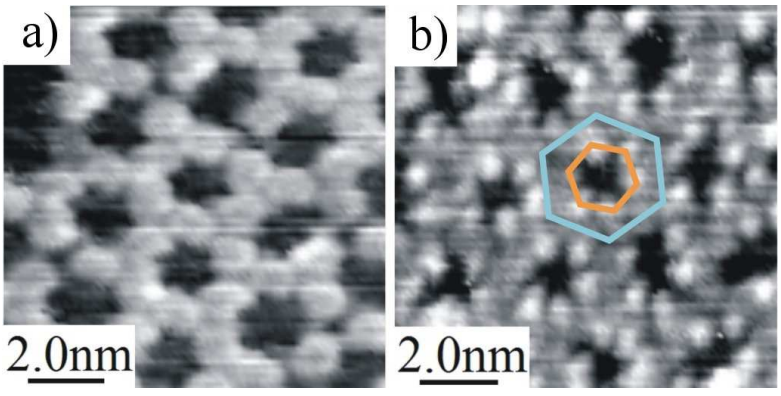

Figure 5.29: (a) higher resolution STM image of a DB-CTCDI hexagonal network on a g/Rh(111) surface and (b) the chirality in the honeycomb network. Images acquired using an STM supplied by *WA Technology*, imaging parameters (a) V_{bias}= 1.5 V, I_t= 50 pA, (b) V_{bias}= -1.5 V, I_t= 50 pA.

chiralities have been observed with average domain sizes of ∼30 nm.

5.2.4 Molecular Adsorption Comparison

The presence of alkyl side-chains was known from previous studies of DP-PTCDI to enhance the stability of a chiral molecular trimer vertex (illustrated in Figure 5.20) as compared with the linear hydrogen-bonded PTCDI-PTCDI junctions [104]. A comparison of Figures 5.14, 5.21 and 5.26 indicates a progressively enhanced stabilisation of a trimer vertex as the alkyl chain length increased from zero length (PTCDI) through to the longest chain (DB-CTCDI). This led to a change in morphology from the rows, for PTCDI, through to the honeycomb DB-CTCDI, with the DP-PTCDI being considered as an intermediate case where linear segments co-existed with junctions of three molecules. The junctions formed and their positions relative to the Moiré superstructure are summarised in Figure 5.30 for each of the three molecules.

The enhanced stability of the trimer vertex for molecules with longer alkane chains was supported by calculations performed using density functional theory (DFT) – all DFT calculations detailed in this thesis were performed by N. Smith and A. Saywell. The molecules were modelled in the gas phase, with the substrate not included in the calculations. Further details on the DFT calculations can be found in the Supplementary Material of Reference [102]. The results of the DFT calculations are shown in Table 5.1, which reveals that the greatest difference between trimer and dimer binding energies was predicted for DB-CTCDI. These data also indicate that, in the gas phase, the trimer was more stable for DP-PTCDI and even for PTCDI. Overall the stability of the trimer junction increased as the alkyl chain length increased, which was observed in the STM images.

Also tabulated in Table 5.1 are the calculated separations of the intermolecular junctions. For dimers formed from all of the molecules investigated the calculated equilibrium separation was very close (within 0.03 nm) to $a_m/2$ (the observed spacing of molecules in the commensurate rows was 1.47±0.03 nm). However, the predicted separation for intermolecular trimer junctions (shown in Table 5.1) was significantly lower (by up to 0.1 nm) than their expected separation in an extended array, $a_m/\sqrt{3}$ (1.70 nm). Thus, it is believed that these junctions were strained in an extended honeycomb array, leading to a reduced binding energy, and accounting for the stability of dimer rows for the two molecules PTCDI and DP-PTCDI, whilst only the molecule with the strongest predicted trimer junction, DB-CTCDI, formed a honeycomb array. There were also clear gaps between

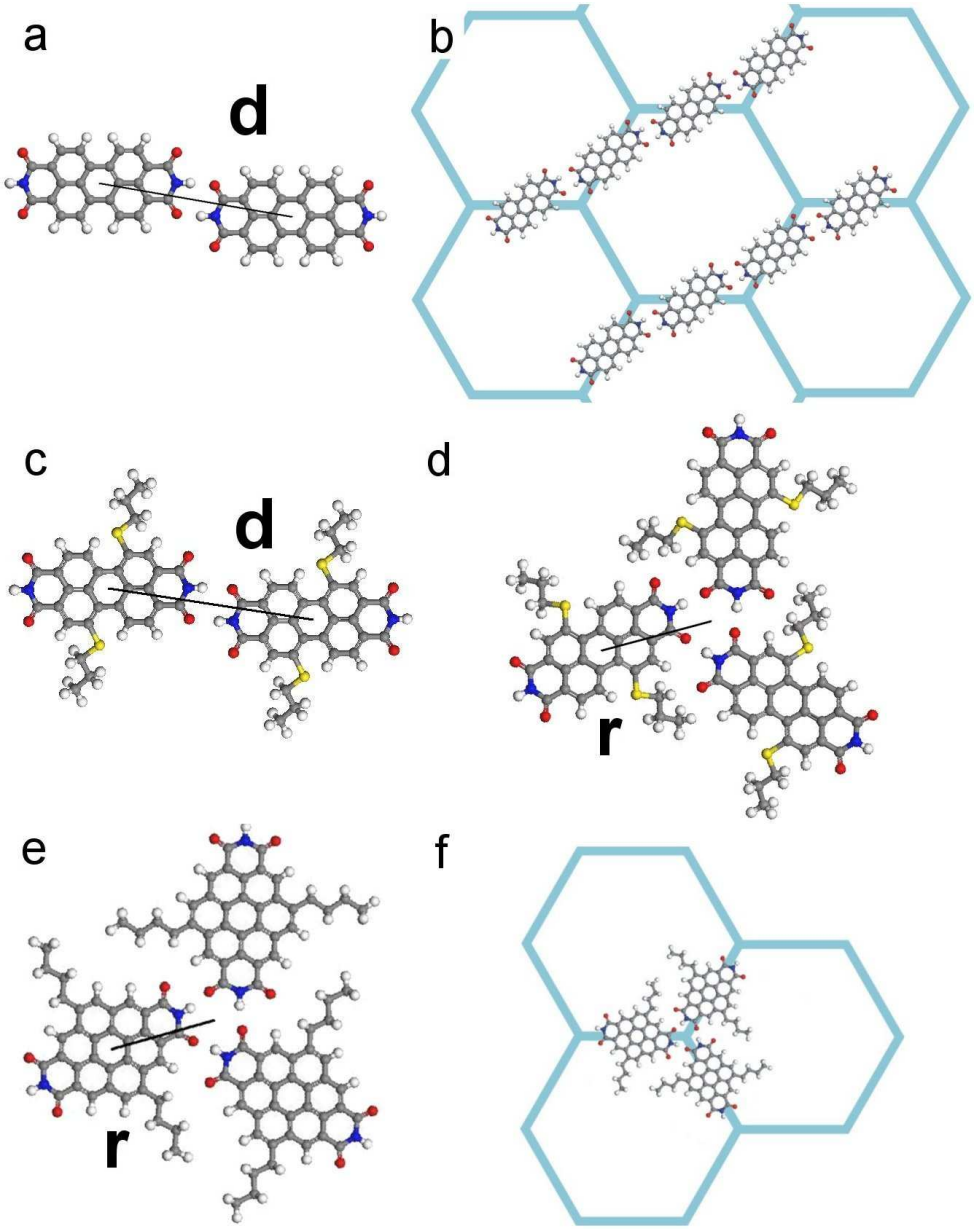

Figure 5.30: Schematics of the PTCDI dimer junction (a), the resulting PTCDI commensurate rows (b), the DP-PTCDI dimer junction (c), the DP-PTCDI trimer junction (d), the DB-CTCDI trimer junction (e) and the positioning of the DB-CTCDI molecules (f), all formed on the Moiré superstructure of the g/Rh(111) surface. The distance between molecules for dimer bonding, d, and distance from the centre of the trimer vertex to the centre of a molecule, r, is also shown.

	E^d_{HB} (eV)	d (nm)	E^t_{HB} (eV)	2r (nm)	E^t_{HB}-E^d_{HB} (eV)
PTCDI	0.46	1.44	0.52	1.61	0.06
DP-PTCDI	0.46	1.45	0.57	1.63	0.11
DB-CTCDI	0.45	1.44	0.57	1.60	0.12

Table 5.1: Binding energies for PTCDI, DP-PTCDI and DB-CTCDI dimer (E^d) and trimer (E^t) junctions calculated using DFT. The dimer and trimer lengths, d and r (as depicted in Figure 5.30), are also calculated. The difference in energies for the dimer and trimer junction for each molecule are also shown.

some of the DB-CTCDI trimers that formed the honeycomb networks, shown in Figure 5.29, further evidence of strain arising from a small mismatch between superstructure and molecular dimensions for the trimer array. This may also account for how molecules were able to sit in neighbouring rows but did not appear to be hydrogen-bonded.

The van der Waals contributions to the interaction energies of the proposed dimer and trimer junctions – that were calculated using DFT – for the three different molecules were also investigated and are discussed in the Supplementary Information of Reference [102]. Briefly, the van der Waals interaction led to slightly higher energies ($\sim$0.2 eV) for trimer junctions involving molecules with side chains, with an increase in energy as the side chain length increased. Thus the trends observed in the DFT results in Table 5.1 – where only hydrogen-bonding energies were taken into account – were further enhanced by the van der Waals interaction.

The STM images of the three adsorbed molecules on the g/Rh(111) surface clearly show that the adsorbed molecules experienced a local potential due to the graphene superstructure which was sufficiently strong to inhibit the formation of two-dimensional islands. The origin of this potential has recently been discussed by Brugger et al. [29] who showed that variations in work function for both graphene and boron nitride monolayers on Ru(0001) led to a periodic potential – also discussed by Dil et.al. [26] for the BN/Rh(111) surface. For graphene on Ru(0001)

the energy minima were shown to form a honeycomb network around a repulsive core at the high symmetry points of the Moiré superstructure. The placement of molecules observed on g/Rh(111) is in excellent agreement with the observations and predictions by Brugger et. al. [29]. The molecules were preferentially adsorbed at the edge-moire areas of the graphene monolayer and were thus positioned on the Moiré superstructure lattice as shown in Figure 5.30.

A distinguishing feature of the adsorption of these three molecules on the g/Rh(111) surface is the observation that the trapping potential was sufficiently compliant to allow the molecules to relax and adopt a local configuration, which was controlled by interactions with molecules trapped in neighbouring energy minima, so that extended, connected structures were formed. The formation of the molecular rows was determined by intermolecular interactions but the placement and separation of the rows was guided by the underlying level of organisation of the Moiré pattern. The control of row separation is shown in Figure 5.14 and more clearly for a higher molecular coverage in Figure 5.17 (the coverage was close to two molecules per unit cell of the Moiré superstructure) where it was clearly observed that the surface was covered with regularly spaced molecular rows separated by $\sqrt{3}\mathrm{a}_m/2$.

This insight also raises interesting questions in relation to graphene electronics. Recent papers have demonstrated that molecules can act as molecular dopants [105] and also that the superstructure arising from a Moiré pattern of graphene grown on Ir(111) gives rise to the formation of a band-gap [106] raising interesting connections with the self-assembled molecular structures detailed here. The interplay between the characteristic dimensions arising from graphene growth and molecular ordering offer many possible routes for further investigation related to both the electronic properties of graphene as well as the formation of complex self-assembled structures.

5.2.5 PTCDI and DB-CTCDI Co-Adsorption

Once the side chain length dependence of the molecular bonding junctions had been established, the adsorption of both PTCDI and DB-CTCDI on the same g/Rh(111) surface was investigated. The resulting network formation was found to be a mixture of both rows and honeycomb arrangements, seemingly from the mixture of PTCDI and DB-CTCDI molecules bonding with each other in both dimer and trimer formations. Figure 5.31 shows a small scan size STM image of the g/Rh(111) surface after deposition of both PTCDI and DB-CTCDI molecules.

Both dimer and trimer junctions are clearly observed, aligned with the underlying Moiré superstructure as was previously the case for individual depositions of each molecule.

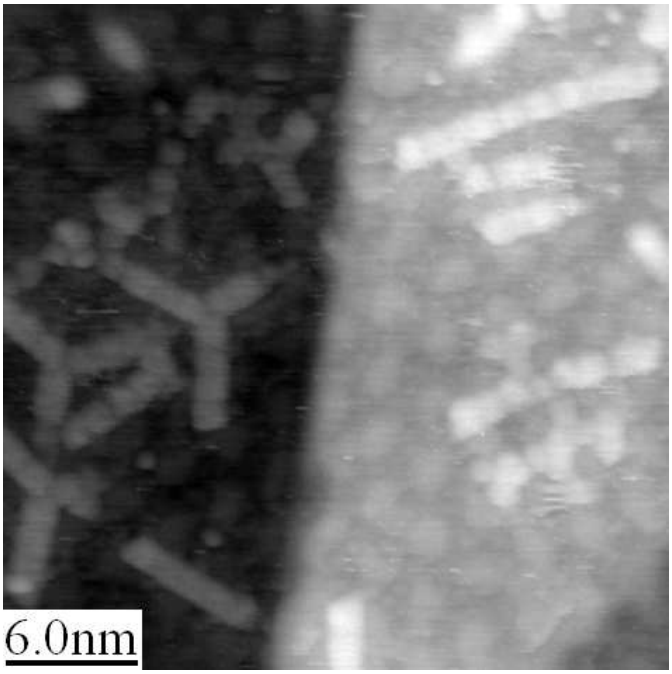

Figure 5.31: STM image of PTCDI and DB-CTCDI molecules adsorbed on a g/Rh(111) surface, both dimer and trimer junctions are observed. Imaging parameters V_{bias}= -1.0 V, I_t= 200 pA.

Although the surface bears similarities to DP-PTCDI adsorption on the same surface, the adsorption of both PTCDI and DB-CTCDI allows the resulting dimer to trimer ratio to be controlled by the corresponding Knudsen cell deposition times rather than relying on the synthesis of molecules with varying length side chains. For this investigation of PTCDI and DB-CTCDI, the occurrence of trimers was greater than for DP-PTCDI adsorption. The resulting nanostructures were composed of separate honeycomb sections and commensurate rows that then appeared to bond together as the surface coverage was increased. Figure 5.31 also shows several instances of a single trimer centrally located between three commensurate rows, this was observed with greater frequency than for DP-PTCDI. The STM images in Figure 5.32 show other structures formed after the PTCDI and DB-CTCDI depositions, including when two commensurate rows were attached by their ends with trimer junctions. However, this type of structure, although interesting in terms of possible properties, was not abundant across the sample.

The structures observed in Figures 5.31 and 5.32 may have been formed by a

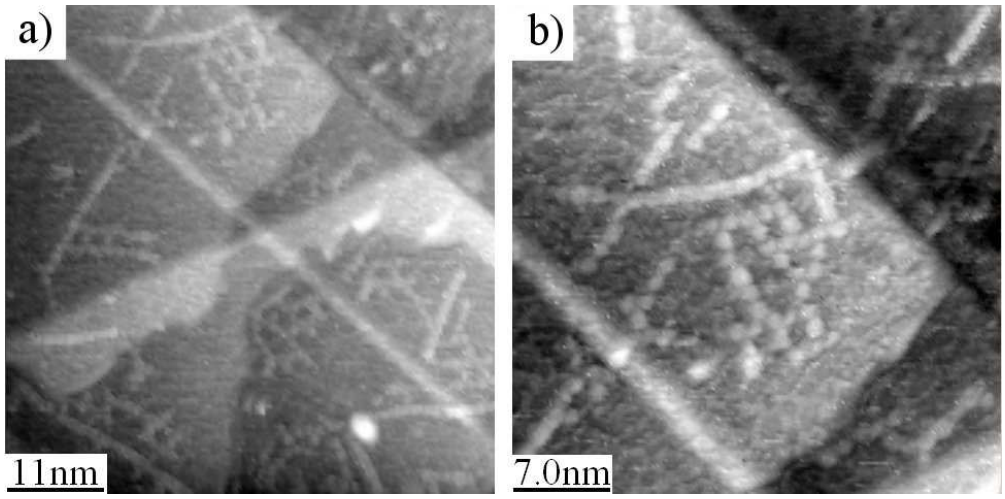

Figure 5.32: STM images of PTCDI and DB-CTCDI molecules adsorbed on a g/Rh(111) surface. Imaging parameters (a) and (b) V_{bias}= -1.0 V, I_t= 150 pA.

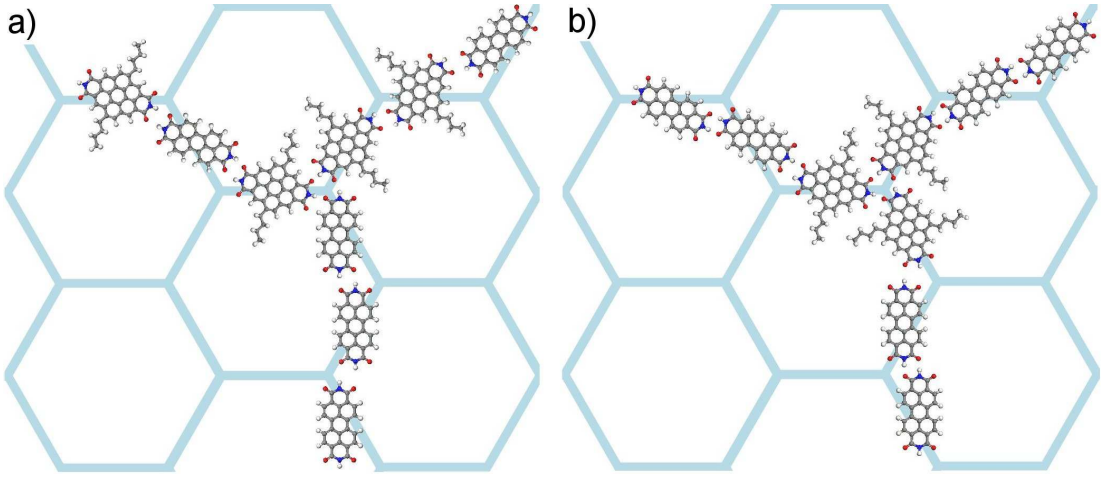

Figure 5.33: Possible placements of PTCDI and DB-CTCDI molecules in terms of Figure 5.32, (a) where a mixture of DB-CTCDI and PTCDI from both a trimer and several dimer configurations and (b) where DB-CTCDI forms a trimer and PTCDI molecules bond in dimer configurations, branching from the central trimer.

mixture of PTCDI and DB-CTCDI molecules (as shown in Figure 5.33a) or by selective bonding on the surface, that is, PTCDI-PTCDI bonding as well as DB-CTCDI bonding with other DB-CTCDI molecules, as shown in Figure 5.33b. The structure in Figure 5.33b, could have been created by different sections of either dimer or trimer bonding that extended across the surface until the sections interact with other sections. However, it was not conclusive that the dimer junctions involved only PTCDI molecules and the trimer bonding was only due to DB-CTCDI molecules, as the STM system could not resolve the side chains of the coronene derivative. Further experiments are required with a greater resolution STM system whilst also varying the deposition ratio of PTCDI and DB-CTCDI. For this experiment, PTCDI and then DB-CTCDI was deposited on the surface, therefore adsorbing the molecules in reverse order may also lead to interesting results.

After performing STM, the sample was annealed at ∼300°C. STM imaging after the anneal revealed there were no molecular rows on the surface, however the exact nature of the resulting formations could not be determined. Honeycomb network islands were found, but whether these islands were purely composed of DB-CTCDI molecules or both DB-CTCDI and PTCDI molecules was unknown. Although close-packed islands were observed in one instance there were other areas of indistinguishable structure. The PTCDI and DB-CTCDI molecules may have segregated to form different types of molecular islands as well as creating a chaotic structure - due to both PTCDI and DB-CTCDI molecules forming both dimer and trimer bonds in a pseudo close-packed arrangement. However, without the study of purely DB-CTCDI molecules after an annealing cycle these results were difficult to determine and would need further experiments with an STM system of improved resolution to be conclusive.

5.2.6 C_{60} Adsorption

The adsorption of buckminsterfullerene, C_{60}, onto the g/Rh(111) surface was also investigated, using a Knudsen cell operating at 399°C with a deposition rate of $\sim 8\times10^{-3}$ MLmin^{-1}. One of the differences between the C_{60} molecule and the previous perylene and coronene derivatives was the lack of imide groups and thus there was no hydrogen-bonding between the C_{60} molecules. There have been many studies of C_{60} adsorption on many different surfaces, but of particular relevance to the g/Rh(111) surface was the investigation of C_{60} on the HOPG surface [107] and on the graphene/SiC 'nanomesh' (g/SiC) [108]. In both cases 2D close-packed

islands of C_{60} were formed on the surface. It was found that the fullerene formed circular islands on the HOPG surface [107] due to the minimal adsorbate-substrate interaction allowing a substantial mobility of the C_{60} molecules. In the case of the g/SiC surface, the islands were found to be irregular in shape which is attributed to the higher diffusion barrier for a graphene sheet with a periodic corrugation compared to the flat HOPG surface [108].

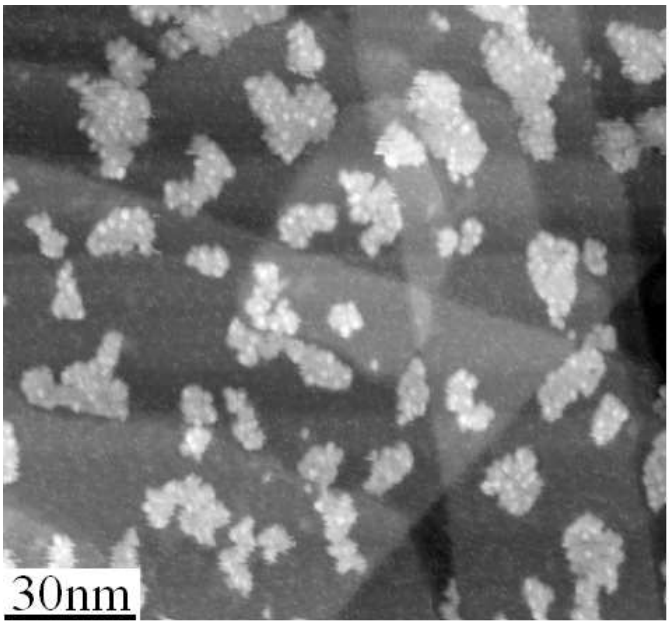

Figure 5.34: STM image of C_{60} molecules adsorbed on the g/Rh(111) surface, many instances of irregular shaped 2D islands are observed. Imaging parameters V_{bias}= -1.2 V, I_t= 50 pA.

Figure 5.34 shows an STM image of approximately 30% coverage of C_{60} on the g/Rh(111) surface, where irregular shaped 2D islands of C_{60} were observed. This was relatively unsurprising as similar results were observed for the g/SiC surface which also displayed a Moiré pattern due to the graphene layer, although with a smaller periodicity of 1.85 nm [108].

Figure 5.35 shows smaller scan size STM images of C_{60} 2D islands, where the close-packed formation of the C_{60} was observed. The fullerene islands were contacting the sides of step edges in the vast majority of cases as per a diffusion-limited aggregation. From Figure 5.35a, there were several directions of C_{60} rows observed within a 2D island, this is understood by the $14° \pm 2°$ lattice mismatch of some C_{60} rows, as shown in Figure 5.35b. There were many instances of C_{60} islands with orientations matched with the Moiré superstructure (as revealed by a C_{60} island in the bottom of Figure 5.35b), therefore neighbouring islands with different

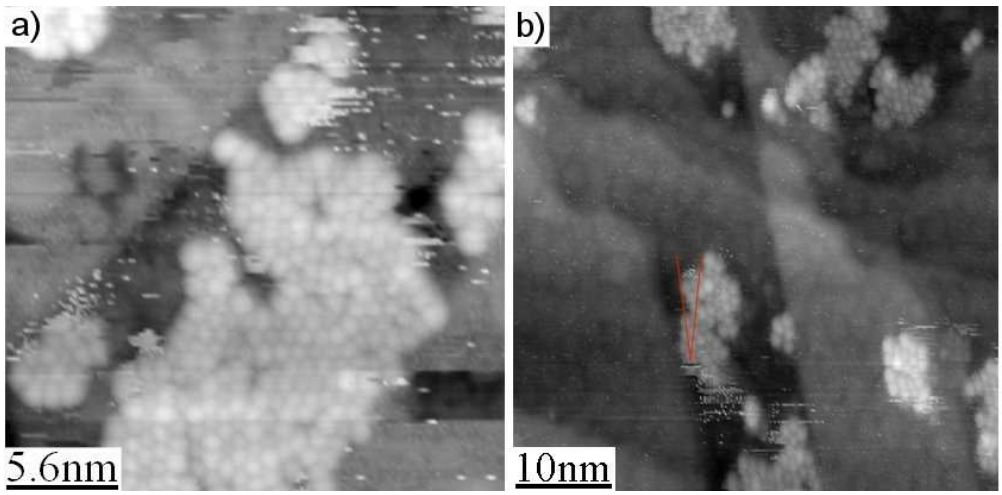

Figure 5.35: STM imaging of C_{60} molecules adsorbed on the g/Rh(111) surface, the close-packed arrangement of the C_{60} within the islands is observed. (a) shows different orientation domains within the C_{60} island, while (b) reveals a mismatch between the Moiré superstructure and the orientation of some C_{60} islands. Imaging parameters (a) V_{bias}= -1.0 V, I_t= 100 pA, (b) V_{bias}= -1.2 V, I_t= 50 pA.

orientations – with respect to the underlying superstructure – may have grown and merged to produce the larger multi-domain island observed in Figure 5.35a. The major difference between the structures formed by the perylene and coronene derivatives and the C_{60} molecules was that the C_{60} molecules were positioned on both the centre- and edge-moire areas of the graphene monolayer. PTCDI, DP-PTCDI and DB-CTCDI formed directional structures according to the edge-moire areas of the graphene and could only form close-packed islands once the sample was annealed. C_{60} did not bond directionally due to the lack of hydrogen-bonding and seemingly diffused more readily over the surface allowing the C_{60} molecules to form close-packed islands without any annealing of the substrate. This mobility of the adsorbed C_{60} influenced the acquisition of STM images and probably accounted for the 'streaking' associated with mobile particles on the surface, as seen in Figure 5.35 and later C_{60} STM images.

C_{60} and PTCDI/DB-CTCDI Adsorption

C_{60} co-adsorption on a graphene monolayer already patterned with an organic molecule was the final investigation for the g/Rh(111) surface. There have been many examples of host-guest architectures over the last few decades, including a more recent example of C_{60} deposited onto the PTCDI-melamine network [5], where the C_{60} molecules were found to become trapped in the pores of the PTCDI-

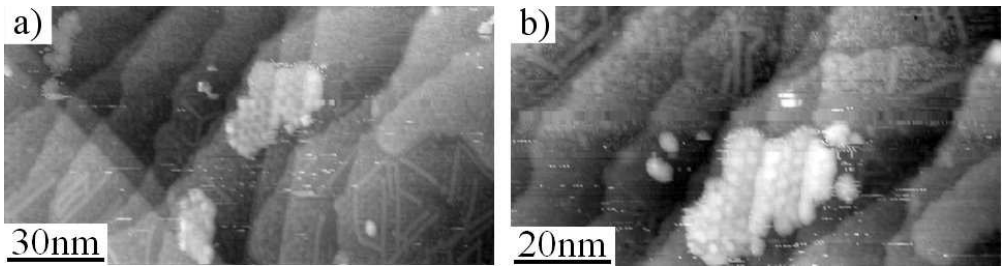

Figure 5.36: STM images of PTCDI and C_{60} adsorption on the g/Rh(111) surface. Imaging parameters (a) V_{bias}= -1.0 V, I_t= 150 pA, (b) V_{bias}= -1.0 V, I_t= 100 pA.

melamine network.

C_{60} was deposited onto a g/Rh(111) surface partially covered with PTCDI commensurate rows. The STM images in Figure 5.36 show that the C_{60} molecules did not interact with the PTCDI network but instead segregated and formed separate 2D islands. The PTCDI and C_{60} molecules behaved as they would have through individual adsorption on a g/Rh(111) surface, but in this case, on separate areas of the surface.

Figure 5.37 shows STM images of a g/Rh(111) surface after DB-CTCDI and then C_{60} had been deposited. A similar result to the PTCDI/C_{60} experiment was achieved, with separate DB-CTCDI honeycomb networks and C_{60} close-packed islands. Although the DB-CTCDI networks formed a network in which the C_{60}

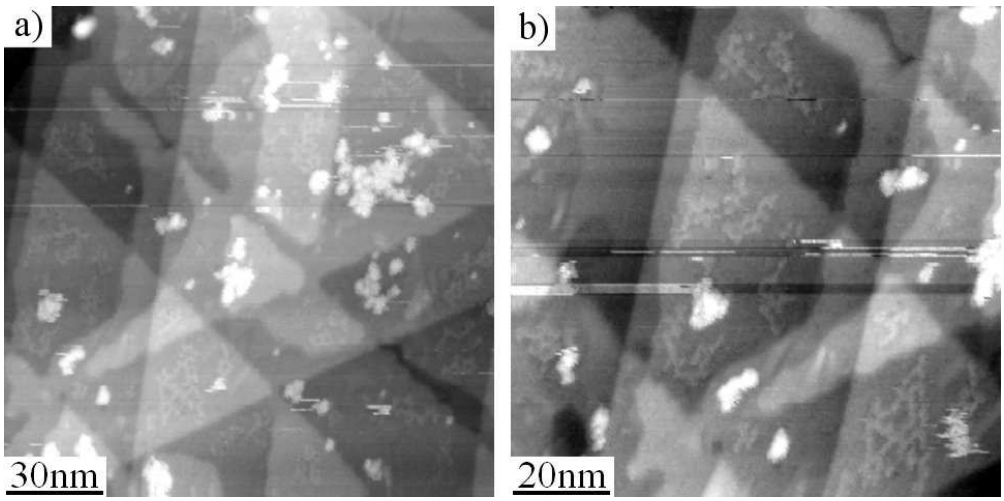

Figure 5.37: STM images of DB-CTCDI and C_{60} adsorption on the g/Rh(111) surface, where image streaking is observed due to the mobility of the C_{60}. Imaging parameters (a) V_{bias}= 1.0 V, I_t= 100 pA, (b) V_{bias}= 1.0 V, I_t= 100 pA.

molecules could be conceivably trapped within, the C_{60} molecules were not, instead aggregating together.

5.3 Summary

A novel method of forming a graphene monolayer on a Rh(111) thin film has been detailed. Instead of an in-situ UHV method of forming graphene on a transition metal, the Rh(111) thin film was immersed in a solvent before annealing in UHV conditions. A single graphene monolayer that covered the metal surface creating a Moiré superstructure was revealed, using several techniques including XPS, XPD, LEED, STM in ambient and UHV conditions, dynamic STM and AFM in UHV conditions. Exposure to propylene in UHV conditions achieved similar results to solvent immersion.

The subsequent adsorption of organic molecules in UHV conditions was also described. PTCDI, DP-PTCDI and DB-CTCDI were all separately deposited onto the g/Rh(111) surface to form hydrogen-bonded dimer or trimer molecular junctions. The length of the side chains of the perylene and coronene derivatives influenced the formation of either dimer or trimer junctions, producing commensurate rows or a honeycomb network respectively. PTCDI – with no side chains – formed commensurate rows, DB-CTCDI molecules – with the longest side chains – formed a hexagonal arrangement, whilst DP-PTCDI was an intermediate. The molecules were positioned on edge-moire areas of the graphene monolayer, that is, areas that were more strongly bound to the Rh(111) surface, at the (fcc,top) and (top,hcp) sites. The molecules experienced a local potential due to the graphene superstructure which was sufficiently strong to inhibit the formation of 2D islands unless the sample was annealed. The formation of the molecular rows was determined by intermolecular interactions but the placement and separation of the rows was guided by the underlying level of organisation of the Moiré pattern.

The adsorption of the buckminsterfullerene on the g/Rh(111) surface was also investigated. Unlike the previously described molecules, 2D close-packed islands were formed at room temperature. Possible host-guest architectures involving the perylene/coronene derivatives and the fullerene were also investigated but no such interaction was found, although further work on higher coverages of PTCDI and DB-CTCDI prior to the subsequent C_{60} deposition should be considered.

Higher coverages of individual depositions of each of the organic molecules could also be investigated to study the growth of more than one monolayer and if there is an effect caused by the underlying superstructure. Further FM-AFM and

force spectra studies could also be performed on the g/Rh(111) surface, as well as any adsorbed organic molecules.

Chapter 6

Graphene Formation on Ni Thin Films

Chapter 5 describes how graphene monolayers were formed on a Rh(111) thin film without the use of gaseous carbon-containing precursors. In this chapter, a route to the growth of graphene monolayers and their release and transfer to another substrate is detailed. Graphene was produced in UHV on a nickel thin film surface via carbon segregation from the bulk of the Ni and subsequently removed from the Ni thin film and isolated on an insulating surface. In-situ UHV-STM and ex-situ AFM imaging of the pre-transfer surface as well as XPS results are discussed. The release of the graphene from the Ni surface and subsequent optical microscopy, scanning electron microscopy (SEM), transmission electron microscopy (TEM) and Raman spectroscopy results are also detailed.

6.1 Graphene Formation Method

In common with recently published work [36, 39, 40] polycrystalline Ni thin films were used as scalable sacrificial substrates. These substrates were Ni thin films deposited onto a 10 mm $\times$ 10 mm section of Si(100) wafer with a 300 nm thick SiO_2 layer. The Ni thin films were deposited onto the SiO_2 substrate using two different systems.

The original method of Ni deposition was thermal sublimation in a commercially available Edwards Auto 306 evaporator system (base pressure of $\sim 10^{-6}$ mbar), which produced 80-100 nm thick Ni films. The Ni thin films were then removed from vacuum and stored under atmospheric conditions for (typically) a few days. The samples were then inserted into the Nanograph STM-01 vacuum system (base

pressure of $\sim 5 \times 10^{-10}$ mbar).

The UHV system housing the Nanograph STM-01 system was later modified to allow Ni deposition within the UHV system itself, so that the Ni thin films were not exposed to ambient conditions before the formation of graphene. One of the Knudsen cells (described in Chapter 2) was replaced with a filament that was specially designed to house small Ni rods for UHV sublimation. Ni thin films of up to 100 nm were produced using this sublimation method and this type of in-situ Ni deposition provided greater control over the initial conditions of the Ni thin film.

The samples introduced to the UHV system were secured in the previously described Nanograph STM-01 UHV sample holder with an incorporated silicon strip heater. The SiO_2/Si(100) substrates included a modified tantalum contact that shielded part of the substrate from the Ni flux during deposition. Therefore no electrical contact was made between the Ni surface and the modified sample contact and thus the heater current would only flow through the silicon backing heater.

The samples were initially outgassed by annealing at 500°C (measured using a pyrometer) for ∼12-18 hours and the samples were then annealed at temperatures in the range of 500–800°C for 15 minutes. The samples were allowed to cool to room temperature after reducing the power to the silicon strip heater to zero over a period of approximately 1-2 min.

Propylene Dosing of Nickel Films

To investigate different methods of producing graphene formation on the Ni thin film surface whilst in UHV, sample dosing with propylene, C_3H_6 (99.95% purity), was performed after the sample had been annealed at temperatures ranging from 500°C to 800°C.

After the sample had been annealed (and imaged with STM if necessary) the sample was secured in the Nanomesh chamber yoke, which was sealed off from the other UHV chambers and pumped through a turbomolecular pump. The sample was annealed to 600°C and then the propylene leak valve was opened to produce a partial pressure of 1×10^{-6} mbar. The sample was dosed with propylene for 5 min and then the propylene leak valve was closed off and the current to the silicon strip heater reduced to zero over a period of approximately 1-2 min.

After the sample preparation process was finished, the Ni thin film surface was imaged with STM whilst still in the UHV system – this was the case for samples

that had been exposed to propylene or only annealed. The samples were then removed from the UHV system for further surface studies.

6.1.1 Nickel Surface Morphology Study

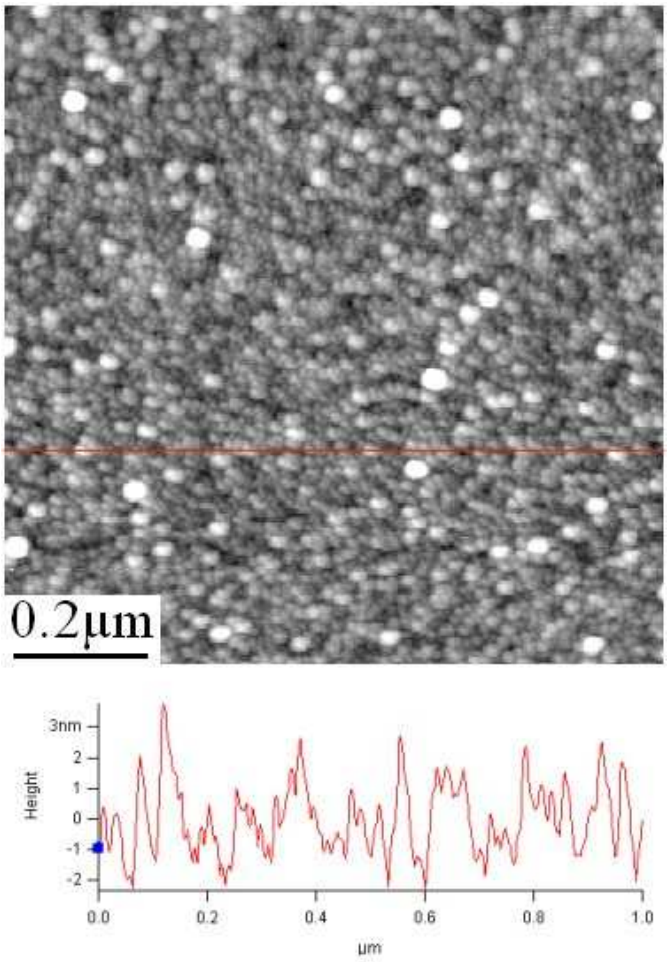

Figure 6.1: AFM image and associated line profile of an untreated Ni thin film on a SiO_2/Si(100) substrate in ambient conditions.

Figure 6.1 shows an ambient AFM image of the Ni thin film surface of a sample prepared in the Edwards system, which was removed to ambient conditions and then imaged before introduction to the Nanograph STM-01 UHV system for the graphene formation procedure. All ambient AFM imaging was performed with an Asylum Research MFP-3D system. Although the peak-to-peak roughness of the sample was only several nanometres, there were no flat areas or terraces found, and the average Ni grain size was only ∼20-30 nm.

The Nanograph STM-01 system was used to image the Ni thin film surface

whilst in UHV to investigate the surface morphology change in-situ. The films were imaged with STM after their initial outgassing at 500°C and for several annealing temperatures between 500°C and 800°C. After each sample was annealed and imaged with STM, it was then removed from the UHV system and imaged using an ambient AFM. STM and AFM imaging was also performed on samples dosed with propylene, however, there was no difference in surface morphology for dosed and undosed samples. Figure 6.2 shows an STM image of a Ni thin film surface after annealing at 500°C for ∼12-18 hours. All STM images in this chapter have been processed using WSxM software [90].

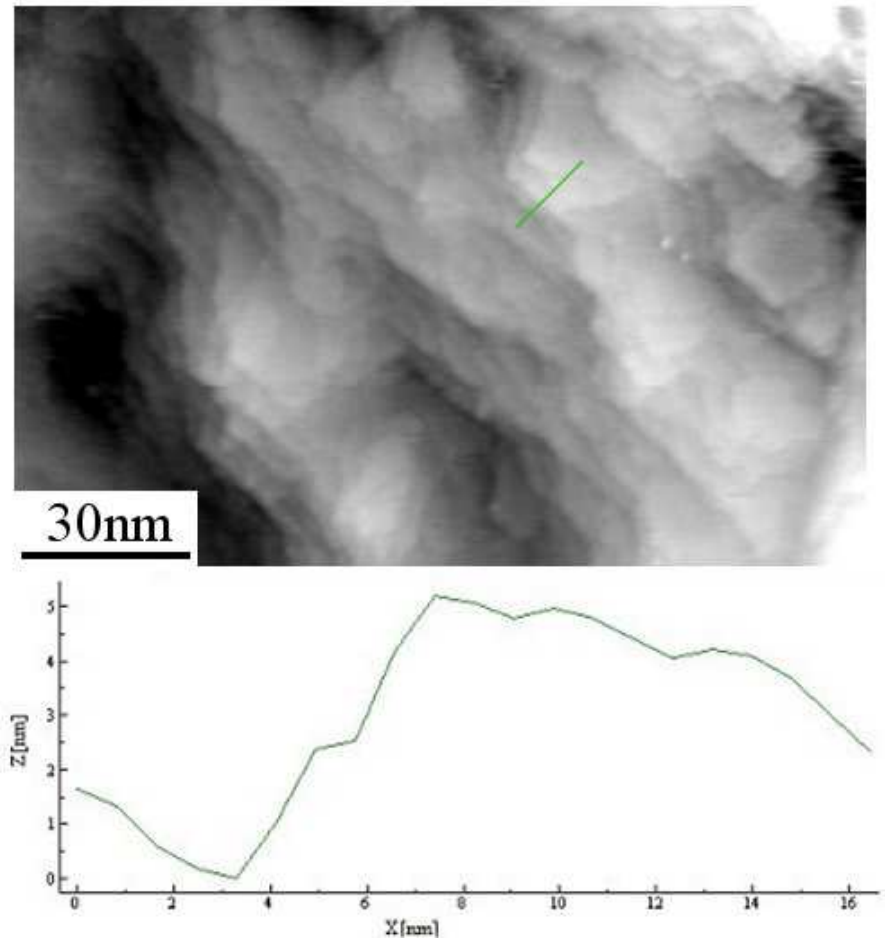

Figure 6.2: STM image of an outgassed Ni thin film on a SiO_2/Si(100) substrate, some small terraces can be seen with many step edges, as shown in the associated line profile. Imaging parameters V_{bias}= 1.0 V, I_t= 150 pA.

STM imaging of the Ni thin film after the initial outgassing of the sample revealed a rough surface, as shown in Figure 6.2, however there was a small amount of terraces observed with lateral sizes $\leq$ 10 nm. The surface primarily consisted

of step edges nanometres in size which created many steep slopes on the surface.

Figure 6.3 shows an ambient AFM image of a 500°C annealed Ni thin film – the change in surface morphology due to the anneal in UHV becomes apparent when comparing Figure 6.3 to Figure 6.1.

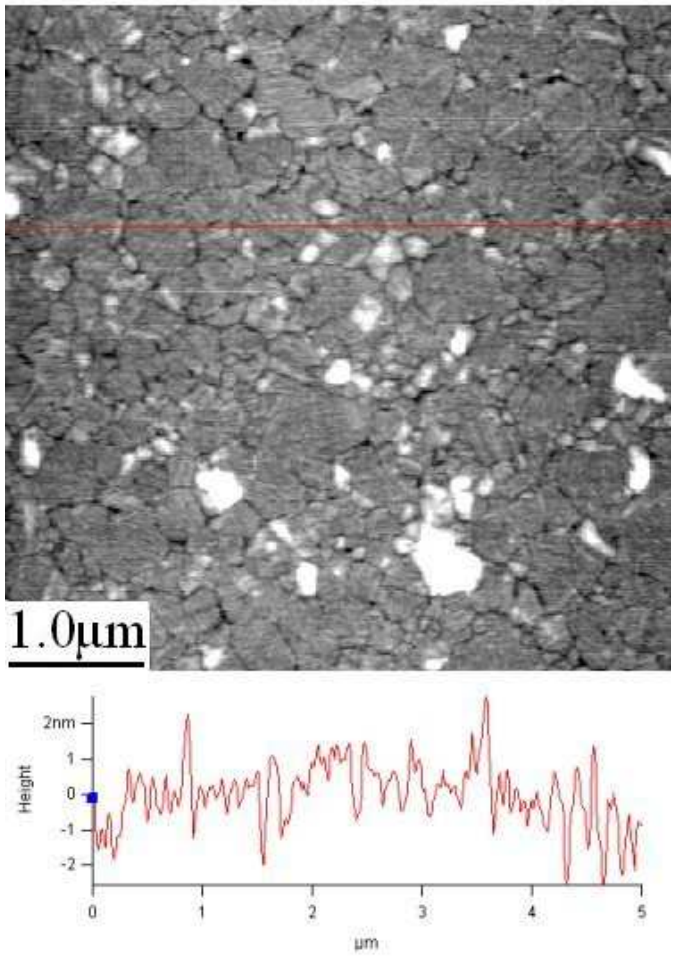

Figure 6.3: AFM image and associated line profile of an outgassed Ni thin film on a SiO_2/Si(100) substrate in ambient conditions.

When the Ni thin film was annealed at a higher temperature of 700°C the terraces on the surface observed with STM became larger, as shown in Figure 6.4. Terraces several tens of nanometres in length scale were observed but these terraces were not in abundance. However, as found before the 700°C anneal, there were many instances of step edges and the surface roughness was nanometre in scale overall. The Ni surface was difficult to image with STM in many instances due to the topography which caused the STM tip to frequently contact the surface.

Figure 6.5 shows the corresponding ambient AFM image of a sample annealed at 700°C, revealing an increase in both surface roughness and nickel grain size.

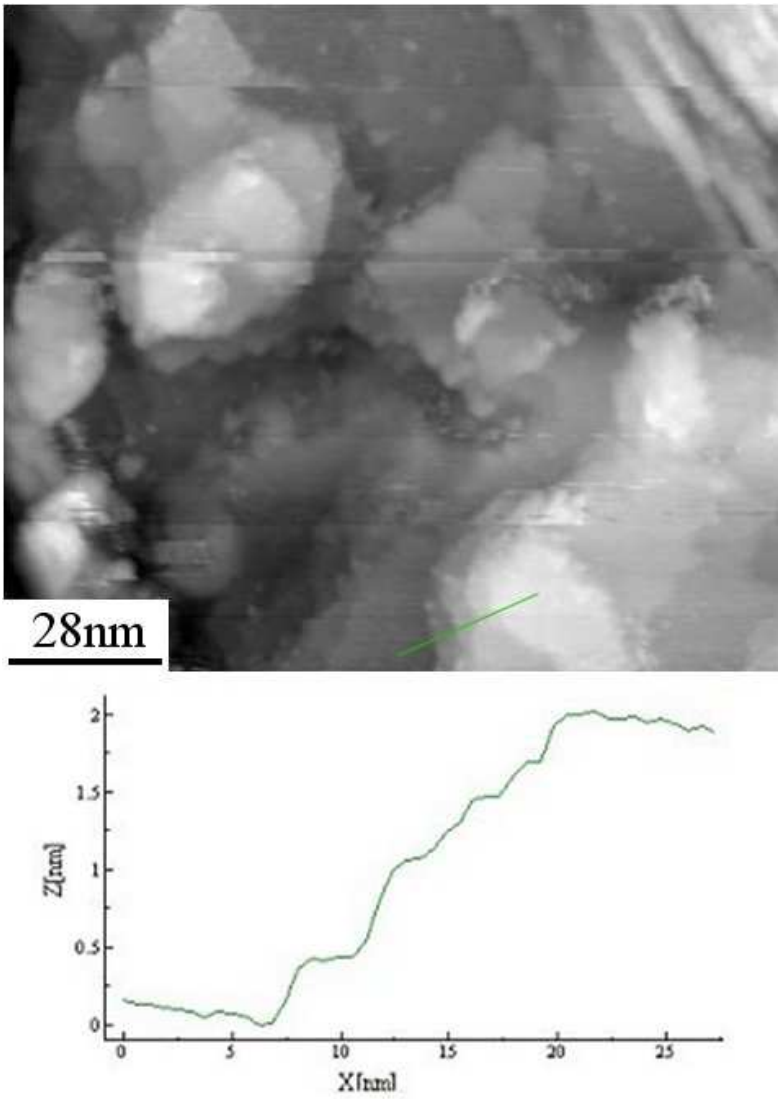

Figure 6.4: UHV-STM image and associated line profile of a Ni thin film on a SiO_2/Si(100) substrate after the sample was annealed to 700°C, STM imaging revealed some terraced areas but with an instability due to the rough surface. Imaging parameters V_{bias}= 1.0 V, I_t= 200 pA.

Many different Ni grain orientations were revealed with associated terraces that were similar to the terraces observed in Figure 6.4.

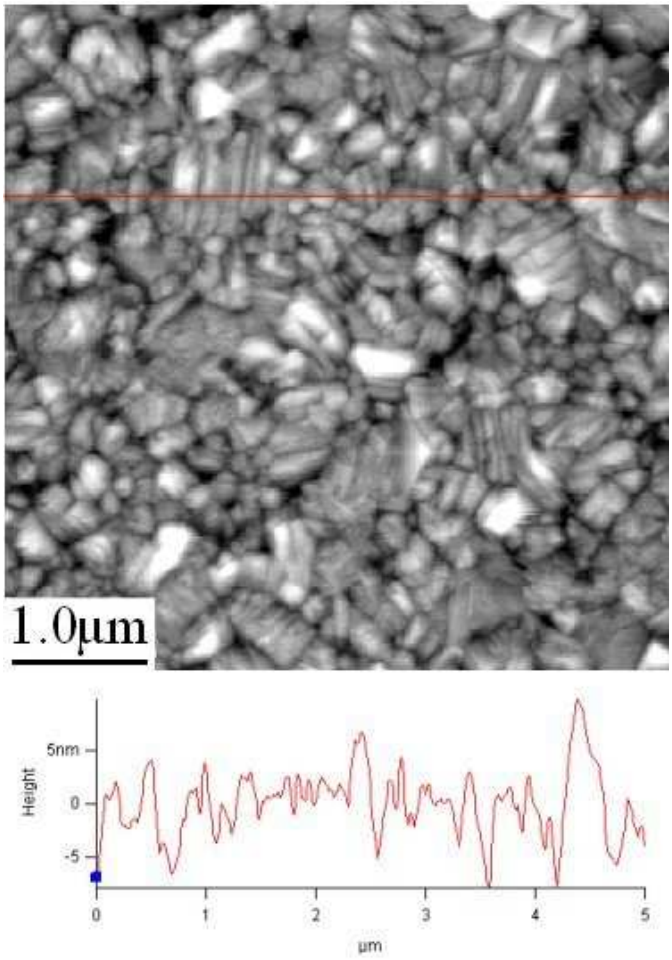

Figure 6.5: AFM image and associated line profile of a Ni thin film on a SiO_2/Si(100) substrate after the sample was annealed to 700°C in UHV and transferred to ambient conditions.

The Ni thin film samples were further annealed to 800°C which caused a radical change in the Ni surface morphology, as shown in Figure 6.6. The surface was predominately terraced, with terrace sizes of up to 100 nm. Although there were still step edges present on the surface these were less abundant and so the slopes of the surface were not as steep. A 'patchwork' terrace formation was also regularly observed on the surface as shown in the bottom part of Figure 6.6b, where several (in this case) hexagon adjacent terraces were imaged with STM.

The corresponding AFM image of the 800°C annealed surface in Figure 6.7 shows a larger scale image of the surface, where large (widths of greater than 1 μm) highly faceted islands were observed (on which the UHV-STM imaging

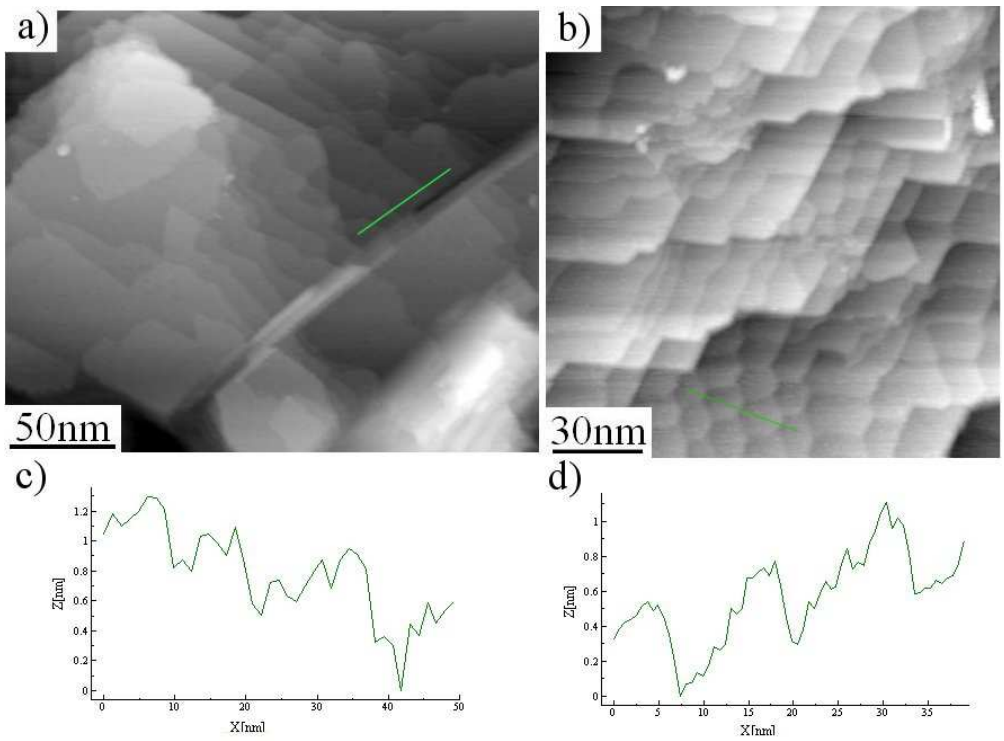

Figure 6.6: UHV-STM imaging of a Ni thin film on a SiO_2/Si(100) substrate after annealing to 800°C. The topography was flat in most areas with examples of (a) large and (b) smaller terraces, a 'patchwork' formation of terraces was also observed. Profiles (c) and (d) correspond to images (a) and (b) respectively. Imaging parameters (a) and (b) V_{bias}= 1.0 V, I_t= 200 pA.

revealed terraces). The 800°C annealed Ni thin films were investigated using X-ray diffraction (XRD) which revealed peaks in a θ-2θ scan consistent with the formation of (111) oriented Ni crystallites [109]. There was a significant change in morphology of the Ni surface after the 800°C anneal, however no difference in morphology was found when the samples were subsequently dosed with propylene after the 800°C anneal.

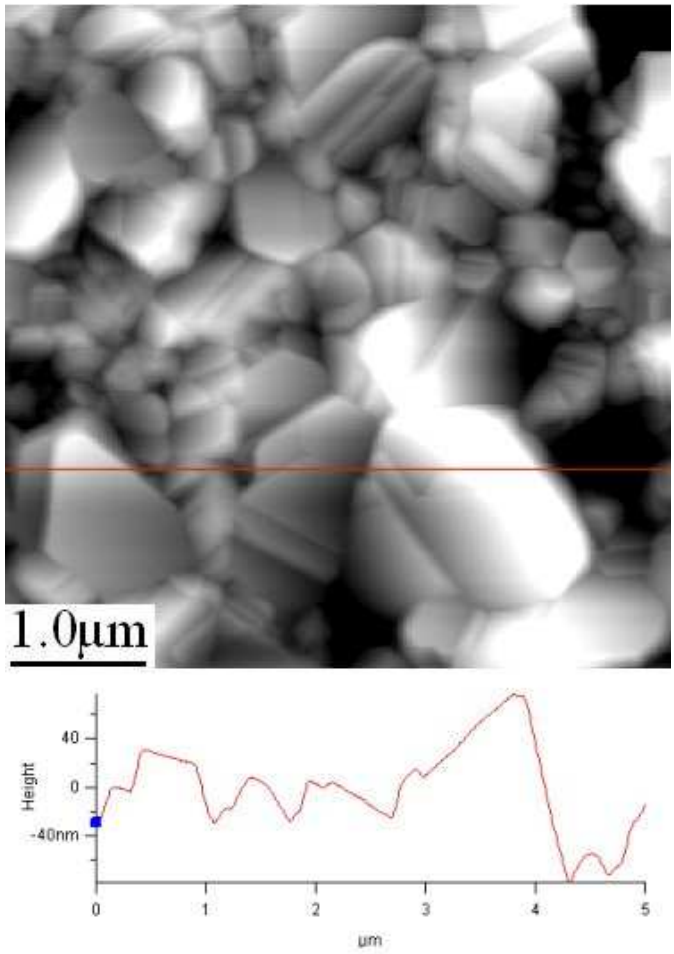

Figure 6.7: Ambient AFM image and line profile of a Ni thin film on a SiO_2/Si(100) substrate after the sample was annealed to 800°C in UHV.

Patchwork terraces were also observed in the STM images shown in Figures 6.8a and 6.8c, but were rectangular and aligned in rows rather than hexagons, as described previously. The rectangular terraces were ∼10 nm in width but their length varied from 10 nm to 40 nm with a median value of ∼15 nm, as shown in Figure 6.8c. The formation mechanism for this patchwork of terraces is not understood. However, terraces that did not exhibit the patchwork formation but were still aligned to the nearby patchwork terraces were observed, as shown in

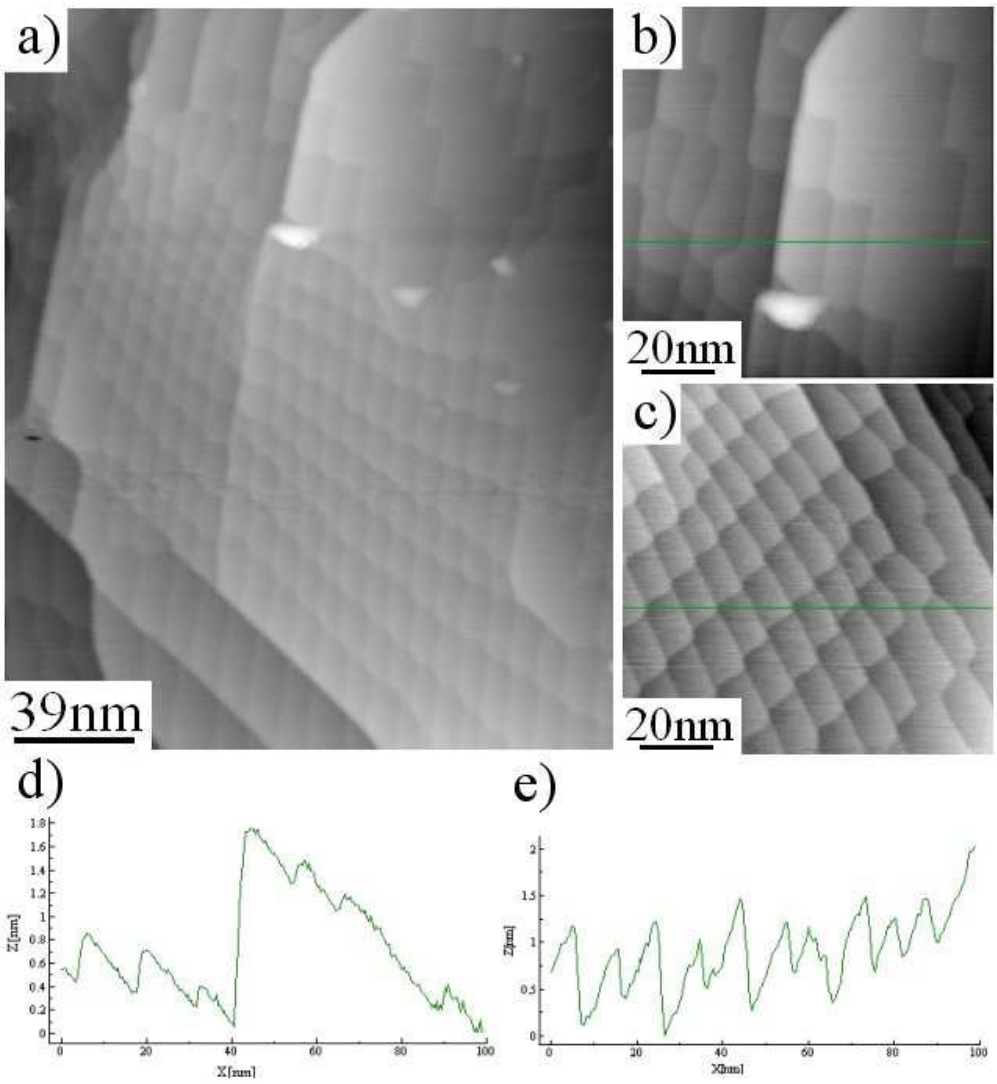

Figure 6.8: UHV-STM imaging of a Ni thin film on a SiO_2/Si(100) substrate after annealing to 800°C, where (b) is a smaller scan of an area in (a). There were many flat terraces over the surface (a), and instances of terraces with laterally rectangular step edges (b), in other areas 'patchwork' terrace formation was observed (c). Profiles (d) and (e) correspond to images (b) and (c) respectively, showing nickel step heights of ≥ 2 Å. Imaging parameters (a) and (b) V_{bias}= -1.0 V, I_t= 200 pA, (c) V_{bias}= -1.0 V, I_t= 150 pA.

Figure 6.8b. Whether these larger terraces would have also produced further patchwork terraces after further annealing is unknown, but these patchwork terraces were only observed when the Ni surface was substantially flatter due to the 800°C anneal.

Figure 6.9 shows two examples of STM images where the grain boundary of a Ni domain was observed. The grain boundaries were easier to distinguish after an 800° anneal than pre-anneal as the surface domains were much smaller for an untreated sample.

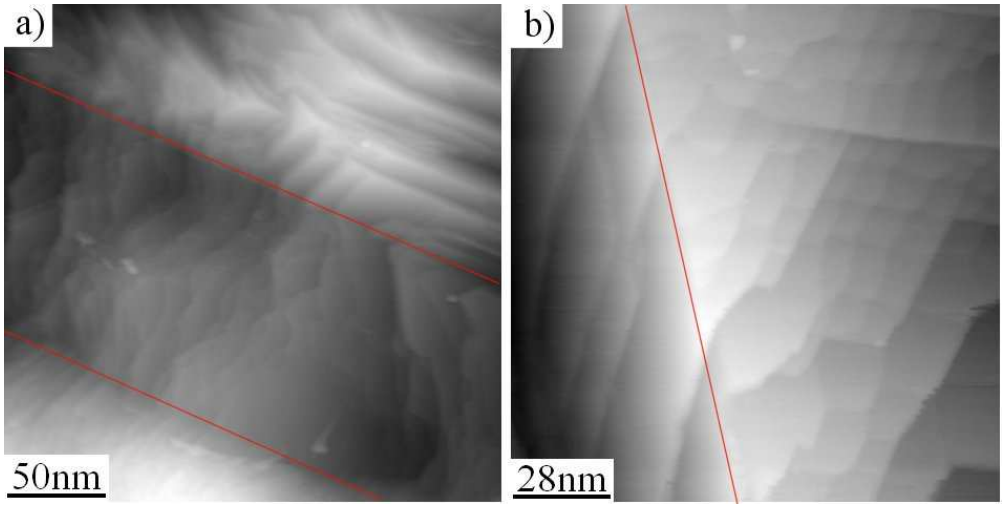

Figure 6.9: UHV-STM images of a Ni thin film on a SiO_2/Si(100) surface after the sample was annealed to 800°C. Grain boundaries formed in the Ni thin film are shown as red lines. Imaging parameters (a) and (b) V_{bias}= 1.0 V, I_t= 200 pA.

The Ni thin film morphology was not investigated after annealing at temperatures higher than 800°C due to degradation of the thin films. SPM imaging performed after the 800°C anneal of the Ni thin film implied that there was a significant diffusion of Ni atoms in the surface to produce the observed large, flat Ni grains. This had a detrimental effect to other areas of the sample as bare areas of SiO_2 were revealed, as observed in an ambient AFM image shown in Figure 6.10. Figure 6.10a shows a 5 μm AFM image where large Ni islands were produced through annealing at 800°C, while Figure 6.10b shows a 10 times larger scan size AFM image of a different area of the surface. Holes in the Ni thin film with widths of several microns and depths of several tens of nanometres are observed in Figure 6.10b, depths approximately equal to the thickness of the Ni thin film. Thus the gaps in the Ni thin film revealed the SiO_2 substrate – confirmed by XPS results in Section 6.1.2.

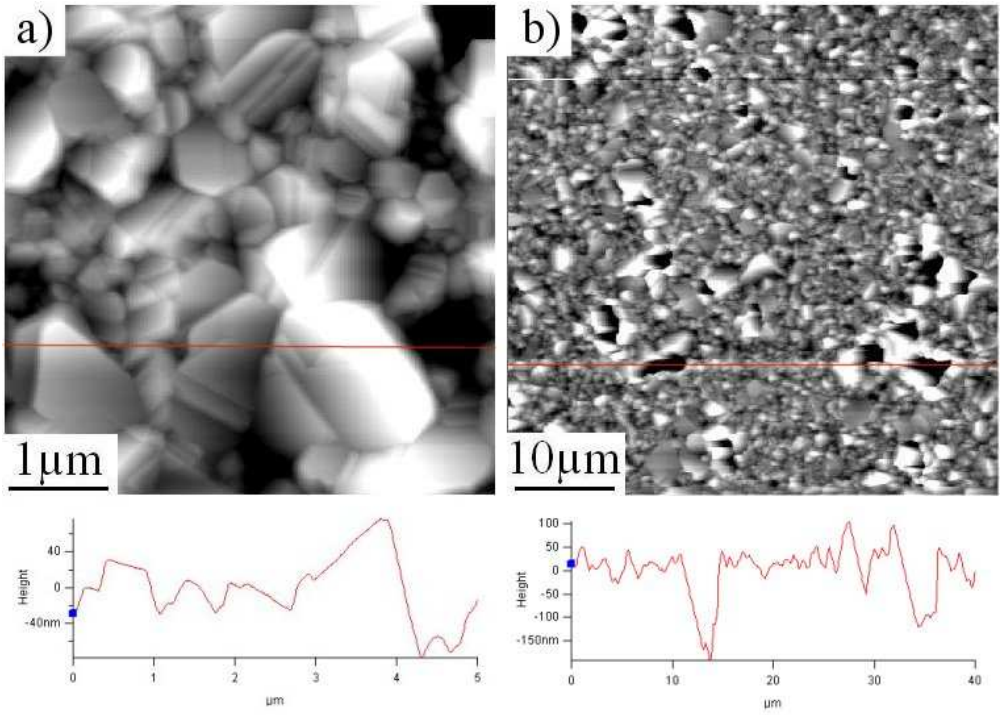

Figure 6.10: AFM images and line profiles of a Ni thin film on a SiO_2/Si(100) substrate after the sample was annealed to 800°C and transferred to ambient conditions. Although the smaller scan size image in (a) shows large, flat Ni grains, the larger scan size image in (b) shows areas of the SiO_2 surface were exposed after the annealing process.

6.1.2 XPS Surface Study

X-ray photoelectron spectroscopy (XPS) is a quantitative technique performed in UHV that measures the elemental composition, and chemical and electronic states of the atoms within the surface of a sample. XPS spectra are acquired by irradiating the sample surface with a beam of X-rays and simultaneously measuring the number of electrons that escape from the surface versus the kinetic energy of the electrons – typically to a depth of 1-10 nm.

Two separate XPS systems (operated by S. Gangopadhyay and I. Villar-Garcia) were used, allowing both in-situ and ex-situ investigation of the Ni thin films. Samples could be prepared in the Edwards system or Nanograph STM-01 UHV system and then transported through ambient conditions to a high resolution XPS system. A Kratos Axis Ultra spectrometer employed a monochromated Al Kα X-ray source and hemispherical analyser which achieved a resolution of $\sim$0.2 eV (for further details see Reference [110]). Untreated or processed Ni thin film samples could also be introduced to a UHV system with a lower resolution XPS system; an Omicron DAR400 Mg Kα X-ray source and VG Scienta R3000 hemispherical analyser with $\sim$0.7 eV resolution that had the facilities to anneal the sample to 800°C.

To investigate the oxidation of the nickel surface a Ni thin film prepared in the Edwards evaporator was introduced to the Omicron XPS UHV system (via ambient conditions) and *in-situ* XPS was performed on the sample before and after a 15 min 500°C anneal. This annealing process replicated the outgassing phase of the sample preparation. Figure 6.11 shows Ni-2p XPS spectra for the sample before and after the anneal. All XPS results in this thesis were analysed using CasaXPS software.

From Figure 6.11, the 15 min in-situ 500°C anneal sharpened the Ni-$2p_1$ (869.9 eV [111]) and Ni-$2p_3$ (852.6 eV [111]) peaks dramatically, corresponding to an increase in elemental nickel in the surface. The nickel oxide peak at 856.1 eV [112] also disappeared after annealing the Ni thin film. The disappearance of the nickel oxide after the 15 min 500°C anneal was confirmed in the O-1s XPS spectra shown in Figure 6.12. Three oxygen peaks were found for the untreated sample, relating to carbon contaminants (531.2 eV [113] and 532.7 eV [114]) and nickel oxide (529.6 eV [111] and 531.3 eV [115]). However, after the low temperature outgassing of the sample all three of these peaks also disappeared, therefore the nickel oxide and associated carbon contaminants had been removed from the surface.

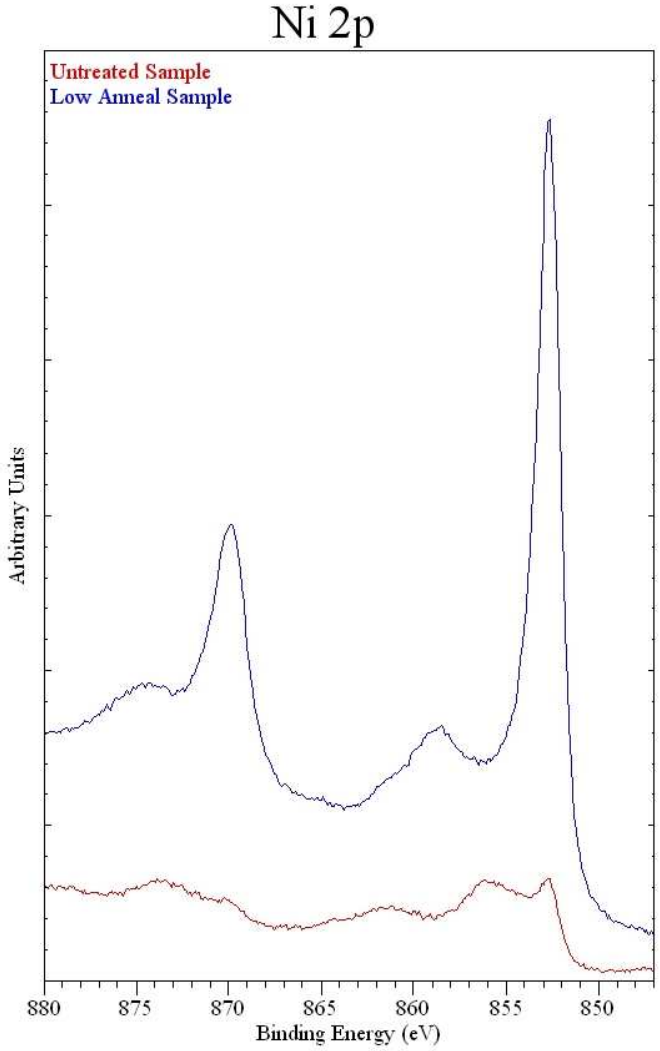

Figure 6.11: XPS Ni-2p spectra for a Ni thin film sample both before and after a 500°C anneal (labelled 'Low Anneal'). The sample was prepared in the Edwards evaporator system before it was transferred to a UHV system (via ambient conditions) for XPS analysis, but was annealed in-situ. XPS performed by Subhashis Gangopadhyay.

Ni thin films produced in the Edwards evaporator were also annealed and then dosed with propylene in the Nanograph STM-01 UHV system and then transferred to the Kratos Axis Ultra XPS system via ambient conditions. Three thin films were investigated with ex-situ XPS (after they had been transferred through ambient conditions): untreated (transferred directly from Edwards evaporator via ambient conditions), annealed at 600°C and then dosed with propylene, and annealed at 800°C and then dosed with propylene. The resulting O-1s peaks are shown in Figure 6.13.

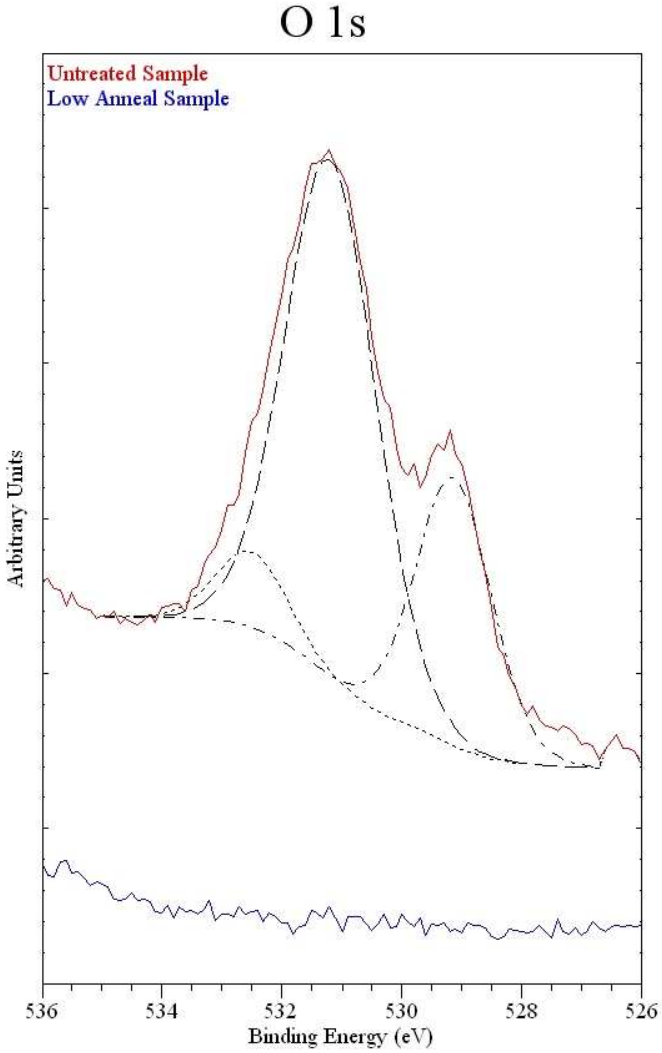

Figure 6.12: XPS O-1s spectra for a Ni thin film sample before and after a 500°C ('Low') anneal. The sample was prepared in the Edwards evaporator system before it was transferred to a UHV system (via ambient conditions) for XPS analysis, but was annealed in-situ. XPS performed by Subhashis Gangopadhyay.

XPS O-1s spectra for the untreated Ni thin film (no anneal or propylene dose) were unsurprisingly similar to the XPS spectra for the untreated Ni thin film in Figure 6.12 – both samples had been produced in the Edwards evaporator and then transferred through ambient conditions to the two different XPS systems.

However, when comparing the XPS spectra for the two 'Low Anneal' samples in Figures 6.12 and 6.13, a large oxygen peak was found for the 600°C ('Low') anneal sample in Figure 6.13 whilst no oxygen peaks were observed for the 500°C ('Low') anneal sample in Figure 6.12. Although the 600°C anneal sample had been dosed with propylene and the 500°C anneal sample had not, it was found

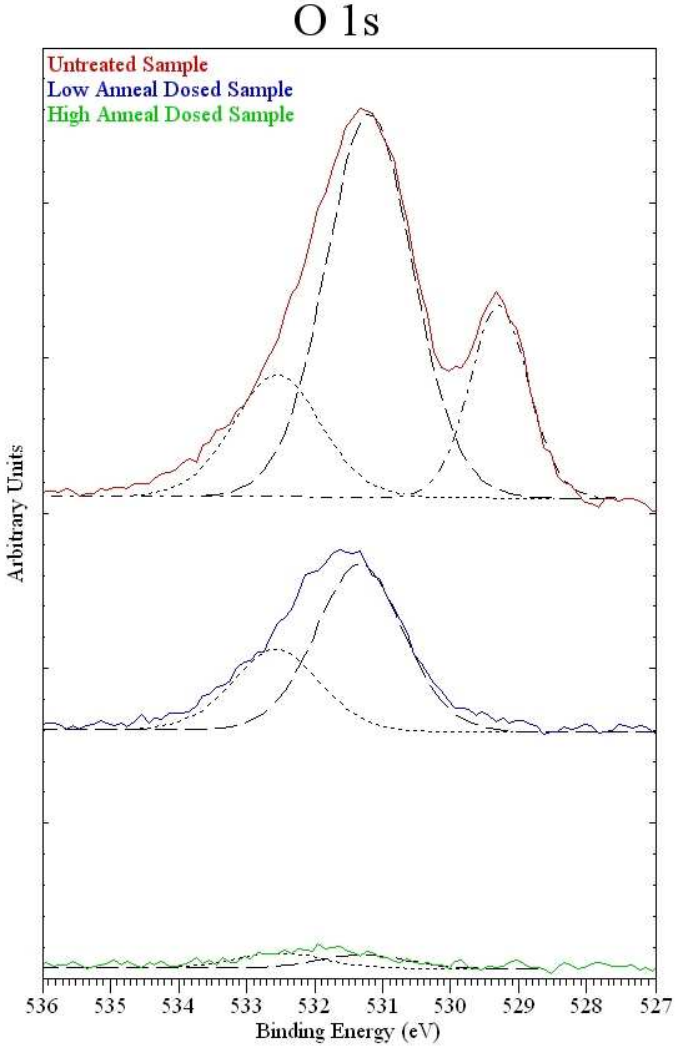

Figure 6.13: XPS O-1s spectra comparing the effect of annealing temperature for three separate samples. The samples investigated were (from top spectra to bottom) an untreated Ni thin film sample, a Ni thin film sample annealed to 600°C ('Low Anneal') and dosed with propylene in UHV, and a Ni thin film sample annealed to 800°C ('High Anneal') and dosed with propylene in UHV. All the Ni thin film samples were produced in the Edwards evaporator system and prepared in a different UHV system other than the ex-situ XPS UHV system. XPS performed by Ignacio Villar-Garcia.

that the appearance of the oxygen peaks was actually due to exposure to ambient conditions before the ex-situ XPS was performed (discussed later in this section).

The 800°C ('High') anneal sample revealed vastly reduced oxygen peaks when compared to the 600°C anneal sample, however there were still very small oxygen peaks observed for the 'High Anneal' sample. After any 500-800°C anneal of the surface the NiO peak at 529.6 eV was completely removed and did not reappear

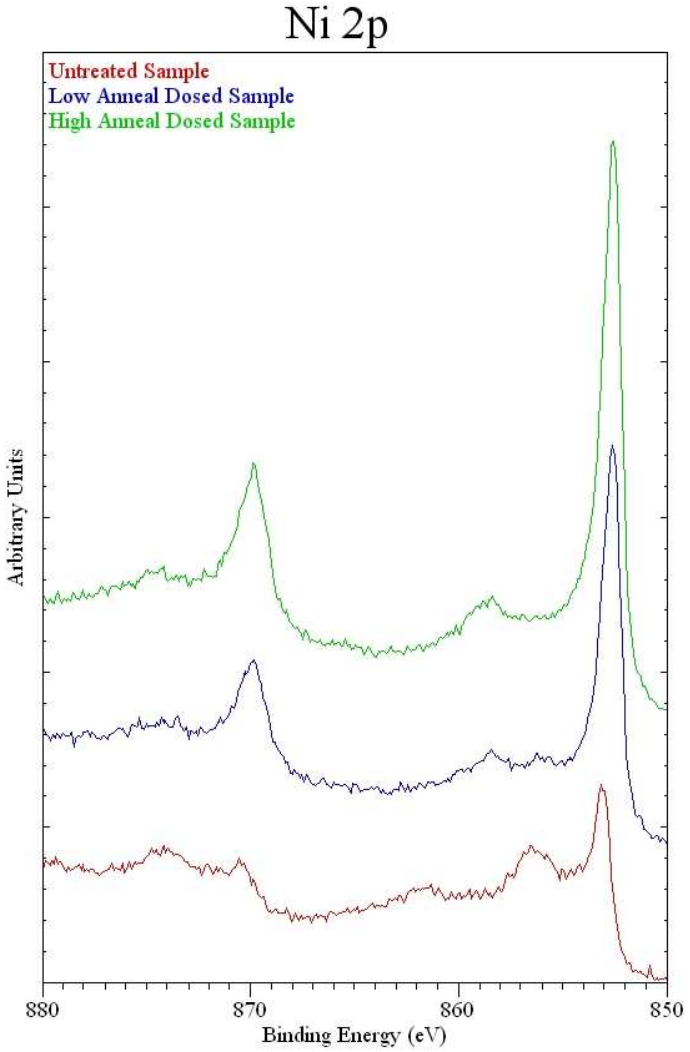

Figure 6.14: XPS Ni-2p spectra comparing the effect of annealing temperature for three separate samples. The samples investigated were (from top spectra to bottom) a Ni thin film sample annealed to 800°C ('High') and dosed with propylene in UHV, a Ni thin film sample annealed to 600°C ('Low') and dosed with propylene in UHV, and an untreated Ni thin film sample. All the Ni thin film samples were produced in the Edwards evaporator system and prepared in a different UHV system other than the ex-situ XPS UHV system. XPS performed by Ignacio Villar-Garcia.

after exposure to ambient conditions for the Ni thin film samples.

Figure 6.14 shows the Ni-2p peaks found for the same three samples shown in Figure 6.13. The untreated sample spectra revealed smaller Ni-$2p_1$ and Ni-$2p_3$ peaks compared to the two annealed samples which showed a drastically increased magnitude and sharpness of the peaks, similar to the ex-situ XPS spectra in Figure 6.11. The sharpness of the nickel $2p_1$ and $2p_3$ peaks for the 800°C anneal

sample was further increased when compared to the 600°C anneal sample. However, the nickel oxide peak (856.1 eV) did not disappear for the lower temperature anneal and was only removed completely for the higher temperature anneal. This would correlate with the observed nickel oxide peaks in the ex-situ O-1s spectra – oxygen was readsorbed on the surface after exposure to the atmosphere for the lower anneal sample.

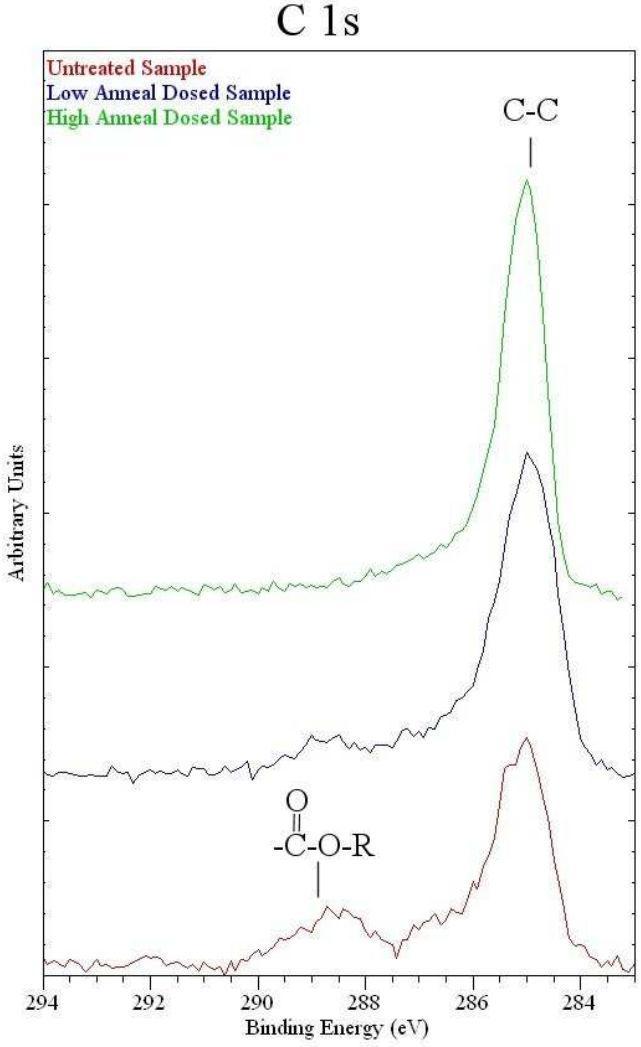

Figure 6.15: XPS C-1s spectra comparing the effect of annealing temperature for three separate samples. The samples investigated were (from top spectra to bottom) a Ni thin film sample annealed to 800°C ('High') and dosed with propylene in UHV, a Ni thin film sample annealed to 600°C ('Low') and dosed with propylene in UHV, and an unannealed Ni thin film sample. All the Ni thin film samples were produced in the Edwards evaporator system and prepared in a different UHV system other than the ex-situ XPS UHV system. XPS performed by Ignacio Villar-Garcia.

Figure 6.15 shows the corresponding C-1s XPS spectra for the three samples. The untreated sample spectra showed the convolution of several peaks with the most prominent C-1s peak at 285.0 eV – which corresponds to C-C bonding – the peak then became sharper as the sample was annealed. Other peaks were also observed for the untreated sample which corresponded to carbon contaminants, these peaks were still present in the lower anneal sample – due to readsorption in ambient conditions – although not to the extent of the untreated sample. There was minimal carbon contamination shown in the XPS spectra for the higher anneal sample which would coincide with the very small O-1s peaks in Figure 6.13. However, the ester (COOR) peak at 288.9 eV was absent for the higher anneal sample and still observed for the lower anneal sample.

Figures 6.11-6.15 suggest that although only a 500°C anneal was required to remove the nickel oxide and carbon contaminants from the Ni thin film samples, upon exposure to ambient conditions nickel oxide and carbon contaminants were re-adsorbed onto the bare Ni surface. However, after an 800°C anneal the surface was almost completely protected from the re-adsorption of both oxygen and carbon contaminants when exposed to ambient conditions. This leads to the hypothesis that graphene layers, formed on the Ni thin film surface after an 800°C anneal, protected the Ni surface from any oxygen or carbon contaminants and thus only a very small amount of contaminants were re-adsorbed, presumably in areas that contained defects in the graphene. This hypothesis was supported by the fact the C-C bonding peak sharpened as the annealing temperature increased.

However, the affect of the propylene dosing of the samples has not yet been considered. To this end an 800°C annealed and propylene dosed sample and a 800°C annealed sample were investigated using XPS, as shown in Figures 6.16 and 6.17. From Figures 6.16 and 6.17, there were no significant differences between propylene dosed and annealed samples that had both been annealed at 800°C.

From the XPS data in Figures 6.11-6.17, the overall graphene formation process can be understood. Upon annealing the Ni thin film in UHV at 500°C or above all the oxygen peaks were removed, the Ni-2p peaks were sharper and associated oxide peaks were removed. For the C-1s spectra the COOR peaks were removed and the C-C bonding peak increased and became sharper. Contamination was revealed for the 800°C anneal samples using ex-situ XPS due to the exposure to ambient conditions, but the intensity of these peaks was drastically reduced compared to lower temperature annealed samples. The annealed and the dosed samples produced approximately the same C:Ni:O ratio of 45:53:2 (found from XPS data shown in Figures 6.16 and 6.17) corresponding to the atoms present in

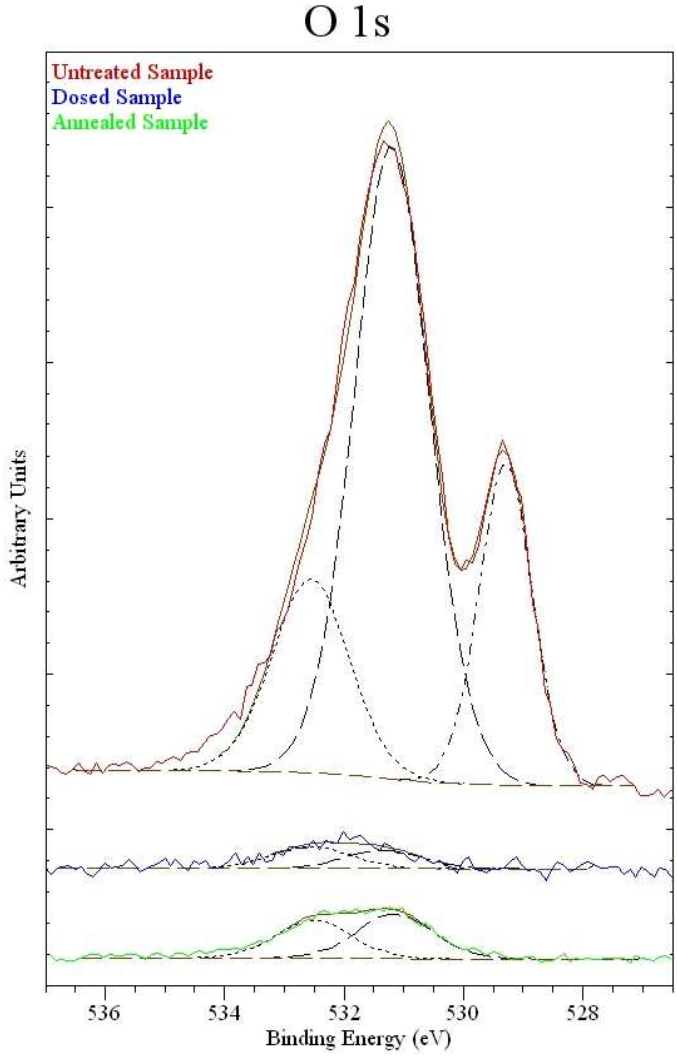

Figure 6.16: XPS O-1s spectra as a comparison between annealing and dosing and solely annealing the Ni thin films. The samples investigated were (from top spectra to bottom) an untreated Ni thin film sample, a Ni thin film sample annealed to 800°C in UHV and subsequently dosed with propylene ('Dosed Sample'), and a Ni thin film sample annealed to 800°C ('Annealed Sample'). XPS performed by Ignacio Villar-Garcia.

the top few nanometres of the surface of the sample. The protection of the Ni surface observed in the XPS data shows that the annealing cycles are critical for the formation of graphene films, with the majority of the surface covered with graphene when anneal temperatures in the range 700-800°C were used.

Increasing the anneal temperature above 800°C produced a high abundance of areas where there was no Ni thin film coverage of the SiO_2 substrate, as discussed in Section 6.1.1. XPS spectra of areas that appeared purple to the naked eye were

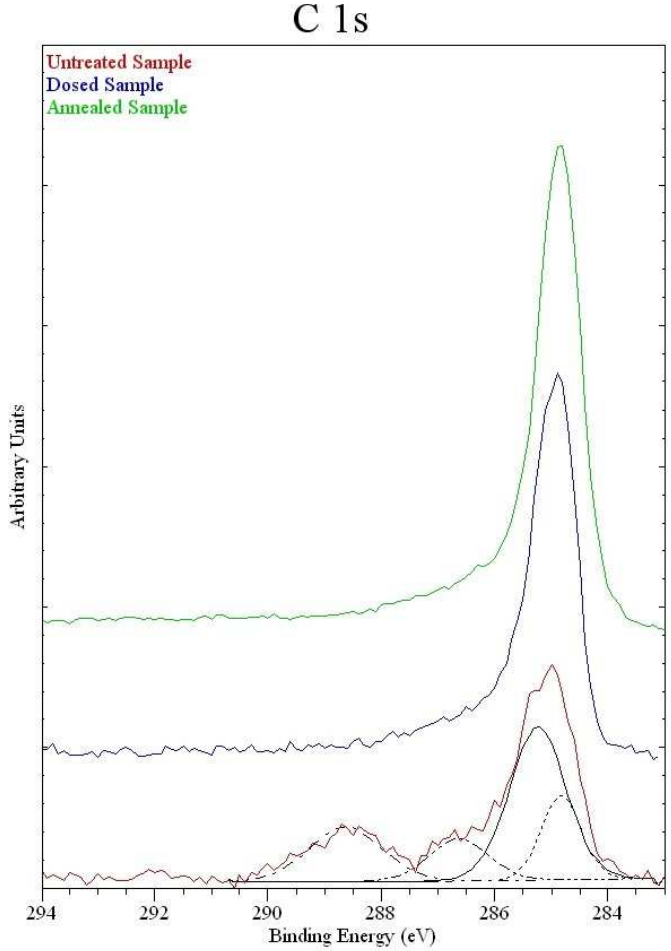

Figure 6.17: XPS C-1s spectra as a comparison between annealing and dosing and solely annealing the Ni thin films. The samples investigated were (from top spectra to bottom) a Ni thin film sample annealed to 800°C ('Annealed Sample'), a Ni thin film sample annealed to 800°C in UHV and subsequently dosed with propylene ('Dosed Sample'), and an untreated Ni thin film sample. XPS performed by Ignacio Villar-Garcia.

found to have small Si and SiO_2 contributions to the Si-2p peaks as well as an SiO_2 contribution to the O-1s peaks. However, the remainder of the sample produced the same XPS spectra previously observed for an 800°C anneal sample, where no silicon contributions were revealed.

6.1.3 Graphene Formation Carbon Source

The graphene films investigated were formed by annealing Ni thin films at 800°C under vacuum conditions and in the absence of any hydrocarbons. The source of carbon that produced the graphene arose from background contamina-

tion in ambient conditions and no additional carbon source was required during annealing. The carbon contamination was already present on the SiO_2 substrates before Ni deposition was performed in either the Nanograph STM-01 UHV system or the Edwards evaporator – Ni thin films formed in either system could produce graphene. However, no graphene was produced if the sample was annealed to 800°C in UHV conditions *before* Ni was deposited onto the substrate and then the Ni thin film sample was annealed to 800°C as usual. This bears a striking resemblance to the fingerprint carbon-contamination that led to graphene formation on Rh(111) thin films, detailed in the Supplementary Information of Reference [99]. Other avenues of exposing the Ni thin film to carbon could be explored to investigate if higher quality graphene layers are produced, avenues such as immersion in acetone, as described for the Rh(111) thin films.

6.2 Extraction of Graphene Layers from Nickel

After their formation in UHV and study in ambient conditions, the graphene layers were released from the Ni thin films by etching the nickel in a $FeCl_3$ solution (1 M) for 12-16 hours, as shown in Figure 6.18. A polymethylmethacrylate (PMMA) thin film of thickness 250 nm was spin-coated onto the sample in order to provide mechanical support and facilitate ease of handling. Following the release etch of the Ni layer the graphene/PMMA layer was submersed in water to remove any excess $FeCl_3$ solution before being placed on a SiO_2/Si(100) wafer (or a holey carbon grid if used for electron microscopy). The SiO_2 substrate was submersed in water underneath the graphene/PMMA layer and used to obtain the graphene/PMMA layer from the water. This process secured the graphene on the SiO_2 surface and reduced any damage that would be caused through handling the graphene/PMMA layer directly. The PMMA layer was then dissolved by immersion in acetone. This entire process produced large areas of graphene, which were predominantly composed of a continuous monolayer, isolated on a dielectric substrate.

In the initial phase of the investigation, Geim et al. at the University of Manchester [109] performed the graphene transfer process until the procedure was reproduced at the University of Nottingham. Once the graphene layer was transferred as a single continuous layer onto a separate surface it was studied with various microscopy methods. These methods included optical microscopy and Raman spectroscopy which were also initially performed by at the University of Manchester and then at the University of Nottingham. However, the electron

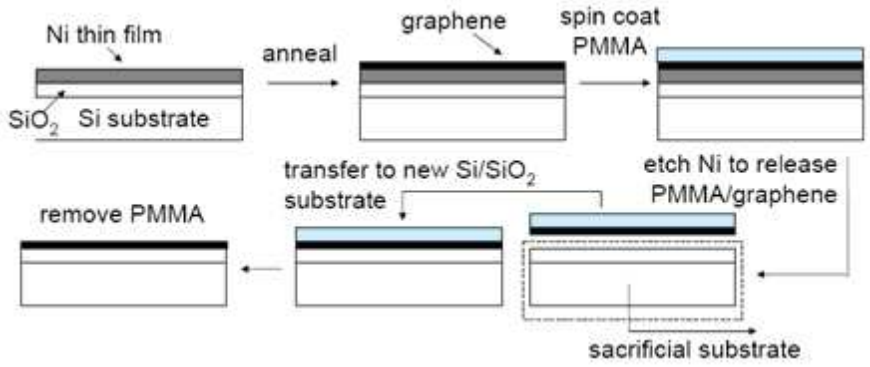

Figure 6.18: Schematic showing the process used to form graphene on Ni then transfer the graphene to a separate insulating substrate [36, 39, 40]. Reprinted with permission from Ref. [109]. © 2009 American Chemical Society.

microscopy investigations of the graphene layers (both SEM and TEM) were performed solely at the University of Manchester.

6.2.1 Optical Microscopy of Isolated Graphene

After extracting the graphene layer and isolating it on a SiO_2 substrate, the graphene layers could be clearly observed using an optical microscope. Although silicon dioxide layers of varying thickness can be used and graphene layers are still observed, a 90 nm thick SiO_2 layer was used to maximise the contrast in optical microscopy [116], as discussed later in this section. This allowed the discrimination between mono- and few-layer graphene, as shown in Figure 6.19. All optical images were acquired with an Olympus BX51 microscope.

A large flake of graphene on a 90 nm thick SiO_2 substrate is clearly observed in Figure 6.19, although the majority of the flake was a monolayer in thickness, there were also some instances of multilayer graphene that appeared darker in contrast. Holes and cracks in the monolayer were also observed, presumably formed by both the grain boundaries in the Ni thin film and the process of transferring the graphene to the SiO_2 substrate.

Figure 6.20 shows graphene produced by annealing the sample (Figure 6.20a) and by annealing and then dosing with propylene (Figure 6.20b) and different appearances of the few-layer graphene common for both types of sample. It was not possible to differentiate between isolated graphene obtained from a propylene dosed or an annealed sample using optical microscopy.

Ni thin films deposited in the Nanograph STM-01 UHV system were also found

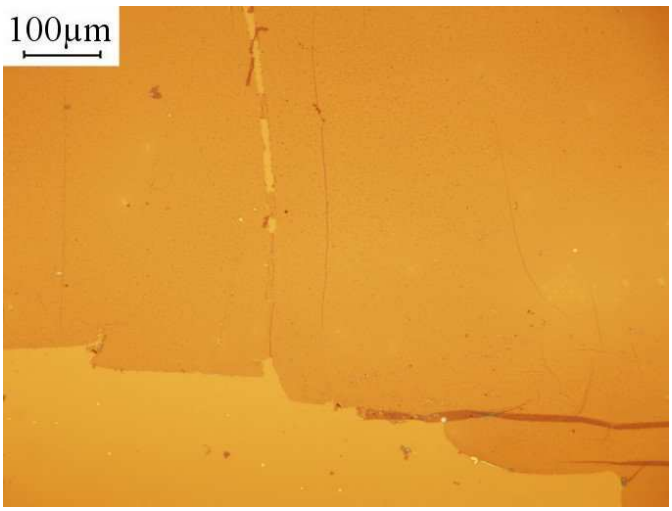

Figure 6.19: Optical microscopy of isolated graphene layers on a SiO_2 (90 nm thick) layer.

to produce the same predominantly monolayer graphene and an example is shown in Figure 6.21.

As previously described in Sections 6.1.1 and 6.1.2, the higher anneal temperatures produced holes in the Ni thin film revealing the bare SiO_2 of the substrate. Areas of the surface where there were holes in the Ni thin film produced graphene flakes that had similar holes, as shown in Figure 6.22. This demonstrated that graphene was most likely formed only on areas of nickel, there were no results that suggested that graphene was produced on the steep slopes of the holes.

Figure 6.22 also illustrates how the difference in contrast for graphene isolated onto a 300 nm thick SiO_2 layer was less pronounced when compared to a 90 nm thick SiO_2 layer (Figures 6.19 to 6.21). Monolayer graphene has been shown to actually be invisible on a 200 nm thick SiO_2 layer with white-light illumination and on a 300 nm SiO_2 layer with blue-light illumination. However, these graphene flakes were visible with blue-light illumination of a 200 nm SiO_2 sample and white-light illumination of a 300 nm SiO_2 sample [116]. This effect was related to the increased optical path and extremely low opacity of graphene, and through theoretical and experimental investigation it was found that a 90 nm SiO_2 layer provided the highest contrast for graphene monolayers for both white-light illumination and when using green filters, as shown in Reference [116].

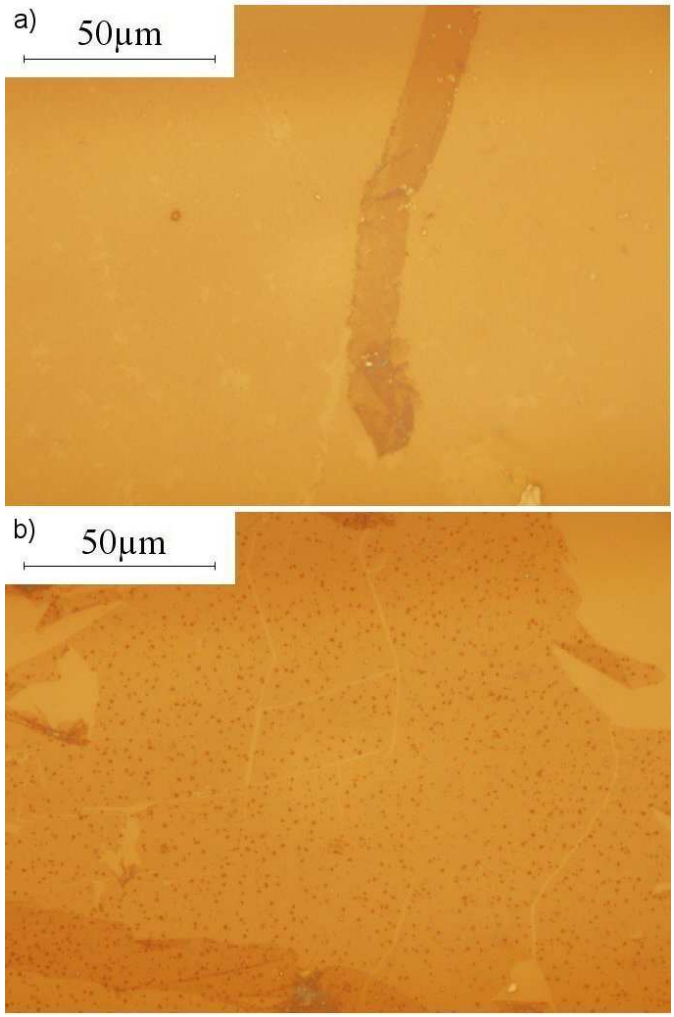

Figure 6.20: Optical microscopy of isolated graphene layers on SiO_2/Si(100) (90 nm thick SiO_2 layer) substrates, graphene was extracted from (a) 800°C annealed Ni thin film and (b) 800°C annealed and propylene dosed Ni thin film.

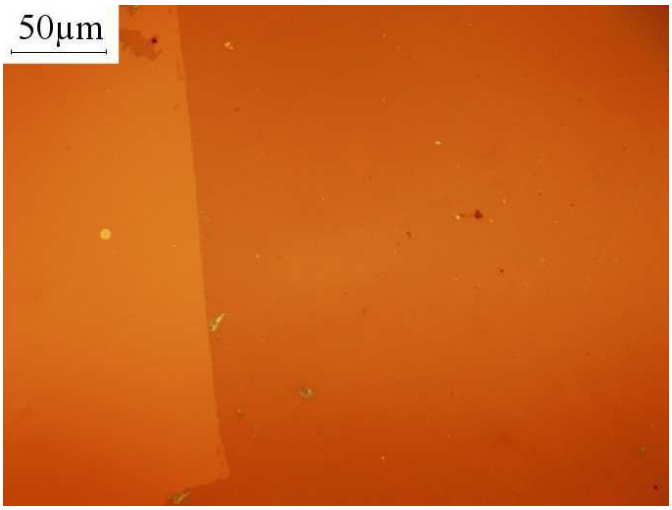

Figure 6.21: Optical microscopy of isolated graphene layers on a SiO_2/Si(100) (90 nm thick SiO_2 layer) substrate. Graphene layers were extracted from a Ni thin film sample that was deposited and then annealed at 700°C in the Nanograph STM-01 UHV system.

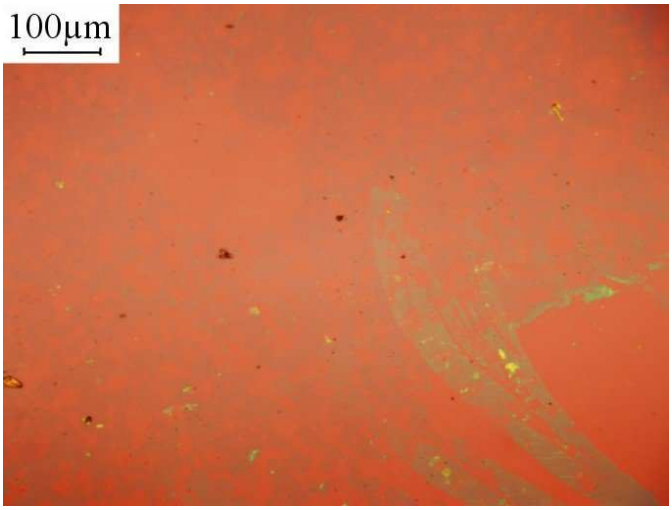

Figure 6.22: Optical microscopy of isolated graphene layers on a SiO_2/Si(100) (300 nm thick SiO_2 layer) substrate. Graphene was extracted from a high temperature annealed Ni thin film.

6.2.2 Electron Microscopy of Graphene

After the initial optical microscopy of an extracted graphene sample had been performed, the sample could be introduced into an SEM system to image the graphene layers. Figure 6.23 shows the similarities of two graphene samples, one that was annealed at 800°C and another sample that was annealed at 800°C and then dosed with propylene. As found with SPM, XPS and optical techniques, the dosing of the Ni thin films with propylene produced negligible differences, with both samples displaying obvious single and few-layer areas of graphene.

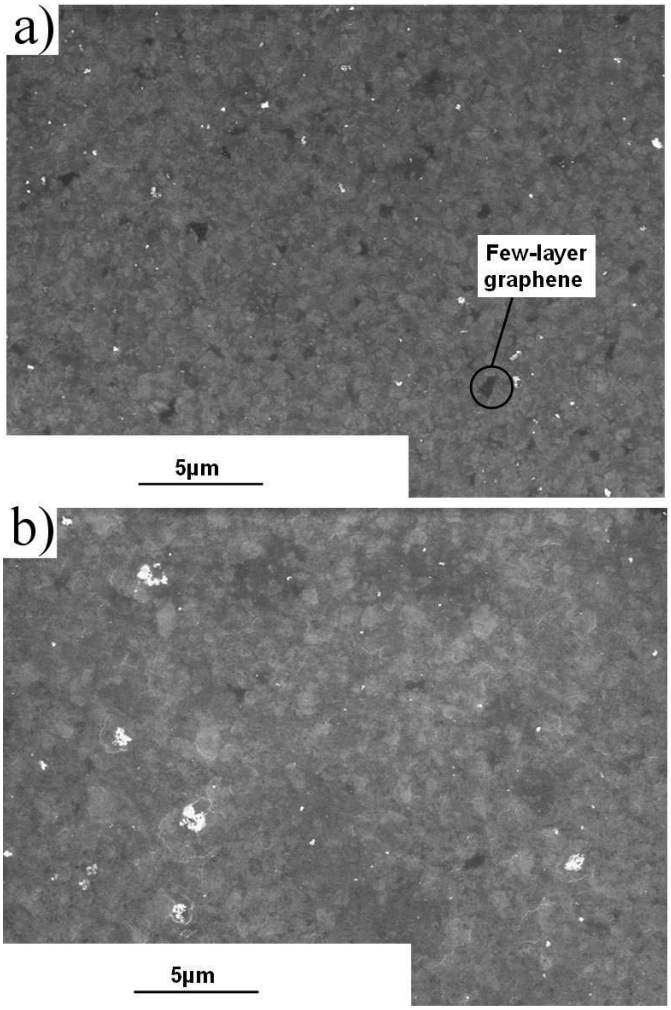

Figure 6.23: (a) SEM image of graphene layers transferred onto a SiO_2/Si(100) substrate after an 800°C anneal and a propylene dose in UHV and (b) an 800°C anneal. Images courtesy of Rahul Nair.

The graphene layers could be extracted onto theoretically any surface after the Ni thin film was etched away and one substrate used was a holey carbon grid –

this enabled the sample to be imaged with a TEM. Figure 6.24 shows both SEM and TEM measurements on graphene layers transferred onto a holey carbon grid.

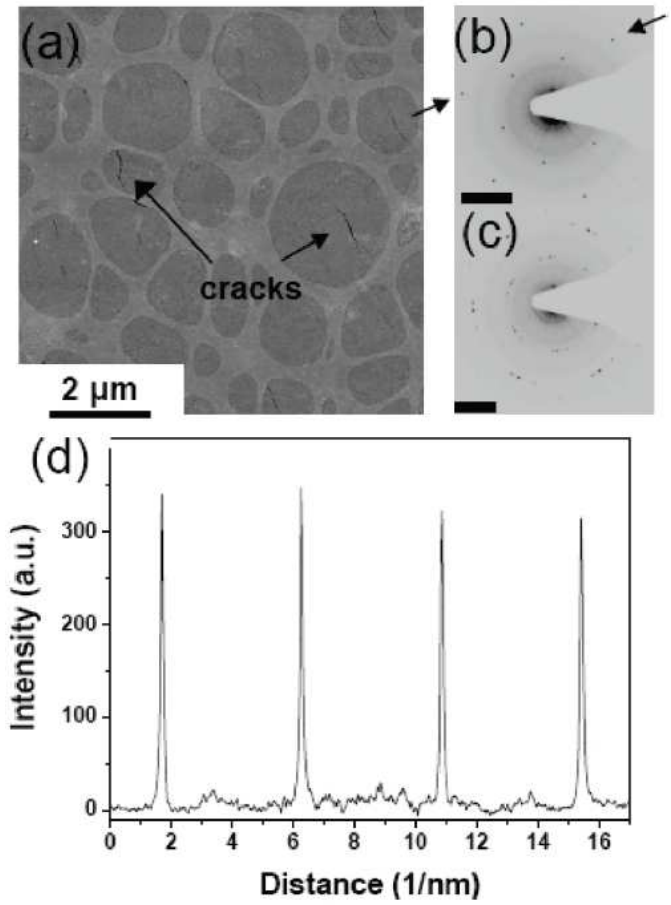

Figure 6.24: (a) SEM image of graphene transferred to a holey carbon TEM sample grid where dark grey regions are graphene, and cracks (black) can also be resolved. (b) and (c) are TEM diffraction patterns (Tecnai F30, accelerating voltage 300 kV) from (b) monolayer (scale bar 4.3 nm^{-1}) and (c) few-layer (scale bar 3.8 nm^{-1}) regions. (d) the intensity of diffraction spots versus position (in reciprocal space) along the line between the points marked by arrows in (b). Results courtesy of Rahul Nair – reprinted with permission from Ref. [109].

SEM images of the graphene layers on the holey carbon grid (Figure 6.24a) show several cracks in the graphene layers (black) not observed in Figure 6.23, these may have been caused by the extraction process itself, or the graphene formation on a Ni thin film with micron-sized grains. TEM diffraction patterns from areas identified as single-layer regions in Figure 6.24b have equally intense first and second order spots, consistent with single-layer graphene [117, 118]. The spot intensity in Figure 6.24b is plotted in Figure 6.24d and can be compared

with a similar dependence shown in Reference [118]. Multilayer graphene areas produced multiple diffraction spots – as shown in Figure 6.24c – due to rotationally disordered (turbostratic) few-layer graphene.

Raman spectroscopy was performed on the graphene layers isolated on SiO_2 with a 50× objective at 514 nm excitation with a Renishaw micro-Raman spectrometer. Areas identified by the corresponding optical microscopy (Figure 6.25a) as single and few-layer graphene were confirmed by the Raman spectra, as shown in Figure 6.25b. A unique signature of single-layer graphene is a single Lorentzian peak at ∼2690 cm^{-1}, which is often referred to as a 2D peak [119]. This single-layer graphene peak was observed with a full-width, half-maximum (FWHM) of 33 cm^{-1} for the isolated graphene.

6.2.3 Raman Spectroscopy of Graphene

The G peak (∼1590 cm^{-1} intensity (as shown in Figure 6.25b)) for areas of few-layer graphene – that had been determined with optical microscopy – revealed a thickness of 3-4 layers. The 2D peak normally develops into a broader 2D band for few-layer graphene [119], however it was found that the few-layer regions still exhibited a single Lorentzian peak that was much wider (FWHM of ∼50 cm^{-1}). Previous behaviour reported for micromechanically cleaved few-layer graphene differs from this result, but this effect has been attributed to non-Bernal (turbostratic) stacking in the multilayer graphene films grown on Ni [39], and these observations were confirmed by TEM, as shown in Figure 6.24.

Defects and/or sub-micron cracks in the graphene flakes were revealed by the disorder-induced low intensity D peak at 1350 cm^{-1} and D band at 1620 cm^{-1} (Figure 6.25). The upper limit of the length scale of the cracks was sub-micron as a ∼2 μm diameter laser spot-size was used for the Raman spectroscopy measurements. These defects or cracks were present within the continuous areas of both monolayer and few-layer graphene flakes observed with optical microscopy. The presence of cracks had been confirmed using SEM – as shown in Figure 6.24 – and thus there were obviously fewer defects in the graphene layers than would have been assumed due to the intensity of the D peak alone. The intensity of these defect-related peaks was smaller than for graphene oxide, reduced graphene oxide [120] and graphane [121], which indicated an improved electronic quality of the graphene films produced on these Ni thin films in UHV. However, the intensity of the disorder induced peaks was still greater than for the graphene films reported in References [36] and [39].

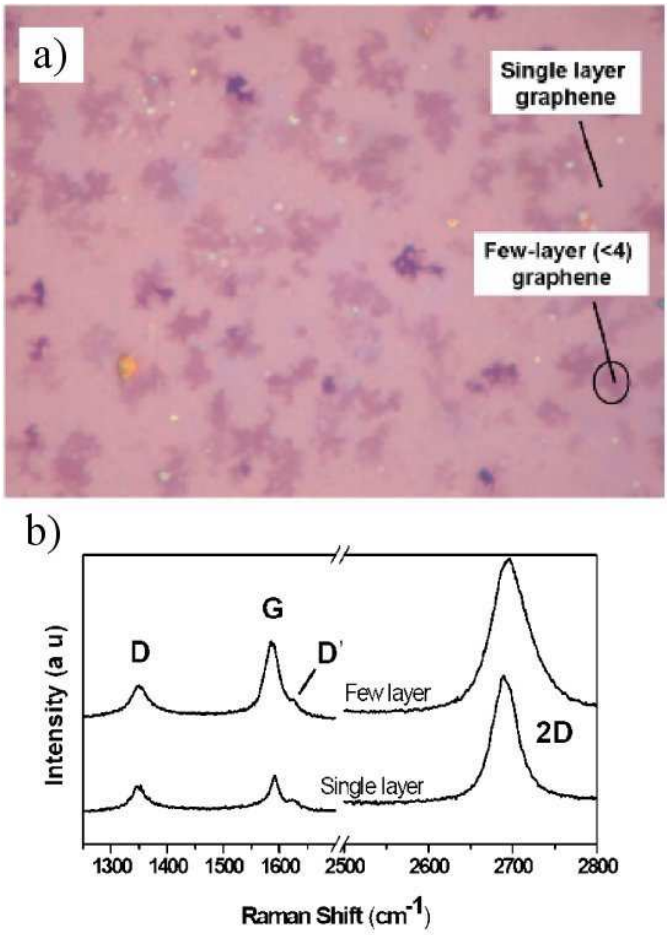

Figure 6.25: (a) Optical microscopy of isolated graphene layers (90 nm thick SiO_2 layer) and (b) Raman spectra found for the single-layer and few-layer areas of graphene labelled in (a). Results courtesy of Rahul Nair – adapted with permission from Ref. [109]. © 2009 American Chemical Society.

After processing the optical images obtained with an image histogram, it was estimated that ∼75% of the film was single-layer graphene, ∼25% was few-layer (< 4 layers) graphene and only 1% of the surface area was occupied with graphene films of greater thickness. This shows graphene layers with a greater percentage of monolayer coverage than the equivalent figure for growth on Ni using methane [36, 39, 40] can be achieved with this simplistic UHV growth process.

6.3 Summary

The formation of graphene layers on a Ni thin film has been detailed. Large continuous graphene sheets isolated on an insulator were achieved by annealing

a Ni thin film sample at 800°C in vacuum and the subsequent transfer of the graphene layers onto a SiO_2/Si(100) sample. Approximately 75% of the surface area of the graphene produced was shown to be a single-layer in thickness.

STM and AFM measurements of the sample surface revealed a radical change in Ni surface morphology after annealing to 800°C whilst in UHV, where large (micron length scale) terraced Ni grains were formed – lower temperature anneals produced only nanometre-sized grains and few terraces. Very recent studies at atmospheric pressure in an inert atmosphere using diffuse reflectance show similar changes in the nickel morphology [122].

Detailed XPS experiments were performed on Ni thin films that had been prepared with different anneal temperatures. A comparison of samples that had been dosed with propylene after annealing, and samples that were only annealed was also performed. Lower temperature (500°C) anneals were shown to remove the nickel oxide present in the Ni thin film surface, but higher anneal temperatures were required to produce the graphene layers that protected the Ni surface from adsorption of contaminants when the sample was removed to ambient conditions. Dosing of the Ni thin films with propylene unexpectedly revealed no significant differences to undosed samples when studying the surface with XPS.

Exposure to hydrocarbons was not required to produce graphene on the Ni surface as the annealing process converted trace amounts of unintentionally introduced carbon into graphene monolayers in a highly reproducible process. These results again highlighted the potential importance of unintentional carbon sources which must be considered when developing models for graphene growth.

The graphene layers were transferred from the Ni thin film to different substrates to allow further characterisation with optical and electron microscopy, and Raman spectroscopy. The results of which revealed the high quality, low defect coverage of the graphene and confirmed the presence and percentage of the monolayer and few-layer areas of graphene. Turbostratic stacking of graphene in few-layer areas was also revealed by Raman spectroscopy

Chapter 7

Conclusions

In conclusion, the construction of a combined AFM/STM system for UHV investigations, the formation of boron nitride and graphene monolayers on transition metal thin films, and a series of UHV-SPM studies of molecular self-assembly, have been described.

The constructed AFM/STM system allowed conventional STM operation with either a conventional STM tip or a tuning fork (TF) tip. The TF tip assemblies could be used for dc-STM or dynamic STM measurements, and different AFM modes with the ability to simultaneously monitor the tunnel current. Unlike the qPlus-sensor arrangement, the TF tip assemblies contained an electrically isolated metal tip for tunnel current measurements and the TF was mechanically excited with a piezoelectric transducer. These modifications allowed an increased signal-to-noise ratio and improved Q-factor.

The AFM/STM system was used to investigate the molecular adsorption of PTCDI on a HOPG surface, as well as graphene monolayers formed on Rh(111) thin films with an alkene cracking technique. Similar results were observed for the graphene produced on the propylene-dosed rhodium thin films and the solvent immersion technique. Interesting results were also revealed in the dissipation images acquired in dynamic STM mode, but further experiments would be required with improved resolution or high resolution FM-AFM to determine the exact cause of this dissipation.

Deposition of PTCDI on a graphite surface resulted in the formation of highly faceted rod-like islands with typical widths of $\sim$6 nm. These islands spread across step edges and formed branched structures, with second layer formation of PTCDI occurring even for submonolayer coverage – indicating a Volmer-Weber growth mode. It was possible to resolve steps of approximately 0.1 nm in FM-AFM mode

and achieve molecular lateral resolution in dynamic STM mode with the combined AFM/STM system. Tunnelling spectroscopy investigations revealed that the 2D islands formed by PTCDI on HOPG produced a large energy gap. Therefore the STM tip-sample separation was reduced over the PTCDI islands during imaging to maintain a constant tunnel current and thus the forces exerted by the tip on the surface were increased. The dynamic STM mode had the advantage of exerting reduced lateral forces on the adsorbed molecules when compared to conventional STM. It was also possible to image PTCDI islands with ac-STM that could not be imaged using dc-STM mode with the same small bias voltages.

A corrugated boron nitride monolayer was formed on the surface of a Rh(111) thin film in UHV, and subsequently investigated with STM whilst in UHV, ambient and liquid conditions. These investigations revealed the durability of the boron nitride nanomesh surface, as it was unaffected when removed from UHV conditions. In-situ STM results of the molecular adsorption of PTCDI and DP-PTCDI whilst in UHV were also included. Irregular 2D close-packed islands were formed for deposition of either molecule on the boron nitride nanomesh surface, and both islands aligned with the Moiré superstructure and islands that were misaligned were observed. PTCDI islands were also shown to have domains of varying orientation within the 2D islands themselves.

The 2 nm pores of the boron nitride layer trapped the PTCDI and DP-PTCDI molecules, with examples of single and multiple molecules situated in the pores. Typically, the single molecules were positioned near the edge of a pore rather than the centre, with one functional end facing towards the edge of the pore. Molecules that were trapped in the pores were imaged with STM within nanometres of the 2D islands also observed. However, annealing the surface at temperatures of less than 300°C removed the PTCDI and DP-PTCDI molecules that had formed the close-packed islands, with only the trapped molecules in the pores of the boron nitride monolayer remaining.

A novel method of immersing a Rh(111) thin film in a solvent – primarily acetone – and subsequently annealing the sample in UHV resulted in the formation of monolayer graphene. A similar graphene monolayer was also formed in UHV by propylene dosing the Rh(111) thin film whilst the sample was at 800°C. A Moiré superstructure was revealed with STM, consisting of 12 × 12 graphene unit cells overlaid on 11 × 11 Rh(111) unit cells, with an overall periodicity of 2.95 nm. XPS, XPD and LEED confirmed the superstructure periodicity and that the graphene was indeed a monolayer in thickness. STM imaging of the surface in ambient conditions concluded that the surface was stable outside of UHV conditions, as

had been shown for the boron nitride monolayer on the same surface.

The adsorption of PTCDI, DP-PTCDI and DB-CTCDI molecules on the graphene surface in UHV conditions was also investigated. Hydrogen-bonded dimer and trimer molecular junctions were revealed using STM that formed either commensurate rows or a honeycomb network. The formation of either dimer or trimer junctions was governed by the length of the side chains of the molecules. PTCDI – with no side chains – formed commensurate rows, DB-CTCDI molecules – with the longest side chains – formed a hexagonal arrangement, whilst DP-PTCDI was an intermediate. The molecules were positioned on areas of the graphene monolayer that were more strongly bound to the Rh(111) surface at the (fcc,top) and (top,hcp) sites. The formation of the molecular rows was determined by intermolecular interactions but the placement and separation of the rows was guided by the underlying level of organisation of the Moiré pattern. This was due to the local potential of the graphene superstructure which inhibited the formation of 2D islands unless the sample was annealed.

This was in contrast to the results of molecular adsorption on the boron nitride monolayer on a Rh(111) thin film and PTCDI adsorption on HOPG, where islands were readily formed. This was due to the weak substrate-adsorbate interaction of the HOPG surface – that allowed Volmer-Weber growth and 3D PTCDI islands to form – and the difference in the boron nitride and graphene superstructures. The boron nitride monolayer was corrugated so that there were 'pores' and 'wires' and thus the molecules were trapped in the pores. However, the graphene monolayers formed 'hills' and 'valleys' and the adsorbed molecules were positioned on the areas of the graphene that were strongly bound to the rhodium atoms. An anneal was required for the organic molecules to overcome the effect of the graphene superstructure to form 2D islands, however, the perylene islands on a boron nitride surface were desorbed after an anneal. Hence the substrate-adsorbate interaction appeared strongest for the graphene superstructure and weakest for the graphite surface, with the boron nitride superstructure as an intermediate. Further investigations of annealed graphite surfaces could determine if there is a similar effect for the adsorbed 3D PTCDI islands as the 2D PTCDI islands on the boron nitride surface after an anneal.

Further experiments could also be performed – with higher resolution – into the co-adsorption of PTCDI and DB-CTCDI molecules on a g/Rh(111) surface, to determine the interactions between the two types of molecule. In this thesis, firstly PTCDI and then DB-CTCDI was deposited onto the surface, and therefore the adsorption of the molecules in reverse order may lead to interesting results. The

variation of the deposition ratio of the PTCDI and DB-CTCDI molecules and the control of the nanostructures formed both before and after annealing the surface could lead to interesting large-scale doping of the graphene monolayer. However, the annealing of purely adsorbed DB-CTCDI should also be investigated to fully understand the behaviour of the PTCDI and DB-CTCDI molecules with each other.

The adsorption of the buckminsterfullerene on the g/Rh(111) surface was also investigated. Unlike the adsorption of perylene and coronene derivatives, 2D close-packed islands (both aligned and misaligned with the Moiré superstructure) were formed without annealing the substrate. Possible host-guest architectures involving the perylene/coronene derivatives and the fullerene were also investigated but no such interaction was found. However, further studies with higher initial coverages of PTCDI and DB-CTCDI prior to C_{60} deposition could be considered. Higher coverages of individual depositions of each of the organic molecules could also be investigated to study the growth mechanisms of more than one molecular layer and if there is an effect caused by the underlying superstructure.

Tunnelling spectroscopy could be performed on the graphene surface and adsorbed organic molecules on the same surface to investigate the potential of an induced band-gap that could be spatially controlled at the nanoscale. The potential of this graphene formation technique and the associated organic nanostructure formation would be greatly increased if a process for detaching and isolating the graphene monolayer from the rhodium substrate was determined. Whether the graphene superstructure and organic nanostructures on the graphene surface (or only one of the two) were still intact after this process could then be investigated with SPM techniques. If these nanostructures were indeed still present, the properties of the nanostructures could be explored with tunnelling spectroscopy or other electrical measurement techniques. Properties such as transparency, flexibility and conductivity of the graphene monolayer could also be investigated and compared with graphene monolayers formed through other formation processes.

Further to this avenue of investigation, the formation, detachment and isolation of graphene layers using a sacrificial Ni thin film was explored. Large continuous graphene sheets isolated on an insulator were achieved by annealing a Ni thin film sample at 800°C in vacuum conditions and then transferring the graphene layers onto a SiO_2/Si(100) sample. Approximately 75% of the surface area of the graphene produced was shown to be a monolayer in thickness.

XPS experiments revealed that 500°C anneals removed the nickel oxide present in the Ni thin film surface, but higher anneal temperatures were required to pro-

duce the graphene layers that protected the Ni surface from adsorption of contaminants when the sample was removed to ambient conditions. STM and AFM measurements of the sample surface confirmed a radical change in Ni surface morphology after annealing to 800°C whilst in UHV, where micron-sized terraced Ni grains were formed – lower temperature anneals produced only nanometre-sized grains and few terraces. Dosing of the Ni thin films with propylene unexpectedly revealed no significant differences when compared to undosed samples.

Exposure to hydrocarbons in UHV was not required to produce graphene on the Ni surface as the annealing process converted trace amounts of unintentionally introduced carbon into graphene monolayers in a highly reproducible process. The novel formation of graphene on rhodium and nickel surfaces using an ex-situ immersion technique, as well as the production of graphene on nickel without any external source of carbon, highlights the importance of unintentional carbon sources which must be considered when developing models for graphene growth.

The graphene layers were transferred from the Ni thin film to different substrates for further characterisation with optical microscopy, electron microscopy, and Raman spectroscopy. The results of which revealed the low defect coverage of the graphene and confirmed the presence and percentage of the monolayer and few-layer areas of graphene. Turbostratic stacking of graphene in few-layer areas was also revealed with Raman spectroscopy.

References

[1] G. M. Whitesides, J. P. Mathias, and C. T. Seto. Molecular self-assembly and nanochemistry: A chemical strategy for the synthesis of nanostructures. *Science*, 254:5036, 1991.

[2] J. V. Barth, G. Costantini, and K. Kern. Engineering atomic and molecular nanostructures at surfaces. *Nature*, 437:671–679, 2005.

[3] S. Hecht. Welding, organizing, and planting organic molecules on substrate surfaces–promising approaches towards nanoarchitectonics from the bottom up. *Angew. Chem. Int. Ed.*, 3:24, 2003.

[4] S. De Feyter and F. C. De Schryver. Two-dimensional supramolecular self-assembly probed by scanning tunneling microscopy. *Chem. Soc. Rev.*, 32:139–150, 2003.

[5] J. A. Theobald, N. S. Oxtoby, M. A. Phillips, N. R. Champness, and P. H. Beton. Controlling molecular deposition and layer structure with supramolecular surface assemblies. *Nature*, 424:1029–1031, 2003.

[6] S. J. H. Griessl, M. Lackinger, F. Jamitzky, T. Markert, M. Hietschold, and W. M. Heckl. Incorporation and manipulation of coronene in an organic template structure. *Langmuir*, 20:9403–9407, 2004.

[7] M. O. Blunt, J. C. Russell, M. D. Giménez-López, J. P. Garrahan, X. Lin, M. Schröder, N. R. Champness, and P. H. Beton. Random tiling and topological defects in a two-dimensional molecular network. *Science*, 322:1077–1081, 2008.

[8] M. Simard, D. Su, and J. D. Wuest. Use of hydrogen bonds to control molecular aggregation. self-assembly of three-dimensional networks with large chambers. *J. Am. Chem. Soc.*, 113:4696–4698, 1991.

[9] A. Nagashima, N. Tejima, Y. Gamou, T. Kawai, and C. Oshima. Electronic dispersion relations of monolayer hexagonal boron nitride formed on the Ni(111) surface. *Phys. Rev. B*, 51:4606–4613, 1995.

[10] A. Nagashima, N. Tejima, Y. Gamou, T. Kawai, and C. Oshima. Electronic-structure of monolayer hexagonal boron-nitride physisorbed on metal-surfaces. *Phys. Rev. Lett.*, 75:3918–3921, 1995.

[11] R. M. Desrosiers, D. W. Greve, and A. J. Gellman. Nucleation of boron nitride thin films on Ni(100). *Surf. Sci.*, 382:35–48, 1997.

[12] M. Corso, W. Auwärter, M. Muntwiler, A. Tamai, T. Greber, and J. Osterwalder. Boron nitride nanomesh. *Science*, 303:217, 2004.

[13] O. Bunk, M. Corso, D. Martoccia, R. Herger, P. R. Willmott, B. D. Patterson, J. Osterwalder, J. F. van der Veen, and T. Greber. Surface X-ray diffraction study of boron-nitride nanomesh in air. *Surf. Sci.*, 601:L7–L10, 2007.

[14] S. Berner, M. Corso, R. Widmer, O. Groening, R. Laskowski, P. Blaha, K. Schwarz, A. Goriachko, H. Over, S. Gsell, M. Schreck, H. Sachdev, T. Greber, and J. Osterwalder. Boron nitride nanomesh: Functionality from a corrugated monolayer. *Angew. Chem. Int. Ed.*, 46:5115–5119, 2007.

[15] R. Laskowski, P. Blaha, T. Gallauner, and K. Schwarz. Single-layer model of the hexagonal boron nitride nanomesh on the Rh(111) surface. *Phys. Rev. Lett.*, 98:106802, 2007.

[16] T. Greber, L. Brandenberger, M. Corso, A. Tamai, and J. Osterwalder. Single layer hexagonal boron nitride films on Ni(110). *e-J. Surf. Sci. Nanotech.*, 4:410, 2006.

[17] A. B. Preobrajenski, A. S. Vinogradov, and N. Martensson. Monolayer of h-BN chemisorbed on Cu(111) and Ni(111): The role of the transition metal 3d states. *Surf. Sci.*, 582:21–30, 2005.

[18] M. T. Paffett, R. J. Simonson, P. Papin, and R. T. Paine. Borazine adsorption and decomposition at Pt(111) and Ru(001) surfaces. *Surf. Sci.*, 232:286–296, 1990.

[19] F Müller, K Stöwe, and H Sachdev. Symmetry versus commensurability: Epitaxial growth of hexagonal boron nitride on Pt(111) from B-trichloroborazine $(ClBNH)_3$. *Chem. Mater.*, 17:3464–3467, 2005.

[20] M. Morscher, M. Corso, T. Greber, and J. Osterwalder. Formation of single layer h-BN on Pd(111) . *Surf. Sci.*, 600:3280–3284, 2006.

[21] M. Corso, T. Greber, and J. Osterwalder. h-BN on Pd(110): a tunable system for self-assembled nanostructures? *Surf. Sci.*, 577:L78–L84, 2005.

[22] T. Greber, M. Corso, and J. Osterwalder. Fermi surfaces of single layer dielectrics on transition metals. *Surf. Sci.*, 603:1373–1377, 2009.

[23] A. Goriachko, Y. He, M. Knapp, H. Over, M. Corso, T. Brugger, S. Berner, J. Osterwalder, and T. Greber. Self-assembly of a hexagonal boron nitride nanomesh on Ru(0001). *Langmuir*, 23:2928–2931, 2007.

[24] R. Laskowski, P. Blaha, and K Schwarz. Bonding of hexagonal BN to transition metal surfaces: An ab initio density-functional theory study. *Phys. Rev. B*, 78:045409, 2008.

[25] R. Laskowski and P. Blaha. Ab initio study of h-BN nanomeshes on Ru(001), Rh(111), and Pt(111). *Phys. Rev. B*, 81:075418, 2010.

[26] H. Dil, J. Lobo-Checa, R. Laskowski, P. Blaha, S. Berner, J. Osterwalder, and T. Greber. Surface trapping of atoms and molecules with dipole rings. *Science*, 319:1824–1826, 2008.

[27] A. B. Preobrajenski, M. L. Ng, N. A. Vinogradov, A. S. Vinogradov, E. Lundgren, A. Mikkelsen, and N. Martensson. Impact of Oxygen Coadsorption on Intercalation of Cobalt under the h-BN Nanomesh. *Nano Lett.*, 9:2780–2787, 2009.

[28] A. Goriachko and H. Over. Modern Nanotemplates Based on Graphene and Single Layer h-BN. *Z. Phys. Chem.*, 223:157–168, 2009.

[29] T. Brugger, S. Günther, B. Wang, J. H. Dil, M.-L. Bocquet, J. Osterwalder, J. Wintterlin, and T. Greber. Comparison of electronic structure and template function of single-layer graphene and a hexagonal boron nitride nanomesh on Ru(0001). *Phys. Rev. B*, 79:045407, 2009.

[30] P. R. Wallace. The band theory of graphite. *Phys. Rev.*, 71:622–634, 1947.

[31] K. S. Novoselov, A. K. Geim, S. V. Morozov, D. Jiang, Y. Zhang, S. V. Dubonos, I. V. Grigorieva, and A. A. Firsov. Electric field effect in atomically thin carbon films. *Science*, 306:666–669, 2004.

[32] A. K. Geim and K. S. Novoselov. The rise of graphene. *Nature Mater.*, 6:183–191, 2007.

[33] J.-H. Chen, C. Jang, S. Xiao, M. Ishigami, and M. S. Fuhrer. Intrinsic and extrinsic performance limits of graphene devices on SiO_2. *Nat. Nanotechnol.*, 3:206–209, 2008.

[34] C. Lee, X. Wei, J. W. Kysar, and J. Hone. Measurement of the elastic properties and intrinsic strength of monolayer graphene. *Science*, 321:385–388, 2008.

[35] R. R. Nair, P. Blake, A. N. Grigorenko, K. S. Novoselov, T. J. Booth, T. Stauber, N. M. R. Peres, and A. K. Geim. Fine structure constant defines visual transparency of graphene. *Science*, 320:1308, 2008.

[36] K. S. Kim, Y. Zhao, H. Jang, S. Y. Lee, J. M. Kim, K. S. Kim, J.-H. Ahn, P. Kim, J.-Y. Choi, and B. H. Hong. Large-scale pattern growth of graphene films for stretchable transparent electrodes. *Nature*, 457:706–710, 2009.

[37] P. Avouris, Z. Chen, and V. Perebeinos. Carbon-based electronics. *Nat. Nanotechnol.*, 2:605, 2007.

[38] A. M. Shikin, D. Farías, V. K. Adamchuk, and K. H. Rieder. Surface phonon dispersion of a graphite monolayer adsorbed on Ni(111) and its modification caused by intercalation of Yb, La and Cu layers. *Surf. Sci.*, 424:155–167, 1999.

[39] A. Reina, X. Jia, J. Ho, D. Nezich, H. Son, V. Bulovic, M. S. Dresselhaus, and J. Kong. Large area, few-layer graphene films on arbitrary substrates by chemical vapor deposition. *Nano Lett.*, 9:30–35, 2009.

[40] Q. Yu, J. Lian, S. Siriponglert, H. Li, Y. P. Chen, and S. S. Pei. Graphene segregated on Ni surfaces and transferred to insulators. *Appl. Phys. Lett.*, 93:113103, 2008.

[41] X. Li, W. Cai, J. An, S. Kim, J. Nah, D. Yang, R. Piner, A. Velamakanni, I. Jung, E. Tutuc, S. K. Banerjee, L. Colombo, and R. S. Ruoff. Large-area synthesis of high-quality and uniform graphene films on copper foils. *Science*, 342:1312–1314, 2009.

[42] S. Bae, H. Kim, Y. Lee, X. Xu, J-S. Park, Y. Zheng, J. Balakrishnan, T. Lei, H. R. Kim, Y. I. Song, Y-J. Kim, K. S. Kim, B. Özyilmaz, J-H. Ahn, B. H. Hong, and S. Iijima. Roll-to-roll production of 30-inch graphene films for transparent electrodes. *Nat. Nanotechnol.*, 5:574–578, 2010.

[43] C. Berger, Z. Song, T. Li, X. Li, A. Y. Ogbazghi, R. Feng, Z. Dai, A. N. Marchenkov, E. H. Conrad, P. N. First, and W. A. de Heer. Ultrathin epitaxial graphite: 2D electron gas properties and a route toward graphene-based nanoelectronics. *J. Phys. Chem. B*, 108:19912–19916, 2004.

[44] C. Berger, Z. Song, X. Li, X. Wu, N. Brown, C. Naud, D. Mayou, T. Li, J. Hass, A. N. Marchenkov, E. H. Conrad, P. N. First, and W. A. de Heer. Electronic confinement and coherence in patterned epitaxial graphene. *Science*, 312:1191–1196, 2006.

[45] J. Coraux, A. T. N'Diaye, C. Busse, and T. Michely. Structural coherency of graphene on Ir(111). *Nano Lett.*, 8:565–570, 2008.

[46] A. T. N'Diaye, J. Coraux, T. N. Plasa, C. Busse, and T. Michely. Structure of epitaxial graphene on Ir(111). *New J. Phys.*, 10:043033, 2008.

[47] P. W. Sutter, J. I. Flege, and E. A. Sutter. Epitaxial graphene on ruthenium. *Nat. Mater.*, 7:406–411, 2008.

[48] D. Martoccia, P. R. Willmott, T. Brugger, M. Björck, S. Günther, C. M. Schlepütz, A. Cervellino, S. A. Pauli, B. D. Patterson, S. Marchini, J. Wintterlin, W. Moritz, and T. Greber. Graphene on Ru(0001): a 25x25 supercell. *Phys. Rev. Lett.*, 101:126102, 2008.

[49] A. B. Preobrajenski, M. L. Ng, A. S. Vinogradov, and N. Martensson. Controlling graphene corrugation on lattice-mismatched substrates. *Phys. Rev. B*, 78:073401, 2008.

[50] G. Binnig, H. Rohrer, Ch. Gerber, and E. Weibel. Surface studies by scanning tunneling microscopy. *Phys. Rev. Lett.*, 49:57–61, 1982.

[51] G. Binnig, H. Rohrer, Ch. Gerber, and E. Weibel. 7×7 reconstruction on Si(111) resolved in real space. *Phys. Rev. Lett.*, 50:120–123, 1983.

[52] C. J. Chen. *Introduction to Scanning Tunneling Microscopy.* Oxford Science Publications, 2nd edition, 1993.

[53] J. Bardeen. Tunnelling from a many-particle point of view. *Phys. Rev. Lett.*, 6:57, 1961.

[54] J. Tersoff and D. R. Hamann. Theory of the scanning tunneling microscope. *Phys. Rev. B*, 31:805, 1985.

[55] K. Besocke. An easily operable scanning tunneling microscope. *Surf. Sci.*, 181:145–153, 1987.

[56] J. Wintterlin, J. Wiechers, H. Brune, T. Gritsch, H. Hofer, and R. J. Behm. Atomic-resolution imaging of close-packed metal-surfaces by scanning tunneling microscopy. *Phys. Rev. Lett.*, 62:59–62, 1989.

[57] R. H. J. Fawcett. *Manipulation of molecules, molecular clusters and supramolecular nanostructures by Scanning Tunnelling Microscopy.* PhD thesis, University of Nottingham, 2006.

[58] G. Binnig and H. Rohrer. Scanning tunneling microscopy - from birth to adolescence. *Rev. Mod. Phys.*, 59:615–625, 1987.

[59] A. L. Robinson. A spatially resolved surface spectroscopy. *Science*, 229:1074–1076, 1985.

[60] R. J. Hamers, R. M. Tromp, and J. E. Demuth. Surface electronic-structure of Si(111)-(7x7) resolved in real space. *Phys. Rev. Lett.*, 56:1972–1975, 1986.

[61] M. Knudsen. Experimental determination of the pressure of saturated mercury steam at 0 degrees and at higher temperatures. *Ann. d. Phys.*, 29:179–193, 1909.

[62] B. L. Rogers, J. G. Shapter, W. M. Skinner, and K. Gascoigne. A method for production of cheap, reliable Pt-Ir tips. *Rev. Sci. Instrum.*, 71:1702–1705, 2000.

[63] G. Binnig, C. F. Quate, and Ch. Gerber. Atomic force microscope. *Phys. Rev. Lett.*, 56:930–933, 1986.

[64] W. Han, S. M. Lindsay, and T. Jing. A magnetically driven oscillating probe microscope for operation in liquids. *Appl. Phys. Lett.*, 69:4111, 1996.

[65] F. J. Giessibl and B. M. Trafas. Piezoresistive cantilevers utilized for scanning tunneling and scanning force microscope in ultrahigh vacuum. *Rev. Sci. Instrum.*, 65:1923, 1994.

[66] D. Rugar and P. Hansma. Atomic force microscopy. *Physics Today*, 43:23, 1990.

[67] G. Binnig, C. Gerber, E. Stoll, T. R. Albrecht, and C. F. Quate. Atomic resolution with atomic force microscope. *Europhys. Lett.*, 3:1281–1286, 1987.

[68] T. R. Albrecht and C. F. Quate. Atomic resolution with the atomic force microscope on conductors and nonconductors. *J. Vac. Sci. Technol. A*, 6:271, 1988.

[69] R. García and R. Pérez. Dynamic atomic force microscopy methods. *Surf. Sci. Rep.*, 47:197, 2002.

[70] R. Erlandsson, L. Olsson, and P. Mårtensson. Inequivalent atoms and imaging mechanisms in ac-mode atomic-force microscopy of Si(111)7×7. *Phys. Rev. B*, 54:8309–8312, 1996.

[71] T. Junno, S. B. Carlsson, H. Q. Xu, L. Montelius, and L. Samuelson. Fabrication of quantum devices by angstrom-level manipulation of nanoparticles with an atomic force microscope. *Appl. Phys. Lett.*, 72:548–550, 1998.

[72] F. J. Giessibl. Atomic resolution of the silicon (111)-(7x7) surface by atomic force microscopy. *Science*, 267:68–71, 1995.

[73] T. Uchihashi, Y. Sugawara, T. Tsukamoto, M. Ohta, S. Morita, and M. Suzuki. Role of a covalent bonding interaction in noncontact-mode atomic-force microscopy on Si(111)7x7. *Phys. Rev. B*, 56:9834–9840, 1997.

[74] A. S. Foster, C. Barth, A. L. Shluger, and M. Reichling. Unambiguous interpretation of atomically resolved force microscopy images of an insulator. *Phys. Rev. Lett.*, 86:2373–2376, 2001.

[75] F. J. Giessibl, H. Bielefeldt, S. Hembacher, and J. Mannhart. Calculation of the optimal imaging parameters for frequency modulation atomic force microscopy. *Appl. Surf. Sci.*, 140:352–357, 1999.

[76] F. J. Giessibl. Advances in atomic force microscopy. *Rev. Mod. Phys.*, 75:949–983, 2003.

[77] F. J. Giessibl. *q*Plus Sensor, 1998.

[78] F. J. Giessibl. High-speed force sensor for force microscopy and profilometry utilizing a quartz tuning fork. *Appl. Phys. Lett.*, 73:3956–3958, 1998.

[79] F. J. Giessibl. Atomic resolution on Si(111)-(7x7) by noncontact atomic force microscopy with a force sensor based on a quartz tuning fork. *Appl. Phys. Lett.*, 76:1470, 2000.

[80] L. Gross, F. Mohn, N. Moll, P. Liljeroth, and G. Meyer. The chemical structure of a molecule resolved by atomic force microscopy. *Science*, 325:1110–1114, 2009.

[81] P. Zahl, M. Bierkandt, S. Schröder, and A. Klust. The flexible and modern open source scanning probe microscopy software package GXSM. *Rev. Sci. Instrum.*, 74:1222–1227, 2003.

[82] M. Herz, F. J. Giessibl, and J. Mannhart. Probing the shape of atoms in real space. *Phys. Rev. B*, 68:045301, 2003.

[83] M. Herz, C. Schiller, F. J. Giessibl, and J. Mannhart. Simultaneous current-, force-, and work-function measurement with atomic resolution. *Appl. Phys. Lett.*, 86:153101, 2005.

[84] L. A. Zotti, W. A. Hofer, and F. J. Giessibl. Electron scattering in scanning probe microscopy experiments. *Chem. Phys. Lett.*, 420:177–182, 2006.

[85] F. J. Giessibl, S. Hembacher, M. Herz, Ch. Schiller, and J. Mannhart. Stability considerations and implementation of cantilevers allowing dynamic force microscopy with optimal resolution: the qPlus sensor. *Nanotechnology*, 15:S79–S86, 2004.

[86] A. E. Gildemeister, T. Ihn, C. Barengo, P. Studerus, and K. Ensslin. Construction of a dilution refrigerator cooled scanning force microscope. *Rev. Sci. Instrum.*, 78:013704, 2007.

[87] C. Ludwig, B. Gompf, J. Petersen, R. Strohmaier, and W. Eisenmenger. STM investigations of PTCDA and PTCDI on graphite and MoS_2 - a systematic study of epitaxy and STM image-contrast. *Phys. B: Condens. Matter*, 93:365–373, 1994.

[88] J. C. Swarbrick, J. Ma, J. A. Theobald, N. S. Oxtoby, J. N. O'Shea, N. R. Champness, and P. H. Beton. Square, hexagonal, and row phases of PTCDA and PTCDI on Ag-Si(111)$\sqrt{3}$ x $\sqrt{3}$R30°. *J. Phys. Chem. B*, 109:12167–12174, 2005.

[89] L. M. A. Perdigão, E. W. Perkins, J. Ma, P. A. Staniec, B. L. Rogers, N. R. Champness, and P. H. Beton. Bimolecular networks and supramolecular traps on Au(111). *J. Phys. Chem. B*, 110:12539–12542, 2006.

[90] I. Horcas, R. Fernández, J. M. Gómez-Rodríguez, and J. Colchero. WSXM: A software for scanning probe microscopy and a tool for nanotechnology. *Rev. Sci. Instrum.*, 78:013705, 2007.

[91] S. Griessl, M. Lackinger, M. Edelwirth, M. Hietschold, and W. M. Heckl. Self-assembled two-dimensional molecular host-guest architectures from trimesic acid. *Single Mol.*, 3:25–31, 2002.

[92] T. G. Gopakumar, J. Meiss, D. Pouladsaz, and M. Hietschold. HOMO-LUMO gap shrinking reveals tip-induced polarization of molecules in ultrathin layers: Tip–sample distance-dependent scanning tunneling spectroscopy on d(8) (Ni, Pd, and Pt) phthalocyanines. *J. Phys. Chem. C*, 112:2529–2537, 2008.

[93] L. Kleiner-Shuhler, R. Brittain, M. R. Johnston, and K. W. Hipps. Scanning tunneling microscopy and orbital-mediated tunneling spectroscopy of N,N '-dioctyl-1,8 : 4,5-naphthalenediimide adsorbed on highly ordered pyrolytic graphite from various solvents and in different environments. *J. Phys. Chem. C*, 112:14907–14912, 2008.

[94] D. L. Keeling, N. S. Oxtoby, C. Wilson, M. J. Humphry, N. R. Champness, and P. H. Beton. Assembly and processing of hydrogen bond induced supramolecular nanostructures. *Nano Lett.*, 3:9–12, 2003.

[95] N. Berdunov, A. J. Pollard, and P. H. Beton. Dynamic scanning probe microscopy of adsorbed molecules on graphite. *Appl. Phys. Lett.*, 94:043110, 2009.

[96] E. W. Perkins, A. J. Pollard, P. H. Beton, K. Schulte, and Z. Li. Perylene behaviour on boron-nitride nanomesh. *In preparation*, 2010.

[97] S. Gsell, M. Fischer, M. Schreck, and B. Stritzker. Epitaxial films of metals from the platinum group (Ir, Rh, Pt and Ru) on YSZ-buffered Si(111). *J. Cryst. Growth*, 311:3731 – 3736, 2009.

[98] L. M. A. Perdigão, A. Saywell, G. N. Fontes, P. A. Staniec, G. Goretzki, A. G. Phillips, N. R. Champness, and P. H. Beton. Functionalized supramolecular nanoporous arrays for surface templating. *Chem. Eur. J.*, 14:7600–76007, 2008.

[99] F. Müller, H. Sachdev, S. Hüfner, A. J. Pollard, E. W. Perkins, J. C. Russell, P. H. Beton, S. Gsell, M. Schreck, and B. Stritzker. How does graphene grow? an easy access to well-ordered graphene films. *Small*, 5:2291–2296, 2009.

[100] G. E. Bacon. Unit-cell dimensions of graphite. *Acta Cryst.*, 3:137, 1950.

[101] H. P. Singh. Determination of thermal expansion of Germanium, Rhodium and Iridium by X-rays. *Acta Cryst.*, A 24:469–471, 1968.

[102] A. J. Pollard, E. W. Perkins, N. A. Smith, A. Saywell, G. Goretzki, A. G. Phillips, S. P. Argent, H. Sachdev, F. Müller, S. Hüfner, S. Gsell, M. Fischer, M. Schreck, J. Osterwalder, T. Greber, S. Berner, N. R. Champness, and P. H. Beton. Supramolecular assemblies formed on an epitaxial graphene superstructure. *Angew. Chem. Int. Ed.*, 49:1794–1799, 2010.

[103] Q. Chen, D. J. Frankel, and N. V. Richardson. Chemisorption induced chirality: glycine on Cu(110). *Surf. Sci.*, 497:37–46, 2002.

[104] F. Nolde, W. Pisula, S. Mueller, C. Kohl, and K. Muellen. Synthesis and self-organization of core-extended perylene tetracarboxdiimides with branched alkyl substituents. *Chem. Mater.*, 18:3715–3725, 2006.

[105] W. Chen, S. Chen, D. C. Qi, X. Y. Gao, and A. T. S. Wee. Surface transfer p-type doping of epitaxial graphene. *J. Am. Chem. Soc.*, 129:10418–10422, 2007.

[106] I. Pletikosić, M. Kralj, P. Pervan, R. Brako, J. Coraux, A. T. N'Diaye, C. Busse, and T. Michely. Dirac cones and minigaps for graphene on Ir(111). *Phys. Rev. Lett.*, 102:056808, 2009.

[107] H. Liu and P. Reinke. C_{60} thin film growth on graphite: Coexistence of spherical and fractal-dendritic islands. *J. Chem. Phys.*, 124:164707, 2006.

[108] W. Chen, H. L . Zhang, H. Xu, E. S. Tok, K. P. Loh, and A. T. S. Wee. C_{60} on SiC nanomesh. *J. Phys. Chem. B*, 110:21873–21881, 2006.

[109] A. J. Pollard, R. R. Nair, S. N. Sabki, C. R. Staddon, L. M. A. Perdigão, C. H. Hsu, J. M. Garfitt, S. Gangopadhyay, H. F. Gleeson, A. K. Geim, and P. H. Beton. Formation of monolayer graphene by annealing sacrificial nickel thin films. *J. Phys. Chem. C*, 113:16565–16567, 2009.

[110] E. F. Smith, F. J. M. Rutten, I. J. Villar-Garcia, D. Briggs, and P. Licence. Ionic liquids in vacuo: Analysis of liquid surfaces using ultra-high-vacuum techniques. *Langmuir*, 22:9386–9392, 2006.

[111] B. V. Crist. *Handbooks of Monochromatic XPS Spectra*, volume 1. Wiley, 1999.

[112] A. F. Carley, S. D. Jackson, J. N. O'Shea, and M. W. Roberts. The formation and characterisation of Ni^{3+} an X-ray photoelectron spectroscopic investigation of potassium-doped Ni(110)O. *Surf. Sci.*, 440:L868–L874, 1999.

[113] Y. Fukuda, M. Nagoshi, T. Suzuki, Y. Namba, Y. Syono, and M. Tachiki. Chemical states of Ba in $YBa_2Cu_3O_{7-\delta}$ studied by X-ray photoelectron spectroscopy. *Phys. Rev. B*, 39:11494–11497, 1989.

[114] P. R. Norton. Surface analysis of platinum by X-ray photoelectron spectroscopy (XPS). *Surf. Sci.*, 44:624–628, 1974.

[115] M. W. Roberts. Chemisorption and reactions at metal surfaces. *Surf. Sci.*, 299-300:769–784, 1994.

[116] P. Blake, E. W. Hill, A. H. Castro Neto, K. S. Novoselov, D. Jiang, R. Yang, T. J. Booth, and A. K. Geim. Making graphene visible. *Appl. Phys. Lett.*, 91:063124, 2007.

[117] J. C. Meyer, A. K. Geim, M. I. Katsnelson, K. S. Novoselov, T. J. Booth, and S. Roth. The structure of suspended graphene sheets. *Nature*, 446:60–63, 2007.

[118] J. C. Meyer, A. K. Geim, M. I. Katsnelson, K. S. Novoselov, D. Obergfell, S. Roth, C. Girit, and A. Zettl. On the roughness of single- and bi-layer graphene membranes. *Solid State Commun.*, 143:101–109, 2007.

[119] A. C. Ferrari, J. C. Meyer, V. Scardaci, C. Casiraghi, M. Lazzeri, F. Mauri, S. Piscanec, D. Jiang, K. S. Novoselov, S. Roth, and A. K. Geim. Raman spectrum of graphene and graphene layers. *Phys. Rev. Lett.*, 97:187401, 2006.

[120] C. Gomez-Navarro, R. T. Weitz, A. M. Bittner, M. Scolari, A. Mews, M. Burghard, and K. Kern. Electronic transport properties of individual chemically reduced graphene oxide sheets. *Nano Lett.*, 7:3499–3503, 2007.

[121] D. C. Elias, R. R. Nair, T. M. G. Mohiuddin, S. V. Morozov, P. Blake, M. P. Halsall, A. C. Ferrari, D. W. Boukhvalov, M. I. Katsnelson, A. K. Geim, and K. S. Novoselov. Control of graphene's properties by reversible hydrogenation: Evidence for graphane. *Science*, 323:610–613, 2009.

[122] J. H. Mun, C. Hwang, S. K. Lim, and B. J. Cho. Optical reflectance measurement of large-scale graphene layers synthesized on nickel thin film by carbon segregation. *Carbon*, 48:447–451, 2010.